Balance and imbalance: a middle Eocene perspective on coupled carbon cycle and climate change

Robin van der Ploeg

ISBN: 978-90-6266-532-7
ISSN: 2211-4335

USES No. 178

Author contact: r.vanderploeg@uu.nl or mail@robinvanderploeg.com

Cover: View of the Yellowstone River in Yellowstone National Park, Wyoming, United States. Photo by Robin van der Ploeg and design by Margot Stoete.

Printed in The Netherlands by Gildeprint

Balance and imbalance: a middle Eocene perspective on coupled carbon cycle and climate change

Balans en onbalans: een midden-Eoceen perspectief op gekoppelde verandering in de koolstofkringloop en het klimaat

(met een samenvatting in het Nederlands)

Proefschrift

ter verkrijging van de graad van doctor aan de Universiteit Utrecht op gezag van de rector magnificus, prof.dr. H.R.B.M. Kummeling, ingevolge het besluit van het college voor promoties in het openbaar te verdedigen op

vrijdag 29 maart 2019 des middags te 4.15 uur

door

Robin van der Ploeg

geboren op 30 juni 1992 te Amersfoort

Promotoren:

Prof. dr. A. Sluijs
Prof. dr. J. J. Middelburg

Copromotor:

Dr. S. M. Bohaty

This thesis was accomplished with funding from the Netherlands Earth System Science Centre (NESSC), which is financially supported by the Ministry of Education, Culture and Science (OCW) of the Netherlands.

Members of the dissertation committee:

Prof. dr. Lee Kump
Pennsylvania State University, United States

Prof. dr. Richard Zeebe
University of Hawaii at Manoa, United States

Dr. Helen Coxall
Stockholm University, Sweden

Prof. dr. Gert-Jan Reichart
Utrecht University, The Netherlands

Prof. dr. Lucas Lourens
Utrecht University, The Netherlands

Contents

12 Chapter 1: Introduction, synopsis and outlook

24 Chapter 2: Reconstructing global chemical weathering: an overview of proxies and their applications, with emphasis on the carbon cycle

Robin van der Ploeg, Karline Soetaert, Jack J. Middelburg and Appy Sluijs

To be submitted

60 Chapter 3: Secular variations in the carbonate chemistry of the oceans over the Cenozoic

Bernard P. Boudreau, Jack J. Middelburg, Appy Sluijs and Robin van der Ploeg

Published in Earth and Planetary Science Letters 512, 194–206 (2019)

90 Chapter 4: Global climate and sea level forcing on Cenozoic neritic carbonate burial

Robin van der Ploeg, Bernard P. Boudreau, Jack J. Middelburg and Appy Sluijs

In revision for Geology

110 Chapter 5: Middle Eocene greenhouse warming facilitated by diminished weathering feedback

Robin van der Ploeg, David Selby, Margot J. Cramwinckel, Yang Li, Steven M. Bohaty, Jack J. Middelburg and Appy Sluijs

Published in Nature Communications 9, 2877 (2018)

140 Chapter 6: Surface ocean warming in the North Atlantic during the Middle Eocene Climatic Optimum

Robin van der Ploeg, Margot J. Cramwinckel, Thomas J. Leutert, Steven M. Bohaty, Chris D. Fokkema, Rogier J. Hidding, Ilja J. Kocken, A. Nele Meckler, Anne E. van der Meer, Jack J. Middelburg, Inigo A. Müller, Francien Peterse, Gert-Jan Reichart, Stefan Schouten, Philip F. Sexton, Paul A. Wilson, Martin Ziegler and Appy Sluijs

To be submitted

168 **Chapter 7: Middle Eocene Climatic Optimum warming followed by organic carbon burial in the Tethys realm**

Robin van der Ploeg*, Margot J. Cramwinckel*, Niels Waarlo, Claudia Agnini, Peter K. Bijl, Annique van der Boon, Henk Brinkhuis, Joost Frieling, Larisa Golovina, Niels A. G. M. van Helmond, Wout Krijgsman, Tamsin Mather, Jack J. Middelburg, Francien Peterse, Sergey V. Popov, Caroline P. Slomp and Appy Sluijs
*Shared first-authorship

To be submitted

180 **Appendix I: ODP Site 1263 data report**

Robin van der Ploeg, Jack J. Middelburg and Appy Sluijs

In preparation for Earth System Science Data

182 **Appendix II: IODP Site U1333 data report**

Robin van der Ploeg, Jack J. Middelburg and Appy Sluijs

In preparation for Earth System Science Data

186 **References**

218 **Summary in Dutch (Samenvatting in het Nederlands)**

232 **Acknowledgements (Dankwoord)**

236 **Curriculum Vitae**

237 **Peer-reviewed publications**

"It seems to me that the natural world is the greatest source of excitement; the greatest source of visual beauty, the greatest source of intellectual interest. It is the greatest source of so much in life that makes life worth living."

Sir David Attenborough

Chapter 1

Introduction, synopsis and outlook

Introduction, synopsis and outlook

1.1 The geological carbon cycle

The carbon cycle is an essential part of the Earth system that connects the biosphere, atmosphere, oceans and geosphere. Importantly, the exchange of carbon between these reservoirs determines the amount of CO_2 in the atmosphere, which regulates the temperature at Earth's surface (Walker et al., 1981; Berner et al., 1983). On geological timescales of hundreds of thousands to millions of years, CO_2 is produced and released to the atmosphere and oceans via volcanic outgassing and the oxidative weathering of organic carbon in sediments (Berner, 2004). Conversely, CO_2 is consumed during the weathering of silicate rocks and eventually sequestered through organic and inorganic carbon burial in sediments (Figure 1). These sources and sinks of CO_2 should be in close balance over geological timescales, if habitable climatic conditions at Earth's surface are to be maintained (Berner, 2004; Zeebe and Caldeira, 2008). This stability in the carbon cycle is thought to be enforced by a negative feedback mechanism in which silicate weathering rates are modulated by climate, tectonic processes and continental weatherability (Walker et al., 1981; Berner et al., 1983; Raymo and Ruddiman, 1992; Kump and Arthur, 1997; Caves et al., 2016). Yet, transient climate and carbon cycle perturbations have occurred during various phases of Earth's history (IPCC, 2014). As such, the geological record provides a unique perspective on the natural causes and consequences of climate change and the timescales associated with recovery from carbon cycle perturbations.

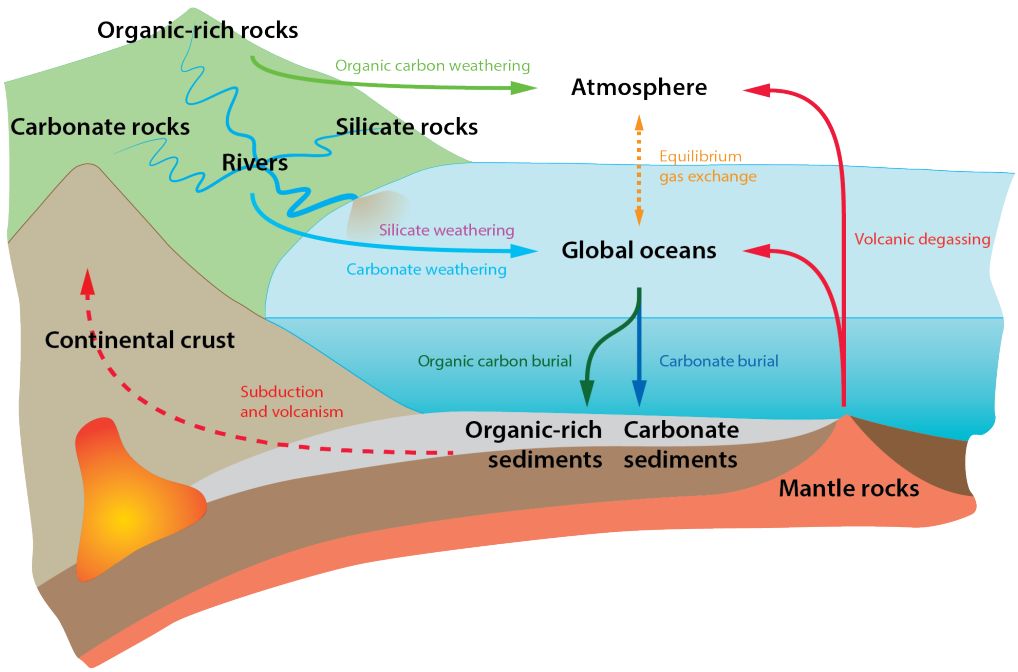

Figure 1: Schematic representation of processes involved in the geological carbon cycle.

1.2 Cenozoic climate and CO_2

The Cenozoic period, which represents the last ~66 million years (Myr) of Earth's history (Gradstein et al., 2012), is characterized by a gradual transition from a warm greenhouse world to a much cooler icehouse world, likely in response to progressively declining atmospheric CO_2 concentrations (Savin, 1977; Kennett, 1982; Zachos et al., 2008; Foster et al., 2017; Cramwinckel et al., 2018) (Figure 2). Over the past ~150 years, atmospheric CO_2 concentrations have risen from approximately 280 parts per million by volume (ppmv) to values exceeding 400 ppmv due to anthropogenic carbon emissions, which has so far resulted in 1 °C of global warming (IPCC, 2018). By comparison, CO_2 concentrations have varied between approximately 180–280 ppmv

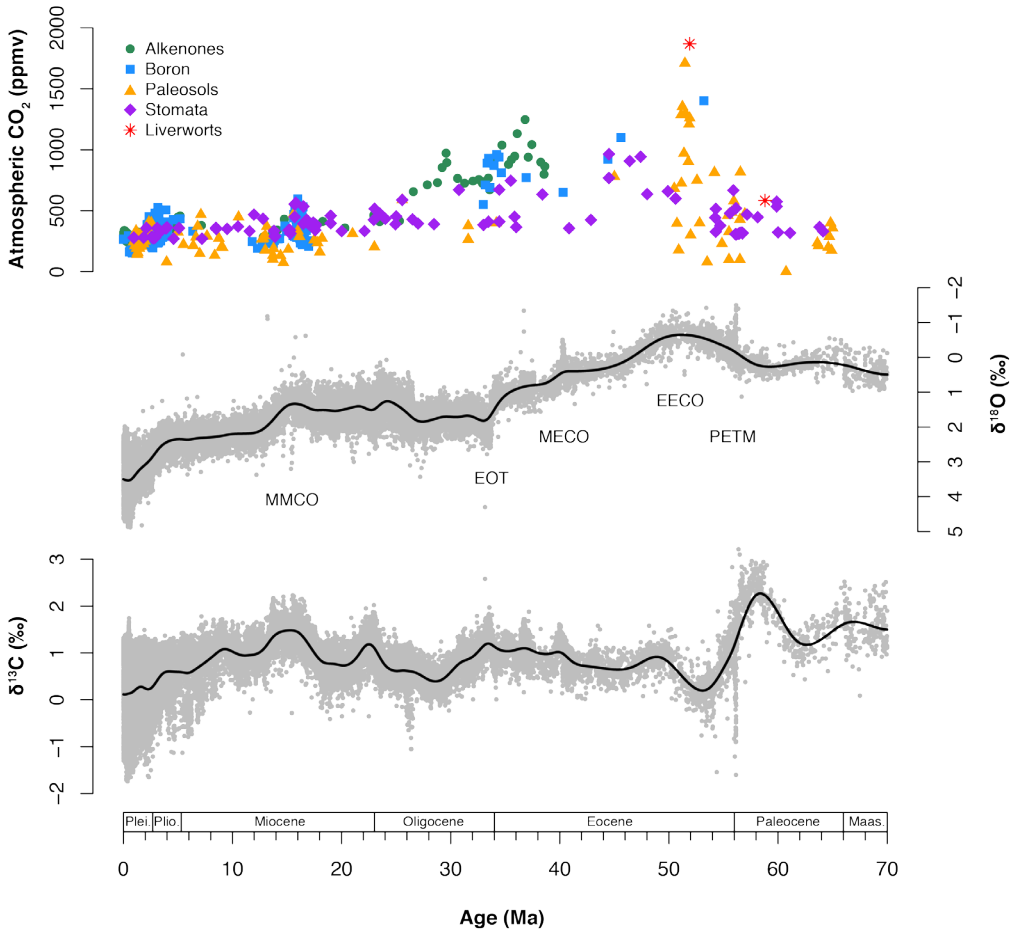

Figure 2: Cenozoic evolution of atmospheric CO_2 and global climate. Atmospheric CO_2 records are from Foster et al. (2017) and references therein, with alkenone-derived estimates as green circles, boron-derived estimates as blue squares, paleosol-derived estimates as orange triangles, stomata-derived estimates as purple diamonds and liverwort-derived estimates as red stars. Benthic foraminiferal oxygen isotope ($\delta^{18}O$) and carbon isotope ($\delta^{13}C$) records are derived from Cramer et al. (2009) and adjusted to the GTS 2012 (Gradstein et al., 2012). Solid black lines represent smoothed fits.

over the glacial-interglacial cycles of the last ~1 Myr (Lüthi et al., 2008). CO_2 concentrations similar to present-day conditions (i.e., ~400 ppmv) were last encountered during the Pliocene, roughly 3–5 million years ago (Ma) (Martínez-Botí et al., 2015). Even further back in time, CO_2 concentrations are estimated to have reached values of ~600 ppmv during the Miocene at ~15 Ma (Sosdian et al., 2018) and values of ~1000 ppmv or more during the Eocene at ~50 Ma (Anagnostou et al., 2016). For most of the Cenozoic, global temperatures and sea levels were much higher than at present (Miller et al., 2005; Herold et al., 2012; Haywood et al., 2016; Cramwinckel et al., 2018). Hence, the various phases of Cenozoic climate evolution represent potential analogues for future climate change due to anthropogenic carbon emissions (Zachos et al., 2008).

Of particular interest for studies of coupled carbon cycle and climate interactions are the so-called hyperthermals of the late Paleocene and early Eocene, including the Paleocene-Eocene Thermal Maximum (PETM; ~56 Ma) and Eocene Thermal Maximum 2 (ETM-2; ~54 Ma). These events represent transient episodes of global warming and ocean acidification that are associated with the rapid release of carbon to the atmosphere and oceans (Dickens et al., 1997; Zachos et al., 2003, 2005; Lourens et al., 2005). In particular, these hyperthermals are characterized by major negative shifts in the stable carbon isotopic composition ($\delta^{13}C$) of exogenic carbon, which indicates that carbon may have been sourced from methane hydrates (Dickens et al., 1995), organic matter (Kurtz et al., 2003) or potentially volcanic sources (Svensen et al., 2004; Gutjahr et al., 2017), or a combination of these mechanisms (Panchuk et al., 2008; Frieling et al., 2016). Importantly, the timescale of climate recovery following these hyperthermals is estimated to be in the order of ~100 kyr (Zachos et al., 2003, 2005), which is mainly attributed to enhanced silicate weathering rates in response to warming (Ravizza et al., 2001; Kelly and Zachos, 2005; Dickson et al., 2015). This fits well with predictions for the silicate weathering thermostat based on theory (Berner, 2004).

The exact role of silicate weathering in the long-term evolution of Cenozoic CO_2 and climate has been much debated since the silicate weathering thermostat hypothesis was originally proposed by Walker et al. (1981) and Berner et al. (1983). For example, Raymo and Ruddiman (1992) have argued that an increase in weathering related to the tectonic uplift of the Himalayas may have acted as a driver of late Cenozoic cooling. This raises the fundamental question whether climatic or tectonic processes have been the dominant control on weathering

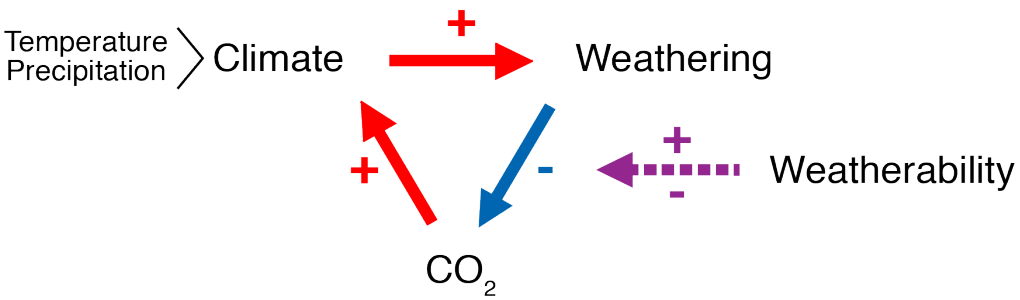

Figure 3: Schematic representation of the concept of continental weatherability, which regulates the strength of the negative silicate weathering feedback. Red arrows and plus symbols indicate processes that have a positive effect, and blue arrows and minus symbols indicate processes that have a negative effect. Changes in continental weatherability can alter the effectiveness of the silicate weathering thermostat.

over the Cenozoic and further back in time. Kump and Arthur (1997) have suggested that these contrasting views may be reconciled with the concept of variable continental weatherability, i.e., the modulation of weathering rates by long-term changes in the reactivity of Earth's surface (Figure 3). Such a variable silicate weathering feedback strength has subsequently been established through modeling of weathering fluxes based on Cenozoic records of atmospheric CO_2 and ocean chemistry (Caves et al., 2016). Importantly, a variable weathering feedback strength implies that weathering fluxes may have actually remained relatively invariant over geological timescales, while still maintaining a balance in the carbon cycle at different background levels of atmospheric CO_2 (Caves et al., 2016). This would be in agreement with weathering reconstructions that show approximately constant global weathering and erosion rates over the last ~10 Myr (Willenbring and Von Blanckenburg, 2010).

1.3 The Middle Eocene Climatic Optimum

Although the interactions between CO_2, climate and weathering in the geological past are increasingly well understood, the Middle Eocene Climatic Optimum (MECO; ~40 Ma) represents a carbon cycle perturbation for which both the cause and the subsequent recovery remain truly enigmatic (Sluijs et al., 2013). The MECO is a widespread warming episode of ~500 kyr that occurred superimposed on the long-term Eocene cooling trend and is associated with CO_2 rise, biotic change and carbonate dissolution in the deep oceans (Bohaty and Zachos, 2003; Bohaty et al., 2009; Bijl et al., 2010). Unlike Paleogene hyperthermals such as the PETM, the MECO is not marked by a negative $\delta^{13}C$ excursion and is characterized by a gradual onset of warming (~400 kyr) followed by a short peak warming phase (~50 kyr) and a relatively rapid cooling phase (~50 kyr) (Bohaty et al., 2009; Sluijs et al., 2013) (Figure 4). This precludes a sudden release of large amounts of $\delta^{13}C$-depleted carbon as a cause of or positive feedback to MECO warming and instead favors a more gradual mechanism resulting in a carbon cycle imbalance over ~500 kyr (Sluijs et al., 2013). Moreover, this duration of ~500 kyr questions the behavior of the silicate weathering thermostat, as enhanced weathering and CO_2 drawdown are thought to result in climatic recovery within 100–200 kyr based on inferences from the Paleogene hyperthermals (Zachos et al., 2005; Kelly et al., 2010). Consequently, the MECO differs from the traditionally identified trends, rhythms and aberrations in the climate system (Zachos et al., 2001) and challenges current understanding of carbon cycle and climate dynamics on intermediate timescales (Sluijs et al., 2013).

In addition to the apparent lack of a weathering response, several other aspects of the MECO are also not yet understood. First of all, while the MECO or its associated environmental changes (e.g., carbonate dissolution) have been identified in all major ocean basins (Bohaty et al., 2009), it is not yet clear if ocean warming was a truly global phenomenon. So far, significant warming has been reported at high-latitude sites in the Southern Ocean (Bohaty et al., 2009; Bijl et al., 2010), mid-latitude sites in the northern and southern Atlantic Ocean (Bohaty et al., 2009; Edgar et al., 2010; Boscolo Galazzo et al., 2014), mid-latitude sites in the Tethys realm (Jovane et al., 2007; Spofforth et al., 2010) and a site in the tropical Atlantic Ocean (Cramwinckel et al., 2018). As with many other deep-time temperature reconstructions, however, most existing MECO records are based on stable oxygen isotopic compositions ($\delta^{18}O$) of foraminifera or bulk carbonate sediments, which are also highly sensitive to local changes in seawater $\delta^{18}O$. Moreover, warming has not yet been established at high-latitude sites in the North Atlantic, or in the Pacific Ocean. Affirming the global character of MECO warming would represent an important step forward in identifying the cause of the event, because global

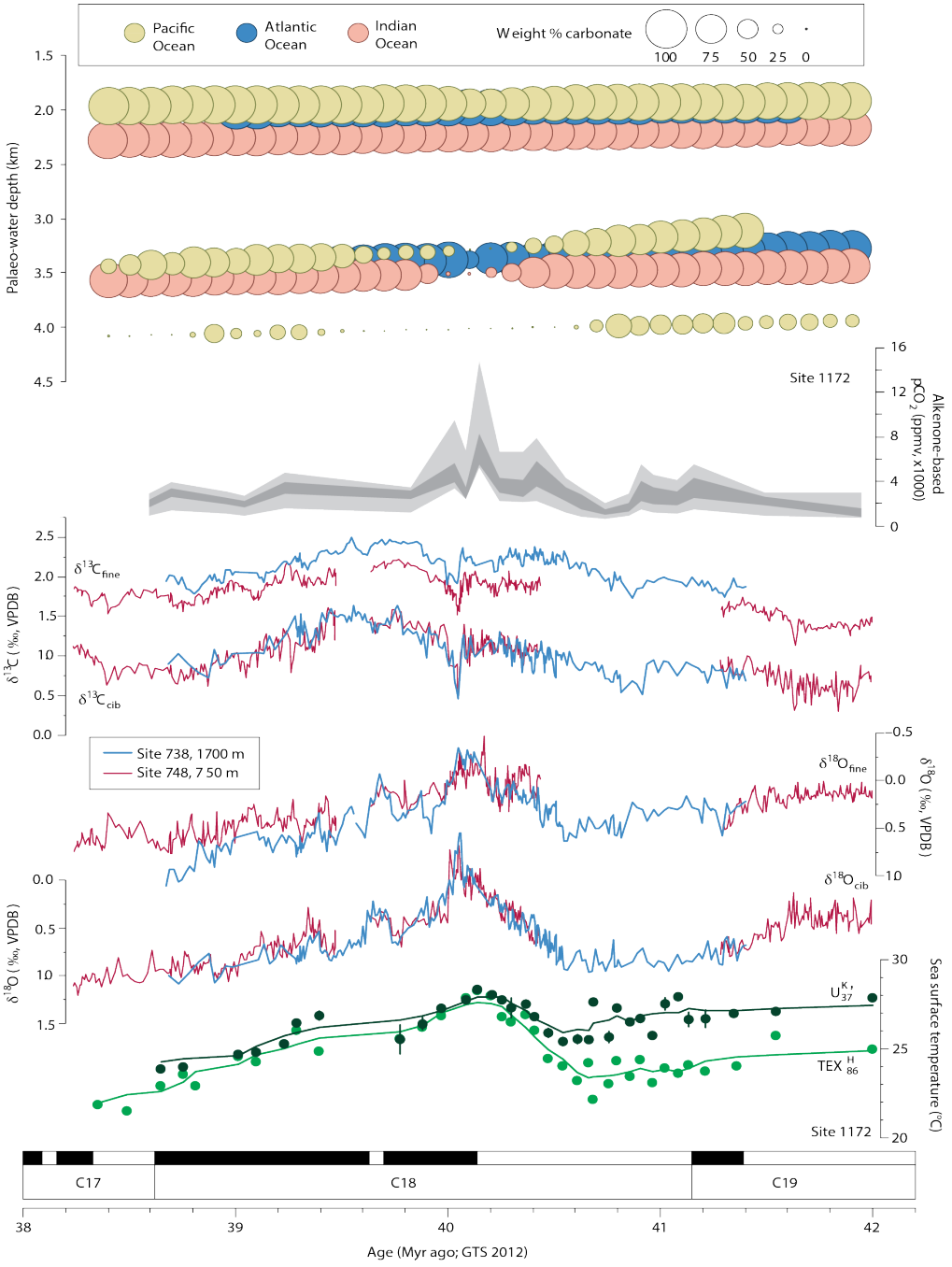

Figure 4: Compilation of MECO records, redrawn from Sluijs et al. (2013). Carbonate content records are from Hancock and Dickens (2005), Lyle et al. (2005) and Bohaty et al. (2009). $\delta^{18}O$ and $\delta^{13}C$ records are from Bohaty and Zachos (2003) and Bohaty et al. (2009). Atmospheric CO_2, TEX_{86}^{H} and $U^{K'}_{37}$ records are from Bijl et al. (2010).

warming would favor greenhouse gas forcing instead of regional processes such as changes in ocean circulation.

While $\delta^{18}O$ records provide good first-order constraints on relative temperature changes across the MECO, additional records from other proxies such as Mg/Ca, TEX_{86} or clumped isotopes (Δ_{47}) are required to more accurately determine absolute ocean temperatures. In a more general sense, this is also of importance for evaluating latitudinal temperature gradients and for further reducing the continued mismatch between temperatures inferred from proxy data and model predictions at high latitudes (Sluijs et al., 2009; Hollis et al., 2012; Frieling et al., 2016; Cramwinckel et al., 2018).

Furthermore, little is known about environmental change in continental shelf settings during the MECO. Sluijs et al. (2013) suggested that carbonate dissolution in the deep oceans during the event may potentially be explained by a shift in carbonate deposition from the deep oceans to shallow-water environments following sea level rise, but so far this hypothesis has not been tested. The shallowest pelagic sites where the MECO has been identified are located in the Tethys realm (Jovane et al., 2007; Spofforth et al., 2010), so this may be a promising area to obtain MECO records from a shelf setting as well.

Finally, the duration and mechanism of the termination of the MECO also remains unclear (Bohaty et al., 2009). The apparent absence of an effective negative silicate weathering feedback raises the question whether other processes may have contributed to the relatively rapid cooling as observed in deep-sea MECO records (Sluijs et al., 2013). One possibility is that organic carbon burial increased in the aftermath of the MECO, as inferred from elevated total organic carbon (TOC) contents at a site in the western Tethys Ocean (Spofforth et al., 2010). However, the scale on which this inferred organic carbon burial occurred remains unknown. Therefore, the characterization of the MECO at additional sites from the Tethys realm is crucial to assess whether organic carbon burial may have indeed contributed to CO_2 drawdown and climatic recovery following MECO warming.

1.4 Thesis scope and synopsis

The scope of this thesis is two-fold. I first explore ways to better understand the weathering history and overall evolution of the carbon cycle across the Cenozoic, and subsequently focus on the enigmatic interactions between CO_2, weathering and climate during the MECO. Within the first theme, I review the established proxies for reconstructions of global chemical weathering and model various weathering scenarios for the Cenozoic (Chapter 2). Then, I model secular changes in Cenozoic carbonate chemistry and test the robustness of published atmospheric CO_2 estimates (Chapter 3). Subsequently, I derive estimates of neritic carbonate burial over the Cenozoic with a model based on a mass balance for carbonate alkalinity (Chapter 4). Next, I present key new records to address the aforementioned outstanding questions regarding the MECO. In particular, I reconstruct changes in global silicate weathering and perform carbon cycle modeling to identify the most plausible cause for the MECO (Chapter 5). To address the issue of warming and potential confounding factors in sea surface temperature proxies during the MECO, I present high-resolution surface ocean temperature records from the North Atlantic based on multiple proxies (Chapter 6). Finally, I report temperatures and environmental change across the MECO from a continental shelf site in the Tethys realm (Chapter 7).

In Chapter 2, I present an overview of established proxies for global chemical weathering reconstructions in the geological past. I review the silicate weathering thermostat hypothesis

and illustrate how the isotope systems of carbon ($\delta^{13}C$), strontium ($^{87}Sr/^{86}Sr$), osmium ($^{187}Os/^{188}Os$), lithium ($\delta^{7}Li$), calcium ($\delta^{44}Ca$) and magnesium ($\delta^{26}Mg$) can be used to infer changes in weathering rates through time. Notably, $^{187}Os/^{188}Os$ is able to record changes in weathering over climatic timescales of 10–100 kyr, whereas the other proxies typically capture changes in weathering on timescales of ~1 Myr or more. I also discuss how various other aspects of the geochemical cycles of these elements are of importance for weathering reconstructions. Finally, I present several weathering scenarios for the Cenozoic based on inverse modeling of the marine $^{87}Sr/^{86}Sr$ and $^{187}Os/^{188}Os$ isotope records, and highlight the sensitivity of such estimates to underlying assumptions.

Changes in marine carbonate chemistry through time serve as an important basis for reconstructions of other aspects of the carbon cycle, including estimates of past atmospheric CO_2 concentrations. In Chapter 3, a model is used to estimate changes in the carbonate chemistry of the pelagic oceans across the Cenozoic. By combining published records of ocean temperatures, atmospheric CO_2 concentrations and the carbonate compensation depth (CCD) with estimates of carbonate ion (CO_3^{2-}) concentrations and pelagic carbonate burial rates, secular changes in dissolved inorganic carbon (DIC), alkalinity and pH are derived. The relative stability of the retrodicted DIC and alkalinity records over the Cenozoic supports a secular equilibrium between carbonate input and output fluxes, but important long-term trends are observed nonetheless. Within this study, I use these new alkalinity estimates to independently test assumptions regarding the carbonate system parameters used in published Cenozoic atmospheric CO_2 concentrations based on the boron isotope ($\delta^{11}B$) proxy. The newly obtained alkalinity estimates generally agree with the values used in the literature and hence most recalculated CO_2 concentrations are well within error of the published values. However, differences are apparent for the Miocene and especially the Eocene. Based on these new alkalinity estimates, I estimate Miocene CO_2 concentrations that are 50–100 ppmv higher than previously reported. In contrast, recalculated CO_2 concentrations for the Eocene are significantly lower than their published estimates, with a difference of more than 500 ppmv in the early Eocene at ~53 Ma. This implies that the evolution of the carbonate system may not be as well-constrained for the Eocene as previously thought and highlights the challenge of reconciling high atmospheric CO_2 concentrations with a shallow position of the CCD.

Carbonate accumulation occurs in pelagic as well as neritic environments, but changes in neritic carbonate burial through time are not well known. Hence, I utilize insights presented in both Chapter 2 and Chapter 3 to reconstruct neritic carbonate burial across the Cenozoic in Chapter 4. To this end, I derive a mass balance for the sources and sinks of carbonate alkalinity in the oceans, which incorporates estimates of alkalinity delivery associated with continental weathering together with independent estimates of pelagic carbonate burial. Resulting changes in neritic carbonate burial appear related to important climatic shifts and the evolution of global sea level over the course of the Cenozoic. Most notably, I predict a large drop in neritic carbonate burial that coincides with cooling and sea level fall at the Eocene-Oligocene Transition (~34 Ma). Similar decreases in neritic carbonate burial are found to correlate with the Mi-1 glaciation (~23 Ma) and the Middle Miocene Climate Transition (~14 Ma). Although the overall trends in neritic carbonate burial across the Cenozoic are ultimately dependent on the weathering scenario used, these transient, climate-related shifts in neritic burial seem robust under a large range of weathering assumptions. This further reinforces the theory that neritic carbonate accumulation is modulated by changes in global climate and sea level on geological timescales.

In Chapter 5, I reconstruct the silicate weathering response during the MECO to gain understanding of changes in carbon cycling on intermediate timescales of ~500 kyr. For this purpose, I present osmium isotope ($^{187}Os/^{188}Os$) records of marine sediments from three sites in the Atlantic and Pacific Oceans. Rather than the $^{187}Os/^{188}Os$ increase that would be expected from enhanced continental weathering in response to greenhouse warming, as has been established for the PETM, I document a modest $^{187}Os/^{188}Os$ decrease of ~0.05 during the MECO. This minor $^{187}Os/^{188}Os$ decrease is most likely related to enhanced volcanism and the associated weathering of fresh basalts, but sustained carbonate dissolution in the deep oceans during the MECO implies that total weathering rates must have remained approximately constant. I subsequently employ simulations with the established Long-term Ocean-atmosphere-Sediment CArbon cycle Reservoir model (LOSCAR; Zeebe, 2012a) to test a range of scenarios involving enhanced volcanism and/or diminished weathering to evaluate how the suite of MECO observations may best be explained. In principle, a 10–20% increase in volcanism over ~500 kyr would be sufficient to cause CO_2 accumulation and hence greenhouse warming. However, such an increase would result in deepening of the CCD instead of the observed shoaling. Crucially, I find that the model is only capable of reproducing a CCD shoaling on the timescale of the MECO by invoking enhanced volcanism in combination with a strongly diminished silicate weathering feedback. I hypothesize that such a reduction in weathering feedback strength could be related to a progressive reduction in continental weatherability during the Eocene (Caves et al., 2016), which allowed for sustained volcanic CO_2 accumulation and hence prolonged greenhouse warming and ocean acidification during the MECO.

In Chapter 6, I present a compilation of new surface ocean temperature records across the MECO from the two sites at the Newfoundland Drifts in the North Atlantic. Due to their high clay contents, these expanded deep-sea sedimentary sequences yield well-preserved foraminifera and abundant organic matter and hence allow for robust multiproxy temperature reconstructions. Here I integrate clumped isotope (Δ_{47}), oxygen isotope ($\delta^{18}O$) and trace element (Mg/Ca) records of planktonic foraminifera with biomarker records based on glycerol dialkyl glycerol tetraether (GDGT) distributions (TEX_{86}) and alkenones ($U^{K'}_{37}$) to fully determine the amplitude of MECO warming in the North Atlantic. The foraminiferal Δ_{47} and $\delta^{18}O$ records display background temperatures of ~20 °C and a substantial surface mixed-layer warming of 3–5 °C during the MECO, as well as a ~1.5‰ shift towards heavier seawater $\delta^{18}O$ compositions that corresponds to a salinity increase of ~2 psu. Together, this suggests that the Newfoundland region of the North Atlantic warmed significantly during the MECO, likely related to northward expansion of warm, saline waters from the subtropical North Atlantic gyre. This represents additional proof that the MECO was a global phenomenon, as also inferred in Chapter 5. In addition, because this is the first high-resolution planktonic foraminiferal Δ_{47}-based temperature record for the Eocene, it also provides an independent test of the validity of the established temperature relationships for the other proxies. Notably, the Mg/Ca-based temperatures are mostly similar to the Δ_{47}-based temperatures in terms of absolute values, but record a more subdued total warming of ~2 °C. This discrepancy suggests that the existing Mg/Ca-temperature relationships for deep-time paleoclimate reconstructions still need to be improved. Furthermore, the TEX_{86}-based temperatures yield the highest absolute values of all proxies (30–31 °C) but record only ~1 °C of warming. Similarly, the $U^{K'}_{37}$ values are consistently at saturation and hence imply temperatures of at least ~28 °C. These differences between the biomarker-based proxies and the foraminiferal proxies may be partly

due to proxies recording temperatures at different water depths and/or seasons. However, given that the study sites are located in a sediment drift, it is also possible that the TEX_{86}-based and $U^{K'}_{37}$-based estimates are affected by lateral transport of GDGTs and alkenones from other, warmer regions in the North Atlantic.

Finally, Chapter 7 presents a suite of Middle Eocene paleoclimate records spanning the MECO interval from the Kuma Formation of the Belaya River section in the North Caucasus, Russia. These laminated sediments were deposited in the Tethys realm in a continental shelf setting under variable suboxic to anoxic conditions. Remarkably, they have generally high carbonate ($CaCO_3$) as well as high total organic carbon (TOC) contents. The MECO interval at this section is identified based on calcareous nannofossil biostratigraphy and a TEX_{86}-based temperature record, but a good age model is currently not yet available. Reconstructed sea surface temperatures are very high throughout the studied interval (32–34 °C) and show a MECO warming of ~2 °C. Interestingly, no significant changes in $CaCO_3$ contents are observed during the MECO warming phase. In addition, the subsequent cooling phase appears to last longer than in deep-sea records from other ocean basins. Bulk carbonate $\delta^{18}O$ values also show little change during MECO warming, but display a transient shift to very negative values during MECO cooling that correlates with an interval of decreased $CaCO_3$ and increased TOC contents. This pattern of MECO warming followed by an interval of increased TOC preservation and/or burial during the subsequent cooling phase has also been recognized in the Alano di Piave section in Italy (Spofforth et al., 2010). As such, these potentially related organic-rich deposits could represent a regional episode of organic carbon burial in the Tethys Ocean that could have contributed to MECO cooling. This would be especially important considering the diminished middle Eocene silicate weathering thermostat as surmised in Chapter 5, because organic carbon burial represents an alternative mechanism for CO_2 sequestration and climatic recovery. Finally, mercury (Hg) contents are used to assess potential sedimentary evidence for volcanic activity over the MECO. However, the initial, low-resolution dataset does not show a significant Hg/TOC enrichment over the studied interval and can therefore not be used to further substantiate the inferred episode of enhanced volcanism as the mechanism responsible for CO_2 rise and MECO warming.

1.5 Outlook

This thesis presents new insights into carbon cycling over the Cenozoic, as well as several new records to better understand coupled carbon cycle and climate change during the MECO. However, it also raises important new questions that warrant further research. Although the evolution of various element cycles through time is becoming increasingly well understood in general, it is still difficult to establish a single, convergent weathering history for the Cenozoic through the inversion of marine isotope records. This is partly due to the fact that weathering proxies respond differently to various forcings, but also because potential changes in the isotopic compositions of important element fluxes are not yet well known, as I have demonstrated in Chapters 2 and 4. One way to better constrain the isotopic compositions of weathering fluxes would be to reconstruct temporal changes in the isotopic compositions of various rock types that contribute to global weathering, based on compilations of sedimentary and igneous rock datasets. This would allow for more quantitative estimates of changes in past weathering fluxes, which in turn would open up new avenues for subsequent modeling studies.

The new MECO records also pose additional questions regarding carbon cycle and climate interactions. If the strength of the negative silicate weathering feedback did indeed decline

progressively over the course of the Eocene in response to reduced continental weatherability, as hypothesized in Chapter 5, such changes should be reflected in a gradual change in the duration of climatic recovery from Eocene hyperthermals relative to their forcing mechanisms. This could potentially be tested by generating additional high-resolution records of weathering fluxes, atmospheric CO_2 concentrations, ocean temperatures and changes in the position of the CCD for hyperthermals in the time interval between the PETM and the MECO. In addition, a diminished silicate weathering feedback may also have acted as a driver of sustained greenhouse warming during other enigmatic episodes of Earth's history, such as the Permian-Triassic transition or the major glaciations of the Paleozoic and Neoproterozoic.

Furthermore, the exact carbon source that resulted in CO_2 rise and MECO warming has not yet been identified. The $^{187}Os/^{188}Os$ records and carbon cycle model simulations presented in Chapter 5 suggest a volcanic source of CO_2 during the MECO, but unlike the Mesozoic Oceanic Anoxic Events (OAEs), there is no evidence for a large igneous province that was emplaced during the Middle Eocene. This study also indicates that CO_2 emissions need not have been extremely high during phases of diminished weathering, so it may ultimately not be realistic to find the exact source. However, future studies could focus on exploring degassing rates from other inferred active volcanic settings, such as continental arcs. This may be coupled with the generation of additional Hg/TOC records across the MECO from sites proximal to a suspected volcanic source.

The surface ocean temperature records for the North Atlantic presented in Chapter 6 show the unique potential of using a multiproxy approach involving Δ_{47} to more robustly reconstruct absolute temperatures. However, the Δ_{47}-based temperature estimates can still be improved by generating additional data to further reduce the associated analytical uncertainties. Moreover, increasing the resolution of the foraminiferal records further would potentially allow for relationships between surface ocean temperatures and orbital climate forcing to be resolved. This is of interest because the Newfoundland Drifts contain the most expanded sedimentary archives of the MECO that are presently available and may be used to establish an astronomically tuned chronology for the event.

Finally, the inferred organic carbon burial episode following MECO warming in the Tethys realm, as described in Chapter 7, should be investigated further. If organic carbon burial did indeed increase in the aftermath of the MECO, the duration of this burial event and the amount of carbon buried should be quantitatively estimated. This will require detailed mapping and much better stratigraphic constraints over a large area. Furthermore, such estimates should be compared against model simulations to evaluate whether these amounts of organic carbon burial are sufficient to drive MECO cooling on a global scale.

Chapter 2

Reconstructing global chemical weathering: an overview of proxies and their applications, with emphasis on the carbon cycle

Reconstructing global chemical weathering: an overview of proxies and their applications, with emphasis on the carbon cycle

Robin van der Ploeg, Karline Soetaert, Jack J. Middelburg and Appy Sluijs

Abstract

Earth's climate is ultimately regulated by the chemical weathering of silicate rocks, which represents the dominant sink for carbon in the atmosphere and oceans. Here, we review the proxies that are available to reconstruct past changes in global chemical weathering on different timescales, using isotope ratios of various trace elements in marine sediments. The applications of these proxies are dependent on various processes that affect the distribution of elements and their isotopes, as well as the oceanic residence times of their respective elements. $^{187}Os/^{188}Os$ values of metalliferous and organic-rich sediments may be used to evaluate global changes in chemical weathering on short (10 – 100 kyr) climatic timescales, whereas the $^{87}Sr/^{86}Sr$, $\delta^{7}Li$, $\delta^{44}Ca$ and $\delta^{26}Mg$ values of marine carbonates may be used to study global changes in chemical weathering on intermediate (~500 kyr) and long (1 – 10 Myr) geological timescales. We highlight remaining challenges towards a full understanding of the geochemical cycles of the elements involved in these proxies, which is essential for accurately reconstructing chemical weathering in the geological record.

2.1 Introduction

The carbon cycle is a crucial component of the Earth system. It determines the amount of carbon in the atmosphere and controls global surface temperatures and climate. It also regulates the temperature and alkalinity of the oceans, crucial for marine life. Therefore, it is important to understand the biological and geological processes that affect the exchange of carbon between different reservoirs, such as the oceans, biosphere, geosphere and atmosphere. Imbalances of the carbon cycle, and especially those associated with changes in atmospheric CO_2 levels, are shown to have had a profound impact on Earth's climate and both surface and deep-water temperatures in the past (Berner et al., 1983; Berner, 1991, 1994; Berner and Kothavala, 2001; Zachos et al., 2001; Royer et al., 2004).

It is generally accepted that on geological timescales, the supply of CO_2 to the atmosphere by volcanism is balanced by a negative feedback mechanism involving the chemical weathering of silicate rocks (Kump et al., 2000). However, it remains unclear to which extent and on which timescale this weathering feedback is modulated by climate through temperature and precipitation (Walker et al., 1981; Berner et al., 1983) and by plate tectonics through orogenesis and sediment supply (Raymo et al., 1988; Raymo and Ruddiman, 1992) during various phases in Earth history.

Silicate and carbonate rocks that are uplifted in mountains as a result of plate tectonics are weathered over time, consuming CO_2 in the process (Berner, 2004). Rivers subsequently deliver the dissolved minerals as cations and alkalinity to the oceans, where they ultimately precipitate as biogenic silica and carbonates. These sedimentary rocks become deeply buried during subduction and are melted into magmas due to exposure to increasing heat and pressure. Magmas are returned to the surface by volcanism, which produces fresh igneous

rocks and releases CO_2 in order to complete the cycle (Figure 1a). It is believed that these processes ultimately govern the rates of CO_2 consumption and production, and therefore act to stabilize Earth's climate (Kump et al., 2000).

The residence time of carbon in the global exogenic carbon pool resulting from this set of feedback mechanisms is in the order of ~100 kyr, as concluded both theoretically (Berner, 2004) and observationally for specific time intervals (e.g., Zachos et al., 2005). However, the Phanerozoic exhibits episodes of massive climate change on timescales longer than the residence time of carbon that are attributed to changes in atmospheric CO_2 concentrations. This implies that imbalances in the feedback loop between carbon input and burial are common.

In the past decades, the connection between weathering and climate has often been invoked to help explain several key events in the geological record. The weathering feedback mechanism (Figure 1b) is relatively well understood on long geological timescales (1 – 10 Myr; Berner, 2004) and short climatic timescales (10 – 100 kyr; Zeebe, 2012b), but on intermediate timescales (~ 500 kyr) the behavior of the weathering feedback is generally not well resolved (Sluijs et al., 2013; Van der Ploeg et al., 2018). The crucial outstanding questions, therefore, are what role weathering plays on which timescale and how we can quantify its impact on the Earth system.

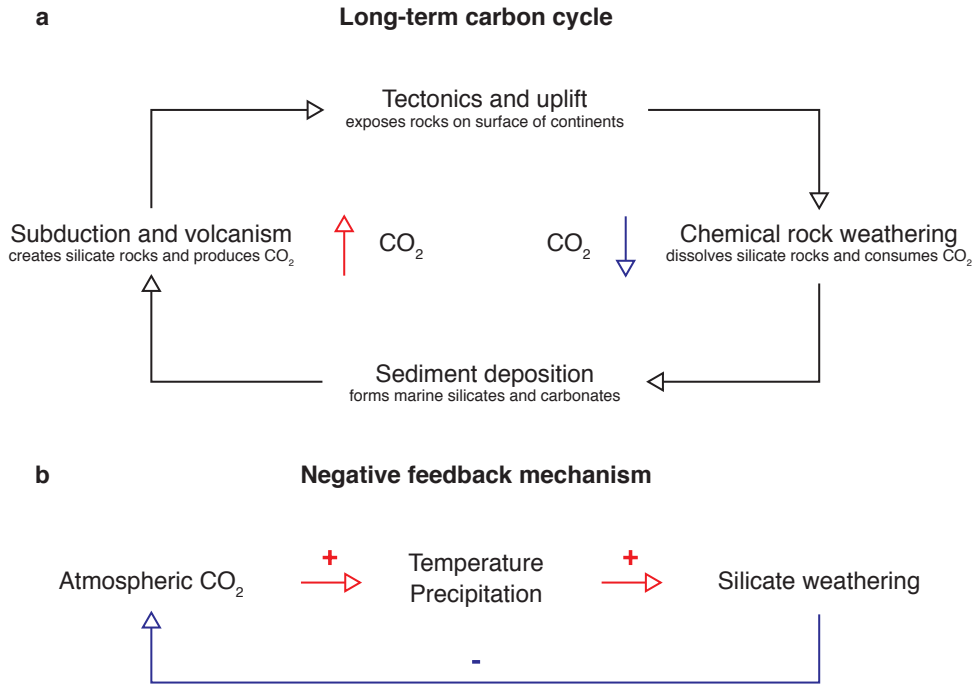

Figure 1: Overview of the mechanisms that regulate atmospheric CO_2 on geological timescales. a, Schematic representation of the long-term carbon cycle, showing the processes that produce and consume CO_2. b, Negative feedback mechanism involving silicate weathering.

A prime example of the interplay between weathering and climate on long geological timescales is the uplift of the Himalayas during the late Cenozoic. This is thought to have greatly increased chemical weathering rates, resulting in lower atmospheric CO_2 levels and dramatic cooling, inducing the transition to an icehouse world (Raymo et al., 1988; Raymo and Ruddiman, 1992). This so-called uplift-weathering hypothesis was originally based on evidence from $\delta^{18}O$, $\delta^{13}C$ and strontium isotope ($^{87}Sr/^{86}Sr$) records of marine carbonates, which revealed both a major increase in continental weathering fluxes and a major decrease in global ocean temperatures since the late Eocene (Zachos et al., 2001). However, subsequent studies have demonstrated that the impact of Himalayan uplift on the carbon and strontium cycles – and by inference global climate – is significantly more complicated (Palmer and Edmond, 1992; Goddéris and François, 1995; Derry and France-Lanord, 1996; Kump and Arthur, 1997; Caves et al., 2016; Bataille et al., 2017).

In addition, weathering is shown to have had an important effect on short climatic timescales in the Paleogene greenhouse world, where atmospheric CO_2 levels and temperatures reached their highest levels of the entire Cenozoic (Beerling and Royer, 2011; Jagniecki et al., 2015; Anagnostou et al., 2016; Foster et al., 2017). The Paleocene and Eocene were characterized by several so-called hyperthermals, transient intervals of widespread – if not global – warming in both surface and deep ocean waters that were accompanied by a significant rise in atmospheric CO_2 levels (Zachos et al., 2008; Sluijs et al., 2009; Dunkley Jones et al., 2013; Littler et al., 2014; Lauretano et al., 2015; Gutjahr et al., 2017). During the Paleocene-Eocene Thermal Maximum (PETM) and the Eocene Thermal Maximum 2 (ETM2), an enhanced hydrological cycle almost certainly resulted in elevated continental weathering rates, acting to balance the excess CO_2 in the ocean-atmosphere system on timescales of approximately 100 kyr (Ravizza et al., 2001; Stap et al., 2009; Zeebe et al., 2009; Kelly et al., 2010). Alternatively, biological carbonate compensation resulting from ocean acidification may have also contributed to climate stabilization following the PETM (Luo et al., 2016; Boudreau et al., 2018).

Further back in time, chemical weathering has also played a major role in regulating Mesozoic climates. The Cretaceous and Jurassic were characterized by several massive carbon cycle perturbations known as Oceanic Anoxic Events (OAEs), which are often associated with dramatic pulses of volcanism leading to CO_2 rise and warming (Schlanger and Jenkyns, 1976; Turgeon and Creaser, 2008; Jenkyns, 2010). Elevated silicate rock weathering rates have been shown to have contributed to eventual climate recovery following the Aptian (OAE1a), Cenomanian-Turonian (OAE2) and Toarcian OAEs on timescales of several 100 kyr (Blättler et al., 2011; Bottini et al., 2012; Pogge von Strandmann et al., 2013; Brazier et al., 2015; Them et al., 2017).

The Middle Eocene Climatic Optimum (MECO) represents a carbon cycle perturbation for which the silicate weathering response is not straightforward, however (Sluijs et al., 2013; Van der Ploeg et al., 2018). This episode of atmospheric CO_2 rise and greenhouse warming occurred on an intermediate timescale of ~500 kyr, but there is no direct evidence for either rapid or sustained carbon release during the event (Bohaty and Zachos, 2003; Bohaty et al., 2009; Bijl et al., 2010; Sluijs et al., 2013). In addition, weathering reconstructions based on osmium isotope ($^{187}Os/^{188}Os$) records preclude an increase in continental silicate rock weathering during the event (Van der Ploeg et al., 2018). As such, the prolonged duration of the MECO may best be explained by a reduced weathering feedback strength following a progressive decrease in continental weatherability during the Eocene (Caves et al., 2016), allowing for the prolonged accumulation of volcanic CO_2 in the ocean-atmosphere system (Van der Ploeg et al., 2018).

In fact, a similar 'failure' of the silicate weathering thermostat has been suggested for the Late Permian-Early Triassic warming episode (Kump, 2018).

The aforementioned examples highlight the fundamental importance of accurate weathering reconstructions in studies of past climate and carbon cycle perturbations. Several proxies have been developed in order to reconstruct changes in weathering and climate in the geological past, including isotope ratios of various trace elements such as Sr and Os. In this paper, we will present an overview of the proxies that are currently available for this purpose and describe their applications for investigating changes in the carbon cycle on various timescales.

2.2 Weathering principles

2.2.1 Silicate and carbonate weathering

Silicate and carbonate weathering are both very important processes in the carbon cycle and are linked through the silicate-carbonate sub-cycle. However, carbonate weathering affects the ocean-atmosphere system in different ways and on different timescales than silicate weathering (Berner, 2004). First, the weathering of carbonate rocks ($CaCO_3$) on the continents may be written as:

$$CaCO_3 + CO_2 + H_2O \rightarrow Ca^{2+} + 2HCO_3^- \quad (1)$$

The Ca^{2+} and HCO_3^- released during carbonate weathering are delivered to the oceans in dissolved form by groundwater and rivers, where they are reprecipitated and ultimately buried as marine carbonates:

$$Ca^{2+} + 2HCO_3^- \rightarrow CaCO_3 + CO_2 + H_2O \quad (2)$$

Together, Equations (1) and (2) constitute the marine carbonate cycle. For one mole of CO_2 consumed during carbonate weathering, one mole of CO_2 is also produced during carbonate precipitation in the marine realm. These processes represent the short-term exchange of carbon between the atmosphere and oceans on climatic timescales of ~10 kyr and are balanced through the $CaCO_3$ saturation state. As a result, carbonate weathering and production are thought to have no net effect on atmospheric CO_2 on geological timescales as long as this balance is maintained (Berner, 2004; Zeebe, 2012b).

The weathering of silicate rocks ($CaSiO_3$) is often expressed as:

$$CaSiO_3 + 2CO_2 + 3H_2O \rightarrow Ca^{2+} + 2HCO_3^- + H_4SiO_4 \quad (3)$$

where $CaSiO_3$ is a hypothetical, generalized calcium silicate mineral. Silicate weathering also releases Ca^{2+} and HCO_3^-, which become part of the carbonate rock cycle and are precipitated as terrestrial or marine carbonates according to Equation (2). In addition, the dissolved silicic acid (H_4SiO_4) released from silicate weathering is precipitated in the oceans as biogenic silica (SiO_2):

$$H_4SiO_4 \rightarrow SiO_2 + 2H_2O \quad (4)$$

The marine carbonates and biogenic silica produced from silicate weathering are eventually buried on the seafloor and incorporated in the geological record. The sum of these processes may therefore be written as:

$$CaSiO_3 + CO_2 \rightarrow CaCO_3 + SiO_2 \quad (5)$$

On geological timescales, the marine carbonates and biogenic silica are ultimately returned to the surface through subduction, volcanism and metamorphism, which results in the reformation of silicate rocks:

$$CaCO_3 + SiO_2 \rightarrow CaSiO_3 + CO_2 \quad (6)$$

Equations (5) and (6) highlight the interactions between the silicate rock cycle and the carbonate rock cycle, which were first described by Ebelmen (1845) and subsequently by Urey (1952). During silicate weathering, one mole of CO_2 is effectively consumed and during silicate formation one mole of CO_2 is produced. These processes represent the long-term exchange of inorganic carbon between the atmosphere, oceans and rocks on geological timescales of 1 - 10 Myr (Berner, 2004; Zeebe, 2012b). Importantly, on such timescales the sources and sinks of carbon should be in secular equilibrium if habitable conditions at Earth's surface are to be maintained (Walker et al., 1981; Berner et al., 1983; Zeebe and Caldeira, 2008).

2.2.2 Organic carbon weathering

The long-term exchange of organic carbon between Earth's surface reservoirs and the rock record is represented by the organic sub-cycle of the carbon cycle (Berner, 2004). Photosynthesis and respiration are generally expressed as:

$$CO_2 + H_2O \rightarrow CH_2O + O_2 \quad (7)$$

$$CH_2O + O_2 \rightarrow CO_2 + H_2O \quad (8)$$

where CH_2O is a generalized description of complex organic matter.

From Equations (7) and (8) it follows that organic carbon is buried in sediments when photosynthesis exceeds respiration. However, this buried carbon is ultimately released back into the atmosphere through oxidative weathering of organic-rich shales or the decomposition of organic matter. These processes also play a major role in determining atmospheric CO_2 concentrations on geological timescales of 1 - 10 Myr (Berner, 2004).

2.2.3 Chemical weathering processes

Chemical weathering reactions of silicate minerals may be either congruent or incongruent. During congruent weathering, primary silicate minerals are completely dissolved and subsequently delivered to the oceans as cations and alkalinity by rivers. During incongruent weathering, primary silicate minerals are partly dissolved and partly transformed into secondary aluminosilicate minerals (clays), after which they are ultimately transported to the oceans as particulate matter. Hence, the congruence of chemical weathering controls the pathway through which elements are transported.

Rates of chemical weathering are governed by a number of different factors, including mineralogy, temperature and humidity. Furthermore, the availability and weatherability of rocks are very important, especially because chemical weathering rates are also influenced by the strength of the hydrological cycle through changes in runoff, physical weathering and erosion (Kump et al., 2000). Biological processes, such as the production of organic acids by land plants, may enhance chemical weathering rates as well.

Weathering regimes can be weathering-limited or transport-limited, depending on the interplay between climate and tectonics (West et al., 2005). In settings characterized by steep continental relief and high erosion rates, silicate weathering rates are kinetically limited by climate through temperature and runoff. In contrast, in settings featuring flat continental relief and low erosion rates, silicate weathering rates are limited by the supply of fresh, weatherable minerals though tectonics and mountain building. As a consequence, the strength of the silicate weathering feedback and its capacity to regulate atmospheric CO_2 concentrations and Earth's temperature are controlled by global topography and the weatherability of the continents (Kump and Arthur, 1997; West, 2012; Maher and Chamberlain, 2014; Caves et al., 2016; Van der Ploeg et al., 2018).

2.3 Silicate weathering proxies

2.3.1 Weathering and ocean chemistry

The chemical composition of Earth's oceans is dependent on the balance of element fluxes into and out of the global oceanic reservoir. For many elements, the influx into the oceans is eventually governed by chemical weathering of rocks exposed on the continents and islands. In principle, a global increase in chemical weathering should therefore result in the enrichment of elements in the global ocean. In addition, the various isotope species of elements are affected by fractionation in natural processes. As a consequence, changes of isotope ratios in seawater over time may indicate changes in the fluxes of elements between the continents and the oceans, resulting from variations in global chemical weathering. These changes are reflected in the geological record, because elements and their respective isotopes are incorporated in marine sediments during their precipitation from seawater.

The global cycles of elements and their isotopes should be understood before they can be used as global ocean weathering proxies. First of all, elements should ideally be conservative, i.e. with a homogeneous distribution throughout the water column and across all different ocean basins. Secondly, the sensitivity of elements to biological cycling and changes in redox conditions should be understood, because these processes may alter the original seawater signature. Finally, the most important property to consider is the oceanic residence time of an element in relation to the mixing time of the global ocean (~1500 yr for the modern ocean; Broecker and Peng, 1982)) and the timescale of interest. With respect to the carbon cycle, we make the distinction between elements that are short-lived (< 10 kyr) and long-lived (> 10 kyr) in the ocean (see Table 1).

Elements with short oceanic residence times, such as Nd, Hf, Pb and Be, are removed from the oceanic reservoir before they are fully mixed and as a result, they will mostly record regional effects of changes in chemical weathering instead of global effects. However, these elements are able to develop different isotopic signatures for different ocean basins and water masses due to regional differences in continental weathering inputs by rivers. Therefore, these elements are widely applied as paleoceanographic tracers (Frank, 2002). Elements with

Table 1: An overview of estimated elemental residence times in present-day seawater. Elements are classified as short-lived or long-lived relative to the mixing time of the global ocean (1 – 2 kyr) and are listed in order of increasing residence time.

Element	Residence time	Reference
Short-lived elements		
Pb	50 – 400 yr	Frank (2002)
Be	200 – 1000 yr	Frank (2002)
Nd	600 – 2000 yr	Frank (2002)
Hf	2000 yr	Frank (2002)
Ocean (modern)	1000 – 2000 yr	Broecker and Peng (1982)
Long-lived elements		
Si	10 kyr	Tréguer and De La Rocha (2013)
Os	10 – 50 kyr	Peucker-Ehrenbrink and Ravizza (2000)
C	100 kyr	Berner (2004)
Ca	0.5 – 1.0 Myr	Fantle (2010)
Li	1.2 Myr	Misra and Froelich (2012)
Sr	2.4 Myr	Ravizza and Zachos (2003)
Mg	10 Myr	Berner and Berner (1996)

intermediate oceanic residence times, including Si and Os, are generally well mixed in the global ocean and are removed from the oceanic reservoir on timescales similar to climatic processes and the short-term carbon cycle. Therefore, these elements are able to record the effects of changes in chemical weathering on global ocean chemistry on short climatic timescales (10 – 100 kyr), as well as longer timescales. However, biological processes and changes in redox conditions can respectively lead to regional differences in seawater Si and Os signatures. Finally, elements with long oceanic residence times, such as Sr, Li, Ca and Mg, are removed from the oceanic reservoir on timescales similar to tectonic processes and the long-term carbon cycle. Consequently, these elements generally reflect the impact of changes in chemical weathering on global ocean chemistry on long geological timescales (1 – 10 Myr).

2.3.2 Weathering and carbon cycle proxies

2.3.2.1 Carbon isotopes

Carbon (C) has two naturally occurring stable isotopes, ^{12}C and ^{13}C, and one naturally occurring radioactive isotope, ^{14}C. This radioactive ^{14}C is produced by cosmic radiation in the upper atmosphere, but because of its relatively short half-life (5.730 kyr), only ^{12}C and ^{13}C are effectively preserved in the rock record beyond ~50 kyr ago. Unlike the other elements that are discussed in this paper, the stable isotopes of carbon are predominantly fractionated during biological processes. In general, organic matter is preferentially enriched in ^{12}C relative to ^{13}C during photosynthesis, which results in lower $\delta^{13}C$ values of organic matter relative to the remaining inorganic carbon. $\delta^{13}C$ is expressed as:

$$\delta^{13}C(‰) = \left(\frac{^{13}C/^{12}C_{sample}}{^{13}C/^{12}C_{standard}} - 1\right) * 1000 \quad (9)$$

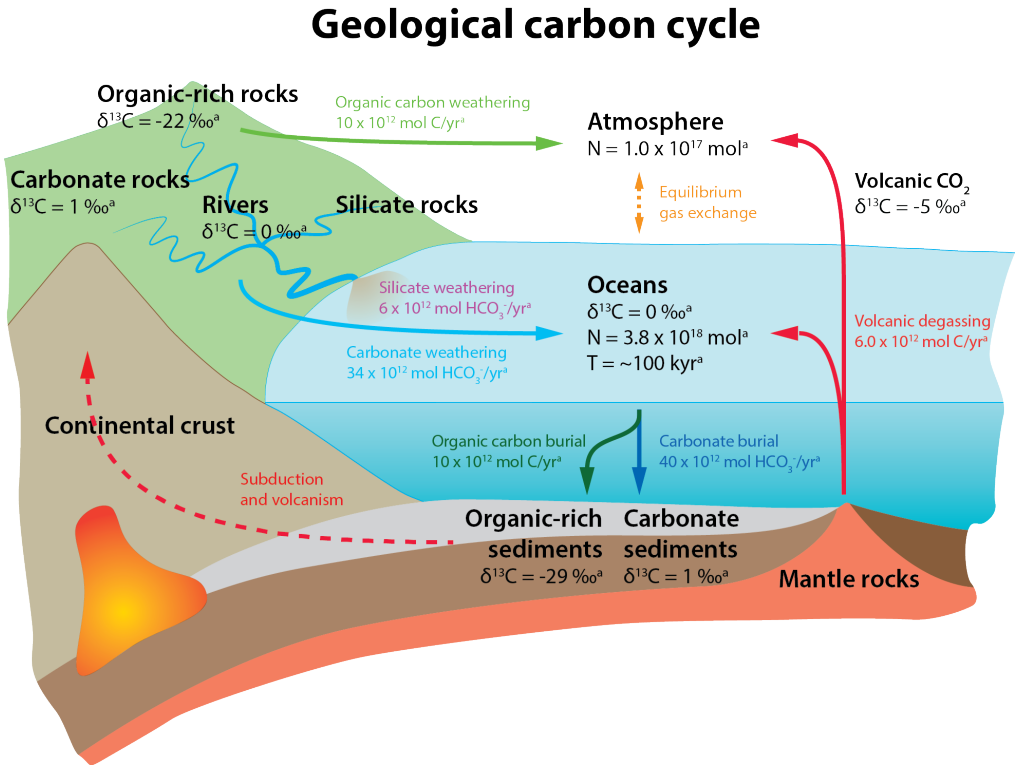

Figure 2: Overview of the geological carbon cycle and systematics of the $\delta^{13}C$ proxy. Values are based on Kump and Arthur, (1999)[a] and represent the average Phanerozoic state of the long-term carbon cycle at elevated CO_2 levels of 560 ppmv. N = inventory, T = residence time.

In the ocean, the $\delta^{13}C$ ratio of water masses is determined by the balance between photosynthesis and respiration, as well as ocean circulation (Broecker and Peng, 1982). On a global scale, however, the $\delta^{13}C$ composition of the exogenic carbon pool is controlled by long-term changes in the balance between volcanic outgassing of CO_2 and oxidative shale weathering versus organic and inorganic carbon burial (Kump and Arthur, 1999; see Figure 2). Changes in the $\delta^{13}C$ composition of the exogenic carbon pool are in turn reflected in the $\delta^{13}C$ ratios of marine sediments (Kump and Arthur, 1999).

The $\delta^{13}C$ records of both carbonate and organic carbon in marine sediments show significant change through time and have been used in conjunction to infer variations in past atmospheric CO_2 and O_2 concentrations (Garrels and Lerman, 1981; Freeman and Hayes, 1992; Falkowski et al., 2005; Katz et al., 2005). In addition to long-term trends, transient $\delta^{13}C$ shifts during major carbon cycle perturbations are of particular interest (Kump and Arthur, 1999). For instance, the Paleogene hyperthermals are characterized by excursions to lower $\delta^{13}C$ values that are attributed to the release of large amounts of ^{12}C-enriched carbon, potentially from the oxidation of methane hydrates or organic matter (Dickens et al., 1995; Kurtz et al., 2003; Zachos et al., 2008; Zeebe et al., 2009).

2.3.2.2 Osmium isotopes

Osmium (Os) has six naturally occurring stable isotopes, ^{184}Os, ^{187}Os, ^{188}Os, ^{189}Os, ^{190}Os and ^{192}Os, as well as one naturally occurring radioactive isotope, ^{186}Os, which has such a long half-life that it can be regarded as stable on geological timescales. All of these isotopes are formed through primordial nucleosynthesis, but ^{187}Os is also produced by the radioactive decay of ^{187}Re, with a half-life of ~43 Gyr. During fractional crystallization, the compatible Os is preferentially enriched in basaltic rocks of the mantle, whereas the incompatible Re remains behind in increasingly differentiated magmas to ultimately be incorporated in silicate rocks of the continental crust. These differences in mineralogical composition result in higher initial Re/Os ratios in continental rocks than in mantle-derived rocks. The subsequent decay of ^{187}Re into ^{187}Os leads to progressively higher $^{187}Os/^{188}Os$ ratios over time, so that old continental rocks generally have higher $^{187}Os/^{188}Os$ ratios than young mantle-derived rocks (Ravizza and Zachos, 2003). This implies that $^{187}Os/^{188}Os$ ratios may be used to distinguish between rocks of different ages and sources, which is subsequently reflected in the $^{187}Os/^{188}Os$ ratios of rivers and oceans because of continental weathering (Peucker-Ehrenbrink and Ravizza, 2000). We note that the Os isotope ratio was initially reported as $^{187}Os/^{186}Os$ in the literature, but this ratio has been abandoned since the discovery of the potential for in-growth due to the radioactive decay of ^{190}Pt to ^{186}Os (Walker et al., 1997; Ravizza and Zachos, 2003). Values can be converted between the $^{187}Os/^{188}Os$ ratio and the $^{187}Os/^{186}Os$ ratio by using the natural isotopic abundances of ^{186}Os and ^{188}Os (Luck and Turekian, 1983).

The $^{187}Os/^{188}Os$ ratio of seawater is governed by continental, mantle and extraterrestrial sources (Peucker-Ehrenbrink and Ravizza, 2000; see Figure 3). Consequently, shifts in the $^{187}Os/^{188}Os$ ratio are indicative of changes in weathering fluxes relative to the other sources. These variations in the $^{187}Os/^{188}Os$ ratio are reflected in metalliferous sediments, ferromanganese crusts and marine carbonates, which are all formed in equilibrium with seawater (Ravizza and Zachos, 2003). For the Cenozoic, as well as further back in time, $^{187}Os/^{188}Os$ records of metalliferous sediments have been shown to vary considerably (Pegram et al., 1992; Peucker-Ehrenbrink et al., 1995; Peucker-Ehrenbrink and Ravizza, 2012). Major excursions to higher $^{187}Os/^{188}Os$ values have been observed for transient events such as the PETM and the Toarcian and Aptian OAEs, and are attributed to increased continental weathering (Ravizza et al., 2001; Cohen et al., 2004; Bottini et al., 2012; Dickson et al., 2015). In contrast, the $^{187}Os/^{188}Os$ ratio of sediments deposited during OAE2 at the Cenomanian-Turonian transition decreased dramatically, which is associated with massive volcanism (Turgeon and Creaser, 2008). Similarly, a minor decrease in $^{187}Os/^{188}Os$ has been reported for the MECO and linked to enhanced volcanism (Van der Ploeg et al., 2018). The $^{187}Os/^{188}Os$ ratio of marine carbonates has also been found to reflect variability in weathering during Pleistocene glacial-interglacial cycles (Burton et al., 2010).

The $^{187}Os/^{188}Os$ ratio of marine sediments has a number of issues that hamper its use for reconstructions of chemical weathering, however. First of all, the $^{187}Os/^{188}Os$ ratio of seawater reflects a balance between Os fluxes from different sources: felsic silicate rocks, organic-rich sediments, mafic silicate rocks and extraterrestrial dust. Shifts in the $^{187}Os/^{188}Os$ ratio of seawater may hence be related to shifts in the sizes or isotopic compositions of any of these fluxes, and not just silicate rock weathering. In addition, because organic-rich sediments are enriched in both Re and Os and have very high Re/Os ratios, there is an increasing potential for in-growth due to radioactive decay of ^{187}Re to ^{187}Os over long geological timescales (Dubin and Peucker-Ehrenbrink, 2015). Therefore, the weathering of old organic-rich sediments

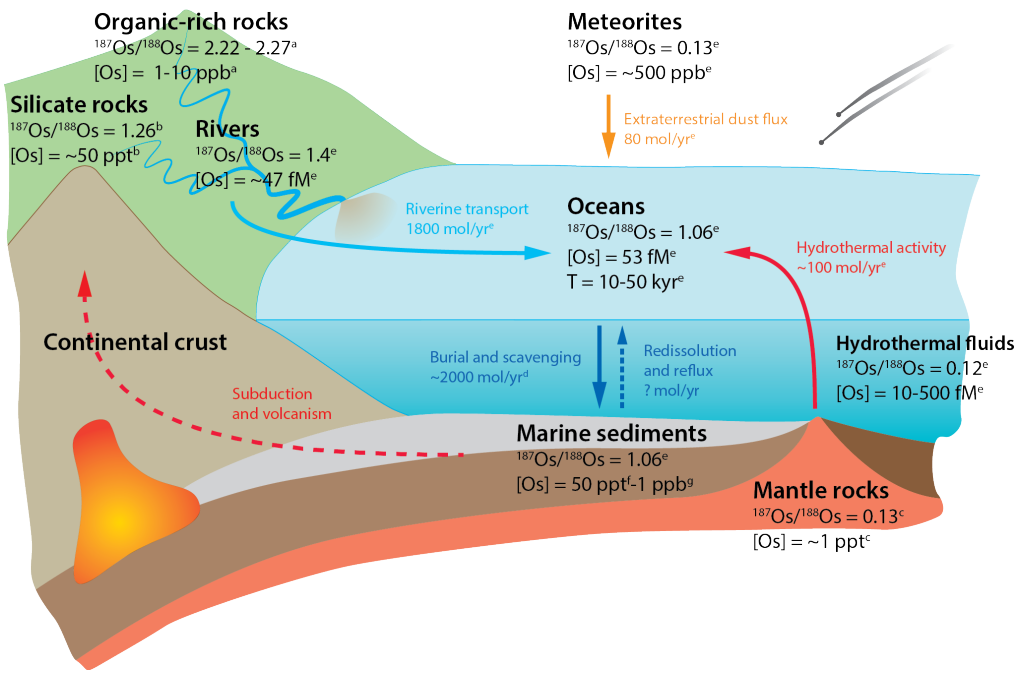

Figure 3: Overview of the present-day osmium cycle and systematics of the $^{187}Os/^{188}Os$ proxy. Values are based on Dubin and Peucker-Ehrenbrink (2015)[a], Esser and Turekian (1993)[b], Martin (1991)[c], Oxburgh (2001)[d], Peucker-Ehrenbrink and Ravizza (2000)[e], Ravizza (1993)[f] and Ravizza et al. (1991)[g]. The $^{187}Os/^{188}Os$ ratio of marine sediments is assumed to be in equilibrium with the $^{187}Os/^{188}Os$ ratio of the oceans. [Os] = Os concentration, T = residence time.

may result in large increases in the $^{187}Os/^{188}Os$ ratio of seawater that are unrelated to the weathering of silicate rocks, and have an opposite effect on atmospheric CO_2 concentrations and the carbon cycle (Peucker-Ehrenbrink and Ravizza, 2000; Georg et al., 2013). Furthermore, because Re and Os are redox-sensitive elements, the $^{187}Os/^{188}Os$ ratio of seawater and marine sediments is affected by changes in redox conditions (Ravizza and Zachos, 2003). Consequently, these elements are actively scavenged under anoxic conditions and incorporated into organic-rich sediments such as black shales, which can result in transient changes in the inventory and residence time of Os in the oceans. Finally, Re and Os have high concentrations in metalliferous sediments and ferromanganese crusts but low concentrations in marine carbonates.

2.3.2.3 Strontium isotopes

Strontium (Sr) has four naturally occurring stable isotopes, ^{84}Sr, ^{86}Sr, ^{87}Sr and ^{88}Sr. Primordial nucleosynthesis is the only source of ^{84}Sr, ^{86}Sr and ^{88}Sr, so their abundance has remained stable since the formation of Earth, but ^{87}Sr is also produced by the radioactive decay of ^{87}Rb, with a half-life of ~ 48.8 Gyr. Sr is compatible in melts and is enriched in the mantle due to fractional crystallization, while Rb is incompatible and is enriched in the continental crust.

Continental rocks therefore have higher initial Rb/Sr ratios than mantle-derived rocks, as well as progressively higher $^{87}Sr/^{86}Sr$ ratios over time due to the decay of ^{87}Rb into ^{87}Sr (Ravizza and Zachos, 2003). Therefore, the $^{87}Sr/^{86}Sr$ ratios of rocks are characteristic for their age and the sources from which they are derived. This results in variability in the $^{87}Sr/^{86}Sr$ ratios of rivers and oceans related to continental weathering.

The $^{87}Sr/^{86}Sr$ ratio of seawater is reflected in marine carbonates, including bulk sediments as well as microfossils and macrofossils (Ravizza and Zachos, 2003). This, in turn, is controlled by fluxes of continental weathering, hydrothermal activity and submarine weathering (McArthur, 1994; see Figure 4). Changes in the $^{87}Sr/^{86}Sr$ ratio may therefore be used as a proxy for the balance between weathering and seafloor spreading in the geological past. The $^{87}Sr/^{86}Sr$ ratio of marine carbonates varied significantly during the Phanerozoic, likely associated with large-scale tectonic processes (Burke et al., 1982; Veizer et al., 1999; McArthur et al., 2012). For example, the major increase in the $^{87}Sr/^{86}Sr$ ratio during the late Cenozoic has been used as important evidence for enhanced continental weathering related to the uplift of the Himalayas (Raymo et al., 1988; Raymo and Ruddiman, 1992). Alternatively, this increase in the $^{87}Sr/^{86}Sr$ ratio has also been related to enhanced weathering related to the onset of glaciation at the Eocene-Oligocene transition (Zachos et al., 1999).

There are several issues that may complicate the use of the $^{87}Sr/^{86}Sr$ ratio of marine carbonates as a proxy for chemical weathering rates. As mentioned above, the $^{87}Sr/^{86}Sr$ ratio of seawater is not only dependent on weathering rates, but also on processes such as the hydrothermal alteration of rocks of the oceanic crust on the seafloor. Therefore, the size and isotopic composition of these fluxes should be known or be constrained in order to accurately reconstruct chemical weathering in the past. Furthermore, the $^{87}Sr/^{86}Sr$ ratios of rivers and oceans are greatly affected by changes in the composition and age of rocks that are weathered (Palmer and Edmond, 1992; Peucker-Ehrenbrink et al., 2010; Bataille et al., 2017). Finally, marine carbonates are affected by diagenetic alteration, which may shift their $^{87}Sr/^{86}Sr$ ratio to values that do not represent the original composition of seawater (Richter and DePaolo, 1988; McArthur, 1994).

2.3.2.4 Lithium isotopes

The stable isotopes of lithium (Li), ^{6}Li and ^{7}Li, are only formed during primordial nucleosynthesis and are almost exclusively present in silicate minerals and aluminosilicate clays. $\delta^{7}Li$ is expressed as:

$$\delta^{7}Li(‰) = \left(\frac{^{7}Li/^{6}Li_{sample}}{^{7}Li/^{6}Li_{standard}} - 1\right) * 1000 \quad (10)$$

The isotopes of Li are fractionated during chemical weathering on land, depending on weathering congruence (Burton and Vigier, 2011). Effectively no fractionation is associated with congruent weathering and therefore, dissolved Li mostly retains the isotopic signature of the source rocks (Pogge von Strandmann et al., 2012). Li incorporated in secondary clay minerals during incongruent weathering, however, is greatly enriched in ^{6}Li relative to ^{7}Li, so that the residual waters becomes increasingly ^{7}Li-enriched (Huh et al., 1998, 2001; Vigier et al., 2009). As a result, regimes of high weathering intensity and congruent weathering are characterized by low $\delta^{7}Li$ values in rivers and high dissolved Li concentrations. Regimes of low weathering intensity and incongruent weathering, however, are characterized by high $\delta^{7}Li$

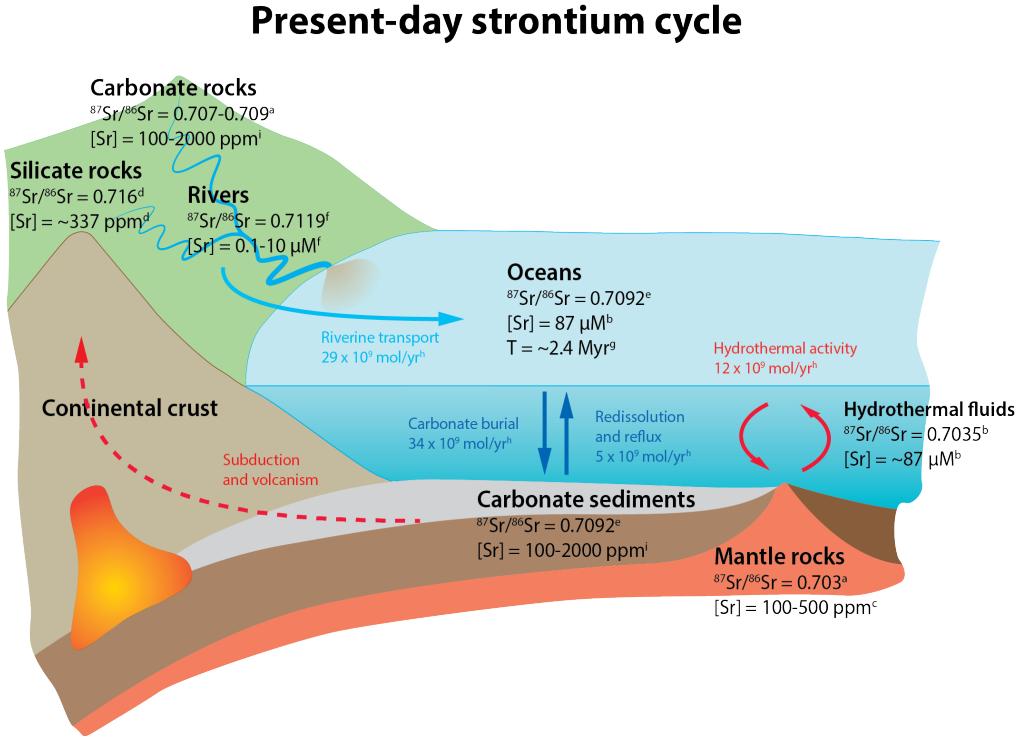

Figure 4: Overview of the present-day strontium cycle and systematics of the $^{87}Sr/^{86}Sr$ proxy. Values are based on Elderfield (1986)[a], Elderfield and Schultz (1996)[b], Engel et al. (1965)[c], Goldstein and Jacobsen (1988)[d], McArthur et al. (2012)[e], Palmer and Edmond (1989)[f], Ravizza and Zachos (2003)[g], Raymo et al. (1988)[h] and Turekian (1964)[i]. The $^{87}Sr/^{86}Sr$ ratio of marine carbonates is assumed to be in equilibrium with the $^{87}Sr/^{86}Sr$ ratio of the oceans. [Sr] = Sr concentration, T = residence time.

values in rivers and low dissolved Li concentrations. The δ^7Li values of rivers and oceans may therefore be used to differentiate between these two end-member weathering models (Froelich and Misra, 2014).

Li isotopes are not fractionated by biological processes on land (Burton and Vigier, 2011), but there are several processes that result in fractionation in the marine realm. First of all, both the inorganic and the biogenic precipitation of marine carbonates introduce isotopic offsets in carbonates towards lower δ^7Li values, which are independent of temperature and salinity, but dependent on carbonate mineralogy (e.g., calcite and aragonite; Marriott et al., 2004). Furthermore, Li isotopes are fractionated during reverse weathering, which is the formation of aluminosilicate clays on the seafloor (Mackenzie and Garrels, 1966). As a consequence, the precipitation of ^7Li-depleted secondary clays drives the δ^7Li values of the oceans higher than the δ^7Li values of rivers (Misra and Froelich, 2012). Finally, hydrothermal fluids have somewhat higher δ^7Li values than mantle-derived rocks (Elderfield and Schultz, 1996).

The δ^7Li composition of seawater is affected by weathering of continental rocks, hydrothermal alteration of mantle-derived rocks and reverse weathering of marine sediments (Froelich and Misra, 2014; see Figure 5). Hence, changes in δ^7Li may be used as a proxy to

evaluate changes in the intensities and rates of chemical weathering on the continents relative to fluxes of hydrothermal activity and reverse weathering (Misra and Froelich, 2012). The δ^7Li value of seawater is reflected in marine carbonates, including bulk carbonates, foraminifera and corals, as well as metalliferous sediments (Burton and Vigier, 2011).

The Cenozoic δ^7Li record shows very low values during the Paleogene, followed by a gradual increase towards the Neogene (Misra and Froelich, 2012). This is interpreted as increasing relief and uplift, decreasing weathering intensity and more incongruent weathering towards the present (Misra and Froelich, 2012; Froelich and Misra, 2014). Also, the increase in Cenozoic δ^7Li values may have been coupled to changes in the reverse weathering and burial fluxes in the oceans (Li and West, 2014). There is also significant variability in δ^7Li records on shorter timescales, for instance during OAE2 at the Cenomanian-Turonian transition. For this event, rapid shifts to low δ^7Li values have been reported, which have been associated with an increase in continental weathering and an enhanced hydrological cycle (Pogge von Strandmann et al., 2013).

Several challenges are involved with the use of δ^7Li values of marine carbonates for chemical weathering reconstructions. First of all, the δ^7Li value of seawater is governed by hydrothermal alteration of mantle-derived rocks and reverse weathering on the seafloor in addition to the weathering of silicate rocks on the continents. Consequently, observed changes in the δ^7Li of seawater may be related to changes in any of these processes, instead of being exclusively related to silicate weathering. Furthermore, the extent of Li isotope fractionation during chemical weathering is dependent on the mineralogy of the secondary clays that are formed (Pistiner and Henderson, 2003; Vigier et al., 2008). A third issue is that additional fractionation of Li isotopes may take place during the biogenic growth of foraminifera because of vital effects (Hathorne and James, 2006). Furthermore, it has been suggested that Li isotope fractionation during biogenic calcification is affected by seawater CO_3^{2-} concentrations (Vigier et al., 2015). In order to interpret changes in δ^7Li as changes in chemical weathering, such fractionation factors have to be estimated, and assumed constant through time or corrected for.

2.3.2.5 Calcium isotopes

The most abundant naturally occurring stable isotopes of calcium (Ca) are ^{40}Ca, ^{42}Ca and ^{44}Ca. ^{40}Ca is produced by the radioactive decay of ^{40}K, but primordial nucleosynthesis is the only source of ^{42}Ca and ^{44}Ca. Ca is present in both carbonate rocks and silicate rocks and their range of Ca isotope ratios (δ^{44}Ca) is relatively similar. δ^{44}Ca is expressed as:

$$\delta^{44}Ca(‰) = \left(\frac{^{44}Ca/^{40}Ca_{sample}}{^{44}Ca/^{40}Ca_{standard}} - 1\right) * 1000 \quad (11)$$

Ca isotopes are fractionated in various natural processes, including chemical weathering on the continents (Fantle and Tipper, 2014). No fractionation is associated with congruent weathering, but secondary carbonates that precipitate in soils during incongruent weathering are enriched in ^{40}Ca and ^{42}Ca, and as a result residual waters are enriched in ^{44}Ca (Tipper et al., 2006b, 2008). Consequently, there is variability in the δ^{44}Ca values of rivers that is related to the congruence of chemical weathering. Ca isotopes are fractionated by biological processes as well, including plant uptake on land and the biogenic precipitation of calcium carbonates in the marine realm (Skulan et al., 1997; Griffith et al., 2008b). Marine biogenic carbonates are preferentially enriched in ^{40}Ca and ^{42}Ca during calcification and as a consequence, seawater

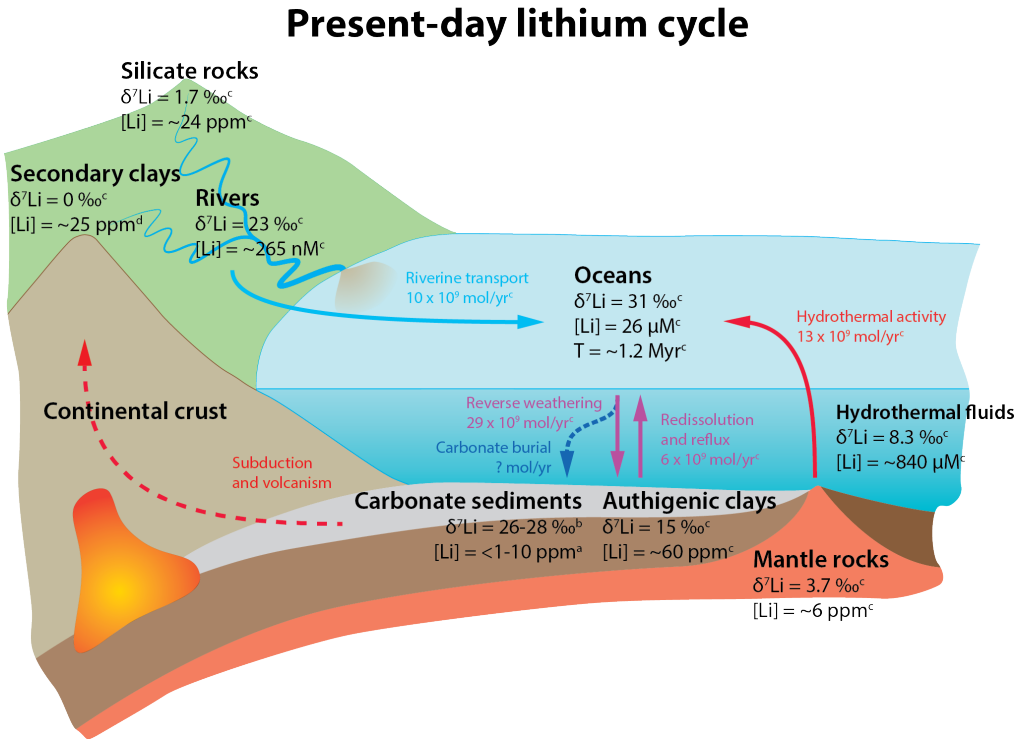

Figure 5: Overview of the present-day lithium cycle and systematics of the δ^7Li proxy. Values are based on Burton and Vigier (2011)[a], Marriott et al. (2004)[b], Misra and Froelich (2012)[c] and Vigier and Goddéris (2015)[d]. The reverse weathering flux is assumed to be equal to the sum of the oceanic input fluxes. δ^7Li values are reported relative to the L-SVEC standard. [Li] = Li concentration, T = residence time.

is enriched in ^{44}Ca. This results in a strong difference between the δ^{44}Ca values of carbonate rocks and seawater (Zhu and Macdougall, 1998; DePaolo, 2004). Fractionation of Ca isotopes has also been observed for hydrothermal activity, but the δ^{44}Ca values of hydrothermal fluids and mantle-derived rocks are relatively similar (Amini et al., 2008; Fantle and Tipper, 2014).

The δ^{44}Ca value of seawater is controlled by fluxes of continental weathering, hydrothermal circulation and biogenic carbonate precipitation (DePaolo, 2004; see Figure 6). As a result, δ^{44}Ca records of marine carbonates reflect changes in the fluxes of carbonate weathering on the continents relative to the other fluxes (Fantle, 2010; Tipper et al., 2010). Cenozoic δ^{44}Ca records include a major decrease at the end of the Eocene, associated with enhanced continental weathering and plate tectonics, as well as significant variability in the Neogene (De La Rocha and DePaolo, 2000; Fantle and DePaolo, 2005, 2007; Sime et al., 2007; Griffith et al., 2008a). Shifts in δ^{44}Ca values have been reported for OAE1a and OAE2 as well, which may indicate an increase in chemical weathering (Blättler et al., 2011), or a change in carbonate precipitation (Du Vivier et al., 2015). An increase in continental weathering based on δ^{44}Ca values of marine carbonates has also been inferred for the Toarcian OAE (Brazier et al., 2015).

The application of δ^{44}Ca values of marine carbonates as a chemical weathering proxy is also not without its problems. First of all, in addition to continental weathering, changes in

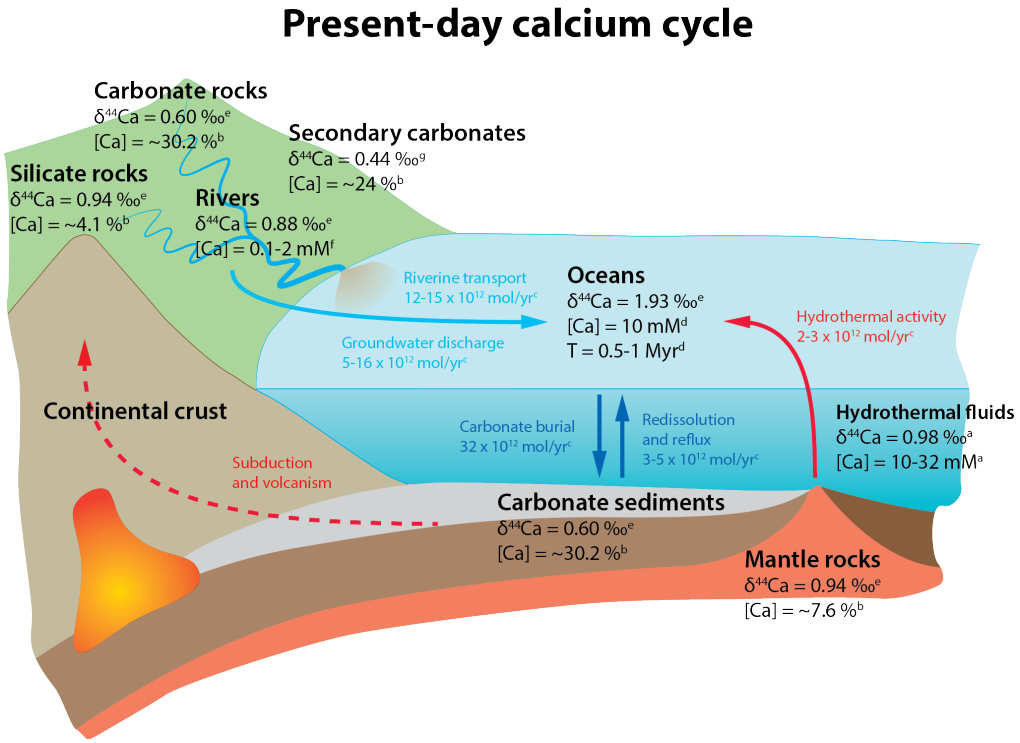

Figure 6: Overview of the present-day calcium cycle and systematics of the $\delta^{44}Ca$ proxy. Values are based on Amini et al. (2008)[a], Capo et al. (1998)[b], DePaolo (2004)[c], Fantle (2010)[d], Fantle and Tipper (2014)[e], Gaillardet et al. (1999)[f] and Tipper et al. (2006)[g]. $\delta^{44}Ca$ values are reported relative to the SRM-915a standard. [Ca] = Ca concentration, T = residence time.

the $\delta^{44}Ca$ values of seawater in the geological record may also be related to differences in fractionation factors depending on temperature and mineralogy. For example, major changes observed in $\delta^{44}Ca$ values of the Phanerozoic are ultimately thought to represent shifts in carbonate deposition between calcite and aragonite seas (Farkaš et al., 2007; Blättler et al., 2012). Therefore, an interpretative framework in which variations in the fractionation factor are constrained is critical to the application of $\delta^{44}Ca$ records as a weathering proxy (Fantle, 2010; Fantle and Tipper, 2014). Furthermore, $\delta^{44}Ca$ values of marine carbonates are affected by carbonate dissolution and diagenetic effects, which has important implications for the application of Ca isotopes in chemical weathering reconstructions (Fantle and Higgins, 2014; Fantle, 2015; Griffith et al., 2015).

2.3.2.6 Magnesium isotopes

Magnesium (Mg) has three stable isotopes that are formed through primordial nucleosynthesis, ^{24}Mg, ^{25}Mg and ^{26}Mg. Mg is present in both silicate and carbonate rocks, with very different respective Mg isotope ratios ($\delta^{26}Mg$) (Pogge von Strandmann et al., 2008; Teng et al., 2010a). $\delta^{26}Mg$ is expressed as:

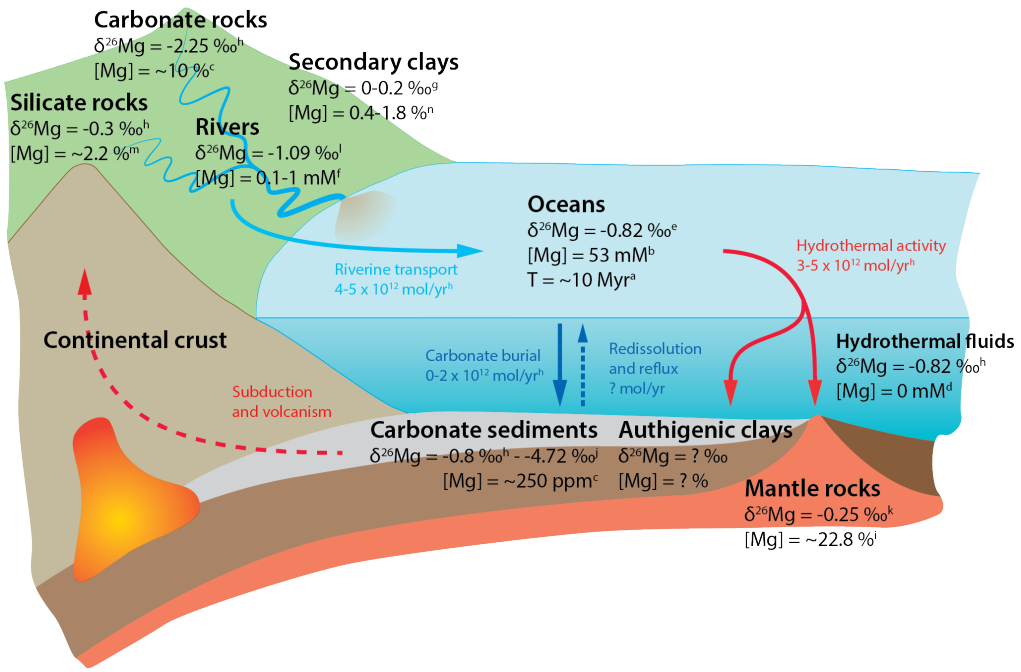

Figure 7: Overview of the present-day magnesium cycle and systematics of the δ^{26}Mg proxy. Values are based on Berner and Berner (1996)[a], Carpenter and Manella (1973)[b], De Nooijer et al. (2014)[c], Elderfield and Schultz (1996)[d], Foster et al. (2010)[e], Gaillardet et al. (1999)[f], Higgins and Schrag (2010)[g], Higgins and Schrag (2015)[h], McDonough and Sun (1995)[i], Pogge von Strandmann (2008)[j], Teng et al. (2010a)[k], Tipper et al. (2006c)[l], Wedepohl (1995)[m] and Wimpenny et al. (2014)[n]. δ^{26}Mg values are reported relative to the DSM-3 standard. [Mg] = Mg concentration, T = residence time.

$$\delta^{26}Mg(‰) = \left(\frac{^{26}Mg/^{24}Mg_{sample}}{^{26}Mg/^{24}Mg_{standard}} - 1\right) * 1000 \quad (12)$$

Mg isotopes are fractionated in various natural processes, including chemical weathering on the continents (Tipper et al., 2006b, 2006c; Pogge von Strandmann et al., 2008). No fractionation is associated with congruent weathering, but ^{24}Mg is preferentially released to the dissolved phase during incongruent weathering, which leaves secondary aluminosilicate clays enriched in ^{26}Mg (Opfergelt et al., 2012; Pogge von Strandmann et al., 2012; Wimpenny et al., 2014). As a result, there is variability in the δ^{26}Mg values of rivers associated with the congruence of chemical weathering. Mg isotopes in the marine realm are fractionated during biogenic carbonate precipitation and the subsequent formation of dolomite, as well as reverse weathering in hydrothermal systems (Higgins and Schrag, 2015). Marine carbonates are preferentially enriched in ^{24}Mg relative to ^{26}Mg during biogenic calcification and as a result, they have δ^{26}Mg values that are very different from those of seawater (Pogge von Strandmann,

2008; Hippler et al., 2009; Wombacher et al., 2011). Hydrothermal alteration at high temperatures introduces no isotopic fractionation, because in these settings all Mg is removed from seawater, but secondary aluminosilicate clays formed at low temperatures are thought to be enriched in ^{26}Mg relative to ^{24}Mg during their formation (Higgins and Schrag, 2010).

The $\delta^{26}Mg$ value of seawater is dominated by fluxes of continental weathering, hydrothermal circulation and biogenic carbonate precipitation (Higgins and Schrag, 2015; see Figure 7). The $\delta^{26}Mg$ value may therefore be used to assess between continental weathering, including the relative contributions of silicate weathering and carbonate weathering, and the other fluxes (Higgins and Schrag, 2015). $\delta^{26}Mg$ records of marine carbonates and foraminifera show relatively little change for the Cenozoic, except for a small, gradual shift towards lower values from the Paleogene to the Neogene (Higgins and Schrag, 2015). However, a different foraminiferal $\delta^{26}Mg$ record appears to be punctuated by shifts towards lower values in the Oligocene and at the present, which are attributed to a reduction in dolomite formation during episodes of climatic cooling (Pogge von Strandmann et al., 2014).

Several challenges are involved with reconstructions of continental weathering based on $\delta^{26}Mg$ values of carbonates. Since the $\delta^{26}Mg$ value of seawater is not only controlled by continental sources, but also by carbonate precipitation and reverse weathering, observed changes in $\delta^{26}Mg$ may be related to any of these processes. In addition, the fractionation of Mg isotopes during chemical weathering is dependent on the mineralogy of the secondary clays that are formed, and importantly, some clay minerals are shown to be enriched in ^{24}Mg relative to ^{26}Mg (Wimpenny et al., 2010, 2014; Pogge von Strandmann et al., 2012). Furthermore, very little is known about Mg isotope fractionation during reverse weathering in marine sediments (Higgins and Schrag, 2015). Finally, marine carbonates are affected by diagenesis and dolomite formation, which may significantly alter their original $\delta^{26}Mg$ values (Fantle and Higgins, 2014; Higgins and Schrag, 2015).

2.4 Discussion

2.4.1 Weathering proxies comparison

2.4.1.1 Proxy systematics

The main differences between the various chemical weathering proxies discussed in this paper are the geological context in which they can be applied and the timescales at which they record changes in global ocean chemistry and the carbon cycle. Importantly, these proxies all represent a measure of continental weathering in addition to several other processes. Furthermore, there are differences regarding the principles and processes responsible for variation in the distribution of elements and their isotopes. Finally, there may be advantages and disadvantages to the use of proxies for specific purposes, or additional assumptions that are required in order to interpret results.

The $^{187}Os/^{188}Os$, $^{87}Sr/^{86}Sr$, $\delta^{7}Li$, $\delta^{44}Ca$ and $\delta^{26}Mg$ proxies may all be used to reconstruct global changes in chemical weathering in the past. However, the processes controlling the $^{187}Os/^{188}Os$ and $^{87}Sr/^{86}Sr$ proxies are different from the processes controlling the other proxies. Os and Sr isotopes are not significantly fractionated during the chemical weathering of silicate rocks, so the $^{187}Os/^{188}Os$ and $^{87}Sr/^{86}Sr$ ratios of seawater mainly reflect changes in the sources of these elements. In contrast, Li, Ca and Mg isotopes have relatively restricted ranges in continental

rocks and the $\delta^{7}Li$, $\delta^{44}Ca$ and $\delta^{26}Mg$ values of seawater are therefore more governed by changes in the balance of fluxes than by differences in the sources of these elements.

In many aspects, the $^{187}Os/^{188}Os$ ratio appears to be analogous to the $^{87}Sr/^{86}Sr$ ratio (Peucker-Ehrenbrink and Ravizza, 2000). However, $^{187}Os/^{188}Os$ records are affected by meteorite impacts, which result in significant shifts to lower values because of their unradiogenic isotopic signature and high Re and Os concentrations. Secondly, the weathering of organic-rich sediments has also been shown to produce changes in the $^{187}Os/^{188}Os$ ratio of seawater, in addition to the weathering of silicate rocks (Dubin and Peucker-Ehrenbrink, 2015). Thirdly, Os has a much shorter residence time in seawater than Sr and is therefore able to record more rapid shifts in the carbon cycle. Finally, the range of natural variations in the $^{187}Os/^{188}Os$ ratio is generally higher than the range of natural variations in the $^{87}Sr/^{86}Sr$ ratio (Peucker-Ehrenbrink and Ravizza, 2012).

Li, Ca and Mg isotopes are all fractionated during incongruent weathering through their incorporation in secondary aluminosilicates and carbonates. However, whereas the secondary phases of Li and Ca are generally enriched in the light isotopes, those of Mg are enriched in heavy isotopes (Teng et al., 2010b; Pogge von Strandmann et al., 2012). Furthermore, the isotopic fractionation of many elements during incongruent weathering is strongly dependent on the mineralogy of the secondary phases.

2.4.1.2 Proxy synthesis

All of the chemical weathering proxies discussed in this paper are affected by different processes and their application is dependent on assumptions. Therefore, the best results are achieved when multiple proxies are combined. The $^{187}Os/^{188}Os$ and $^{87}Sr/^{86}Sr$ ratios are among the best proxies to reconstruct changes in chemical weathering in the geological record, but they are not exclusively associated with the weathering of silicate rocks (Ravizza and Zachos, 2003). Because they are also affected by the weathering of organic-rich sediments and carbonate rocks, respectively, it is difficult to use variations in the $^{187}Os/^{188}Os$ and $^{87}Sr/^{86}Sr$ ratios of seawater individually for quantitative reconstructions of silicate weathering and CO_2 consumption rates. The $\delta^{7}Li$ proxy, in contrast, is based on isotopes that are almost exclusively present in silicate rocks and the $\delta^{7}Li$ of seawater is therefore not affected by other sources of continental weathering. Hence, combining the $^{187}Os/^{188}Os$, $^{87}Sr/^{86}Sr$ and $\delta^{7}Li$ proxies may provide very valuable insights on continental weathering (Misra and Froelich, 2012). Still, the $\delta^{7}Li$ proxy is related to the congruence of chemical weathering and as a result it reflects the efficiency of CO_2 consumption through continental weathering rather than the total amount of CO_2 consumption (Pogge von Strandmann and Henderson, 2015).

Ca and Mg are both elements that are directly involved in the carbonate rock cycle, which makes them especially promising for reconstructions of chemical weathering in relation to climatic events. In addition, the Ca and Mg budgets of the global ocean are closely related, because Ca and Mg are exchanged during the dolomitization of carbonate rocks and the hydrothermal alteration of mantle-derived rocks (Higgins and Schrag, 2015). The use of the $\delta^{44}Ca$ and $\delta^{26}Mg$ proxies together with other isotope systems may allow for a comparison between silicate- and carbonate weathering.

2.4.1.3 Cenozoic records of chemical weathering

Together, the $^{187}Os/^{188}Os$, $^{87}Sr/^{86}Sr$, $\delta^{7}Li$, $\delta^{44}Ca$, $\delta^{26}Mg$, $\delta^{13}C$ and $\delta^{18}O$ records of the Cenozoic reflect the evolution of Earth's oceans in relation to changes in chemical weathering, the carbon

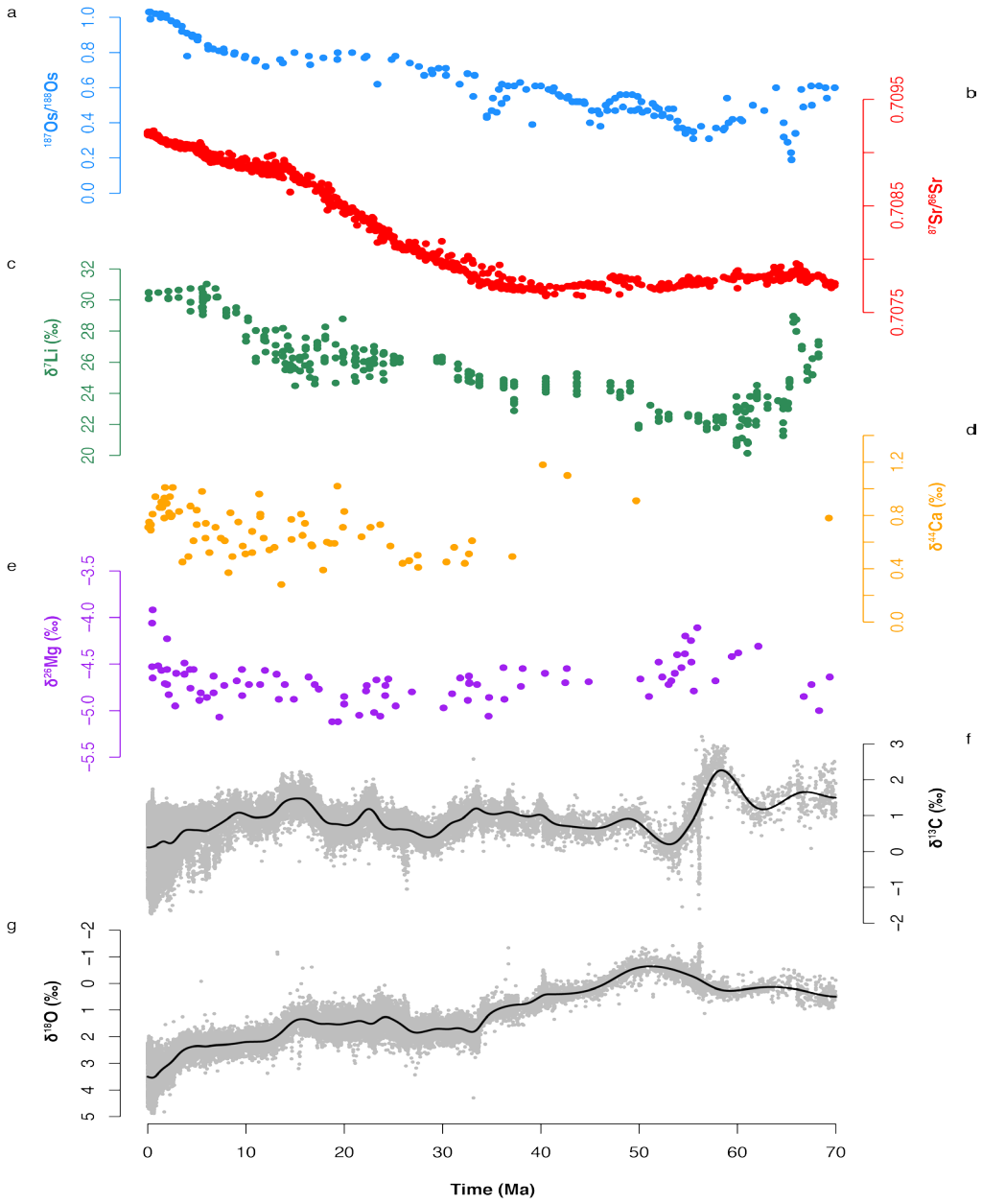

Figure 8: Compilation of chemical weathering records for the Cenozoic. a, $^{187}Os/^{188}Os$ record of ferromanganese crusts from Klemm et al. (2005) and Burton (2006), updated to the age model of Nielsen et al. (2009). b, $^{87}Sr/^{86}Sr$ record of marine carbonates as compiled by McArthur et al. (2012). c, $\delta^{7}Li$ record of planktonic foraminifera (Misra and Froelich, 2012). d, $\delta^{44}Ca$ record of marine carbonates (Fantle, 2010; Fantle and Tipper, 2014). e, $\delta^{26}Mg$ record of marine carbonates (Higgins and Schrag, 2015). f, $\delta^{13}C$ and g, $\delta^{18}O$ records of benthic foraminifera as compiled by Cramer et al. (2009), updated to the age model of the GTS 2012 (Gradstein et al., 2012).

cycle and climate (see Figure 8). One of the most striking features is that $^{187}Os/^{188}Os$, $^{87}Sr/^{86}Sr$ and $\delta^{7}Li$ values of seawater all show a general increase from the Paleocene and Eocene towards the present. Furthermore, $\delta^{44}Ca$ values show a major decrease at the end of the Eocene, although changes of similar amplitude are also apparent for the Neogene. $\delta^{26}Mg$ values appear to be relatively stable for the majority of the Cenozoic, however.

The increase in $^{87}Sr/^{86}Sr$ ratios has been interpreted as an increase in continental weathering during the Cenozoic related to the uplift of the Himalayas, according to the uplift-weathering hypothesis (Raymo et al., 1988; Raymo and Ruddiman, 1992). $^{187}Os/^{188}Os$ ratios are associated with a general increase in continental weathering as well, but they are also affected by meteorite impacts and rapid climatic shifts (Peucker-Ehrenbrink and Ravizza, 2000, 2012). Similarly, the increase in $\delta^{7}Li$ values has been attributed to a decrease in weathering intensity and an increase in incongruent weathering, associated with enhanced uplift in mountainous regions (Misra and Froelich, 2012; Froelich and Misra, 2014).

However, there are several lines of evidence that challenge the traditional views of the uplift-weathering hypothesis. First and foremost, the late Cenozoic increase in the $^{87}Sr/^{86}Sr$ ratio of seawater may not reflect an absolute increase in global weathering fluxes, but rather a shift in $^{87}Sr/^{86}Sr$ composition of rocks that are weathered following Himalayan uplift (Edmond, 1992; Lear et al., 2003; Bataille et al., 2017). Second, the increase in the $^{187}Os/^{188}Os$ ratio of seawater during the Cenozoic is suggested to be caused by a global increase in continental weathering – not by a regional increase in the Himalayan region (Sharma et al., 1999). Nevertheless, the recycling and weathering of organic-rich sediments with high $^{187}Os/^{188}Os$ ratios, even at a relatively constant rate, may also have contributed to the increase in the $^{187}Os/^{188}Os$ ratio of seawater (Peucker-Ehrenbrink and Ravizza, 2000; Dubin and Peucker-Ehrenbrink, 2015). Furthermore, the shift in the $\delta^{7}Li$ value of seawater associated with increased incongruent weathering on the continents is more likely to be attributed to enhanced formation of floodplains, than to enhanced weathering in mountain belts (Pogge von Strandmann and Henderson, 2015). In addition, a recent modeling study has found that the strength of the silicate weathering feedback has varied significantly over the Cenozoic, while silicate and carbonate weathering fluxes have remained largely invariant (Caves et al., 2016). Moreover, the uplift-weathering hypothesis has been challenged based on $^{10}Be/^{9}Be$ records, which show no variability during the late Cenozoic and indicate that global erosion rates were very stable, instead of gradually increasing (Willenbring and Von Blanckenburg, 2010).

2.4.1.4 Insights from inverse modeling of the marine Sr isotope record

In order to quantitatively estimate changes in element fluxes through time, an inverse modeling approach is often applied to available proxy records (Garrels and Lerman, 1981; Berner et al., 1983; Delaney and Boyle, 1988; Kump, 1989; Richter and Turekian, 1993; Li and Elderfield, 2013). Here we illustrate this inverse modeling approach by presenting various Cenozoic weathering scenarios based on the marine $^{87}Sr/^{86}Sr$ record. In general, the evolution of the Sr inventory and $^{87}Sr/^{86}Sr$ composition of the ocean (N_{Sr} and R_{sw}, respectively) over time can be written as:

$$\frac{dN_{Sr}}{dt} = F_{riv} + F_{hyd} + F_{dia} - F_{sed} \quad (13)$$

$$\frac{N_{Sr}}{9.43+R_{sw}}\frac{dR_{sw}}{dt} = F_{riv}\left(\frac{R_{riv}-R_{sw}}{9.43+R_{riv}}\right) + F_{hyd}\left(\frac{R_{hyd}-R_{sw}}{9.43+R_{hyd}}\right) + F_{dia}\left(\frac{R_{dia}-R_{sw}}{9.43+R_{dia}}\right) - F_{sed}\left(\frac{R_{sed}-R_{sw}}{9.43+R_{sed}}\right) \quad (14)$$

where N_{Sr} represents the seawater Sr inventory (in mol), *F* represents the fluxes of Sr (in mol/yr) from and to the various reservoirs, *R* represents the $^{87}Sr/^{86}Sr$ composition of the various reservoirs and the subscripts *sw*, *riv*, *hyd*, *dia* and *sed* represent the seawater, riverine, hydrothermal, diagenetic and sediment reservoirs, respectively. In addition, the factor of 9.43 is used to normalize $^{87}Sr/^{86}Sr$ compositions for the natural abundances of ^{87}Sr and ^{86}Sr (Li and Elderfield, 2013). We note that the hydrothermal Sr flux (F_{hyd}) influences the $^{87}Sr/^{86}Sr$ composition of seawater (R_{sw}) but does not result in net addition of Sr to the oceans (Elderfield and Schultz, 1996). By contrast, the sedimentary Sr flux (F_{sed}) does not affect R_{sw} because there is no isotopic fractionation associated with Sr burial.

Equations (13) and (14) can be solved for changes in the riverine Sr flux (F_{riv}) through time, if the other parameters can be constrained. Here we generate multiple F_{riv} solutions for the Cenozoic based on a simplified version of the present-day Sr cycle as modeled by Li and Elderfield (2013) (Table 2) and highlight the implications of common model forcings and assumptions. First of all, we use the established, smoothed seawater $^{87}Sr/^{86}Sr$ compilation derived from marine carbonates (McArthur et al., 2012) to constrain changes in R_{sw}. Second, we use seafloor spreading and/or degassing rate reconstructions as a forcing for the hydrothermal Sr flux (F_{hyd}) – specifically, we explore four different scenarios based on the reconstructions of Berner (1994), Müller et al. (2008), Rowley (2002) and Van der Meer et al. (2014). Similar to Li and Elderfield (2013), we assume that the diagenetic Sr flux (F_{dia}) has remained constant over the Cenozoic because it is only a minor component of the Sr cycle. We also assume that the $^{87}Sr/^{86}Sr$ compositions of the hydrothermal and diagenetic fluxes (R_{hyd} and R_{dia}, respectively) have remained constant over time. Because the $^{87}Sr/^{86}Sr$ composition of the riverine flux (R_{riv}) is a major source of uncertainty, we have developed five scenarios that represent a range of probable values for the Cenozoic that would be compatible with gradually increasing seawater $^{87}Sr/^{86}Sr$ compositions, potentially related to Himalayan uplift (Table 2). Similarly, we assume three different scenarios for the seawater Sr inventory (N_{Sr}) to capture the range of any probable variations across the Cenozoic (Table 2). However, we make no inferences about the sedimentary Sr flux (F_{sed}). Rather, we calculate F_{riv} directly from Equation (14) based on the sizes and isotopic compositions of the Sr input fluxes.

Most of our F_{riv} estimates based on modeling of the marine $^{87}Sr/^{86}Sr$ record show a modest decrease between 70 Ma and 35 Ma, followed by a large increase towards present-day values in response to increasing R_{sw} (Figure 9; Figure 10; Figure 11). Importantly, for a given value of R_{riv}, the various seafloor spreading and/or degassing rate reconstructions used to drive F_{hyd} result in relatively minor F_{riv} differences (Figure 9). Although the shape of the early Cenozoic F_{riv} decrease is somewhat different for each F_{hyd} scenario, the long-term F_{riv} minimum at ~35 Ma and the subsequent F_{riv} increase towards the present are apparent in all estimates, regardless of which F_{hyd} scenario is used. Crucially, the different scenarios for the evolution of R_{riv} have a much larger impact on F_{riv} estimates, especially for the early Cenozoic (Figure 10). If we assume that R_{riv} remained invariant and that changes in R_{sw} reflect shifts in the balance between F_{riv} and F_{hyd} only (Caldeira, 1992; Raymo and Ruddiman, 1992), we obtain very low F_{riv} values between 70 and 35 Ma (~0.5x present-day values). However, if we assume that R_{riv} has increased over the course of the Cenozoic (Edmond, 1992; Lear et al., 2003), either gradually or more rapidly due to Himalayan uplift, we find significantly higher early Cenozoic F_{riv} values that are more comparable to or potentially higher than present-day values – as would be expected from the silicate weathering thermostat operating in globally warm climates (Berner et al., 1983; Zachos et al., 2008). Interestingly, these F_{riv} estimates under progressively increasing R_{riv} also show

some resemblance to the continental weatherability reconstructions of Caves et al. (2016), both in terms of overall shape and amplitude of change. Finally, the size of the seawater Sr inventory (N_{Sr}) has a negligible effect on F_{riv} estimates derived from Sr input fluxes only (Figure 11).

Table 2: Overview of all parameters used in Sr cycle modeling. Present-day values are taken from the literature or fitted to match the present-day steady state observations. The Cenozoic scenarios for N, F_{hyd} and R_{riv} are independent of each other.

Parameter	Parameter description	Value	Reference and Comments
Present-day			
N_{Sr}	Sr inventory in oceans	1.25 x 10^{17} mol	Palmer & Edmond (1989)
F_{riv}	Riverine flux of Sr to oceans	3.40 x 10^{16} mol/Myr	Li & Elderfield (2013), following Davis et al. (2003)
F_{hyd}	Hydrothermal flux of Sr to oceans	1.46 x 10^{16} mol/Myr	Li & Elderfield (2013), taken as the sum of the island basalt weathering and hydrothermal fluxes
F_{dia}	Diagenetic flux of Sr to oceans	7.40 x 10^{15} mol/Myr	Calculated to arrive at steady state of R_{sw} = 0.709175
R_{riv}	$^{87}Sr/^{86}Sr$ composition of riverine flux	0.7116	Li & Elderfield (2013), following Davis et al. (2003)
R_{hyd}	$^{87}Sr/^{86}Sr$ composition of hydrothermal flux	0.7037	Li & Elderfield (2013), following Bach & Humphris (1999)
R_{dia}	$^{87}Sr/^{86}Sr$ composition of diagenetic flux	0.7084	Li & Elderfield (2013), following Elderfield & Gieskes (1982)
R_{sw}	$^{87}Sr/^{86}Sr$ composition of seawater	0.709175	McArthur et al. (2012)
Cenozoic			
N_{Sr}	Sr inventory in oceans	Variable	
N_1	Scenario 1	1.25 x 10^{17} mol	Constant, present-day value
N_2	Scenario 2	2.50 x 10^{17} mol	Constant, 2x present-day value
N_3	Scenario 3	6.25 x 10^{16} mol	Constant, 0.5x present-day value
F_{riv}	Riverine flux of Sr to oceans	Variable	Calculated as model result from Equation (14)
F_{hyd}	Hydrothermal flux of Sr to oceans	Variable	Scaled to seafloor spreading and/or degassing rate reconstructions
F_{hyd1}	Scenario 1	Variable	Berner (2004)
F_{hyd2}	Scenario 2	Variable	Rowley (2002)
F_{hyd3}	Scenario 3	Variable	Müller et al. (2008)
F_{hyd4}	Scenario 4	Variable	Van der Meer et al. (2014)
F_{dia}	Diagenetic flux of Sr to oceans	7.40 x 10^{15} mol/Myr	Constant, present-day value
R_{riv}	$^{87}Sr/^{86}Sr$ composition of riverine flux	Variable	
R_{riv1}	Scenario 1	0.7116	Constant, present-day value
R_{riv2}	Scenario 2	0.7106 at 70 Ma 0.7116 at 0 Ma	Linear increase from 70 Ma to 0 Ma
R_{riv3}	Scenario 3	0.7096 at 70 Ma 0.7116 at 0 Ma	Linear increase from 70 Ma to 0 Ma
R_{riv4}	Scenario 4	0.7126 at 70 Ma 0.7116 at 0 Ma	Linear decrease from 70 Ma to 0 Ma
R_{riv5}	Scenario 5	0.7106 at 70 Ma 0.7106 at 35 Ma 0.7116 at 15 Ma 0.7116 at 0 Ma	Constant from 70 Ma to 35 Ma, linear increase from 35 Ma to 15 Ma, constant from 15 Ma to 0 Ma
R_{hyd}	$^{87}Sr/^{86}Sr$ composition of hydrothermal flux	0.7037	Constant, present-day value
R_{dia}	$^{87}Sr/^{86}Sr$ composition of diagenetic flux	0.7084	Constant, present-day value
R_{sw}	$^{87}Sr/^{86}Sr$ composition of seawater	Variable	McArthur et al. (2012)

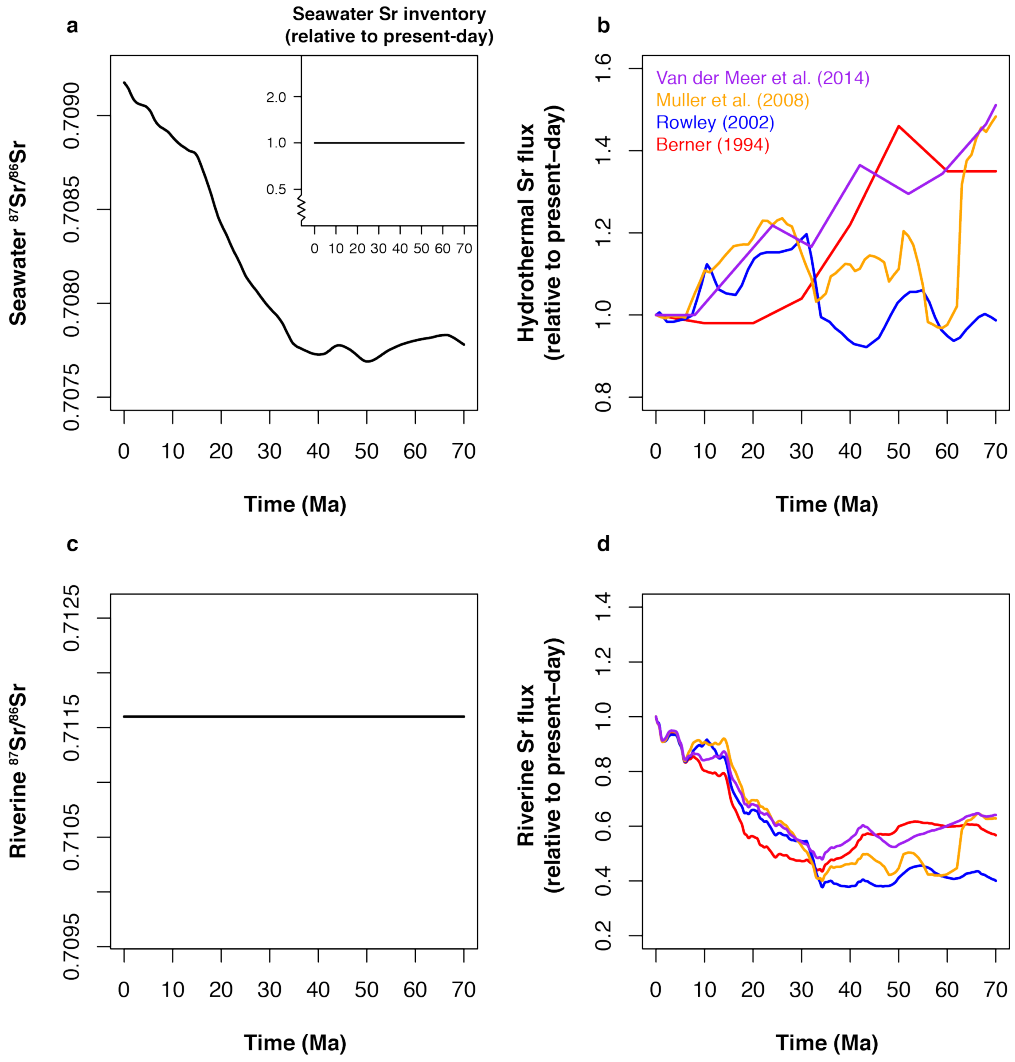

Figure 9: Cenozoic Sr cycle modeling and riverine Sr flux estimates based on different scenarios for the hydrothermal Sr flux. a, Seawater $^{87}Sr/^{86}Sr$ composition, as inferred from the smoothed record of McArthur et al. (2012) (in black). The inset represents the assumed seawater Sr inventory (N_1, in black). b, Hydrothermal Sr flux (F_{hyd}) based on the seafloor spreading and/or degassing rate reconstructions of Berner (1994) (F_{hyd1}, in red), Rowley (2002) (F_{hyd2}, in blue), Müller et al. (2008) (F_{hyd3}, in orange) and Van Der Meer et al. (2014) (F_{hyd4}, in purple), as outlined in Table 2. c, Assumed riverine $^{87}Sr/^{86}Sr$ composition (R_{riv1}, in black). d, Calculated riverine Sr flux (F_{riv}) based on corresponding F_{hyd} scenarios.

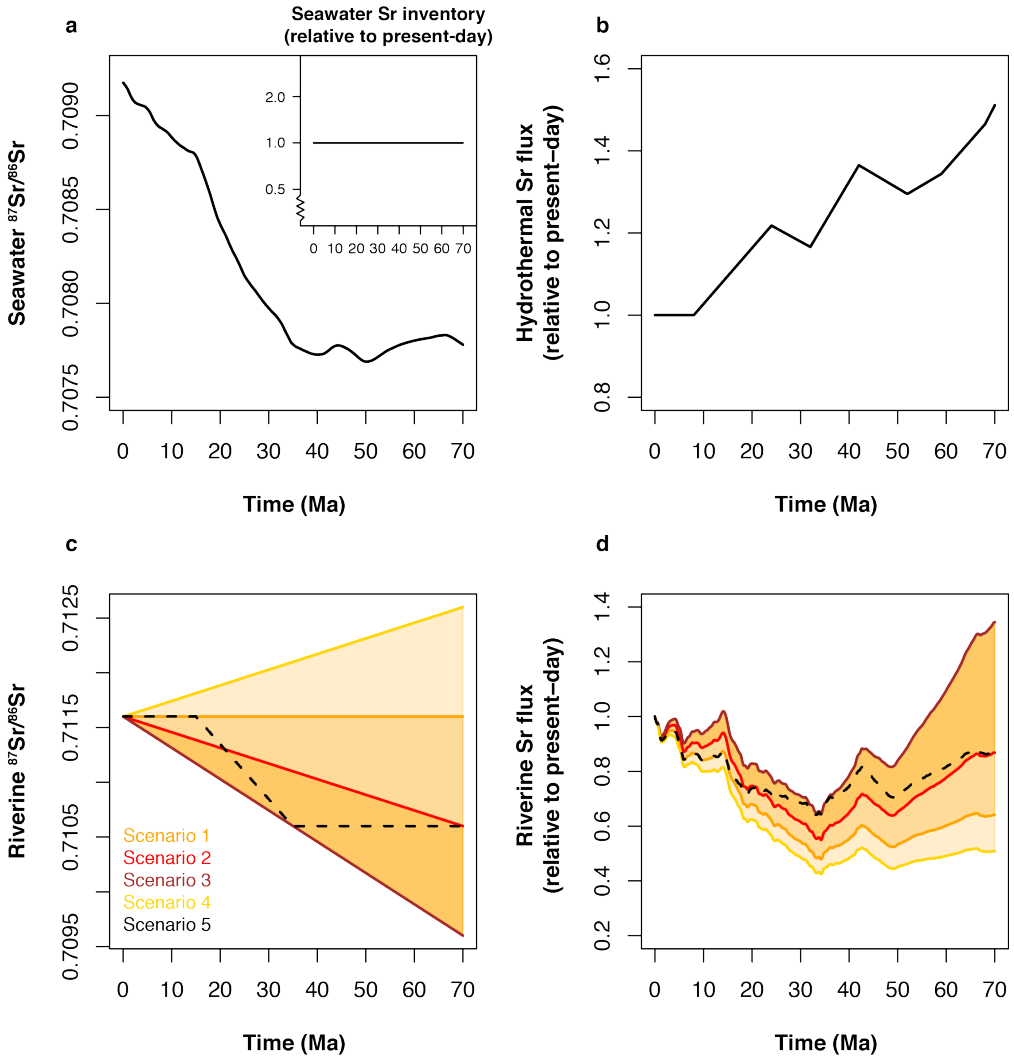

Figure 10: Cenozoic Sr cycle modeling and riverine Sr flux estimates based on different scenarios for riverine $^{87}Sr/^{86}Sr$ compositions. a, Seawater $^{87}Sr/^{86}Sr$ composition, as inferred from the smoothed record of McArthur et al. (2012) (in black). The inset represents the assumed seawater Sr inventory (N_1, in black). b, Hydrothermal Sr flux (F_{hyd}) based on the seafloor spreading and/or degassing rate reconstructions of Van Der Meer et al. (2014) (F_{hyd4}, in black). c, Assumed riverine $^{87}Sr/^{86}Sr$ composition, as outlined in Table 2 (R_{riv1}, dark orange solid line; R_{riv2}, red solid line; R_{riv3}, brown solid line; R_{riv4}, light orange solid line; R_{riv5}, black dashed line). Shaded areas represent ranges of intermediate values. d, Calculated riverine Sr flux (F_{riv}), based on corresponding R_{riv} scenarios.

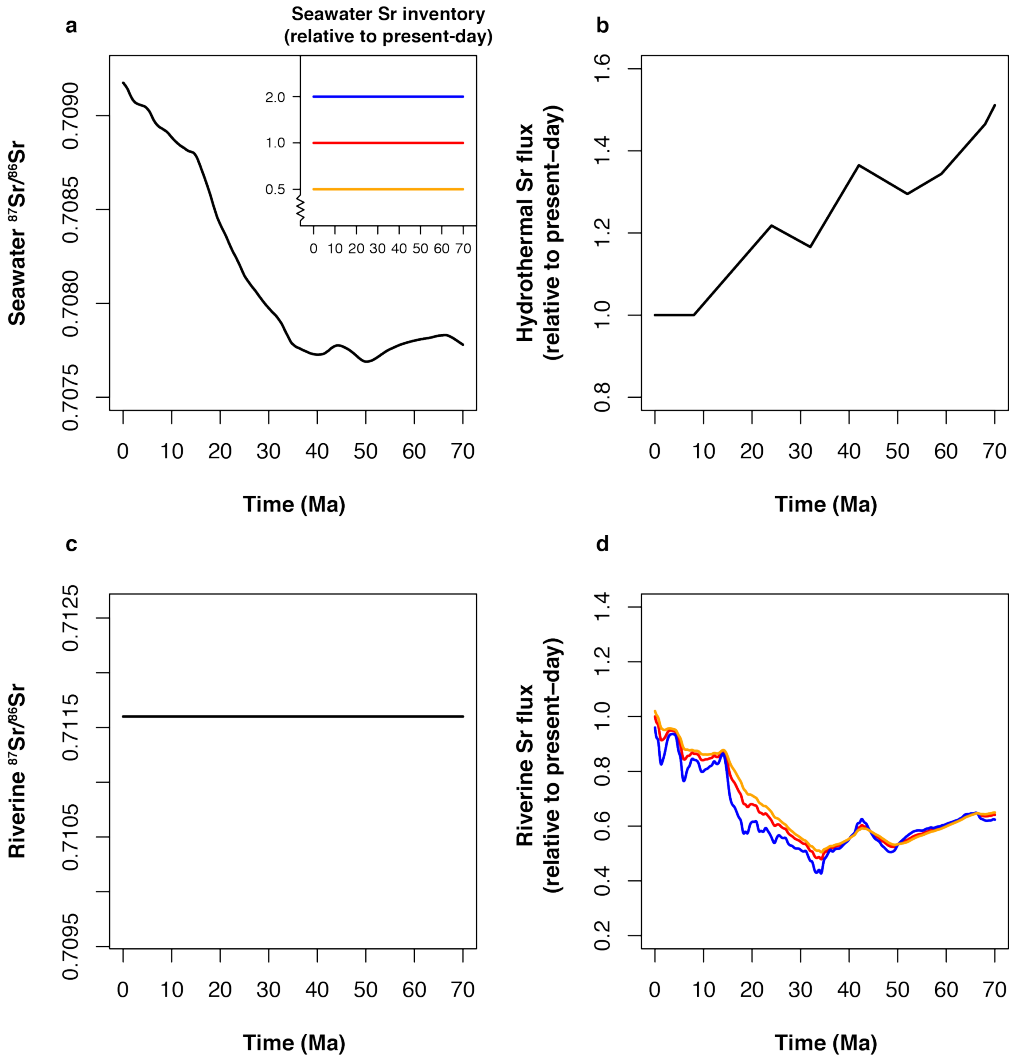

Figure 11: Cenozoic Sr cycle modeling and riverine Sr flux estimates based on different scenarios for seawater Sr inventories. a, Seawater $^{87}Sr/^{86}Sr$ composition, as inferred from the smoothed record of McArthur et al. (2012) (in black). The inset represents the assumed seawater Sr inventory, as outlined in Table 2 (N_1, in red; N_2, in blue; N_3, in orange). b, Hydrothermal Sr flux (F_{hyd}) based on the seafloor spreading and/or degassing rate reconstructions of Van Der Meer et al. (2014) (F_{hyd4}, in black). c, Assumed riverine $^{87}Sr/^{86}Sr$ composition (R_{riv1}, in black). d, Calculated riverine Sr flux (F_{riv}), based on corresponding R_{riv} scenarios.

2.4.1.5 Insights from inverse modeling of the marine Os isotope record

An analogous inverse modeling approach can be applied to the marine $^{187}Os/^{188}Os$ isotope record. The evolution of the Os inventory and $^{187}Os/^{188}Os$ composition of the ocean (N_{Os} and R_{sw}, respectively) over time can be written as:

$$\frac{dN_{Os}}{dt} = F_{riv} + F_{hyd} + F_{ext} - F_{sed} \quad (15)$$

$$\frac{N_{Os}}{7.4+R_{sw}}\frac{dR_{sw}}{dt} = F_{riv}\left(\frac{R_{riv}-R_{sw}}{7.4+R_{riv}}\right) + F_{hyd}\left(\frac{R_{hyd}-R_{sw}}{7.4+R_{hyd}}\right) + F_{ext}\left(\frac{R_{ext}-R_{sw}}{7.4+R_{ext}}\right) - F_{sed}\left(\frac{R_{sed}-R_{sw}}{7.4+R_{sed}}\right) \quad (16)$$

where N_{Os} represents the seawater Os inventory (in mol), F represents the fluxes of Os (in mol/yr) from and to the various reservoirs, R represents the $^{187}Os/^{188}Os$ composition of the various reservoirs and the subscripts *sw*, *riv*, *hyd*, *ext* and *sed* represent the seawater, riverine, hydrothermal, extraterrestrial and sediment reservoirs, respectively. In addition, the factor of 7.4 is used to normalize $^{187}Os/^{188}Os$ compositions for the natural abundances of ^{187}Os and ^{188}Os (Li and Elderfield, 2013). We note that the sedimentary Os flux (F_{sed}) does not affect R_{sw} because there is no isotopic fractionation associated with Os burial. A complete derivation of Equations (15) and (16) is presented in Van der Ploeg et al. (2018).

We use a similar suite of methods as described above for the Sr isotope system and generate multiple F_{riv} solutions for the Cenozoic based on a simplified version of the present-day Os cycle as modeled by Li and Elderfield (2013) (Table 3). First, we constrain changes in R_{sw} by using a smoothed fit to the $^{187}Os/^{188}Os$ record of ferromanganese crusts from Klemm et al. (2005) and Burton (2006), updated to the age model of Nielsen et al. (2009). Second, we use the seafloor spreading and/or degassing rate reconstructions of Berner (1994), Müller et al. (2008), Rowley (2002) and Van der Meer et al. (2014) as a forcing for the hydrothermal Os flux (F_{hyd}). We further assume that the extraterrestrial Os flux (F_{ext}) and the $^{187}Os/^{188}Os$ compositions of the hydrothermal and extraterrestrial Os fluxes have remained constant over the Cenozoic (Peucker-Ehrenbrink, 1996; Pegram and Turekian, 1999). Finally, we develop a range of scenarios for the $^{187}Os/^{188}Os$ composition of the riverine Os flux (R_{riv}) and the seawater Os inventory (N_{Os}) across the Cenozoic. We make no inferences about the sedimentary Os flux (F_{sed}) and calculate F_{riv} directly from Equation (16) based on the sizes and isotopic compositions of the Os input fluxes.

Most F_{riv} estimates based on modeling of the marine $^{187}Os/^{188}Os$ record show a progressive increase from the early Cenozoic towards the present (Figure 12; Figure 13; Figure 14), broadly consistent with the estimates obtained from modeling of the marine $^{87}Sr/^{86}Sr$ record. However, several differences between the Os-based and Sr-based F_{riv} estimates are apparent. First of all, the differences between the seafloor spreading and/or degassing rate reconstructions used as forcings for F_{hyd} have a virtually negligible effect on F_{riv} estimates from the Os isotope system (Figure 12). As with the Sr isotope system, the evolution of R_{riv} over the Cenozoic is the dominant source of uncertainty in Os-based F_{riv} estimates (Figure 13). Yet, for the early Cenozoic these Os-based F_{riv} estimates seem to be less affected by the different R_{riv} scenarios than the Sr-based F_{riv} estimates. This suggests that the Os cycle may actually be fairly well-constrained for the early Cenozoic using the assumptions listed above, despite the sensitivity of the $^{187}Os/^{188}Os$ ratio of seawater to potential contributions from the weathering of organic-rich sediments (Georg et al., 2013; Dubin and Peucker-Ehrenbrink, 2015). However, none of these Os-based estimates are able to reproduce high F_{riv} values for the early Eocene. If riverine

Table 3: Overview of all parameters used in Os cycle modeling. Present-day values are taken from the literature or fitted to match the present-day steady state observations. The Cenozoic scenarios for N_{Os}, F_{hyd} and R_{riv} are independent of each other.

Parameter	Parameter description	Value	Reference and Comments
Present-day			
N_{Os}	Os inventory in oceans	6.83×10^7 mol	Oxburgh (2001)
F_{riv}	Riverine flux of Os to oceans	1670×10^6 mol/Myr	Li & Elderfield (2013), following Li et al. (2009), taken as the sum of the silicate weathering and sediment weathering fluxes
F_{hyd}	Hydrothermal flux of Os to oceans	710×10^6 mol/yr	Li & Elderfield (2013), taken as the sum of the island basalt weathering and hydrothermal fluxes
F_{ext}	Extraterrestrial flux of Os to oceans	89×10^6 mol/Myr	Calculated to arrive at steady state of R_{sw} = 1.02
R_{riv}	$^{187}Os/^{188}Os$ composition of riverine flux	1.54	Li & Elderfield (2013), following Levasseur et al. (1999)
R_{hyd}	$^{187}Os/^{188}Os$ composition of hydrothermal flux	0.126	Li & Elderfield (2013), following Allègre & Luck (1980)
R_{ext}	$^{187}Os/^{188}Os$ composition of extraterrestrial flux	0.126	Li & Elderfield (2013), following Allègre & Luck (1980)
R_{sw}	$^{187}Os/^{188}Os$ composition of seawater	1.02	Klemm et al. (2005), Burton (2006), Nielsen et al. (2009), obtained using a smoothing spline
Cenozoic			
N_{Os}	Os inventory in oceans	Variable	
N_1	Scenario 1	6.83×10^7 mol	Constant, present-day value
N_2	Scenario 2	6.83×10^8 mol	Constant, 10x present-day value
N_3	Scenario 3	6.83×10^6 mol	Constant, 0.1x present-day value
F_{riv}	Riverine flux of Os to oceans	Variable	Calculated as model result from Equation (16)
F_{hyd}	Hydrothermal flux of Os to oceans	Variable	Scaled to seafloor spreading and/or degassing rate reconstructions
F_{hyd1}	Scenario 1	Variable	Berner (2004)
F_{hyd2}	Scenario 2	Variable	Rowley (2002)
F_{hyd3}	Scenario 3	Variable	Müller et al. (2008)
F_{hyd4}	Scenario 4	Variable	Van der Meer et al. (2014)
F_{ext}	Extraterrestrial flux of Os to oceans	89×10^6 mol/Myr	Constant, present-day value
R_{riv}	$^{187}Os/^{188}Os$ composition of riverine flux	Variable	
R_{riv1}	Scenario 1	1.54	Constant, present-day value
R_{riv2}	Scenario 2	1.24 at 70 Ma 1.54 at 0 Ma	Linear increase from 70 Ma to 0 Ma
R_{riv3}	Scenario 3	0.94 at 70 Ma 1.54 at 0 Ma	Linear increase from 70 Ma to 0 Ma
R_{riv4}	Scenario 4	1.84 at 70 Ma 1.54 at 0 Ma	Linear decrease from 70 Ma to 0 Ma
R_{riv5}	Scenario 5	1.24 at 70 Ma 1.24 at 35 Ma 1.54 at 15 Ma 1.54 at 0 Ma	Constant from 70 Ma to 35 Ma, linear increase from 35 Ma to 15 Ma, constant from 15 Ma to 0 Ma
R_{hyd}	$^{187}Os/^{188}Os$ composition of hydrothermal flux	0.126	Constant, present-day value
R_{ext}	$^{187}Os/^{188}Os$ composition of extraterrestrial flux	0.126	Constant, present-day value
R_{sw}	$^{187}Os/^{188}Os$ composition of seawater	Variable	Klemm et al. (2005), Burton (2006), Nielsen et al. (2009), obtained using a smoothing spline

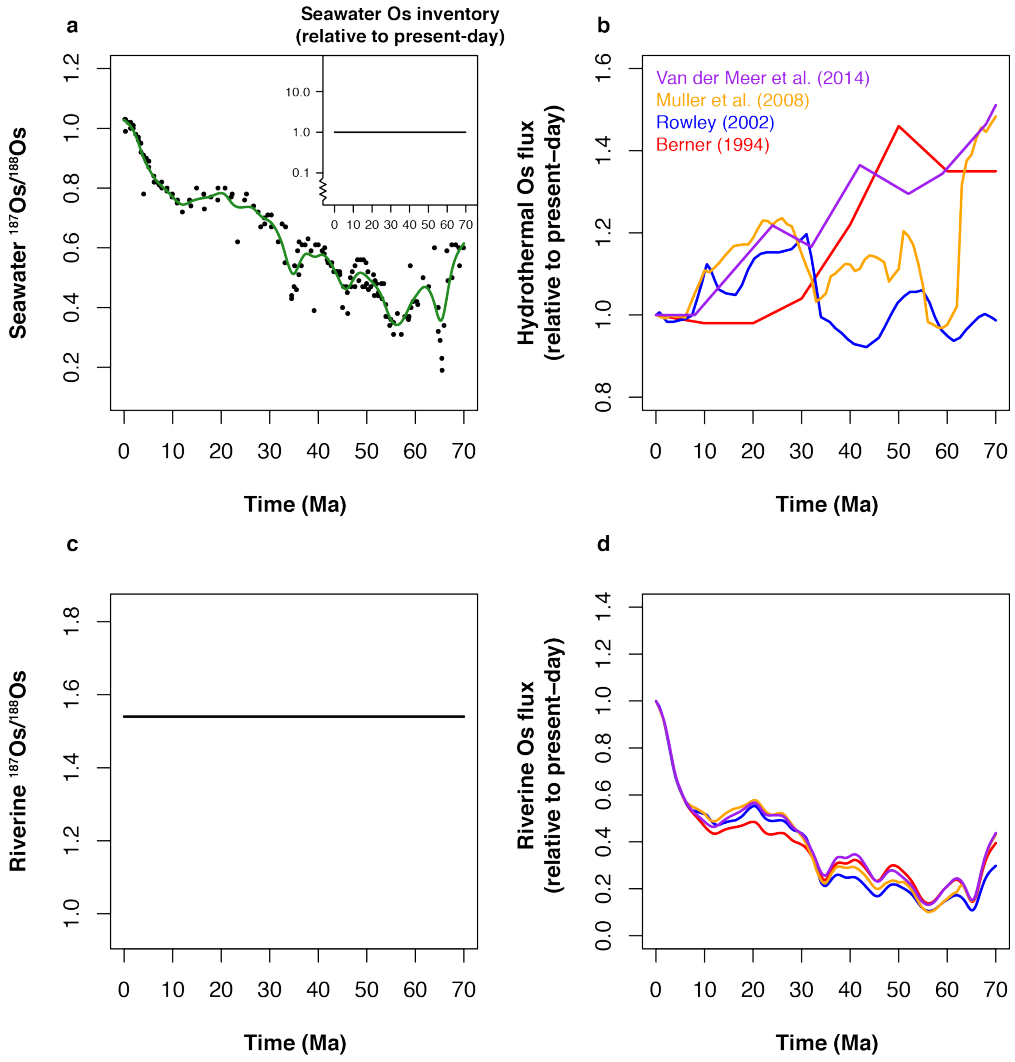

Figure 12: Cenozoic Os cycle modeling and riverine Os flux estimates based on different scenarios for the hydrothermal Os flux. a, Seawater $^{187}Os/^{188}Os$ records of Klemm et al. (2005) and Burton (2006), updated to the age model of Nielsen et al. (2009). The green line represents the smoothed fit used in our model calculations. The inset represents the assumed seawater Os inventory (N_1, in black). b, Hydrothermal Os flux (F_{hyd}) based on the seafloor spreading and/or degassing rate reconstructions of Berner (1994) (F_{hyd1}, in red), Rowley (2002) (F_{hyd2}, in blue), Müller et al. (2008) (F_{hyd3}, in orange) and Van Der Meer et al. (2014) (F_{hyd4}, in purple), as outlined in Table 2. c, Assumed riverine $^{187}Os/^{188}Os$ composition (R_{riv1}, in black). d, Calculated riverine Os flux (F_{riv}) based on corresponding F_{hyd} scenarios.

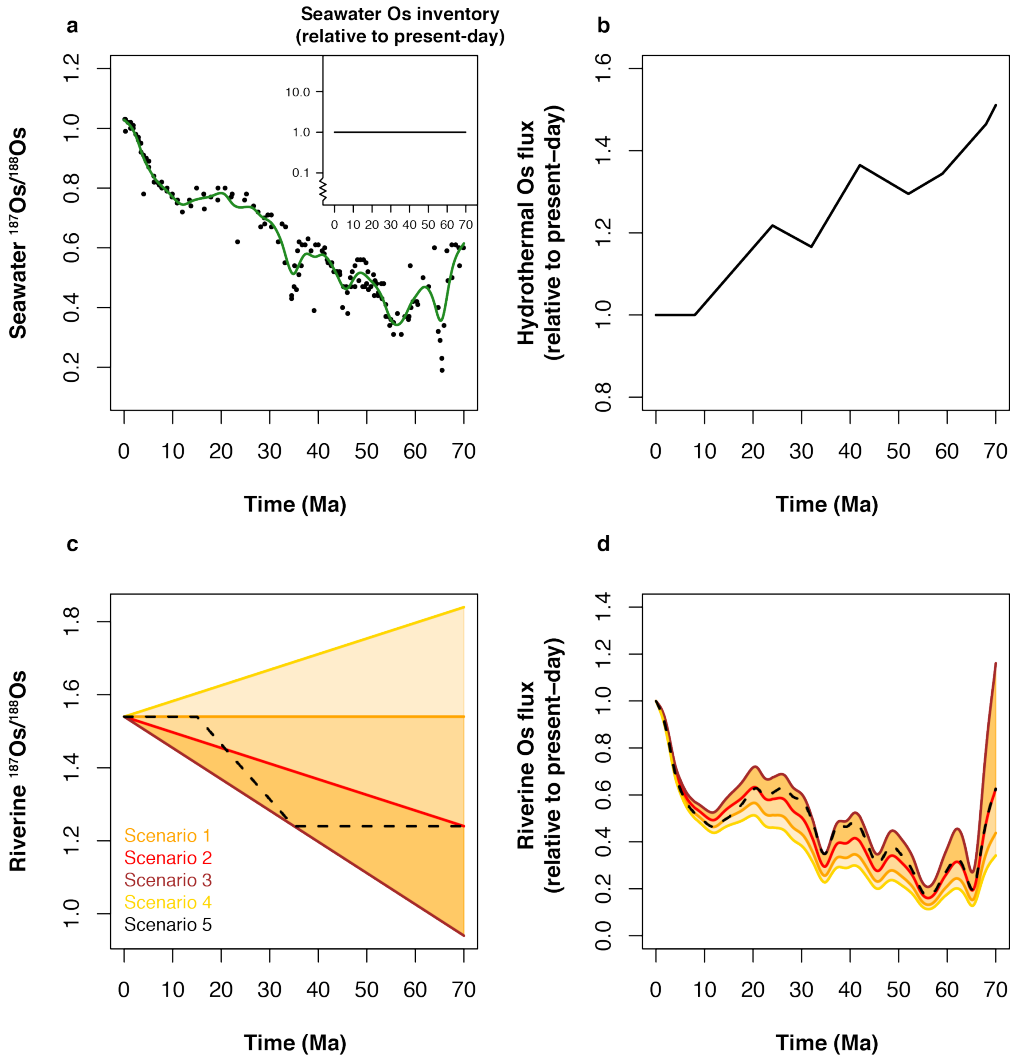

Figure 13: Cenozoic Os cycle modeling and riverine Os flux estimates based on different scenarios for riverine $^{187}Os/^{188}Os$ compositions. a, Seawater $^{187}Os/^{188}Os$ composition, as inferred from the smoothed record of McArthur et al. (2012) (in black). The inset represents the assumed seawater Os inventory (N_t, in black). b, Hydrothermal Os flux (F_{hyd}) based on the seafloor spreading and/or degassing rate reconstructions of Van Der Meer et al. (2014) (F_{hyd4}, in black). c, Assumed riverine $^{187}Os/^{188}Os$ composition, as outlined in Table 2 (R_{riv1}, dark orange solid line; R_{riv2}, red solid line; R_{riv3}, brown solid line; R_{riv4}, light orange solid line; R_{riv5}, black dashed line). Shaded areas represent ranges of intermediate values. d, Calculated riverine Os flux (F_{riv}), based on corresponding R_{riv} scenarios.

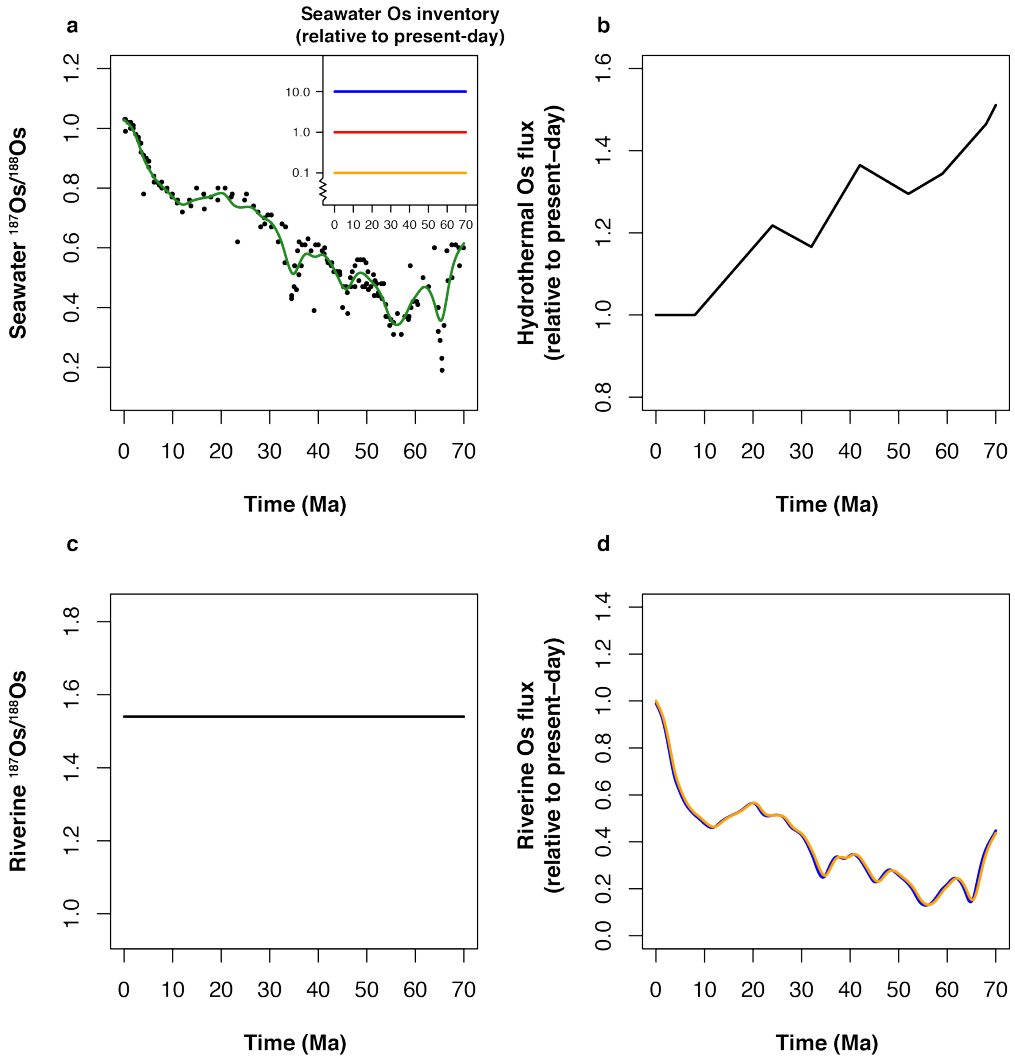

Figure 14: Cenozoic Os cycle modeling and riverine Os flux estimates based on different scenarios for seawater Os inventories. a, Seawater $^{187}Os/^{188}Os$ composition, as inferred from the smoothed record of McArthur et al. (2012) (in black). The inset represents the assumed seawater Os inventory, as outlined in Table 2 (N_1, in red; N_2, in blue; N_3, in orange). b, Hydrothermal Os flux (F_{hyd}) based on the seafloor spreading and/or degassing rate reconstructions of Van Der Meer et al. (2014) (F_{hyd4}, in black). c, Assumed riverine $^{187}Os/^{188}Os$ composition (R_{riv1}, in black). d, Calculated riverine Os flux (F_{riv}), based on corresponding R_{riv} scenarios.

Os fluxes are generally representative of silicate weathering and CO_2 consumption rates, this would be directly at odds with the paradigm of elevated weathering rates in globally warm climates resulting from the silicate weathering thermostat (Berner et al., 1983; Zachos et al., 2008). Clearly, the relationships between riverine Os fluxes and silicate weathering rates will need to be better resolved in future studies. Finally, changes in the size of the seawater Os inventory (N_{Os}) have no discernable effect on F_{riv} estimates derived from Os input fluxes only (Figure 14).

2.4.2 Further considerations

2.4.2.1 Weathering and geochemical cycles

Many of the processes that affect the distribution of elements and isotopes employed in the various chemical weathering proxies are relatively well understood. However, several aspects of these interactions in element cycles remain unresolved, especially regarding the sizes and isotopic compositions of several element fluxes. This has important consequences for mass balance calculations and estimates of oceanic residence times, both at the present and in the past. Moreover, shifts in the balance between fluxes into and out of the global ocean may have significantly altered the residence times of elements in the past. For example, the oceanic residence time of Sr is shown to have fluctuated between 1 Myr and 20 Myr during the Phanerozoic as a result of major flux imbalances and changes in ocean chemistry (Vollstaedt et al., 2014).

Continental weathering processes are strongly linked to river chemistry. In most studies of global river transport fluxes, data are generally based on a selection of Earth's major rivers (Gaillardet et al., 1999). However, it has also been suggested that small, mountainous rivers have a larger influence on sediment and element budgets than the major rivers (Milliman and Syvitski, 1992). This would imply that the global average isotopic composition of river water used in most studies is not representative of the rivers that contribute most to chemical weathering. Furthermore, weathering fluxes calculated from modern rivers are likely still dominated by enhanced weathering following the last glacial-interglacial cycle, and are therefore thought to be out of equilibrium on these timescales (Vance et al., 2009).

In addition, not all dissolved minerals released from the weathering of silicate rocks reach the global ocean directly, because they may be retained on the continents in vegetation and soils. The storage of Ca, Mg and Li on the continents is also thought to have affected the global cycles of these elements in the past, for example during the Paleogene (Tipper et al., 2006b; Fantle and Tipper, 2014; Vigier and Goddéris, 2015). Importantly, the impact of element storage depends on the residence time on the continents relative to the residence time in the oceans.

2.4.2.2 Weathering and climate

According to theory, rates of silicate weathering are expected to increase as a result of warmer and wetter climates in order to draw down CO_2 (Walker et al., 1981). However, the link between chemical weathering and physical weathering through climate may change the effectiveness of this negative feedback mechanism (Kump et al., 2000). Physical weathering is believed to enhance chemical weathering and CO_2 consumption rates on a global scale (Gaillardet et al., 1999; Millot et al., 2002), but this may be different depending on the timescales involved. For example, an increase in runoff, physical weathering and erosion during the last deglaciation resulted in a decrease in the importance of chemical weathering in the Himalayas (Dosseto

et al., 2015). Moreover, the effect of climate on chemical weathering rates is shown to be dependent on uplift rates (West et al., 2005; West, 2012). In fact, carbonate weathering can also as a source of CO_2 in areas with very high erosion rates due to sulfide oxidation (Torres et al., 2016). This highlights the importance of understanding the feedbacks between climate and chemical weathering on different spatial and temporal scales.

Major events in the evolution of the climate system, such as the development of ice sheets, may also affect chemical weathering feedbacks (Vance, 2011). For example, weathering variability on glacial-interglacial timescales is shown to be negligible, because during glacials reduced chemical weathering rates are balanced by increased exposure and weathering of continental shelves (Foster and Vance, 2006). However, on long geological timescales, enhanced weathering during interglacials is thought to contribute to CO_2 drawdown.

In addition, the relative amounts of silicate and carbonate weathering may vary with seasonal changes in runoff (Tipper et al., 2006a). The relative amount of silicate weathering increases during the dry season, whereas the relative amount of carbonate weathering increases during the wet season because of faster dissolution kinetics. Furthermore, the relative importance of silicate and carbonate weathering is dependent on physical weathering and erosion (Jacobson and Blum, 2003; Jacobson et al., 2003). This is crucial to the application of proxies that are sensitive to changes in the balance of silicate and carbonate weathering.

2.5 Conclusions

The chemical weathering of silicate rocks on land regulates and balances atmospheric CO_2 levels and global temperatures on geological timescales. There are various proxies to reconstruct changes in chemical weathering in the past, which have been reviewed and compared in this paper. The selection of the best proxies for specific scenarios is dependent on the geological context in which they can be applied and the timescales at which they record changes in chemical weathering and the carbon cycle.

Global chemical weathering proxies may be classified on the basis of the oceanic residence times of their respective elements. We distinguish between elements that are short-lived (< 10 kyr) and long-lived (> 10 kyr) relative to the mixing time of the global ocean. $^{187}Os/^{188}Os$ is able to record continental weathering variations on timescales similar to climatic processes because of its intermediate oceanic residence time, which makes it an excellent proxy to investigate changes in the short-term carbon cycle. By contrast, given their long oceanic residence times, the $^{87}Sr/^{86}Sr$, $\delta^{7}Li$, $\delta^{44}Ca$ and $\delta^{26}Mg$ proxies reflect the effects of global changes in chemical weathering on timescales similar to tectonic processes. As a result, these proxies are good choices to evaluate changes in the long-term carbon cycle and the chemical evolution of the oceans. While individual proxies may provide valuable results, the best results are achieved when multiple proxies are combined.

In the future, further research may be focused on gaining an even better understanding of the element cycles and isotope distributions employed in the various chemical weathering proxies. Elemental and isotopic budgets are crucial to the application of these proxies, but still values of element fluxes and their isotopic composition are based on assumptions or remain unknown. Improving our knowledge of the processes that affect the distribution of these elements and their isotopes may therefore provide a better framework in which weathering studies can be interpreted. As we have demonstrated by inverse modeling of the marine $^{87}Sr/^{86}Sr$ and $^{187}Os/^{188}Os$ isotope records, it is especially important for accurate weathering

reconstructions to constrain temporal changes in the contributions of different rock types to the global weathering flux.

Acknowledgements

This work was carried out under the program of the Netherlands Earth System Science Centre (NESSC), which is financially supported by the Ministry of Education, Culture and Science (OCW) of the Netherlands. RvdP thanks Ton Markus (Utrecht University) for aid with figure design.

Chapter 3

Secular variations in the carbonate chemistry of the oceans over the Cenozoic

Secular variations in the carbonate chemistry of the oceans over the Cenozoic

Bernard P. Boudreau, Jack J. Middelburg, Appy Sluijs and Robin van der Ploeg

Abstract

Oceanic carbonate chemistry during the Cenozoic has affected the climatology, ecology, and marine geology of our planet; yet, we have limited means to know the evolution of that chemistry, due to a lack of preserved and unaltered seawater samples and a continuing paucity of proxies. Modelling is often used to address this problem; here, we offer a simple, data-driven, secular time-scale, inverse model for the mean, Cenozoic, carbonate chemistry of the oceans. Inputs for the model include carbonate compensation depth (CCD), $CaCO_3$ burial, seawater temperature, atmospheric CO_2 and carbonate ion records, as well as a simple set of original, but justified, assumptions. The model retrodicts the total dissolved inorganic carbon (DIC), carbonate alkalinity (CAlk), and pH of the surface and deep waters of the ocean. The retrodicted DIC and CAlk records do not indicate any unusually elevated values in the early Cenozoic, as found in some past studies. If the CCD record from Lyle et al. (2008) is employed, the changes in DIC and CAlk appear entirely related to changes in the alkalinity input to the pelagic oceans and atmospheric CO_2; however, with the CCD from Pälike et al. (2012), the increases in DIC and CAlk during the last 15 Ma reflect the effects of ocean cooling. Using either CCD-record, our model provides consistent retrodictions of the available pH record. Our results are not consistent with many past modelling assumptions, such as constancy of alkalinity in surface waters, or the ratio of shallow and deep carbonate ion concentrations. Finally, we use our results to provide new estimates of atmospheric CO_2 based on Boron isotopes and find significantly lower CO_2 values in the Early Cenozoic than previous values.

3.1 Introduction

Understanding how the carbonate chemistry of the oceans has evolved on a time scale of 100 million years constitutes a central theme of paleoceanographic research. The nature of that evolution is imperative in comprehending changes in the deposition and preservation of biogenic sediments, past shifts in marine biological species (including extinctions), variations in carbon isotopic records found in sediments, and the history of the CO_2 content of the atmosphere.

The most coveted information of this type is arguably the carbonate system chemistry of past oceans. There exist unfortunately no unaltered samples of ancient seawater (e.g., as inclusions) that can be analyzed for carbonate system components, i.e., dissolved carbon dioxide (CO_2), bicarbonate ion (HCO_3^-) and carbonate ion (CO_3^{2-}), nor their analytical surrogates, i.e., titration total alkalinity and total dissolved inorganic carbon (DIC = CO_2 + HCO_3^- + CO_3^{2-}). Although proxies for some carbonate components have been advanced, these proposals are either confounded by other factors (e.g., B/Ca proxy for CO_3^{2-}; Yu and Elderfield, 2007), or cannot be applied on secular timescales, e.g., the δ^7Li proxy for total dissolved inorganic carbon (Vigier et al., 2015) because of long-term changes in δ^7Li (Misra and Froelich, 2012). pH now has a proxy (δ^{11}B), and that does place some constraints on the carbonate system

(e.g., Spivack et al., 1993; Palmer et al., 1998; Palmer and Pearson, 2003; Yu and Elderfield, 2007; Honisch et al., 2009; Anagnostou et al., 2016).

This lack of data has inspired the marine and geochemical modeling communities to formulate and solve (long-term) mathematical models that aim, as part of their results, to provide some measure of the carbonate chemistry of the oceans. Initial versions of such models treated the oceans simply as a single reservoir in a large multi-reservoir representation of the carbon cycle of the earth as it evolved through time, e.g., Berner et al. (1983). Any retrodictions, i.e. predictions of the past, of the carbonate chemistry of the oceans from such models, including their similarly constructed progeny (Mackenzie et al., 1993; Wallmann, 2001; Arvidson et al., 2006; Berner, 2006), only provide gross averages, at best, which limits their utility for many paleoceanographic applications. The dichotomy in the dissolved carbonate chemistry between the surface and the deep waters of the oceans, and the differing processes that create this situation, are fundamental to credible retrodiction. Conversely, the lateral gradients in the oceans are far smaller and can often be ignored to a first approximation, as discussed below.

Paleoceanographic models that have the essential vertical resolution have appeared over the past 15 years, either as multi-box models of the ocean (e.g., Keir, 1988; Caldeira and Rampino, 1993; Ridgwell et al., 2003; Zeebe and Zachos, 2007; Zeebe, 2012; Omta et al., 2013; Caves et al., 2016), as spatially resolved intermediate complexity models (e.g., Maier-Reimer, 1993; Ridgwell and Hargreaves, 2007; and the review by Hülse et al., 2017), and even in fully coupled GCMs (e.g., Winguth and Winguth, 2012; Heinze and Ilyina, 2015).

As with all conservation models involving time stepping, i.e., either ordinary or partial differential equations, such models face one enormous hurdle: what initial conditions do you set for the model? The problem here is that the initial carbonate chemistry is no more known than that chemistry at any later time, except for the present of course. The models are unstable to march backwards in time, so that cannot be done to eliminate this problem. To make matters worse, most (if not all) of these models are under-determined, i.e., more unknowns, both variables and parameters, than equations, and additional data or assumptions must be introduced. Adding related variables, like stable carbon isotope ratios ($\delta^{13}C$), might alleviate some of the problems, but usually one must introduce various new additional assumptions. Modeling the oceans of the past is not for the fainthearted.

The most commonly made assumptions are:

(1) The mean calcite saturation state of the surface oceans has remained approximately constant over the Cenozoic (Tyrrell and Zeebe, 2004; Caves et al., 2016);
(2) The ratio of the carbonate ion concentrations in the surface and deep water has remained constant (Tyrrell and Zeebe, 2004);
(3) The ratio of the export flux of organic matter (productivity) to the export flux of $CaCO_3$ tests (calcification) is, at least, piecewise fixed (Sigman and Boyle, 2000);
(4) The alkalinity of the surface ocean is constant or has a fixed relation to salinity (Hönisch and Hemming, 2005);
(5) The depth where the export flux of $CaCO_3$ is exactly matched by the rate of dissolution at the seafloor, i.e., the carbonate compensation depth (CCD), is the same as the depth where seawater first becomes undersaturated with respect to calcite, i.e., the saturation depth, z_{sat} (Tyrrell and Zeebe, 2004; Caves et al., 2016).

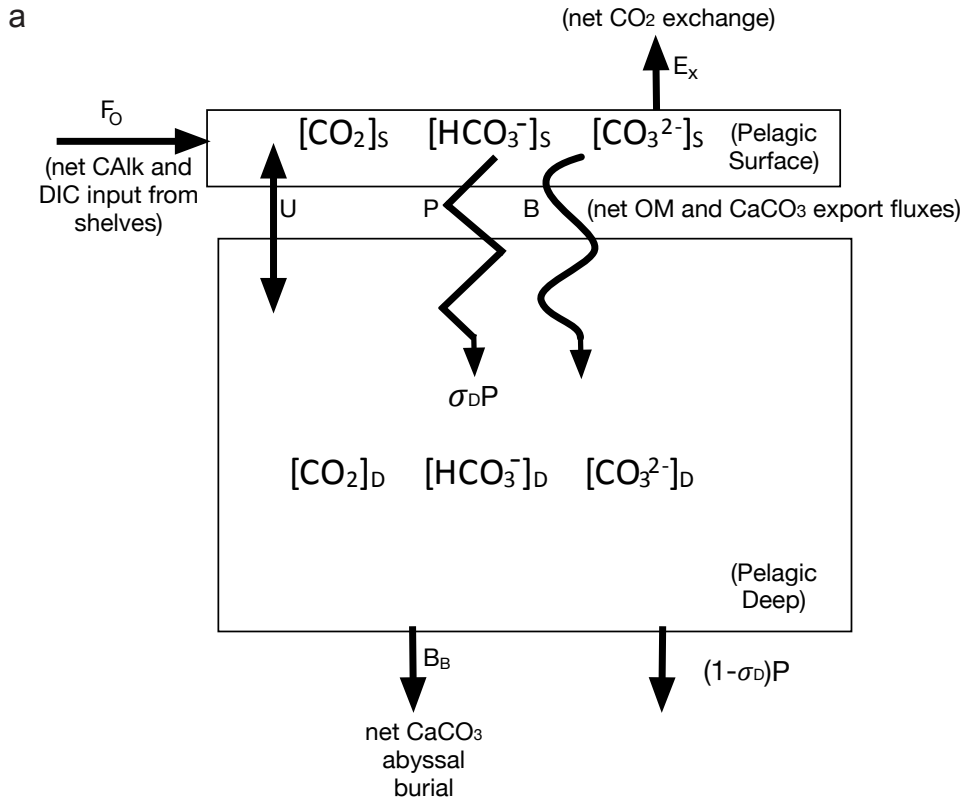

Figure 1a: Model overview and description. Conceptual diagram of the two-box dissolved carbonate system model used in this paper. Terms are also defined in panel (b).

Attempts have been made by Tyrrell and Zeebe (2004) and others to justify these assumptions based on paleoceanographic data, e.g., calcite snowline records, i.e., the depth where the $CaCO_3$ content of sediments drops effectively to zero. Some papers (e.g., Tyrrell and Zeebe, 2004; Caves et al., 2016), have also included an effort to evaluate the sensitivity of their results to likely variability associated with their assumption(s).

There is a means, however, to incorporate more paleoceanographic data into the formulation and solution of a model. Such models are inverse models *sensu lato,* as they use data that characterize the output of a system, e.g., burial, CCD and atmospheric CO_2 records, to glean information about the input, variables, the composition of the oceans and parameters of that system, e.g., alkalinity flux to the deep ocean, calcification rates, etc.

More than a decade ago, Tyrrell and Zeebe (2004) constructed an early form of such a model, but still needed to invoke some of the assumptions listed above. More recently, Boudreau and Luo (2017) created a more advanced example of this type of procedure. In that study, the records of the past positions of the carbonate compensation depth (z_{cc}) were used to infer rates of calcification and $CaCO_3$ burial in the deep ocean on secular time scales (≥ 1 Ma). None of assumptions (1)-(5) listed above were employed in that study. In fact, only one assumption was invoked, i.e., that the *shape* of the $CaCO_3$-content profile with ocean depth

b

Surface Water Box:

$$U([CO_2]_D + [HCO_3^-]_D + [CO_3^{2-}]_D - [CO_2]_S - [HCO_3^-]_S - [CO_3^{2-}]_S) - B - P + F_O - Ex = 0 \quad (1)$$

$$U([HCO_3^-]_D + 2[CO_3^{2-}]_D - [HCO_3^-]_S - 2[CO_3^{2-}]_S) - 2B + F_O = 0 \quad (2)$$

$$K_{eq}^{s}([CO_2]_S [CO_3^{2-}]_S) - ([HCO_3^-]_S)^2 = 0 \quad (3)$$

$$[CO_2]_S = K_0 [CO_2]_a \quad (4)$$

Deep Water Box:

$$U([CO_2]_S + [HCO_3^-]_S + [CO_3^{2-}]_S - [CO_2]_D - [HCO_3^-]_D - [CO_3^{2-}]_D) + (B - B_B) + \sigma_D P = 0 \quad (5)$$

$$U([HCO_3^-]_S + 2[CO_3^{2-}]_S - [HCO_3^-]_D - 2[CO_3^{2-}]_D) + 2(B - B_B) = 0 \quad (6)$$

$$K_{eq}^{D}([CO_2]_D [CO_3^{2-}]_D) - ([HCO_3^-]_D)^2 = 0 \quad (7)$$

Glossary:

$[CO_2]_a \equiv$ atmospheric carbon dioxide concentration

$[CO_2]_i$, $[HCO_3^-]_i$, $[CO_3^{2-}]_i \equiv$ Concentrations of the three dissolved carbonate species in reservoir i, with i = D or S for Deep and Surface waters, respectively

$B \equiv$ net rate of calcification ($CaCO_3$) exported from the surface water to the deep water

$U \equiv$ net water exchange rate between the surface and deep water boxes

$P \equiv$ net rate of organic matter (OM) productivity exported from the surface water to the deep

$\sigma_D \equiv$ fraction of OC export P regenerated in deep waters (set to one except in Section 4.2)

$F_O \equiv$ net rate of alkalinity & DIC addition to the surface pelagic oceans from shallow waters (not to be confused with F_{Alk} in Boudreau et al., 2010)

$Ex \equiv$ net rate of CO_2 gas exchange between the surface ocean and the atmosphere

$B_B \equiv$ net rate of burial of $CaCO_3$ in deep-sea sediments

$K_0 \equiv$ Henry's Law constant for gas equilibrium

$K_{eq}^{i} \equiv$ stoichiometric equilibrium constant in reservoir i for the reaction:

$$(CO_2)aq + CO_3^{2-} + H_2O \leftrightarrow 2\,HCO_3^- \quad (8)$$

Thus, K_{eq}^{i} is the ratio of the first dissociation constant of carbonic acid (K_1) to the second dissociation constant (K_2), i.e., $K_{eq} = K_1/K_2$.

Figure 1b: Model overview and description. Equations describing the secular state of the dissolved carbonate system in a two-box model of the oceans. We note that F_O in equation (1) is the net rate of alkalinity input to the pelagic oceans, i.e., the difference between the input from rivers (due to weathering) and the net rate of alkalinity removal or addition by nearshore processes, while discounting significant hydrothermal input (Berner and Berner, 1996). F_O is a calculated quantity and not assigned. HCO_3^- is the dominant form of DIC and CAlk in ocean water (Sarmiento and Gruber, 2006); thus, F_O appears in equation (2) as a source of DIC to the pelagic ocean. We thus assume that DIC/Calk ratio of the input F_O is one and invariant.

could be calculated simply from values of the compensation and saturation depths and the depositional rate of non-carbonate sediment (clay). Note that even that shape assumption is not necessary if the $CaCO_3$ burial and CCD records can be shown to be mutually consistent, as they appear to be over the past 30 Ma (Boudreau and Luo, 2017).

Here, we present an inverse model for the mean dissolved carbonate chemistry of the *pelagic* ocean over the Cenozoic. Our model does not try to invert a complete earth system

science model, but instead the small set of equations that account for conservation of the dissolved carbonate species of a mean pelagic ocean, surface and deep; consequently, only carbonate alkalinity (CAlk = HCO_3^- +2 CO_3^{2-}), total dissolved inorganic carbon (DIC = CO_2(aq) + HCO_3^- + CO_3^{2-}), seawater pH, and atmospheric CO_2 are addressed and the processes that directly influence them.

We need to introduce our own assumptions to solve our equations, but none of those listed above. For example, we assume that all organic matter export from the surface pelagic oceans is regenerated in the deep water and not preserved in sediments. To put that assumption in context, according to Sarmiento and Gruber (2006), the present pelagic oceans export ~550 Tmol C a^{-1} at 100 m water depth, but ultimately bury in pelagic sediments only 1.6 Tmol C a^{-1}; thus, the leak through burial is only 0.3 % of export. Our model predicts an export of 170 Tmol a^{-1}, but at 200m, and burial would account for a loss of ~1%. These number explain why we set regeneration equal to export in our model; however, we demonstrate explicitly the weak influence of deep-sea carbon preservation later in our paper. Similarly, we decouple organic and inorganic carbon diagenesis in sediments, i.e., organic matter oxidation does not significantly affect pelagic $CaCO_3$ burial, contrary to the hypothesis offered by Emerson and Bender (1981); despite wide use, little empirical evidence has accumulated that demonstrates the validity of this hypothesis (e.g., Jahnke and Jahnke, 2004).

Our aims with the present contribution are (1) to provide a secular-scale estimate of the chemical conditions for the carbonate system, i.e., carbonate alkalinity, DIC and pH, and (2) to examine if the results of our alternative model suggest that any of the assumptions in the list above are universal and independent of the model employed, so that they may safely be adopted regardless of the model. This latter point is particularly important when trying to estimate past oceanic carbonate chemistry or atmospheric CO_2 levels from proxies, e.g., from Boron isotopes. Finally, we employ our results to provide new estimates of surface seawater pH over the Cenozoic from the Boron-isotope record.

3.2 Model and inputs

3.2.1 Model specification

Central in our approach is the surface to deep water dichotomy in their carbonate chemistries; as such, a single box model of the oceans is inadequate. However, lateral gradients, within either the surface or deep oceans, are of second order importance to the overall dynamics of the inorganic carbonate chemistry of the oceans. More specifically, while we fully realize that horizontal gradients exist in the oceans, they pale in magnitude to those in the vertical direction. For example, both CAlk and DIC change by as much as 300 μM vertically over <5 km; horizontal gradients of these same variables are of the order of 200 μM over 25000 km (e.g., Sarmiento and Gruber, 2006). When fully resolved, biogeochemical models are applied to the past, their predictions remain in line with these estimates (e.g., Heinze and Ilyina, 2015). Consequently, unless there is a real need to resolve the horizontal changes, they can be ignored safely if the mean behavior of the oceans is the focus of the model, as it is here.

The simplest model that can capture a vertical dichotomy, while ignoring horizontal gradients, is a two-box model. One could argue that a three-box model that contains a high-latitude box for deep convection, i.e., a Harvardton-Bear model (Knox and McElroy, 1984; Sarmiento and Toggweiler, 1984; Siegenthaler and Wenk, 1984; Broecker et al., 1999; Boudreau et al., 2010) might better represent the dynamics of the ocean, but that is only on "short" time

scales. On a secular timescale, i.e. ≥ 1 Ma (Boudreau and Luo, 2017), which concerns the present paper, the high-latitude box adds nothing substantial. The transit time is too short and its volume too small to influence any of our conclusions; thus, it is left out of our model.

The dependent variables in our model are the concentrations of the dissolved carbonate species in surface and deep reservoirs. A conceptual diagram for our model is presented in Fig. 1a, and the conservation equations for these quantities for our two model boxes are displayed in Fig. 1b – the first two equations for each box are for DIC and CAlk. Our model is based on CAlk because the latter is sufficient to fully specify ocean carbonate chemistry. Our CAlk results can easily be converted into total alkalinity (TAlk) – see Supplementary Fig. 7 for an example. Our equations are simple algebraic balances because the carbonate chemistry of the oceans is essentially in a quasi-steady state on secular time scales (~3X the residence time of the HCO_3^- in the oceans). The other two equations are statements of thermodynamic equilibrium between the carbonate species in each reservoir. The other rate terms in these equations are defined in Fig. 1b.

The assumptions in these equations are: a) a two-box model provides an acceptable representation of oceanic carbonate chemistry on a time scale ≥ 10^6 years; b) a simple exchange flow, U, is a satisfactory parameterization of secular time-scale water exchange; c) no appreciable organic matter is buried in the deep sea, i.e., less than 0.3 % of export flux is buried (Sarmiento and Gruber, 2006); consequently, so that organic carbon export production P in (1) is balanced by a negative σ_D P in (5), where σ_D is the fraction of exported carbon that is regenerated in deep waters. Initially we assume σ_D = 1, and we demonstrate the accuracy of this assumption in Section 3.4.2; and, d) the net alkalinity input to the pelagic ocean, F_O, is an unknown; F_O can also be equated to the net DIC input to the pelagic ocean needed to support the inorganic carbon balance, which is well approximated in the oceans where the bicarbonate concentration is ~20X the carbonate ion concentration. Thirdly, we ignore any dissolution of $CaCO_3$ within sediments (Emerson and Bender, 1981) because that process has not been convincingly demonstrated as important in pelagic sediments (Jahnke et al., 1994; Jahnke and Jahnke, 2004).

The 7 equations in Fig. 1 apparently contain 16 unknowns, i.e., $[CO_2]_S$, $[HCO_3^-]_S$, $[CO_3^{2-}]_S$, $[CO_2]_D$, $[HCO_3^-]_D$, $[CO_3^{2-}]_D$, U, B, P, F_O, Ex, $[CO_2]_a$, K_{eq}^S, K_{eq}^D, K_o, and B_B; thus, there are 9 extra unknowns (σ_D is discussed in Section 3.4.2). That situation looks bleak and typical of all such models of the past. There are, fortunately, assumptions, simplifications and additional relations that can be used. Simplification starts by adding (2) and (6) to get:

$$F_O = 2\,B_B \quad (9)$$

which means that the input of (carbonate) alkalinity and DIC to the pelagic oceans to support the inorganic carbon balance is twice the burial rate of $CaCO_3$. Equation (9) allows us to calculate F_O if we know B_B and that will replace equation (6). In addition, combining equations (1), (5) and (9) gives:

$$Ex = B_B \quad (10)$$

which says that the rate of $CaCO_3$ burial is equal to the net CO_2 flux out of the (pelagic) surface oceans. Note that we assume that volcanic emissions are direct to the atmosphere and

thus captured in our CO_2 record so that they do not appear in our equations. Consequently, equation (10) can replace equation (5).

Next, we add new information to resolve the unknowns. First, assume that $[CO_2]_a$ is known from proxies and other measurements (Beerling and Royer, 2011) and can be represented by the smooth curve in Fig. 2a. (The Boron-isotope-based CO_2 data have been removed from this compilation for reasons explained below). This approach removes one extra unknown, and because of equation (4), $[CO_2]_S$ is immediately calculable. We fully realize that adopting the $[CO_2]_a$ curve in Fig. 2a is a significant step, and we test its influence in Supplementary Fig. 3. Furthermore, the pCO_2 record is under constant revision, so much so that our results can only be considered provisional – see Supplementary Fig. 8.

Results from Boudreau and Luo (2017) provide both $[CO_3^{2-}]_D$ and B_B time series, as functions of the CCD records offered respectively by Lyle et al. (2008) and Pälike et al. (2012); using these former series thereby drops the unknowns to 6 – see Fig. 2b-d. The Lyle et al. (2008) record is a recalibration of the (scientifically ancient) Van Andel (1975) record, and the latters coarseness does limit its utility. The Pälike et al. Pacific CCD record shares some of the data of the Lyle et al. (2008) ocean-wide CCD record, but is chrono-stratigraphically better constrained and temporally better resolved, thus revealing finer detail; nevertheless, the Pälike et al.-record relies upon equatorial cores and some of the observed structure may simply be related to long-term shifts in the ITCZ and the corresponding location of peak surface ocean productivity, rather than overall changes in ocean carbonate chemistry. We can expect some divergence in predictions from these two records, especially in the last 30 Ma of the Cenozoic. Note also that the Boudreau and Luo (2017) burial retrodictions are not in agreement, in either magnitude or trends, with those offered by Hilting et al. (2008), based on carbon-isotope modelling, and that issue cannot be resolved here.

The thermodynamic constants K_{eq}^{S}, K_{eq}^{D} and K_o can be calculated from the equations in Hain et al. (2015) – see Fig. 2e, using ocean and atmospheric temperature records (Beerling and Royer, 2011; Hansen et al., 2013) and the secular changes in dissolved Ca^{2+} and Mg^{2+} given in Hain et al. (2015). We considered the effects of the error in K_1 noted by Zeebe and Tyrrell (2018) in the Hain et al. (2015) formulation and found it to be small (see Supplementary Fig. 2). We also tested thermodynamic constants derived with temperatures set to ±2 °C from the Hansen et al. curve, which had no tangible effect on our results. There are now only 3 extra unknowns, P, B and U.

Berger and Herguera (1992) have collected data on present-day export fluxes of organic matter and $CaCO_3$. Using their data, we derived the relationship

Figure 2 (right): Input data used in the model presented in Figure 1. a, Atmospheric CO_2 data from Beerling and Royer (2011), without Boron-isotope-based values, and the secular (averaged) trend in that data given by the red line. We also explored the use of the database at http://www.p-co2.org/data/ (Foster et al., 2017), and the related results can be found in Supplementary Fig. 1. b, Deep-water carbonate ion records, as calculated by Boudreau and Luo (2017). c, Cenozoic $CaCO_3$ burial records as calculated by Boudreau and Luo (2017). d, Carbonate (calcite) compensation depth reconstructions for the global ocean from Lyle et al. (2008) and for the Pacific Ocean from Pälike et al. (2012). e, Time series of the thermodynamic constants K_{eq}^{S}, K_{eq}^{D} and K_o – see Fig. 1b, as calculated from the equations in Hain et al. (2015) and the calcium and magnesium ion concentration records found in that same paper. Note the error in K_{eq}, via K_1, identified by Zeebe and Tyrrell (2018) has less than a 0.2% effect on its value – see Supplementary Fig. 2. f, Linear regression of the Berger and Herguera (1992) data relating the $CaCO_3$ flux to the deep ocean to the organic carbon (OC) flux.

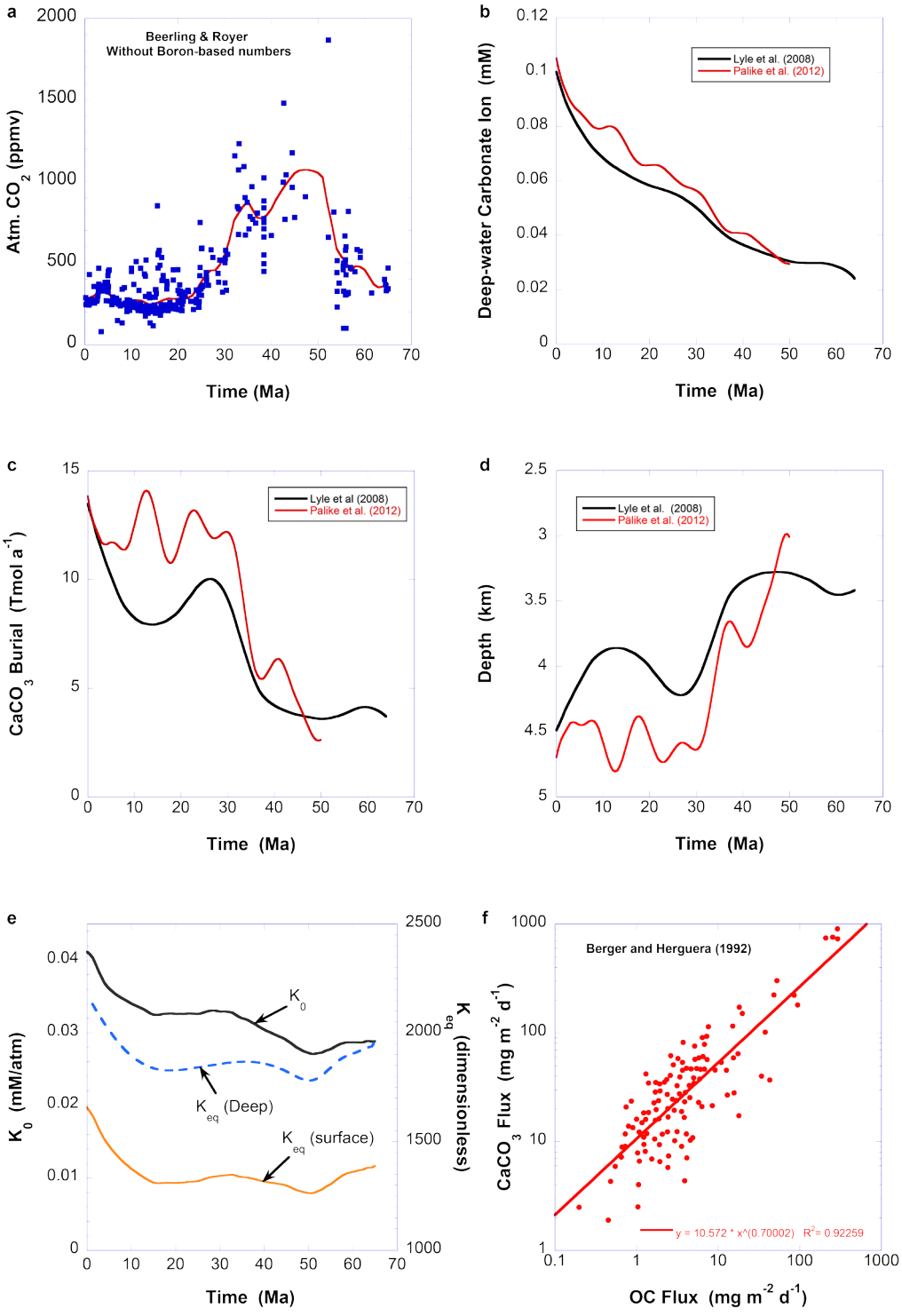
a
Beerling & Royer
Without Boron-based numbers
Atm. CO2 (ppmv)
Time (Ma)
b
Lyle et al. (2008)
Palike et al. (2012)
Deep-water Carbonate Ion (mM)
Time (Ma)
c
Lyle et al (2008)
Palike et al. (2012)
CaCO3 Burial (Tmol a-1)
Time (Ma)
d
Lyle et al. (2008)
Palike et al. (2012)
Depth (km)
Time (Ma)
e
K0
Keq (Deep)
Keq (surface)
K0 (mM/atm)
Kba (dimensionless)
Time (Ma)
f
Berger and Herguera (1992)
y = 10.572 * x^(0.70002) R2= 0.92259
CaCO3 Flux (mg m-2 d-1)
OC Flux (mg m-2 d-1)

$$P = fB^m \quad (11)$$

where f and m are fitting constants. Fig. 2f shows that our best fit to this data results from f = 0.04 and m = 1.43 when B and P are in units of Gmol a^{-1}. We assume that this present-day equation can be applied in the past, and we admit to the uncertainty of that extrapolation. To test that assumption, we also solved our model with a constant of P = 2x10^5 Gmol a^{-1}, i.e., the value observed today, P = 4B, a commonly stated approximation (e.g., Broecker and Peng, 1982); however, the exact P to B relationship is of second-order importance (Supplementary Fig. 4). The extra unknown count is down to 2.

Boudreau and Luo (2017) used their model not only to generate a consistent $CaCO_3$ burial record (B_B), but to calculate the total rain rate of $CaCO_3$ to the sediment-water interface of the pelagic oceans, B_{SR}. This is relevant because B is related to B_{SR}; specifically,

$$B - B_{NS} = B_{SR} \quad (12)$$

where B_{NS} is the amount of the export of $CaCO_3$ that dissolves in the water column. Fiadeiro (1980), Milliman (1993), Milliman et al. (1999), Sabine et al. (2002) and Feely et al. (2004) have all argued for the existence of an alkalinity source from water-column dissolution of $CaCO_3$, particularly at depths just below the thermocline, but above the saturation horizon. Many mechanisms have been proposed for this source, including aragonite and Mg-calcite dissolution, forcing by CO_2 generated by microbial reactions, and digestion in animal guts. The exact mechanism is not important to our study other than the fact that it seems largely independent of the calcite saturation state of the water mass in which it occurs.

Based on their data, Feely et al. (2004) advance that B_{NS} is about 50% of B. It is completely unknown if this fraction was at a similar level in the past. Assuming that B_{NS} is driven by CO_2 from the oxidation of associated organic matter, then to a first approximation, the rate of water column dissolution scales with B:

$$B_{NS} = \epsilon B \quad (13)$$

where ϵ is the fraction dissolved in the water column. We use ϵ equal to 0.5 (Feely et al., 2004); this is likely to be a maximum value as the saturation horizon for calcite was shallower in the past, which would shrink the depth range wherein B_{NS} could be generated. The effects of changing ϵ are illustrated in Supplementary Fig. 5. These are not large for dissolved species and pH, but the retrodicted P exhibits some sensitivity to the value of ϵ. Finally, using equation (12) and (13):

$$B = B_{SR}(1 - \epsilon)^{-1} \quad (14)$$

and as a result, another extra unknown is eliminated.

This only leaves the water exchange rate between the surface and deep oceans, U. Sadly, the variation of U over the Cenozoic is unknown. Except in sub-oceans for sub-secular time scales, there is no strong evidence from GCM models that the overall overturning rate of the oceans was very different in the past (Bice and Marotzke, 2001; Heinze and Ilyina, 2015). The present-day value is between 30-50 Sv (Sarmiento and Toggweiler, 1984; Broecker et al., 1999).

Propitiously, our results do not depend overly on the exact value of U – see Supplementary Fig. 6. That fortunate result allows us to set U = 50 Sv, with a reasonable degree of confidence that the carbonate chemistry results are robust relative to this parameter. The model is now completely specified.

3.2.2 Model solution

There are now 9 equations, i.e., equations (1)-(4), (7), (9)-(10), (11) and (14), that can be employed to calculate 9 unknowns, i.e., $[CO_2]_S$, $[HCO_3^-]_S$, $[CO_3^{2-}]_S$, $[CO_2]_D$, $[HCO_3^-]_D$, B, P, F_O, and Ex, because U is a fixed known value, $[CO_2]_a$ is taken from Beerling and Royer (2011) and Foster et al. (2017), B_B and $[CO_3^{2-}]_D$ are taken from Boudreau and Luo (2017), and the thermodynamic constants are calculated according to Hain et al. (2015). The solution of these equations can be obtained by a simple bisection-and-iteration method. The FORTRAN code that implements that method is also part of the Supplementary Information.

3.3 Results

Fig. 3 displays the retrodicted records of CAlk and DIC based on the CCD records from both Lyle et al. (2008) and Pälike et al. (2012) – see Fig. 2e. Fig. 4 illustrates the retrodicted pH (total hydrogen ion scale) records; this figure also contains estimated surface pH values from the Boron-proxy (Pearson and Palmer, 2000; Foster et al., 2017), despite any continuing debate on the accuracy of that approach (e.g., Nir et al., 2015). Fig. 5 displays the retrodicted export productivity P and the export calcification rate, B, as well as their ratio, P/B. B is perhaps surprisingly constant, regardless of the chosen CCD record, while both P and the P/B ratio exhibit weak dependencies on time over the Cenozoic. Unlike our B_B retrodiction, our modelled P is similar to that predicted by Hilting et al. (2008).

As discussed in the Introduction, other authors have adopted a variety of assumptions to resolve the indeterminacy of their retrodiction models, including constant surface alkalinity or calcite saturation with time and a constant ratio of surface to deep water CO_3^{2-} concentrations. To examine whether these assumptions are likely to be model independent, we present in Fig. 6a-b the retrodicted carbonate ion ratio and in Fig. 6c-d the retrodicted surface saturation. In addition, the assumption of constancy of surface alkalinity can be addressed with the results shown in Fig. 3.

3.4 Discussion

3.4.1 CAlk and DIC trends

As a first step, we need to explain the overall trends in the retrodicted time series of CAlk, DIC and pH in Fig. 3 and Fig. 4 in relation to the deep-water dissolved carbonate ion concentration, $[CO_3^{2-}]_D$ (Fig. 2b), the $CaCO_3$ burial rate, B_B (Fig. 2c), the CCD positions, z_{cc} (Fig. 2d), the atmospheric CO_2 record (Fig. 2a), and the calcification rate, B (Fig. 5). Differences in predicted carbonate chemistry between results obtained using the Lyle et al. CCD record and the Pälike et al. CCD record, as illustrated in these figures, appear to be almost trivial, but there is a marked disparity in implied cause. We begin by focusing on the Lyle et al.-based results, as this constitutes a simpler CCD record. Again, we note our model is restricted to the pelagic realm and cannot offer any specifics about the removal of alkalinity on shelves or in shallow seas. (Further, we display borate-corrected total alkalinity in Supplementary Fig. 7 to illustrate the ease of conversion of our results to TAlk.)

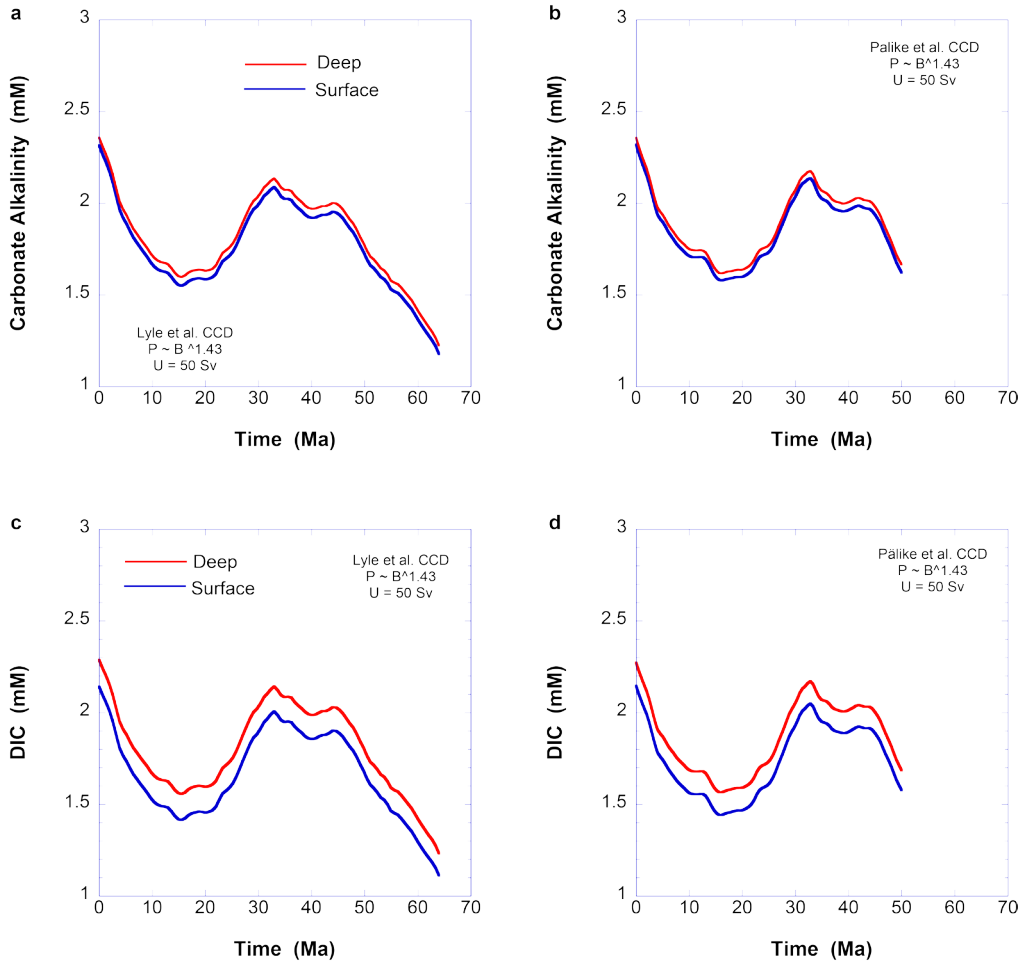

Figure 3: Retrodicted time series of carbonate alkalinity (CAlk) and total dissolved inorganic carbon (DIC). a, Retrodiction of CAlk using the Lyle et al. (2008) CCD record. b, Retrodiction of CAlk using the Pälike et al. (2012) CCD record. c, Retrodiction of DIC using the Lyle et al. (2008) CCD record. d, Retrodiction of DIC using the Pälike et al. (2012) CCD record.

3.4.1.1 Results based on the Lyle et al.-CCD record

The Lyle et al. CCD record shows an overall deepening with Cenozoic progression (Fig. 2d), which result from an increase in either the input of alkalinity (F_O) to the pelagic realm or in the pelagic calcification rate (B). Our results show that B remained essentially constant during the Cenozoic (Fig. 5). This immediately demands a long-term increase in F_O as the driver of the mean burial change (Fig. 2c), as required by Equation 9. A deepening CCD and increased burial should coincide with increased bottom water carbonate ion concentration (Fig. 2b), which was shown to be the case by Boudreau and Luo (2017), as also consistent with Tyrrell and Zeebe (2004).

The Lyle et al.-based burial rate (Fig. 2d) exhibits a weak broad maximum between 56 and 40 Ma (Eocene), centered at ~48 Ma, which parallels an equally weak maximum in atmospheric CO_2 between those times. Note that when Boudreau and Luo (2017) employ the Slotnick et al. (2015) CCD curve, they also retrodict a weak burial maximum (their Fig. 4), centered at ~52 Ma. This weak peak in burial requires a similar trend in alkalinity input (F_O) to the pelagic ocean from the nearshore, i.e., Equation (9), but the cause cannot be addressed

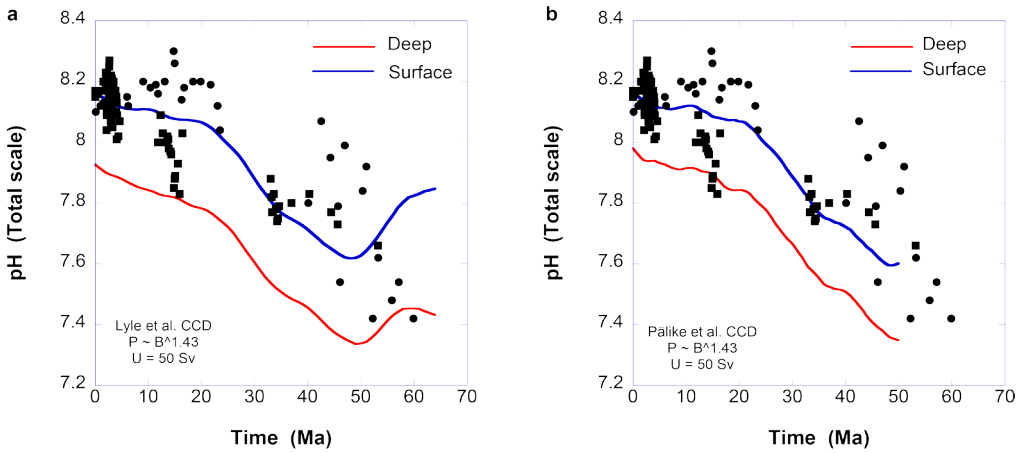

Figure 4: Retrodicted pH records in comparison to published surface water pH reconstructions. Retrodictions (solid lines) are shown against surface pH data derived from the Boron proxy (Pearson and Palmer, 2000 (black circles); Foster et al., 2017 (black squares)). a, Retrodictions based on the Lyle et al. (2008) CCD record. b, Retrodictions based on the Pälike et al. (2012) CCD record. (The retrodictions are predictions of the past and not fits of the data.)

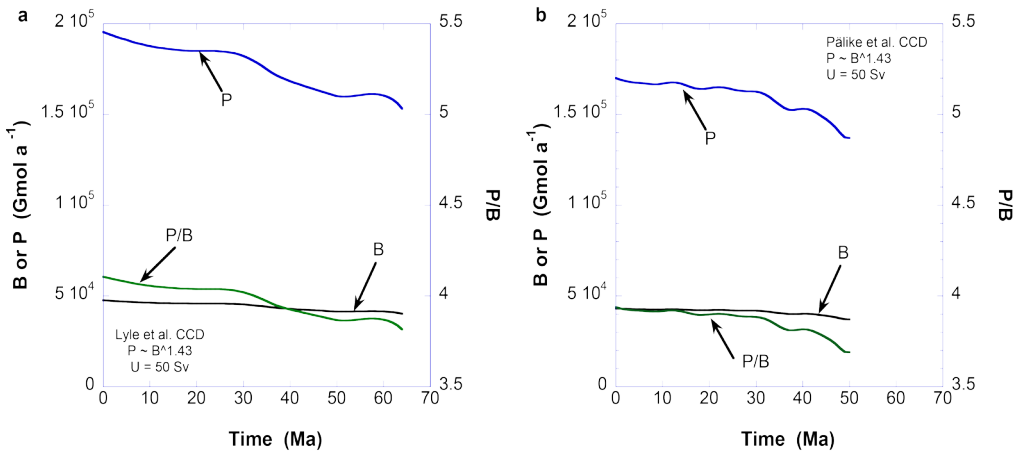

Figure 5: Retrodicted records of export calcification (B), export productivity (P) and their ratio (P/B). a, Retrodictions based on the Lyle et al. (2008) CCD record. b, Retrodictions based on the Pälike et al. (2012) CCD record.

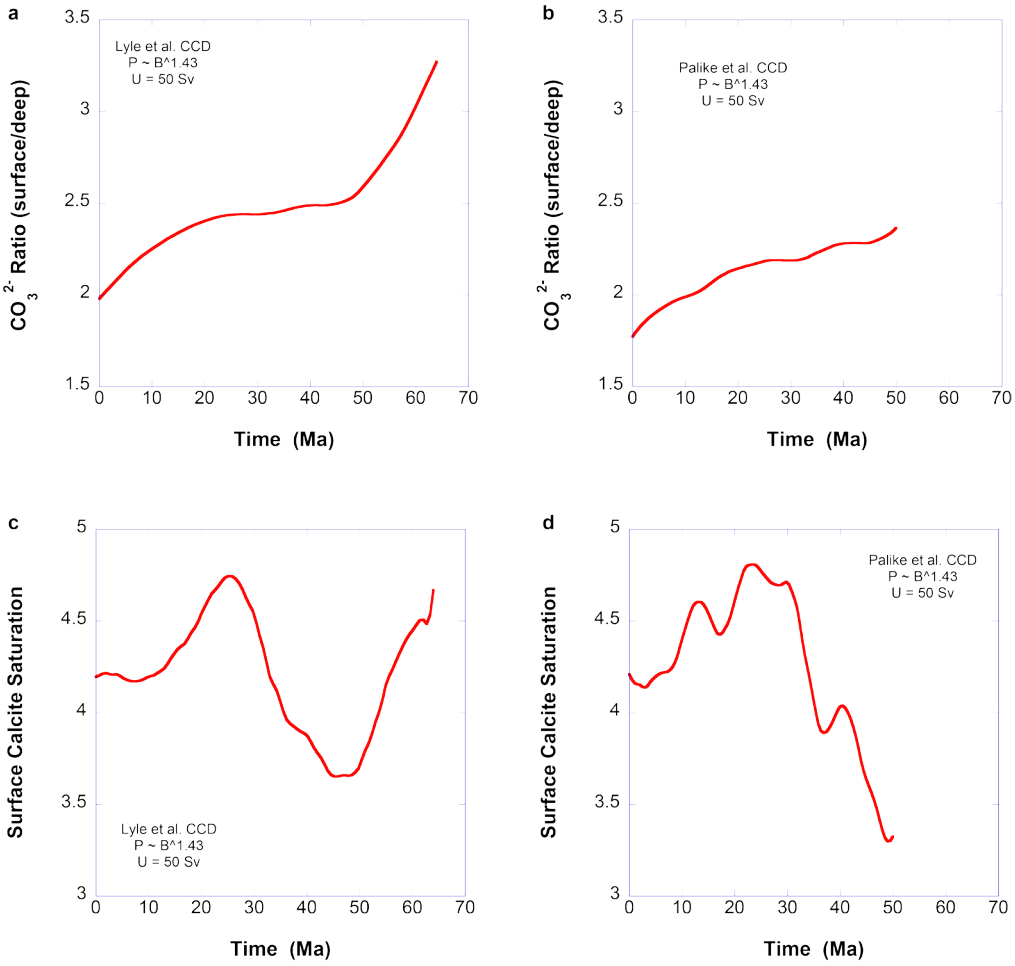

Figure 6: Retrodicted surface to deep water carbonate ion ratios and surface water calcite saturation states. a, Retrodicted ratio of the surface to deep water carbonate ion concentration using the Lyle et al. (2008) CCD record. b, Retrodicted ratio of the surface to deep water carbonate ion concentration using the Pälike et al. (2012) CCD record. c, Retrodicted calcite saturation of the surface water using the Lyle et al. (2008) CCD record. d, Retrodicted calcite saturation of the surface water using the Pälike et al. (2012) CCD record.

with our model. The plateau in CO_2 between 58–52 Ma then corresponds to a weak decrease in $CaCO_3$ burial (Fig. 2c), despite the fact that this period also contains episodes of strong and rapid $CaCO_3$ dissolution and preservation, e.g., the PETM at ~56 Ma.

The subsequent increased $CaCO_3$ burial and $[CO_3^{2-}]_D$ between ~50 and ~30 Ma, i.e., near the onset of Antarctic glaciation, correlate with elevated, but mainly decreasing, atmospheric CO_2. The increasing burial (Fig. 2c), in turn, demands increased delivery of alkalinity (F_O) to the pelagic oceans.

Between ~30 and ~15 Ma (i.e., the Middle Miocene Climate Transition – MMCT), $CaCO_3$ burial falls, but stays well above the pre-48 Ma levels, which indicates a modest fall in the

alkalinity input (F_O). This decrease in accumulation accompanies a reduction in atmospheric CO_2 to levels below those at the beginning of the Cenozoic, while the accumulation of carbonate ion in deep water decelerates (Fig. 3a). After ~15 Ma, carbonate burial again increases, even though atmospheric CO_2 remains low, which requires a net increase in the alkalinity input, i.e., increased weathering, or decreased alkalinity interception, or both.

Unlike the retrodicted deep-water carbonate ion concentration (Boudreau and Luo, 2017), which increases with time (Fig. 2b), both CAlk and DIC display about ±25% fluctuations (Fig. 3), such that these concentrations are currently at their highest levels. Between 65–32 Ma, the increased CAlk and DIC (Fig. 3) broadly correlate with the rise in atmospheric CO_2 (Fig. 2a). In fact, there are local CAlk and DIC maxima at ~48 Ma (the beginning of the Eocene cooling trend) and ~32 Ma (near the start of the Oligocene and the glaciation of Antarctica and possibly the opening of the Drake Passage) that correspond with similar CO_2 peaks. Enhanced alkalinity input (F_O) to the pelagic ocean is one logical explanation, which again could be due to increased chemical weathering or lowered alkalinity interception, or both; however, increased atmospheric CO_2 in itself could cause such changes.

Between ~32 Ma and ~15 Ma, the Lyle et al.-based results demand that F_O must have dropped because we observe decreasing burial and concentrations of CAlk and DIC. Finally, burial rises strongly after 15 Ma, as a result of increased F_O, which in turn leads to an increase in both CAlk and DIC (Fig. 3). All of this conforms to a widely held view of the evolution of the carbonate chemistry of the oceans during the Cenozoic, e.g., as reconstructed by Raymo and Ruddiman (1992) or Tyrrell and Zeebe (2004). However, our reconstructed fluctuations in CAlk are considerably smaller than those advanced by Pearson and Palmer (2000), but similar to those in Caves et al. (2016).

3.4.1.2 Results based on the Pälike et al.-CCD record

The Pälike et al.-based model contains a surprise. Retrodicted CAlk and DIC records trend similarly to the Lyle et al.-based model (Fig. 3), if shifted downward slightly; yet, the Pälike et al.-based model retrodicts a dissimilar burial record (Fig. 2c) and, consequently evolution of F_O. Earlier in the Cenozoic (50 to ~32 Ma), the burial generally increases, meaning that F_O does so too, and CAlk and DIC rise. However, after ~32 Ma, the CAlk and DIC fall, while the burial is, to a reasonable approximation, constant with smaller variations about that mean (~12.5 Tmol a^{-1}). There is no substantial fall in F_O between ~32 Ma and ~15 Ma to drive the decreases in CAlk and DIC.

The clear correlation with the fall in CAlk and DIC is the drop in atmospheric CO_2. When $[CO_2]_a$ falls, $[CO_2]_S$ changes proportionately. During the ~32 Ma and ~15 Ma period, $[CO_2]_S$ drops far more than $[CO_3^{2-}]_s$ rises (Fig. 6), i.e., 62% drop versus a 30% rise. Accordingly, the bicarbonate ion must decrease to maintain Equation (3), and a reduction in bicarbonate ion lessens both CAlk and DIC, as seen in Fig. 3.

Between ~15 Ma and today, the CAlk and DIC rose considerably (Fig. 3), whereas there was no systematic raise in burial (Fig. 2c) and thus F_O. Atmospheric CO_2 remained essentially flat. This draws our attention to the K_{eq} records (Fig. 2d), which climb in both deep and surface oceans with decreasing ocean temperature over the last 15 Ma. These increases in K_{eq} account precisely for the increases in CAlk and DIC. This role of thermodynamics in the carbonate system of the world's oceans during the past 15 Ma is a novel finding, and contrasts with the weathering-alkalinity input control suggested by the Lyle et al.-based model. Note that a thermodynamically controlled situation would not rule out increased weathering over the last

~15 Ma, only that the resulting alkalinity does not reach the pelagic ocean due to nearshore removal. (Note that the Lyle et al.-based CAlk and DIC also have this effect, but in that case, it is small compared to the alkalinity forcing.)

3.4.1.3 Results based on a revised Pälike et al.-CCD record

The Lyle et al.-based and Pälike et al.-based retrodictions of CAlk, DIC and pH (Fig. 3 and Fig. 4) are not identical, but the differences are second order on secular time scales, even though the implied mechanisms causing these trends during the last 15 Ma are decidedly different. The Pälike et al. (2012) record effectively begins at 50 Ma, and we were curious if this record was extended to 55 Ma, whether this similarity continued. Therefore, the pre-44 Ma data found in Fig. 2 in Pälike et al. (2012) can be interpreted somewhat differently and combined with that in Leon-Rodriguez and Dickens (2010) to create an alternative CCD record for the period 44–55 Ma; this is illustrated in our Fig. 7a. The revised z_{cc} record is then deeper by between 0.4 and 0.9 km.

From this revised z_{cc} record, we are able to calculate corresponding revised z_{sat} (saturation horizon depths – Fig. 7b) and a revised calcite-carbon burial record (Fig. 7c) using the model in Boudreau and Luo (2017). z_{sat} is distinctly lower and, consequently, more calcite is preserved. However, the latter comes at a time of highly diminished $CaCO_3$ preservation in the deep oceans, so that this increase in preservation is small in absolute terms.

Fig. 7d illustrates the retrodicted carbonate alkalinity of the surface waters and a small peak now appears at around 48 Ma and the revised values are higher, but the difference with the original Pälike et al.-based curve is very small, i.e., ~2.5%. Fig. 7e displays the calcite saturation state of the surface, and the difference with the original retrodiction is about 0.5 out of a background of about 3.8, which is modest. Finally, Fig. 7f shows that the retrodicted pH of the surface waters is trivially dissimilar to the original Pälike et al.-based retrodiction. All this confirms that our dissolved carbonate chemistry results are not greatly sensitive to the details of the input CCD records.

3.4.2 Effects of organic carbon burial

The assumption of no pelagic organic carbon (OC) burial may seem controversial, but it is easily shown that even a strongly exaggerated pelagic OC burial does not affect our finding in any significant way. We re-ran our model with a fixed (non-zero) fraction of organic carbon burial (σ_D). As noted earlier, today's pelagic oceans export (our P) ~550 Tmol C a^{-1} at 100 m (Sarmiento and Gruber, 2006), but ultimately bury in pelagic sediments only 1.6 Tmol C a^{-1}; thus, the leak through burial is only 0.3% of export. These numbers explain why we previously set regeneration equal to export in our model. Meanwhile our model predicts an export of 170 Tmol a^{-1}, but that is between at ~200 m, and burial would account for a loss of ~1%. So, we

Figure 7 (right): Retrodictions using a revised Pälike et al.-based CCD record. a, Original (blue) and revised (red) CCD records based on the data in Pälike et al. (2012) and Leon-Rodriguez and Dickens (2010). b, Retrodicted positions of the saturation horizon calculated from the CCD records in panel (a) using the Boudreau and Luo (2017) model. c, Retrodicted calcite carbon burial from the records in panel (a) using the Boudreau and Luo (2017) model. d, Retrodicted surface carbonate alkalinity for the CCD records in panel (a) using the model in Fig. 1. e, Retrodicted surface calcite saturation for the CCD records in panel (a) using the model in Fig. 1. f, Retrodicted surface pH for the CCD records in panel (a) using the model in Fig. 1.

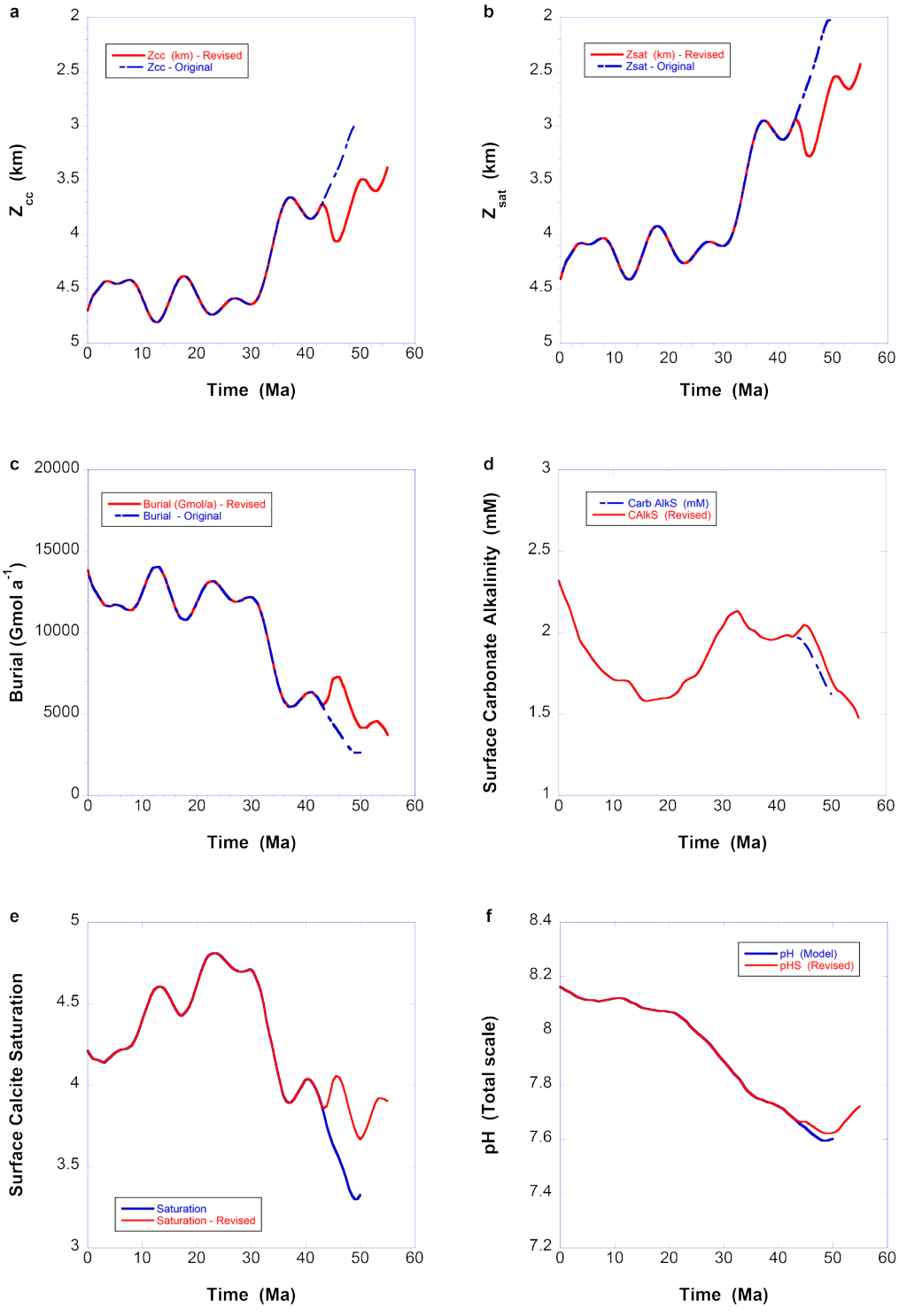
a
Zcc (km) - Revised
Zcc - Original
Z cc (km)
Time (Ma)
b
Zsat (km) - Revised
Zsat - Original
Z sat (km)
Time (Ma)
c
Burial (Gmol/a) - Revised
Burial - Original
Burial (Gmol a-1)
Time (Ma)
d
Carb AlkS (mM)
CAlkS (Revised)
Surface Carbonate Alkalinity (mM)
Time (Ma)
e
Saturation
Saturation - Revised
Surface Calcite Saturation
Time (Ma)
f
pH (Model)
pHS (Revised)
pH (Total scale)
Time (Ma)

generously assume that 10% of the OC export is buried. Fig. 8 displays re-calculations of the retrodictions of surface pH, CAlk and saturation with a 10% leak (σ_D = 0.9).

Clearly, these figures demonstrate that a leak of this (large) magnitude does not produce a measurable difference in retrodicted pH (about 1%) and only modest differences in surface CAlk (<6%) and saturation (<3%); deep water response is entirely similar. Yet, this model leak is massively greater than the known present-day escape from benthic regeneration, i.e., 10% versus 1%; if we had used 0.3% escape, there would be no quantitative differences at all. These results highlight that our treatment of OC burial is entirely justified.

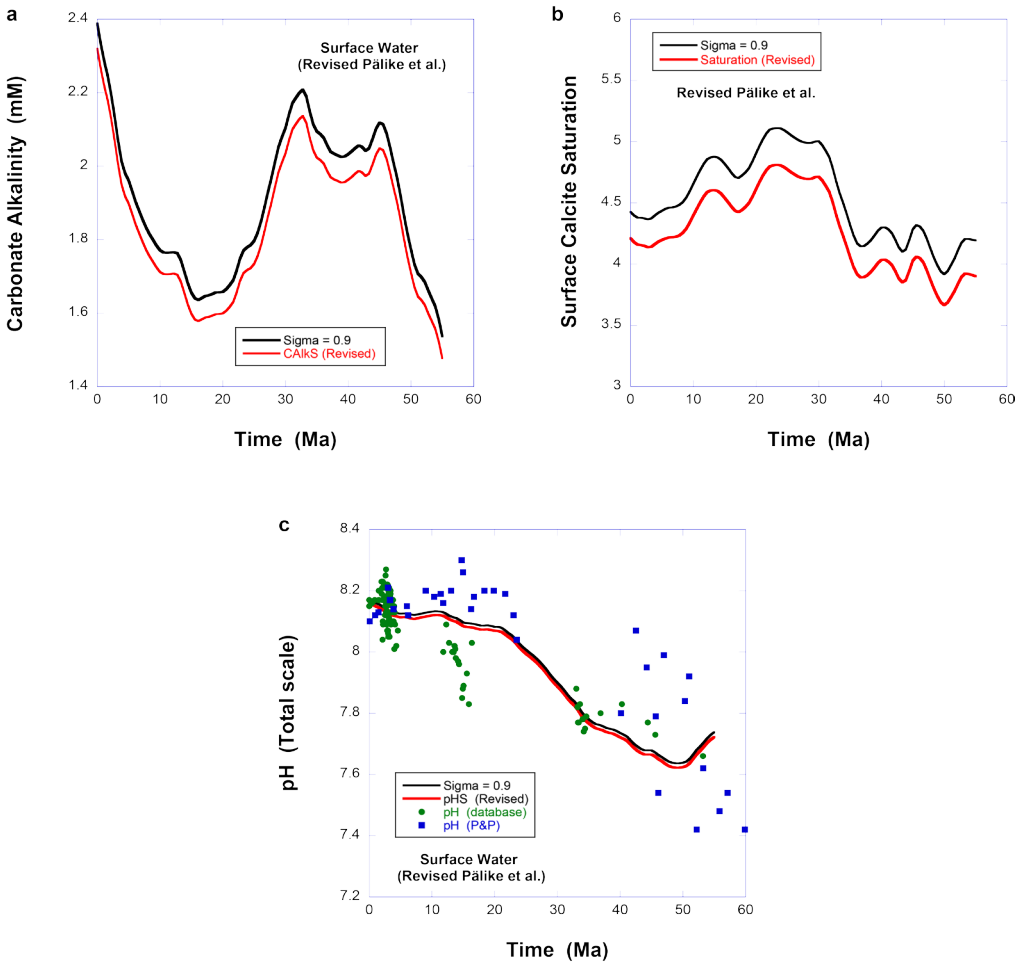

Figure 8: Comparison of retrodictions without pelagic organic carbon burial and with an exaggerated 10% (σ_D) preservation of the export flux. a, CAlk records. b, Surface water saturation records. c, Surface water pH records, compared to data derived from the Boron proxy (Pearson and Palmer, 2000 (blue squares); Foster et al., 2017 (green circles)). Retrodictions are based on the revised Pälike et al. (2012) CCD, as in Fig. 7. See text for further discussion.

3.4.3 pH records

Fig. 4 illustrates the retrodicted pH time series with both the Lyle et al.-based model and the Pälike et al.-based model. Also displayed are paleo-pH estimates from Boron-proxy measurements (compiled at http://www.p-co2.org/data/). These model pH records are predictions, not fits, and the concurrence between Boron-isotope data and models is an encouraging sign of the validity of our results. Moreover, our predictions are consistent with those of Tyrrell and Zeebe (2004) for the last 50 Ma, but they deviate for earlier times based on the Lyle et al-CCD record.

Surface water pH reached a minimum at the height of atmospheric CO_2 around 48 Ma. Between ~48 and ~15 Ma, pH rose as atmospheric CO_2 stabilized and then dropped. Thereafter, $[CO_2]_a$ is roughly constant and so is the surface pH. The deep-water pH simply mirrors the deep-water value, offset by a small value as a result of higher DIC.

3.4.4 Past assumptions

As stated in the Introduction, past attempts to retrodict the ocean's carbonate chemistry have invoked three common assumptions: (1) constant surface alkalinity, (2) constant surface saturation, and (3) constant $[CO_3^{2-}]_S$ to $[CO_3^{2-}]_D$ ratio. If they are model-independent results, then they should emerge from our own calculations.

Fig. 3 shows that we retrodict a 67% change in CAlk of surface waters over the Cenozoic, as opposed to the constancy or salinity dependence adopted by Hönisch and Hemming (2005). That is not a trivial variation, and it has implications for calculating $[CO_2]_a$ from pH proxy data (e.g., Pearson and Palmer, 2000; Hönisch and Hemming, 2005; Foster, 2008). Fig. 6c-d display the calcite surface saturation retrodiction and that quantity changes by ~30% over the Cenozoic; the deviation from constancy seems modest; however, this 30% variation corresponds with a 3X change in retrodicted $[CO_2]_S$. The difference in a retrodicted $[CO_2]_a$ using our varying $[CO_3^{2-}]_S$ and a $[CO_2]_a$ from an assumed constant saturation could be great indeed. Finally, Fig. 6a-b display the $[CO_3^{2-}]_S/[CO_3^{2-}]_D$ ratio with time. This quantity changes by ~30% in the Pälike et al.-based model and 63% in the Lyle et al.-based model. Such deviations from constancy could result in significant uncertainties, particular in any prediction of $[CO_2]_a$ from $[CO_3^{2-}]_D$. It remains to be seen which set of assumptions, i.e., ours versus those in past studies, better approximates the oceans.

One interesting result from our model is that both B and P (calcification and productivity rates) vary relatively weakly over the Cenozoic, which suggests that an assumption of constant B or P or B/P should generate results compatible with our own.

3.4.5 Implications for Boron-based pCO_2 reconstructions

Boron isotopes are a robust proxy for pH, but the constrained estimation of pCO_2 requires a second parameter of the carbonate system (Foster and Rae, 2016), which in turn requires additional assumptions. To independently test the validity of these assumptions, we have taken the TAlk values and $[CO_3^{2-}]$ values (converted to total alkalinity equivalents) used in the Cenozoic $\delta^{11}B$-based pCO_2 compilation of Foster et al. (2017) and compared them to our independently modeled calculated TAlk records (Fig. 9a). Then, we recalculated these $\delta^{11}B$-based pCO_2 estimates based on our new TAlk records (Fig. 9b) to see if this resulted in significant differences with respect to the original reconstructions. (These calculations were made with the R package *seacarb*, using modern values for the thermodynamic constants K_0, K_1 and K_2, and using temperature and salinity values as reported in the original publications.)

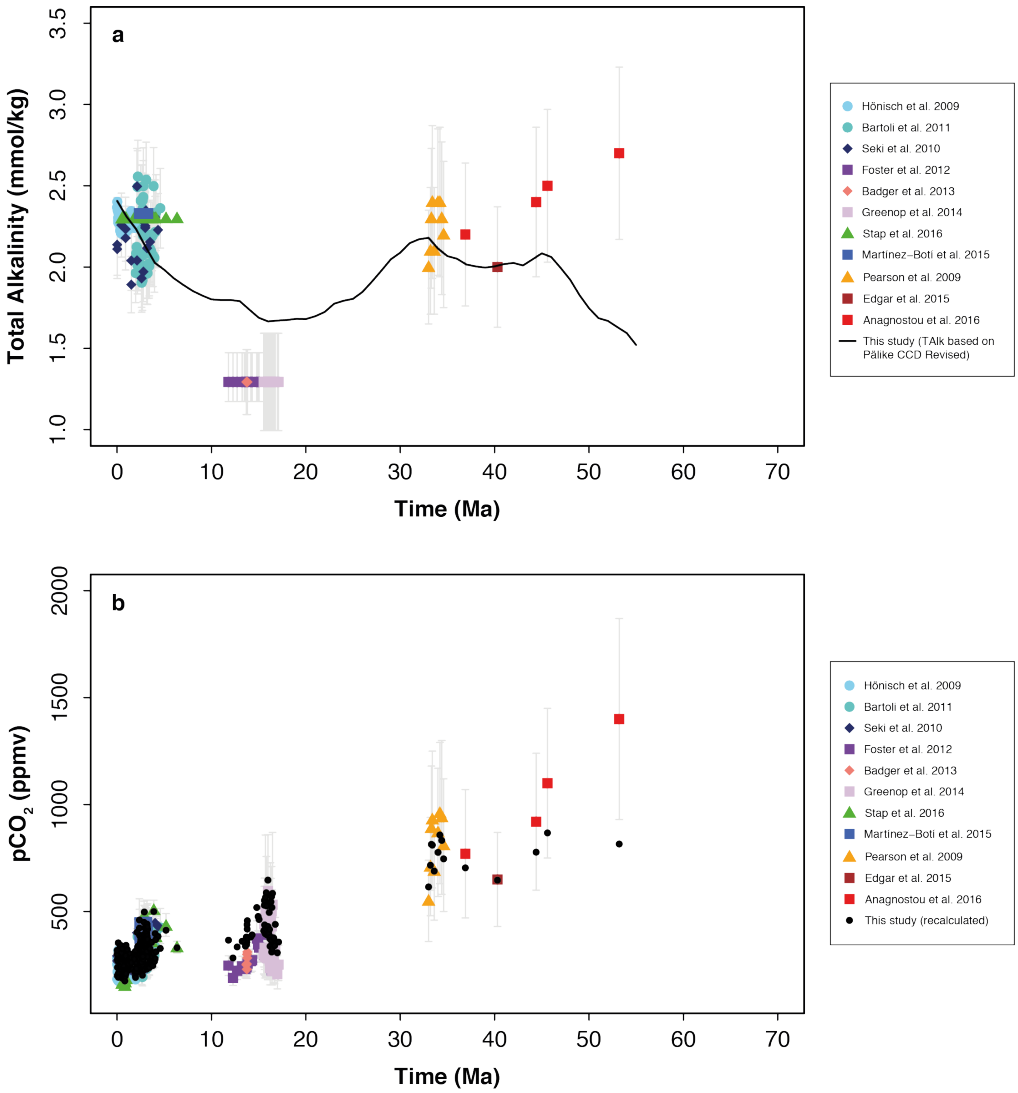

Figure 9: Retrodicted total alkalinity records and implications for Cenozoic pCO_2 estimates. a, Comparison between the total alkalinity values used in the Cenozoic $\delta^{11}B$-based pCO_2 compilation of Foster et al. (2017) (colored symbols, with the grey error bars representing the uncertainties as reported in the original publications), and our modeled TAlk record based on the revised Pälike et al. (2012) CCD (black line). b, Comparison between the published $\delta^{11}B$-based pCO_2 estimates (colored symbols, with the grey error bars representing fully propagated uncertainties as reported in the original publications) and recalculated pCO_2 estimates using our TAlk record based on the revised Pälike et al. (2012) CCD (black circles). The recalculated pCO_2 estimates have the same total uncertainties as the original estimates, but for clarity these are not displayed again.

Our model TAlk values agree with those used in $\delta^{11}B$-based pCO_2 reconstructions (Fig. 9a) and consequently, the differences between published pCO_2 values and recalculated pCO_2 values (Fig. 9b) are small for most of the Cenozoic. For the Pleistocene and Pliocene, all pCO_2 values are comparable within their respective errors, but for the Miocene, our model actually offers slightly higher alkalinity values and hence pCO_2 values, i.e., elevated by approximately 50-100 ppmv. Further back in time, more significant differences become apparent. For the Eocene, our retrodicted CAlk record generally yields much lower pCO_2 values than the published values, with a dramatic difference of more than 500 ppmv for the Early Eocene at ~53 Ma, much more consistent with the secular trend in Beerling and Royer (2011) – see Fig. 2a. If these recalculated pCO_2 estimates are to be taken at face value, average Early Eocene CO_2 concentrations may have been much lower and more stable than inferred by Anagnostou et al. (2016). If anything, this major difference highlights the fundamental challenges in understanding the evolution of ocean carbonate chemistry under Early Eocene greenhouse climates. We suggest that our retrodicted TAlk record can be used as a new framework for future pCO_2 reconstructions and that future studies should focus on reconciling the mismatch between a shallow CCD and very high CO_2 concentrations.

3.5 Conclusions

The secular state and variations of the carbonate system chemistry of the oceans can be retrodicted with a relatively simple, data-driven, inverse model, using available atmospheric CO_2 records, e.g., Beerling and Royer (2011) or the database at http://www.p-co2.org/data/, the carbonate ion record from Boudreau and Luo (2017), and the dissolved calcium and magnesium records in Hain et al. (2015), and a small number of justified assumptions. Our model provides an excellent retrodiction of the Boron-based pH of the surface waters of the Cenozoic seas, supplying some degree of confidence in our results. We also employed our results to recalculate the atmospheric pCO_2 record from Boron isotopes and showed that our retrodictions agree well with past estimates after 45 Ma, but that between 45–55 Ma, our estimates are far lower than reported in other studies.

The retrodictions of the CAlk and DIC of the oceans are almost identical when driven by either the Lyle et al. (2008) or the Pälike et al. (2012) CCD records, or as modified by the Leon-Rodriguez and Dickens (2010) data. Nevertheless, the causes of the variations in these records are decidedly different in the later Cenozoic (last ~15 Ma). In this interval, the Lyle et al.-based model links CAlk and DIC changes to changes in the alkalinity input (F_O) to the pelagic oceans, while the Pälike et al.-based model drives the CAlk and DIC variations with changes in atmospheric CO_2 and changing values of the thermodynamic constants of the carbonate system with a general cooling of the oceans, which is a radically different explanation.

Assumptions used in past models, e.g., constant surface alkalinity, constant surface saturation, and constant $[CO_3^{2-}]_S$ to $[CO_3^{2-}]_D$ ratio, are not reproduced by our model; this does not invalidate these past assumptions, but it certainly means that their adoption requires justification, as do our own. We offer one final caveat, which is true of all model studies: if new data is later found to disagree with our retrodictions, this may indicate that one or more of our assumptions is wrong, e.g., ignoring OC-oxidation-driven dissolution in pelagic sediments and the resulting one-to-one alkalinity to DIC flux.

Acknowledgments

B.P.B. gratefully acknowledges funding from NSERC. J.J.M., A.S. and R.v.d.P. were supported by the Netherlands Earth System Science Center (NESSC), as was a sabbatical stay in Utrecht by B.P.B.. We thank Jeremy Caves-Rugenstein and two other anonymous reviewers, as well as our Editor (J.A.), for their thought provoking and challenging comments; hopefully we have adequately addressed them so that a future reader will also be satisfied with our exposition of this problem.

Code availability

The Fortran code accompanying this study can be found in the online version of the Supplementary Information.

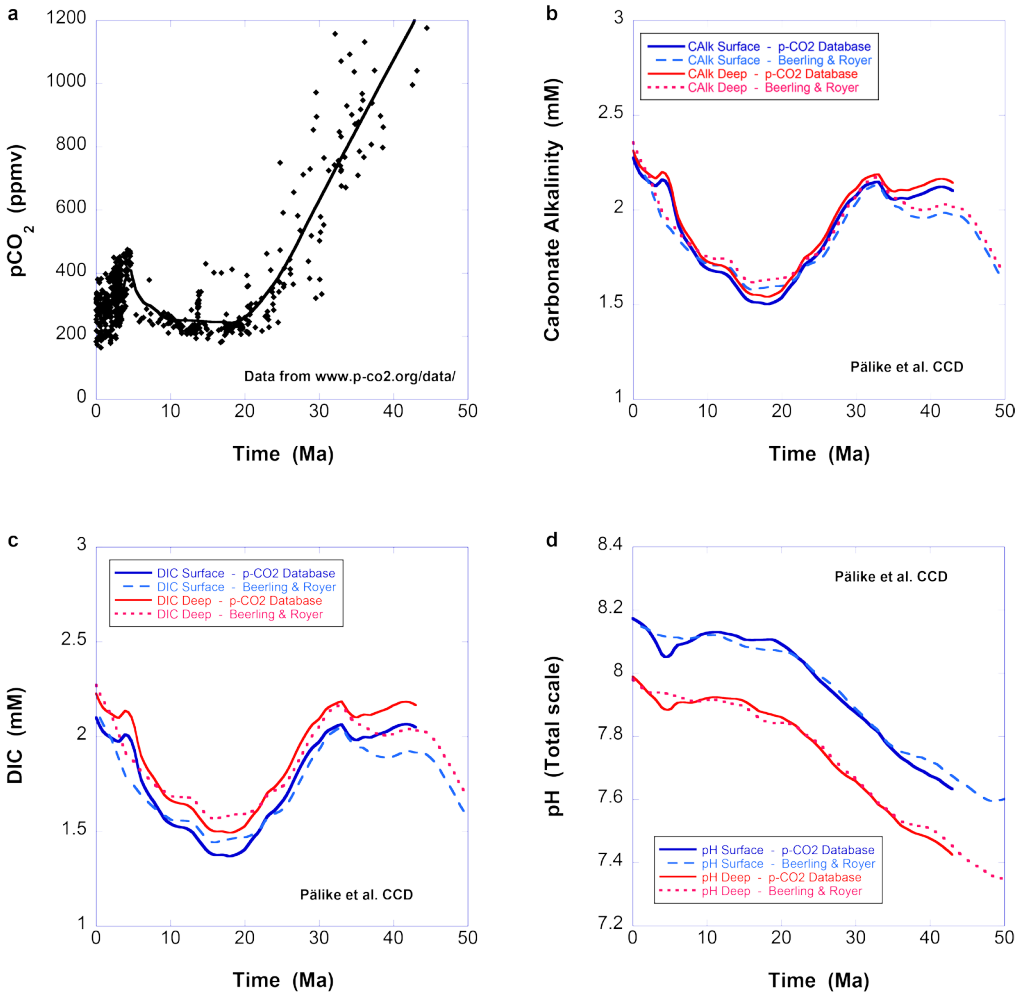

Supplementary Figure 1: Results using the alternative pCO_2 data at http://www.p-co2.org/data/ (Foster et al., 2017) - alkenones only. a, Raw data from the database (diamonds) and a smooth secular average (black line). b, Retrodicted carbonate alkalinity in surface and (blue) and deep (red) waters of the ocean using the p-co2.org database (solid lines) and the Beerling and Royer (2011) data (dashed lines). c, Retrodicted DIC in surface and (blue) and deep (red) waters of the ocean using the p-co2.org database (solid lines) and the Beerling and Royer (2011) data (dashed lines). d, Retrodicted pH in surface and (blue) and deep (red) waters of the ocean using the p-co2.org database (solid lines) and the Beerling and Royer (2011) data (dashed lines).

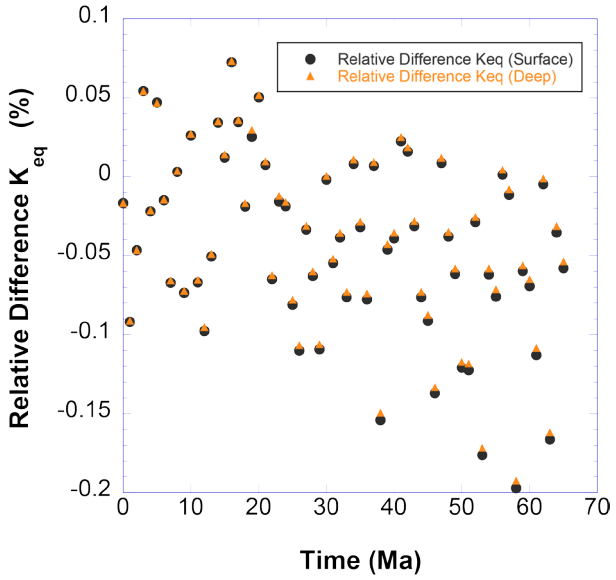

Supplementary Figure 2: Relative difference in K_{eq} from the original Hain et al. (2015) equations and corrected for the error noted by Zeebe and Tyrrell (2018). Relative error is the original value, minus the corrected value, all divided by the corrected value, and then multiplied by 100. Errors are less than 0.2% overall.

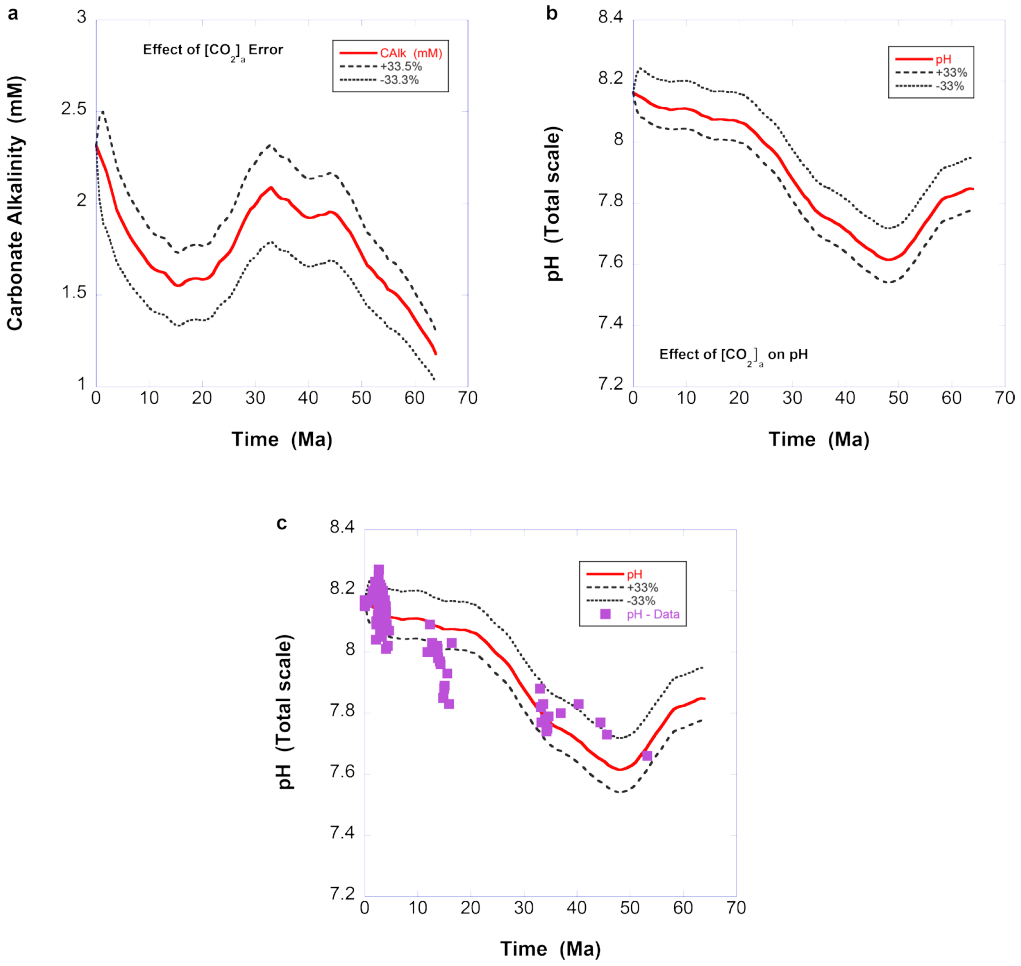

Supplementary Figure 3: Illustration of the effects of uncertainty in atmospheric pCO_2 from Beerling and Royer (2011) on retrodicted carbonate alkalinity and pH, using the Lyle et al.-based CCD record. a, Retrodicted CAlk from Fig. 3 (red line) and retrodictions with 33.3% more (labeled +33%) and with 33.3% less CO_2 (labeled -33%) in the $[CO_2]_a$ record taken from Beerling and Royer (2011). b, Retrodicted pH under the same conditions. c, Same retrodicted pH, but now compared to the pH data in Foster et al. (2017); the latter shows that variations in pCO_2 larger than 33% would cause the retrodiction of pH to diverge seriously from the data.

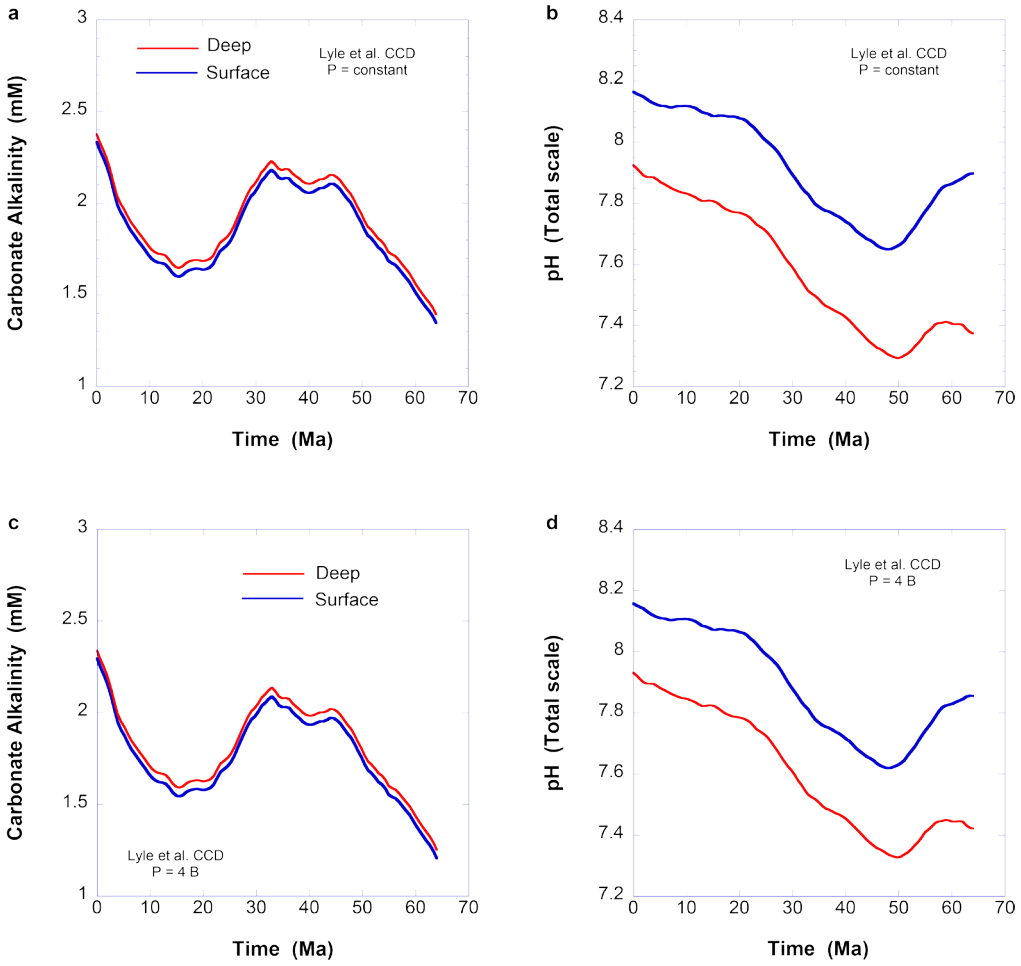

Supplementary Figure 4 (top): Illustration of the dependence of P on B and how this influences our retrodictions. These figures are generated with P = $2x10^5$ Tmol a^{-1} and P = 4xB. If one compares these results with those in Fig. 3, the differences are trivial. (Results with the Pälike et al. CCD record are similar.) a, Retrodicted CAlk using P = constant and the Lyle et al. CCD record. b, Retrodicted pH using P = constant the Lyle et al. CCD record. c, Retrodicted CAlk using P = 4xB and the Lyle et al. CCD record. d, Retrodicted pH using P = 4xB and the Lyle et al. CCD record.

Supplementary Figure 5 (right): Tests of the effect of the parameter ε in Equations 13 and 14 on retrodicted CAlk and pH, and export calcification and productivity rates (B & P) and their ratio, using the Pälike et al. (2012) CCD record. The effects of a 20% and then 40% drop in ε cause less than a 10% change in the retrodictions of CAlk and pH. By contrast, the effects of a 20% and then 40% drop in ε cause significant changes in retrodicted export production rates (a 40% drop from Fig. 5 to Supplementary Fig. 5), but the changes in B are far more modest. a, Retrodicted CAlk with ε = 0.4. b, Retrodicted pH ε = 0.4. c, Retrodicted CAlk with ε = 0.3. d, Retrodicted pH with ε = 0.3. e, Retrodicted B and P with ε = 0.4. f, Retrodicted B and P with ε = 0.3.

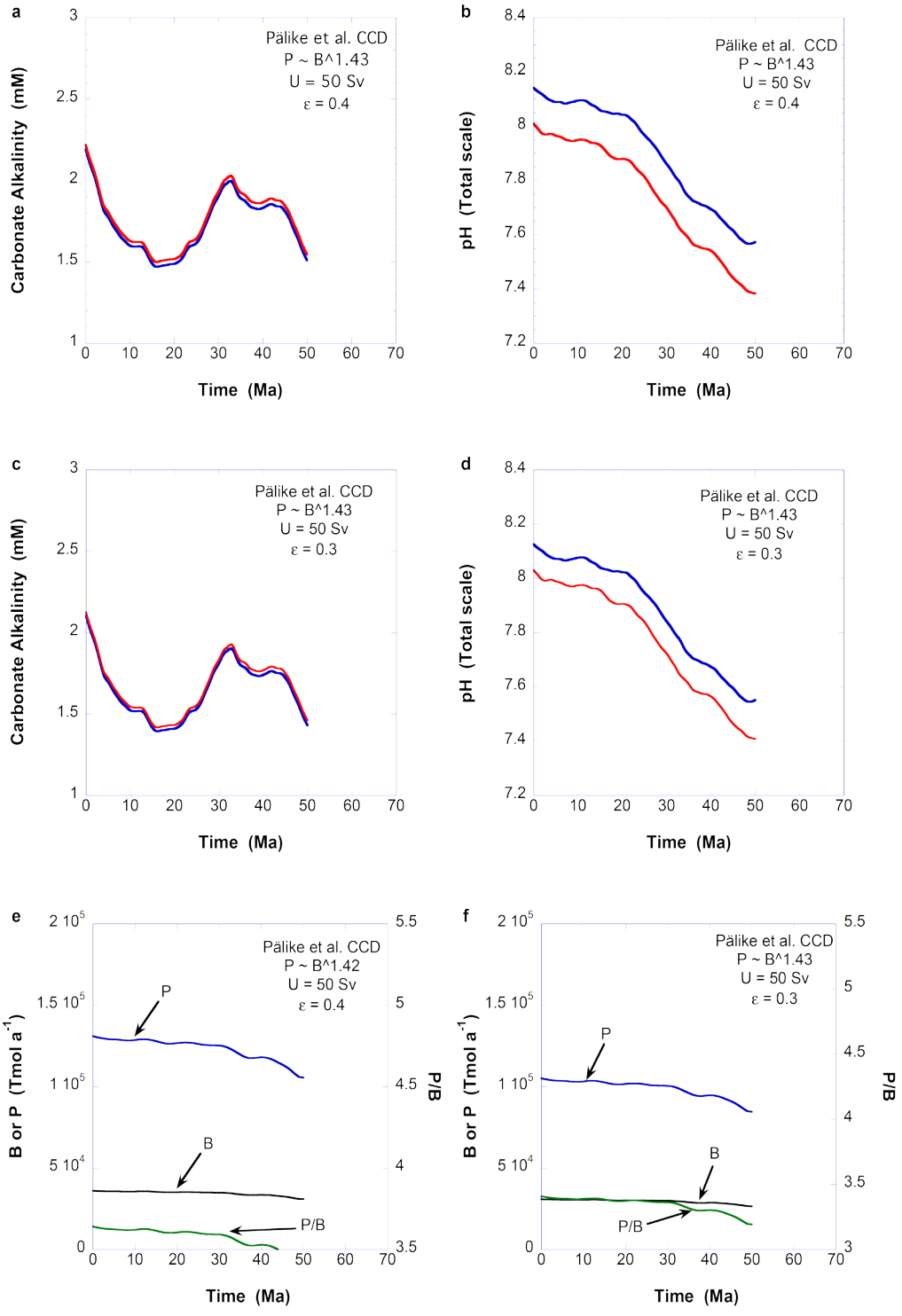
a
Carbonate Alkalinity (mM)
Pälike et al. CCD
P ~ B^1.43
U = 50 Sv
ε = 0.4
Time (Ma)
b
pH (Total scale)
Pälike et al. CCD
P ~ B^1.43
U = 50 Sv
ε = 0.4
Time (Ma)
c
Carbonate Alkalinity (mM)
Pälike et al. CCD
P ~ B^1.43
U = 50 Sv
ε = 0.3
Time (Ma)
d
pH (Total scale)
Pälike et al. CCD
P ~ B^1.43
U = 50 Sv
ε = 0.3
Time (Ma)
e
B or P (Tmol a-1)
P/B
Pälike et al. CCD
P ~ B^1.42
U = 50 Sv
ε = 0.4
P
B
P/B
Time (Ma)
f
B or P (Tmol a-1)
P/B
Pälike et al. CCD
P ~ B^1.43
U = 50 Sv
ε = 0.3
P
B
P/B
Time (Ma)

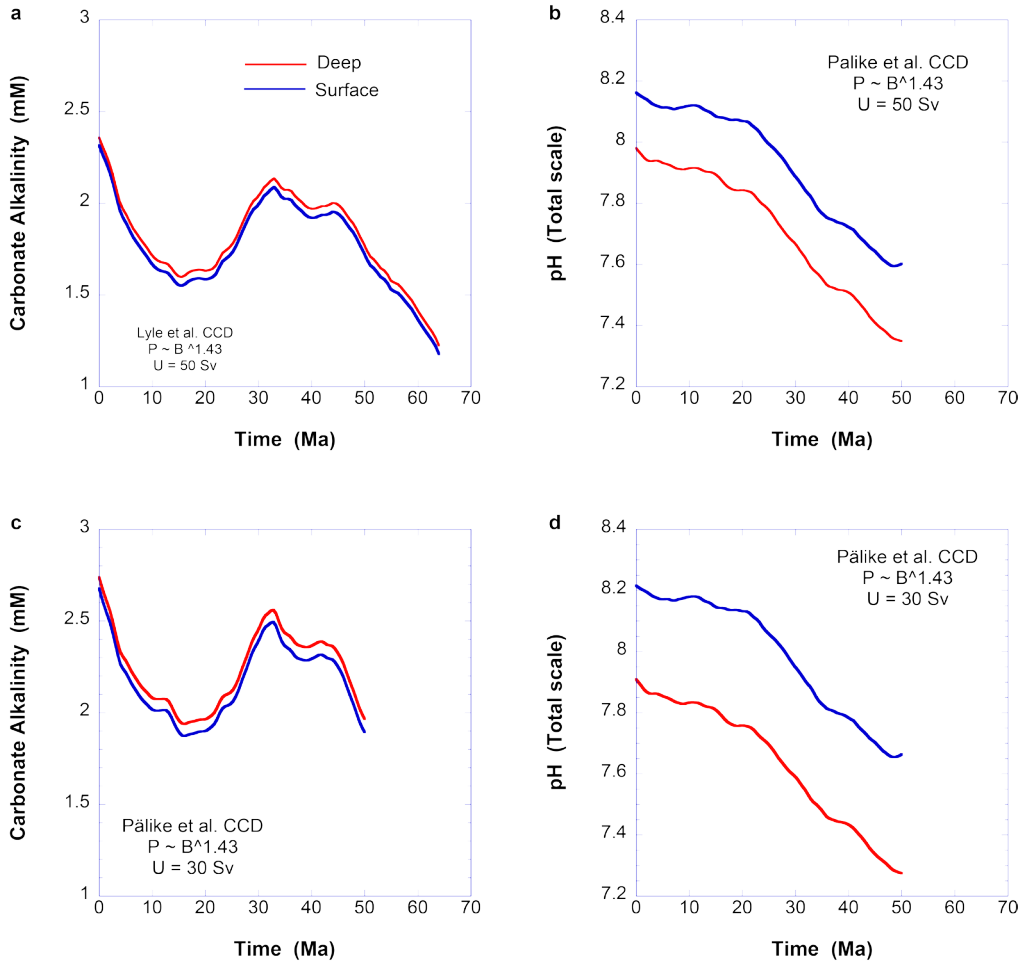

Supplementary Figure 6: Tests of the effect of the exchange/overturning velocity parameter U on retrodicted CAlk and pH, using the Pälike et al. (2012) CCD record. The effects of a 40% drop in this parameter is to cause a 16% change in the CAlk retrodictions, but less in the pH retrodictions (this is a logged variable). a, Retrodicted CAlk with U = 50 Sv. b, Retrodicted pH U = 50 Sv. c, Retrodicted CAlk with U = 30 Sv. d, Retrodicted pH with U = 30 Sv.

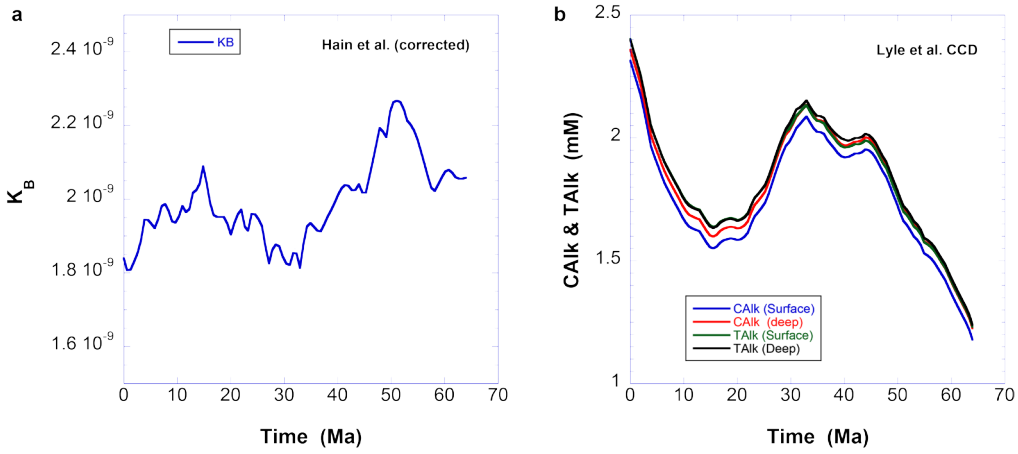

Supplementary Figure 7: A plot to illustrate the easy conversion between CAlk and TAlk, using the temperature, salinity, calcium and magnesium ion records in Figure 2, and the pH retrodictions in Figure 4. a, Value of the boric acid, stoichiometric, dissociation constant as a function of time, as calculated from the Hain et al. (2015) equations and used to obtain panel (b). b, A plot of retrodicted CAlk and TAlk for surface and deep waters. The difference is small, as expected, and the trends are entirely similar.

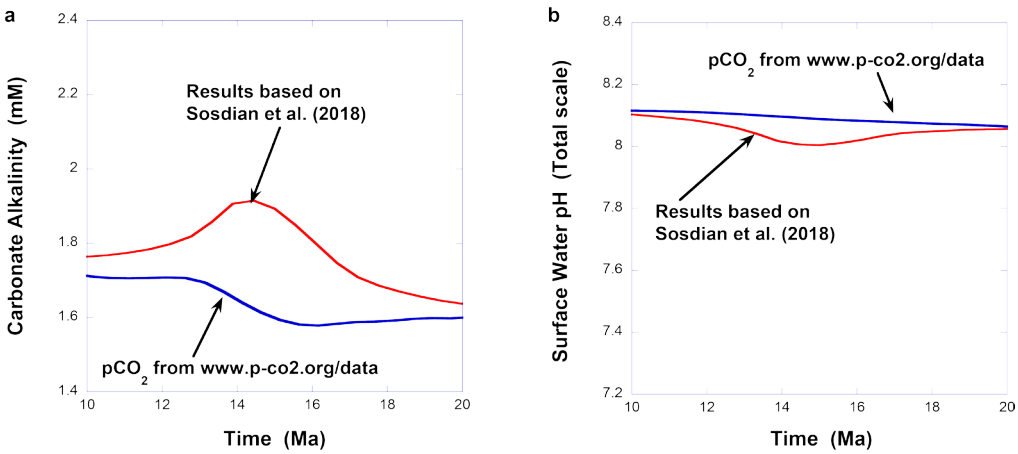

Supplementary Figure 8: Our model run with a secular-averaged pCO_2 record for the Miocene from (Sosdian et al., 2018). These results are somewhat different, but not so much as to change our conclusions.

Chapter 4

Global climate and sea level forcing on Cenozoic neritic carbonate burial

Global climate and sea level forcing on Cenozoic neritic carbonate burial

Robin van der Ploeg, Bernard P. Boudreau, Jack J. Middelburg and Appy Sluijs

Abstract

Marine carbonate burial represents the largest long-term carbon sink at the Earth's surface, occurring in both deep-sea (pelagic) and shallow-water (neritic) environments. The distribution of pelagic versus neritic carbonate accumulation has varied over geological history and impacts both the carbon cycle and ocean chemistry, but remains difficult to quantitatively constrain. Here we reconstruct Cenozoic neritic carbonate burial using a mass balance for global carbonate alkalinity, which integrates independent estimates for continental weathering and pelagic carbonate burial. Our results indicate that major changes in neritic carbonate burial are associated with important climate and sea level change events, including the Eocene-Oligocene Transition (~34 Ma), the Mi-1 glaciation (~23 Ma) and the Middle Miocene Climate Transition (~14 Ma). Remarkably, however, from ~10 Ma to the present we retrodict increasing neritic carbonate burial despite continued sea level fall. In our model, this late Neogene increase in neritic carbonate burial, which appears coincident with the proliferation of coral reefs, is driven by a major increase in continental weathering, potentially related to Himalayan uplift. This implies that changes in global climate, sea level and continental weathering have all impacted neritic carbonate burial over the Cenozoic, but that the relative importance of these processes has varied through time.

4.1 Introduction

Calcium carbonate ($CaCO_3$) deposition in the marine realm occurs primarily in reefs, on continental shelves and slopes, and in the open ocean (Milliman, 1993). At present, deep-sea (hereafter, termed pelagic) carbonate burial represents approximately 70 % of global carbonate burial, while carbonate accumulation in marine shallow waters (hereafter, termed neritic) accounts for the rest (Mackenzie and Morse, 1992). Carbonate alkalinity is delivered to the oceans by continental silicate and carbonate weathering, and removed by carbonate burial, either in neritic or pelagic environments (Supplementary Figure 1). These alkalinity input and output rates must balance in order to maintain a secular equilibrium over geological timescales (Berner, 2004; Ridgwell and Zeebe, 2005). This does not require true steady state, but it implies that the long-term evolution of the global carbonate alkalinity cycle is sufficiently slow for the input and output processes to adjust to any changes so that they are (mathematically) almost in balance at any given time (Boudreau et al., 2019). Consequently, the total amount of carbonate exchanged through the geochemical carbonate cycle at Earth's surface is largely invariant through time (Opdyke and Wilkinson, 1988). However, the nature and the dominant location of carbonate accumulation are known to have shifted over geological history, in association with changes in plate tectonics, global sea level, climate, ocean chemistry and the biology of calcifying organisms (Mackenzie and Morse, 1992; Stanley and Hardie, 1998; Ridgwell and Zeebe, 2005). High sea levels resulted in extensive shallow-water carbonate accumulation in epicontinental seas during parts of the Phanerozoic, most notably during the Carboniferous

and Cambrian (Hay, 1985; Opdyke and Wilkinson, 1988; Walker et al., 2002), while pelagic carbonate burial was insignificant until the evolutionary success of coccolithophores and planktonic foraminifera in the Mesozoic (Martin, 1995; Ridgwell, 2005). A progressive decline in neritic deposition since the Late Cretaceous in response to falling sea levels and a reduction in epicontinental shelf areas may have resulted in a further increase in pelagic deposition towards the present (Opdyke and Wilkinson, 1988; Walker et al., 2002).

Resolving temporal changes in neritic and pelagic carbonate burial and their respective contributions to global carbonate accumulation are important for reconstructions of carbon cycle and climate change. The location of carbonate burial determines the likelihood of carbonate recycling and return of CO_2 to the atmosphere through subduction and metamorphism, because pelagic carbonates have a much higher chance of being deeply buried in subduction zones than shallow-water carbonates (Caldeira, 1992; Berner, 2004). Additionally, neritic carbonates are deposited as aragonite, calcite and magnesium-rich calcite, whereas pelagic carbonates are deposited primarily as calcite. Because of these differences in carbonate mineralogy, shifts in the balance between neritic and pelagic carbonate burial may also drive changes in ocean chemistry (Berner, 2004). Significant progress has been made to estimate pelagic carbonate burial rates across the Cenozoic (Boudreau and Luo, 2017), but relatively little is still known about secular changes in neritic carbonate burial. Here we employ a mass balance for global carbonate alkalinity to estimate neritic carbonate burial rates for the Cenozoic, by independently deriving continental weathering and pelagic carbonate burial histories.

4.2 Methods

We calculate changes in the total carbonate alkalinity delivery to the oceans derived from continental weathering ($F_{weathering}$) for the Cenozoic based on inverse modeling of the marine strontium (Sr) and osmium (Os) isotope records, two well-established proxies for tracing weathering inputs to the global ocean (Ravizza and Zachos, 2003). The $^{87}Sr/^{86}Sr$ and $^{187}Os/^{188}Os$ isotopic compositions of seawater are predominantly governed by inputs from continental and mantle sources, with relatively well-constrained sizes and isotopic compositions for the present-day (Palmer and Edmond, 1989; Vance et al., 2009) (Supplementary Table 1). We use published seawater $^{87}Sr/^{86}Sr$ records (McArthur et al., 2012) and $^{187}Os/^{188}Os$ records (Klemm et al., 2005; Burton, 2006; Nielsen et al., 2009) for the Cenozoic in combination with reconstructions of seafloor spreading and/or degassing rates (Van der Meer et al., 2014) to estimate changes in continental silicate weathering and sediment weathering – the sum of carbonate weathering and organic-rich sediment weathering – back in time (Supplementary Figure 2 – 6). Although this approach is inspired by previous modelling studies (Delaney and Boyle, 1988; G. Li et al., 2009; Li and Elderfield, 2013), uniquely, we do not assume a-priori equilibrium between inputs and outputs in our weathering reconstructions. Rather, we consider the Sr and Os isotope systems without incorporating additional mass balance constraints (e.g., C isotopes), which enables us to independently use the carbonate alkalinity mass balance to subsequently derive neritic carbonate burial. We present a range of scenarios for continental silicate weathering and sediment weathering based on different sets of assumptions regarding the evolution of their respective $^{87}Sr/^{86}Sr$ and $^{187}Os/^{188}Os$ compositions across the Cenozoic (Supplementary Table 2; Supplementary Figure 6). These continental silicate and sediment weathering estimates are proportionally added to obtain the total carbonate alkalinity delivery associated with continental weathering.

Boudreau and Luo (2017) have retrodicted changes in alkalinity outputs associated with pelagic carbonate burial ($F_{pelagic}$), independently of any continental weathering reconstructions. These retrodictions are derived using a set of equations that relate pelagic burial rates to the positions of the calcite saturation horizon and the carbonate compensation depth (CCD) using a canonical $CaCO_3$ profile. Based on this work, we calculated two different scenarios for $F_{pelagic}$, driven by either the global Cenozoic CCD curve (Lyle et al., 2008) or the Pacific CCD curve for the last 50 Myr (Pälike et al., 2012). Finally, changes in alkalinity outputs related to neritic carbonate burial ($F_{neritic}$) were estimated from a mass balance for carbonate alkalinity, in which $F_{neritic}$ is calculated as the difference between $F_{weathering}$ and $F_{pelagic}$, with propagation of their respective uncertainties.

4.2.1 The present-day global alkalinity mass balance

A present-day global budget for carbonate alkalinity was established from silicate weathering and carbonate weathering estimates (Gaillardet et al., 1999), which have been adjusted from mol C yr^{-1} to mol HCO_3^- yr^{-1} equivalents. For the present-day, we assume that the global alkalinity flux associated with carbonate burial (F_{carbb}) is equal to the total carbonate alkalinity flux delivered from weathering ($F_{weathering}$). Following Boudreau and Luo (2017), we derive present-day estimates for the pelagic carbonate burial flux ($F_{pelagic}$) from Davies and Worsley (1981) and Mackenzie and Morse (1992), and then calculate estimates for the neritic carbonate burial flux ($F_{neritic}$) as the difference between F_{carbb} and $F_{pelagic}$. See Supplementary Table 1 for an overview of these present-day parameters and Supplementary Figure 1 for a graphical representation of the present-day global carbonate alkalinity mass balance.

4.2.2 Cenozoic alkalinity fluxes associated with weathering

We estimated changes in the total carbonate alkalinity delivery to the oceans associated with weathering based on inverse modelling of the marine strontium (Sr) and osmium (Os) isotope records, two well-established proxies for tracing weathering inputs to the global ocean (Ravizza and Zachos, 2003). Both the $^{87}Sr/^{86}Sr$ ratio and the $^{187}Os/^{188}Os$ ratio of seawater are controlled by inputs from continental and mantle-derived sources, with relatively well-constrained isotopic compositions at present-day. Sr is delivered to the oceans via silicate weathering, carbonate weathering, hydrothermal activity and, to a lesser extent, by diagenetic fluxes, while Os is sourced by silicate weathering, organic-rich sediment weathering, hydrothermal activity and extraterrestrial fluxes. No isotopic fractionation is associated with Sr and Os burial and consequently, changes in the $^{87}Sr/^{86}Sr$ and $^{187}Os/^{188}Os$ isotope ratios of seawater over time are governed entirely by changes in the sizes or isotopic compositions of the inputs. Building on previous studies (Delaney and Boyle, 1988; Richter and Turekian, 1993; Li and Elderfield, 2013), we use the following equations to model the $^{87}Sr/^{86}Sr$ and $^{187}Os/^{188}Os$ isotope ratios of seawater:

$$\frac{N_{Sr}}{9.43+R_{sw}}\frac{dR_{sw}}{dt} = F_{silw}\left(\frac{R_{silw}-R_{sw}}{9.43+R_{silw}}\right) + F_{carbw}\left(\frac{R_{carbw}-R_{sw}}{9.43+R_{carbw}}\right) + F_{hyd}\left(\frac{R_{hyd}-R_{sw}}{9.43+R_{hyd}}\right) + F_{dia}\left(\frac{R_{dia}-R_{sw}}{9.43+R_{dia}}\right) \quad (1)$$

$$\frac{N_{Os}}{7.4+R_{sw}}\frac{dR_{sw}}{dt} = F_{silw}\left(\frac{R_{silw}-R_{sw}}{7.4+R_{silw}}\right) + F_{orgw}\left(\frac{R_{orgw}-R_{sw}}{7.4+R_{orgw}}\right) + F_{hyd}\left(\frac{R_{hyd}-R_{sw}}{7.4+R_{hyd}}\right) + F_{ext}\left(\frac{R_{ext}-R_{sw}}{7.4+R_{ext}}\right) \quad (2)$$

where *N* represents the total inventory of Sr or Os in the oceans, *F* represents the fluxes of Sr or Os to the oceans from various sources, *R* represents the $^{87}Sr/^{86}Sr$ or $^{187}Os/^{188}Os$ composition of these sources and the subscripts *sw, silw, carbw, orgw, hyd, dia* and *ext* represent seawater,

silicate weathering, carbonate weathering, organic-rich sediment weathering, hydrothermal, diagenetic and extraterrestrial sources, respectively. For a complete derivation of the equation for the $^{187}Os/^{188}Os$ ratio of seawater, we refer to Van der Ploeg et al. (2018) – the derivation for the $^{87}Sr/^{86}Sr$ of seawater is analogous. The factors of 9.43 and 7.4 are respectively used to derive isotopic compositions that are normalized for the natural abundances of ^{87}Sr and ^{86}Sr, and ^{187}Os and ^{188}Os (Li and Elderfield, 2013).

This system of two equations allows us to numerically solve for two unknowns – silicate and sediment weathering fluxes, in this case – if the other parameters can all be constrained. To this end, we follow a simplified version of the approach taken by Li and Elderfield (2013). The evolution of the $^{87}Sr/^{86}Sr$ and $^{187}Os/^{188}Os$ isotopic composition of seawater across the Cenozoic is well documented: for the $^{87}Sr/^{86}Sr$ ratio we use the compilation of existing data by McArthur et al. (2012), and for the $^{187}Os/^{188}Os$ ratio we use a smoothed fit to the data published in Klemm et al. (2005) and Burton (2006), updated to the age model of Nielsen et al. (2009). We force the hydrothermal Sr and Os fluxes (F_{hyd}) with a range of seafloor spreading and/or degassing rate reconstructions. We explore the use of the reconstructions of Berner (1994), Rowley (2002), Müller et al. (2008) and Van der Meer et al. (2014), but these different forcings for F_{hyd} have a relatively minor impact on modelled changes in the various weathering fluxes (Supplementary Figure 2) and consequently we adopt the subduction zone length-based reconstructions of Van der Meer et al. (2014) in the main text. As in previous studies (Li and Elderfield, 2013), we assume that the diagenetic Sr flux (F_{dia}) and the extraterrestrial Os flux (F_{ext}) have remained invariant over the timescale of the Cenozoic (Peucker-Ehrenbrink, 1996; Pegram and Turekian, 1999). Finally, although the seawater Sr and Os inventories have likely changed over time, on timescales of millions of years these changes are of negligible importance in comparison to the sizes of the various inputs (Li and Elderfield, 2013) and hence we assume N_{Sr} and N_{Os} to be constant.

We assume that the $^{87}Sr/^{86}Sr$ and $^{187}Os/^{188}Os$ compositions of the hydrothermal, diagenetic and extraterrestrial Sr and Os fluxes (R_{hyd}, R_{dia} and R_{ext} respectively) have remained constant at present-day values. However, the $^{87}Sr/^{86}Sr$ and $^{187}Os/^{188}Os$ compositions of the various weathering fluxes (R_{silw}, R_{carbw} and R_{orgw}) have most likely varied through time due to changing contributions from different source rock types. Because the quantitative evolution of these parameters is difficult to constrain independently (Ravizza and Zachos, 2003), we have developed several scenarios to explore the sensitivity of our results to different assumptions regarding these parameters. In Scenario 1, we assume that present-day R_{silw}, R_{carbw} and R_{orgw} values have remained unchanged during the Cenozoic, with uniform uncertainty distributions. However, this default assumption is most likely too simplistic given the range of studies that report variable isotopic compositions of weathering fluxes related to plate tectonic processes or climate events during the Cenozoic (Raymo and Ruddiman, 1992; Zachos et al., 1999; Lear et al., 2003). Therefore, we test for the effects of a progressive evolution in each of these parameters in additional scenarios. In Scenario 2 – 6, we assume a linear increase in one or more parameters from a minimum at 70 Ma towards present-day values, reflecting the impact of weathering fluxes with progressively more radiogenic $^{87}Sr/^{86}Sr$ or $^{187}Os/^{188}Os$ isotopic compositions over time. Such increases in R_{silw}, R_{carbw} and R_{orgw} would – to a first approximation – be compatible with the gradually increasing $^{87}Sr/^{86}Sr$ and $^{187}Os/^{188}Os$ isotopic compositions of seawater that have been reported for the Cenozoic (Lear et al., 2003; Ravizza and Zachos, 2003), and could potentially be related to Himalayan uplift (Colleps et al., 2018). In Scenario 2, we increase the $^{87}Sr/^{86}Sr$ composition of silicate weathering linearly from 0.7183 at 70 Ma to

0.7203 at present-day, while in Scenario 3, we increase the $^{87}Sr/^{86}Sr$ composition of carbonate weathering increase linearly from 0.7057 at 70 Ma to 0.7077 at present-day. In Scenario 4, we increase the $^{187}Os/^{188}Os$ composition of silicate weathering linearly from 0.60 at 70 Ma to 1.05 at present-day, and in Scenario 5, we increase the $^{187}Os/^{188}Os$ composition of organic-rich sediment weathering linearly from 1.00 at 70 Ma to 1.78 at present-day. Finally, in Scenario 6, we combine the increase in the $^{87}Sr/^{86}Sr$ composition of silicate weathering as in Scenario 2 with the increase in the $^{187}Os/^{188}Os$ composition of organic-rich sediment weathering as in Scenario 5, because these parameters are thought to have a large impact on weathering flux estimates (Peucker-Ehrenbrink and Ravizza, 2000; G. Li et al., 2009). Together, Scenarios 1 – 6 provide solutions for these weathering fluxes under a range of probable isotopic compositions.

Finally, we adopt the assumption that carbonate weathering (F_{carbw}) and organic-rich sediment weathering (F_{orgw}) are proportional to each other on a global scale, and that these two fluxes can be combined as global sediment weathering (F_{sedw}) (Derry and France-Lanord, 1996; Li and Elderfield, 2013). This leaves us with only two remaining unknowns, F_{silw} and F_{sedw}, which can be solved numerically for the Cenozoic with the above equations. The total carbonate alkalinity flux from continental weathering ($F_{weathering}$) is then given by:

$$F_{weathering} = F_{silw} + F_{sedw} \quad (3)$$

in which the fluxes are calculated relative to their present-day values.

See Supplementary Table 1 for an overview of all present-day parameter values used for Sr and Os cycle modelling and Supplementary Table 2 for an overview of the different scenarios described above. The model results for these scenarios are shown in Supplementary Figure 3 – 5. We use minimum, mean and maximum estimates based on the full range of these scenarios (Supplementary Figure 6) for our main $F_{weathering}$ estimates shown in Figure 1.

4.2.3 Cenozoic alkalinity fluxes associated with pelagic carbonate burial

The alkalinity output flux associated with carbonate burial in the pelagic oceans ($F_{pelagic}$) is calculated following Boudreau and Luo (2017). Here, we take the retrodicted pelagic carbonate burial rates of Boudreau and Luo (2017) (in mol $CaCO_3$ / Myr) that were driven by the global Cenozoic CCD curve of Lyle et al. (2008) and the Pacific CCD curve for the last 50 Myr of Pälike et al. (2012), and adjust their values to alkalinity equivalents (in mol HCO_3^- / Myr). We also incorporate uncertainties in the size of the present-day pelagic carbonate burial flux by using minimum and maximum estimates based on Davies and Worsley (1981) and Mackenzie and Morse (1992). The resulting estimates are shown in Figure 1.

4.2.4 Cenozoic alkalinity fluxes associated with neritic carbonate burial

With both $F_{weathering}$ and $F_{pelagic}$ constrained, the alkalinity output flux associated with carbonate burial in the neritic oceans ($F_{neritic}$) can be calculated using a mass balance for global carbonate alkalinity:

$$\frac{dN_{Alk}}{dt} = F_{weathering} - F_{neritic} - F_{pelagic} \quad (4)$$

in which N_{Alk} represents the total inventory of carbonate alkalinity in the oceans.

We calculate $F_{neritic}$ values with propagation of the uncertainties for $F_{weathering}$ and $F_{pelagic}$ described above using the root of the mean square errors. We assess the impact of potential

temporal changes in N_{Alk} using the Cenozoic carbonate alkalinity reconstructions of Boudreau et al. (2019) to account for any imbalances in the global inputs and outputs of carbonate alkalinity (Supplementary Figure 7). We convert these modelled carbonate alkalinity concentrations from mmol HCO_3^- kg^{-1} to a total carbonate alkalinity inventory in mol HCO_3^- by assuming a seawater density of 1.035 kg L^{-1} and a global ocean volume of 1.33 x 10^{21} L following Charette and Smith (2000). Importantly, the maximum imbalance calculated from the reconstructions of Boudreau et al. (2019) is up to two orders of magnitude smaller than the sizes of the alkalinity fluxes, so the effect of any changes over time in N_{Alk} on $F_{neritic}$ is negligible (Supplementary Figure 7). Hence, we assume N_{alk} to be constant and dN_{alk}/dt to be zero for our main $F_{neritic}$ estimates shown in Figure 1.

4.3 Results

Our range of $F_{weathering}$ scenarios displays a gradual increase from the early Cenozoic towards the present (Figure 1a), a result consistent with previous modeling studies in terms of general shape and magnitude (Delaney and Boyle, 1988; Li and Elderfield, 2013). Moreover, our $F_{weathering}$ estimates are quite similar to total global carbonate burial estimates based on reconstructions of the extent and volume of carbonate rocks through time (Opdyke and Wilkinson, 1988). Both $F_{pelagic}$ scenarios show an overall increase towards the present, but they diverge during the Oligocene and especially the Miocene (Figure 1b). $F_{weathering}$ and $F_{pelagic}$ track each other relatively well over the timescale of the Cenozoic, but significant secular changes in $F_{neritic}$ are observed nonetheless (Figure 1c).

The Lyle et al.-based $F_{neritic}$ scenario is relatively invariant for most of the Cenozoic, except for two intervals of rapid change. After a gradual increase in the Eocene, $F_{neritic}$ displays a major decrease between 38 – 34 Ma, followed by an interval where the rates become negative, which indicates net removal (weathering and erosion) of previously buried carbonate material. These negative values persist during most of the Oligocene until ~23 Ma, after which $F_{neritic}$ recovers and remains constant until the end of the Miocene. A final increase is observed between the Pliocene and the present.

The Pälike et al.-based $F_{neritic}$ scenario displays more dramatic shifts than the Lyle et al. -based scenario, but does not extend beyond 50 Ma. Following a slight decline in the Eocene, it is characterized by a pronounced interval of very negative values between 36 – 10 Ma, punctuated by distinct minima at ~32 Ma, ~23 Ma and ~12 Ma. It also features a large increase to present-day values from ~10 Ma onwards that is not apparent in the Lyle et al.-based scenario.

4.4 Discussion

We find that the overall patterns in $F_{neritic}$ correlate with the Cenozoic evolution of global sea level and climate (Figure 1d; Figure 1e). For the early Cenozoic, we estimate relatively high $F_{neritic}$ values corresponding to globally warm climates (Zachos et al., 2008) and high sea levels (Miller et al., 2005), while subsequent long-term cooling is generally mirrored by a decline in $F_{neritic}$ values. Importantly, shifts towards negative $F_{neritic}$ values imply that the supply of alkalinity to the pelagic realm exceeded the weathering influx, pointing to active weathering of neritic carbonates. Although the absolute values we obtain for the Pälike et al.-based scenario may be too low due to a potential overestimation of $F_{pelagic}$ values, the distinct minima in $F_{neritic}$ correlate with important episodes of climatic change. For example, the large $F_{neritic}$ shift at ~36 Ma occurs just prior to the Eocene-Oligocene Transition (EOT; ~34 Ma) and the onset of

Antarctic glaciation (Lear et al., 2000), which is characterized by an episode of major sea level fall and CCD deepening (Coxall et al., 2005; Merico et al., 2008). Similarly, the minimum at ~23 Ma is virtually synchronous with ice sheet expansion during the Mi-1 glaciation (Miller et al., 1991; Zachos et al., 2001), and the minimum at ~12 Ma, which is only apparent in the Pälike et al.-based scenario, follows ice sheet expansion just after the Middle Miocene Climate Transition (MMCT; ~14 Ma) (Flower and Kennett, 1994; Shevenell et al., 2004). The strong correlations between episodes of decreasing or negative $F_{neritic}$ and major episodes of cooling and ice sheet expansion suggest that these phenomena are related through changes in global sea level.

Strikingly, our $F_{neritic}$ estimates deviate from these aforementioned long-term Cenozoic trends over the last 10 Myr. The final increase we predict for $F_{neritic}$ is most evident in the Pälike et al.-based scenario and is opposite to the continued decrease in neritic carbonate burial that has been inferred by other studies (Hay, 1985; Opdyke and Wilkinson, 1988; Walker et al., 2002) and that would be expected based on progressive Cenozoic sea level fall (Haq et al., 1987; Miller et al., 2005; Müller et al., 2008). In our model, this $F_{neritic}$ increase is driven primarily by a large increase in $F_{weathering}$, which coincides roughly with the final stage of Himalayan uplift (Raymo et al., 1988). Although the impact of Himalayan uplift on continental weathering rates is still not resolved (Edmond, 1992; Lear et al., 2003; Willenbring and Von Blanckenburg, 2010; Caves et al., 2016), this inferred $F_{neritic}$ increase appears to be in agreement with the late Neogene proliferation of coral reefs following a progressive decrease in atmospheric CO_2 concentrations and shift in global carbonate burial from primarily calcite-dominated deposition towards more aragonite-dominated deposition (Sosdian et al., 2012). However, we are not able to discriminate between changes in carbonate burial on reefs versus continental shelves and slopes to test this further.

4.5 Conclusions

We present estimates of neritic carbonate burial for the Cenozoic using a mass balance for global carbonate alkalinity that incorporates independent estimates of continental weathering and pelagic carbonate burial. The correlation between the inferred changes in $F_{neritic}$ and the

Figure 1 (right): Modelled continental weathering and carbonate burial rates for the Cenozoic in relation to global climate and sea level. a, Total continental weathering rates, inferred from Sr and Os cycle modelling. The shaded areas represent minimum and maximum estimates based on the full range of scenarios as outlined in the Methods and Supplementary Table 2, with the solid red line representing the mean of these estimates. The dashed yellow line represents global carbonate burial rates as reconstructed by Opdyke and Wilkinson (1988). b, Pelagic carbonate burial rates, calculated from the pelagic carbonate burial retrodictions of Boudreau and Luo (2017), following either the Lyle et al. (2008) CCD (lightblue) or the Pälike et al. (2012) CCD (darkblue). The shaded areas represent minimum and maximum estimates based on the present-day pelagic carbonate burial flux estimates of either Davies and Worsley (1981) or Mackenzie and Morse (1992) (see Methods). The dashed blue line represents pelagic carbonate burial rates as reconstructed by Opdyke and Wilkinson (1988). c, Neritic carbonate burial rates, calculated as the difference between the continental weathering rates and the pelagic carbonate burial rates, following either the Lyle et al. (2008) CCD (pink) or the Pälike et al. (2012) CCD (purple) (see Methods). The dashed purple line represents neritic carbonate burial rates as reconstructed by Opdyke and Wilkinson (1988), taken as the sum of their estimates for carbonate platform and slope-rise systems. d, Global sea level curve of Miller et al. (2005) as obtained from Müller et al. (2008). e, Benthic foraminiferal $\delta^{18}O$ compilation as published in Cramer et al. (2009), shown as individual data points (in grey) and as a smoothed fit (in blue).

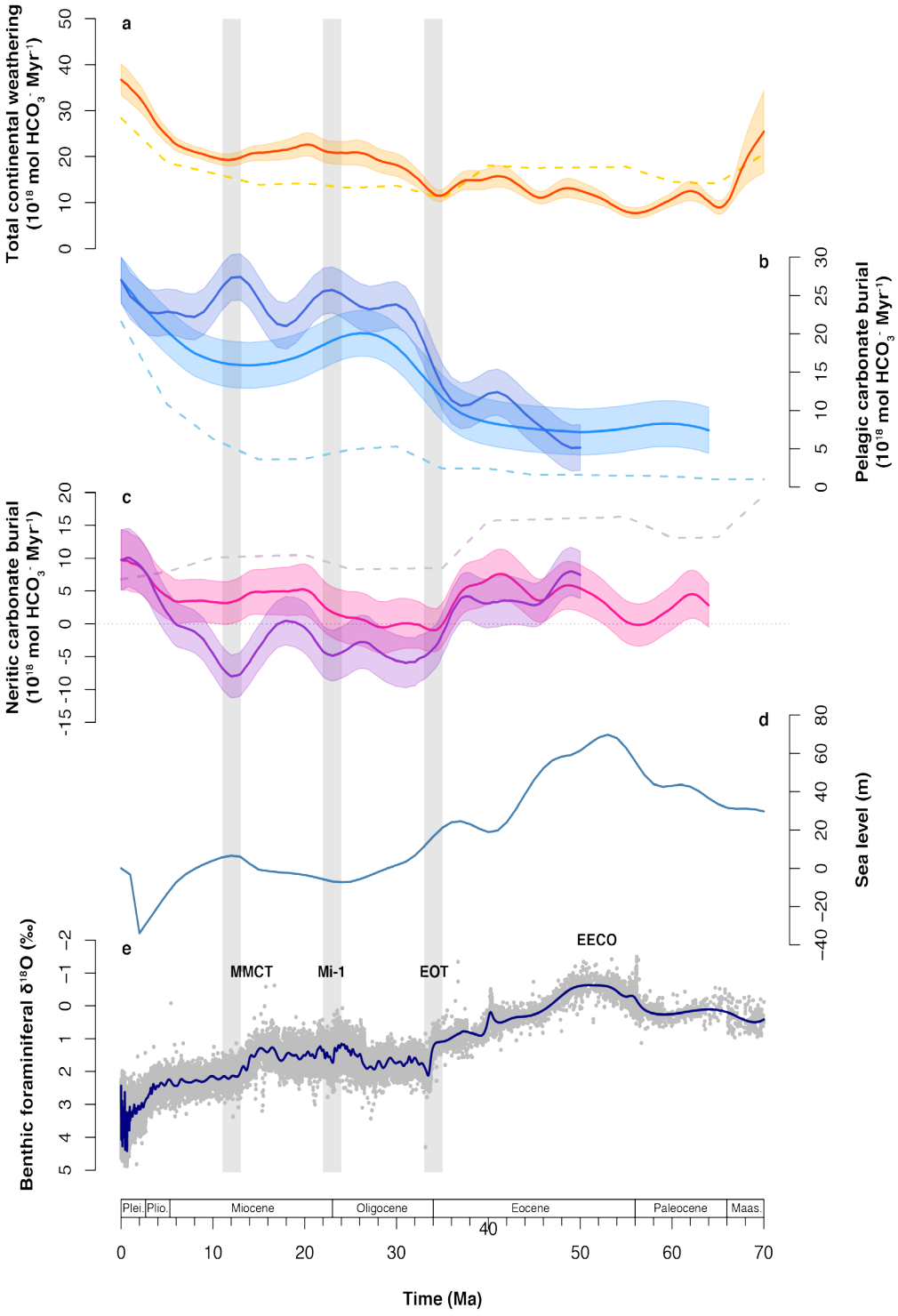
a
b
c
d
e
Total continental weathering
(10^18 mol HCO3- Myr-1)
Pelagic carbonate burial
(10^18 mol HCO3- Myr-1)
Neritic carbonate burial
(10^18 mol HCO3- Myr-1)
Sea level (m)
Benthic foraminiferal δ18O (‰)
MMCT
Mi-1
EOT
EECO
Plei.
Plio.
Miocene
Oligocene
Eocene
Paleocene
Maas.
Time (Ma)

interplay of global climate, sea level and continental weathering implies that these processes have all impacted neritic carbonate burial over the Cenozoic, but that the relative importance of these processes has likely changed over time. In summary, global cooling and sea level fall may have driven the progressive, long-term decline in neritic carbonate burial that we observe for most of the Cenozoic, while an increase in continental weathering related to tectonic uplift in the late Neogene may have subsequently resulted in the final neritic carbonate burial increase towards the present. Additionally, these long-term trends appear modulated by transient climate events such as the EOT, Mi-1 glaciation and MMCT. Episodes of negative neritic carbonate burial associated with such climate events may indicate large-scale weathering and erosion of previously deposited carbonate material and transport of alkalinity from the neritic to the pelagic oceans, which is consistent with the concept of shifting carbonate accumulation through time.

Acknowledgements

This work was carried out under the program of the Netherlands Earth System Science Centre (NESSC), which is financially supported by the Ministry of Education, Culture and Science (OCW) of the Netherlands.

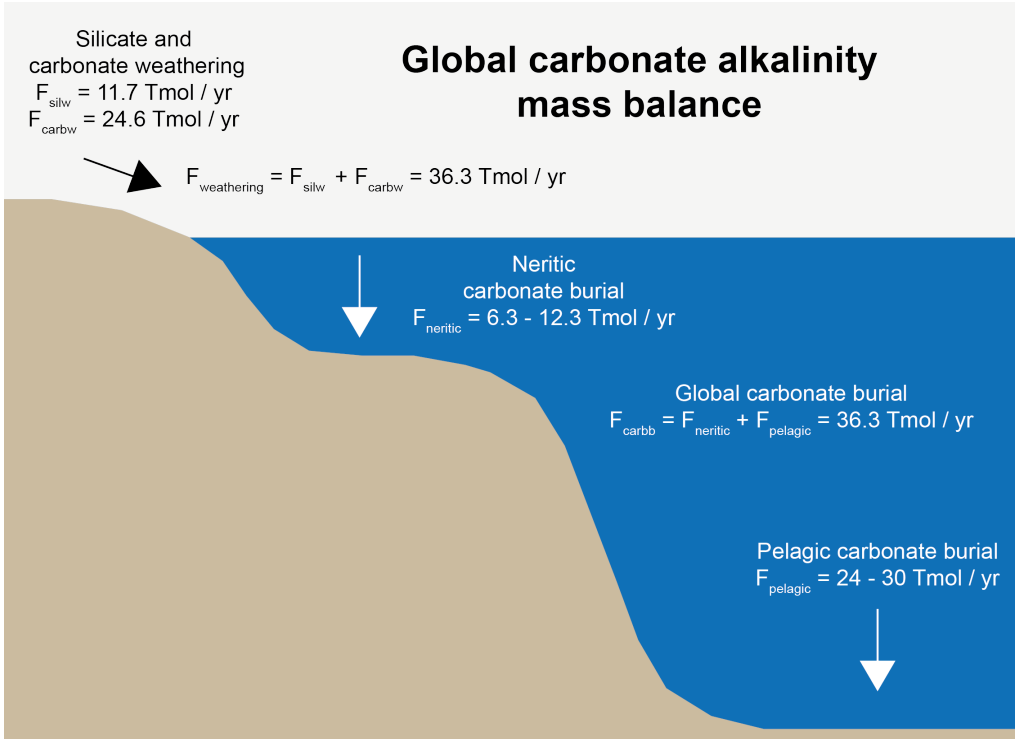

Supplementary Figure 1: Schematic representation of the present-day global carbonate alkalinity mass balance. Present-day silicate and carbonate weathering rates (F_{silw} and F_{carbw}) are taken from Gaillardet et al. (1999), and at steady state the global carbonate burial rate (F_{carbb}) is assumed to be equal to the total weathering rate ($F_{weathering}$). The pelagic carbonate burial rate ($F_{pelagic}$) is derived from Boudreau and Luo (2017) and the neritic carbonate burial rate ($F_{neritic}$) is calculated as the difference between F_{carbb} and $F_{pelagic}$. Values are expressed as Tmol HCO_3^- yr^{-1}.

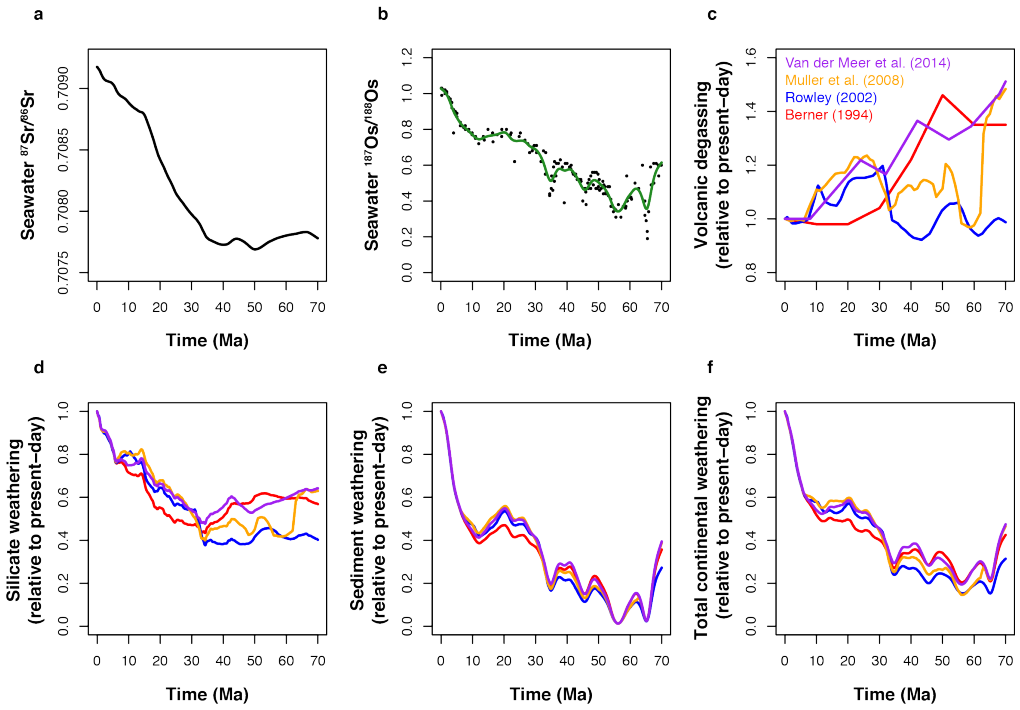

Supplementary Figure 2: Sensitivity of the modelled continental weathering rates to different hydrothermal flux forcings. a, Seawater $^{87}Sr/^{86}Sr$ compilation of McArthur et al. (2012) (in black). b, Seawater $^{187}Os/^{188}Os$ records of Klemm et al. (2005) and Burton (2006), updated to the age model of Nielsen et al. (2009). The green line represents the smoothed fit used in our model calculations. c, Volcanic degassing rates relative to present-day values used as forcings for the hydrothermal Sr and Os fluxes (F_{hyd}). Shown are the reconstructions of Berner (1994) (in red), Rowley (2002), Müller et al. (2008) (in orange) and Van Der Meer et al. (2014) (in purple). d, Modelled silicate weathering rates (F_{silw}) and e, sediment weathering rates (F_{sedw}) relative to present-day values resulting from the forcings in (a), (b) and (c) and the parameters of Scenario 1. f, Modelled total continental weathering rates ($F_{weathering}$) relative to present-day values, obtained by proportionally adding F_{silw} and F_{sedw} as in (d) and (e).

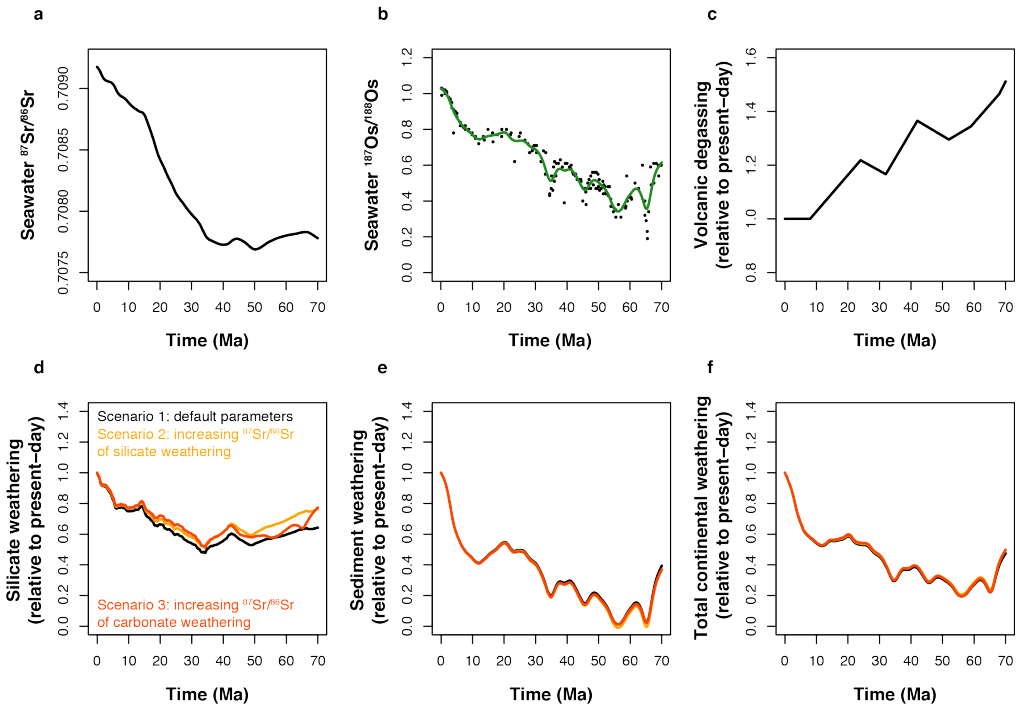

Supplementary Figure 3: Sensitivity of the modelled continental weathering rates to changes in isotopic compositions of weathering sources. a, Seawater $^{87}Sr/^{86}Sr$ compilation of McArthur et al. (2012) (in black). b, Seawater $^{187}Os/^{188}Os$ records of Klemm et al. (2005) and Burton (2006), updated to the age model of Nielsen et al. (2009). The green line represents the smoothed fit used in our model calculations. c, Volcanic degassing rates relative to present-day values, based on subduction zone length-based degassing rate reconstructions (Van Der Meer et al., 2014). d, Modelled silicate weathering rates (F_{silw}) and e, carbonate and organic-rich sediment weathering rates (F_{sedw}) relative to present-day values, resulting from the forcings shown in (a), (b) and (c) and the parameters of Scenario 1 (in black), Scenario 2 (in orange) and Scenario 3 (in red). f, Modelled total continental weathering rates ($F_{weathering}$) relative to present-day values, obtained by proportionally adding F_{silw} and F_{sedw} as in (d) and (e).

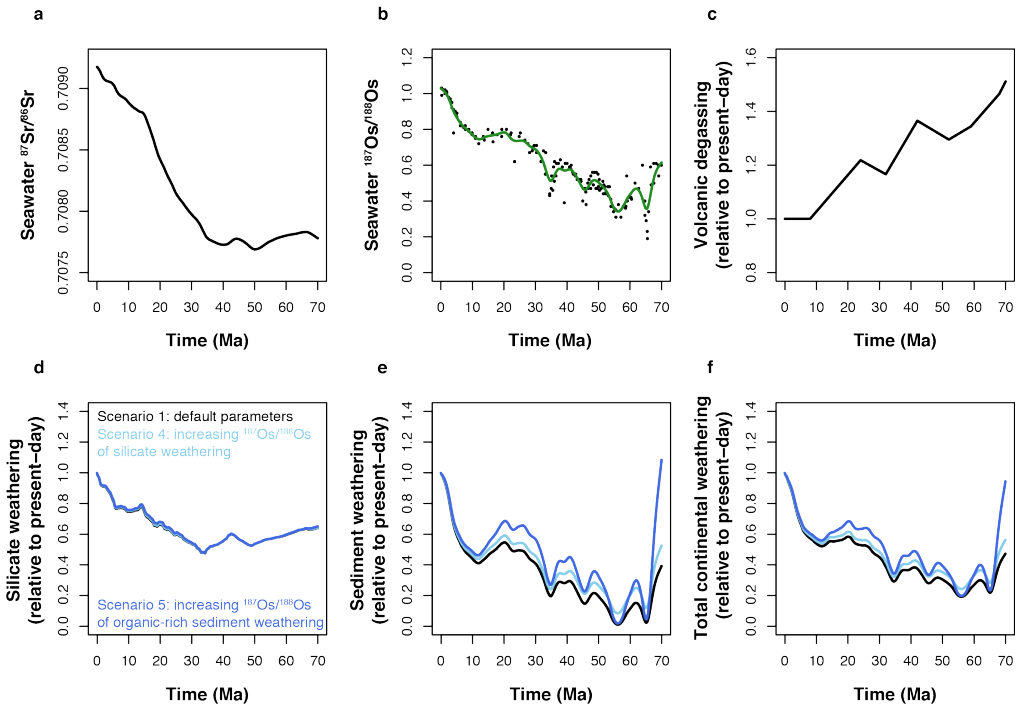

Supplementary Figure 4: Sensitivity of the modelled continental weathering rates to changes in isotopic compositions of weathering sources. a, Seawater $^{87}Sr/^{86}Sr$ compilation of McArthur et al. (2012) (in black). b, Seawater $^{187}Os/^{188}Os$ records of Klemm et al. (2005) and Burton (2006), updated to the age model of Nielsen et al. (2009). The green line represents the smoothed fit used in our model calculations. c, Volcanic degassing rates relative to present-day values, based on subduction zone length-based degassing rate reconstructions (Van Der Meer et al., 2014). d, Modelled silicate weathering rates (F_{silw}) and e, carbonate and organic-rich sediment weathering rates (F_{sedw}) relative to present-day values, resulting from the forcings shown in (a), (b) and (c) and the parameters of Scenario 1 (in black), Scenario 4 (in light blue) and Scenario 5 (in dark blue). f, Modelled total continental weathering rates ($F_{weathering}$) relative to present-day values, obtained by proportionally adding F_{silw} and F_{sedw} as in (d) and (e).

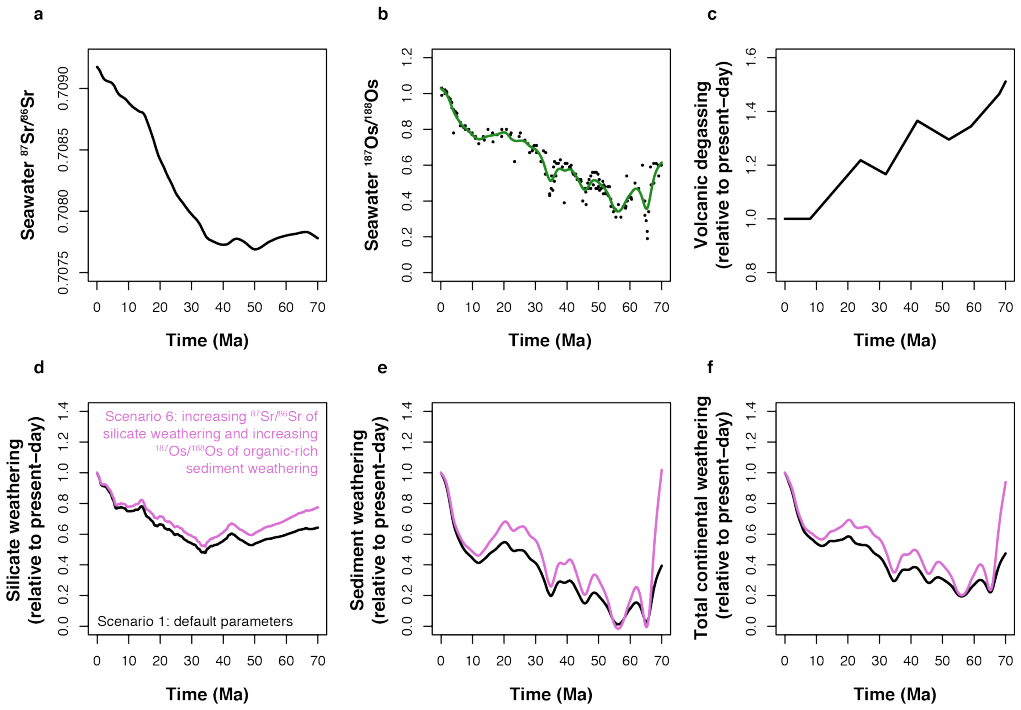

Supplementary Figure 5: Sensitivity of the modelled continental weathering rates to changes in isotopic compositions of weathering sources. a, Seawater $^{87}Sr/^{86}Sr$ compilation of McArthur et al. (2012) (in black). b, Seawater $^{187}Os/^{188}Os$ records of Klemm et al. (2005) and Burton (2006), updated to the age model of Nielsen et al. (2009). The green line represents the smoothed fit used in our model calculations. c, Volcanic degassing rates relative to present-day values, based on subduction zone length-based degassing rate reconstructions (Van Der Meer et al., 2014). d, Modelled silicate weathering rates (F_{silw}) and e, carbonate and organic-rich sediment weathering rates (F_{sedw}) relative to present-day values, resulting from the forcings shown in (a), (b) and (c) and the parameters of Scenario 1 (in black) and Scenario 6 (in purple). f, Modelled total continental weathering rates ($F_{weathering}$) relative to present-day values, obtained by proportionally adding F_{silw} and F_{sedw} as in (d) and (e).

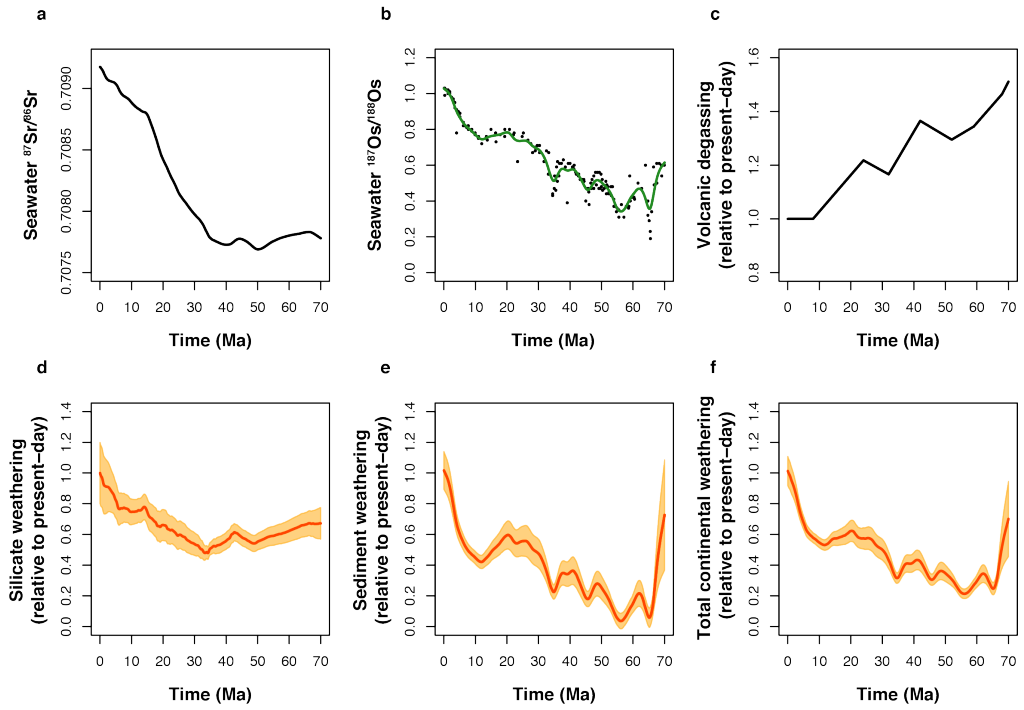

Supplementary Figure 6: Summary of scenarios for modelled continental weathering rates for the Cenozoic. a, Seawater $^{87}Sr/^{86}Sr$ compilation of McArthur et al. (2012) (in black). b, Seawater $^{187}Os/^{188}Os$ records of Klemm et al. (2005) and Burton (2006), updated to the age model of Nielsen et al. (2009). The green line represents the smoothed fit used in our model calculations. c, Volcanic degassing rates relative to present-day values, based on subduction zone length-based degassing rate reconstructions (Van Der Meer et al., 2014). d, Modelled silicate weathering rates (F_{silw}) and e, carbonate and organic-rich sediment weathering rates (F_{sedw}) relative to present-day values. The shaded areas correspond to the minimum and maximum estimates based on the full range of Scenarios 1 – 6 as in Supplementary Figure 3 – 5, with the red line representing the mean of these estimates. f, Modelled total continental weathering rates ($F_{weathering}$) relative to present-day values, obtained by proportionally adding F_{silw} and F_{sedw} as in (d) and (e).

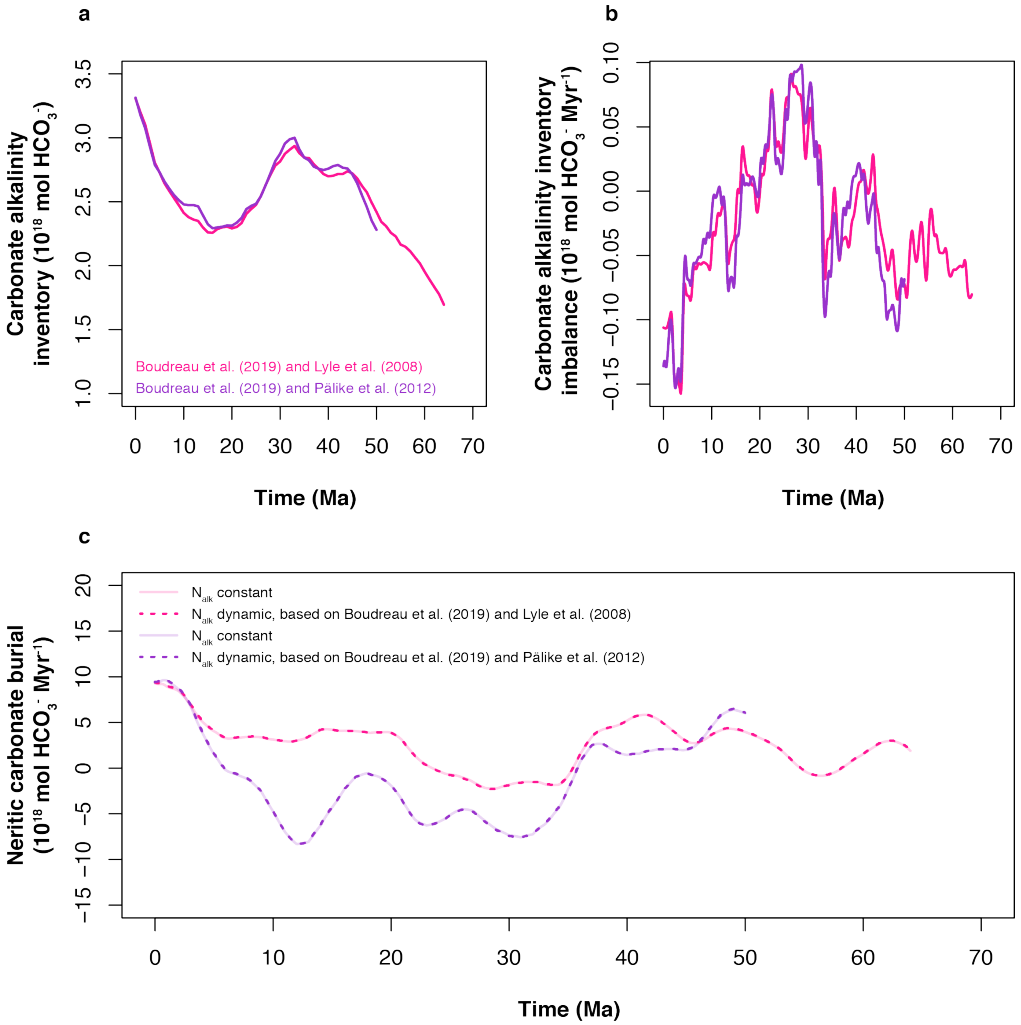

Supplementary Figure 7: Sensitivity of neritic carbonate burial to changes in the alkalinity inventory of the global ocean. a, Global carbonate alkalinity inventory (N_{alk}) as estimated by Boudreau et al. (2019), based on the Lyle et al. (2008) CCD (in pink) or the Pälike et al. (2012) CCD (in purple). b, Imbalance in the global carbonate alkalinity inventory, obtained as dN_{alk}/dt from the estimates in (a). c, Neritic carbonate burial rates ($F_{neritic}$) calculated by assuming constant N_{alk} (solid lines) or dynamic N_{alk} (dashed lines) following the estimates in (a) and (b). Total continental weathering rates ($F_{weathering}$) are based on the parameters of Scenario 1 and the pelagic burial rates ($F_{pelagic}$) are based either on the Lyle et al. CCD (pink) or the Pälike et al. CCD (purple). The difference between constant and dynamic N_{alk} is negligible and hence the solid and dashed lines overlap.

Supplementary Table 1: Overview of all parameters used in alkalinity, Sr and Os cycle modelling. All values are present-day values taken from the literature or fitted to match the present-day steady state observations.

Parameter	Parameter description	Value	Reference and Comments
Alkalinity			
F_{silw}	Silicate weathering flux of alkalinity to oceans	11.7 x 10^{18} mol/Myr	Gaillardet et al. (1999)
F_{carbw}	Carbonate weathering flux of alkalinity to oceans	24.6 x 10^{18} mol/Myr	Gaillardet et al. (1999)
F_{carbb}	Carbonate burial flux of alkalinity from oceans	36.3 x 10^{18} mol/Myr	Calculated assuming steady state by adding F_{silw} and F_{carbw}
$F_{pelagic}$	Pelagic carbonate burial flux of alkalinity from oceans	24 – 30 x 10^{18} mol/Myr	Boudreau and Luo (2017), following Davies and Worsley (1981) and Mackenzie and Morse (1992)
$F_{neritic}$	Neritic carbonate burial flux of alkalinity from oceans	6.3 – 12.3 x 10^{18} mol/Myr	Calculated assuming steady state by subtracting $F_{pelagic}$ from F_{carbb}
Sr			
N	Sr inventory in oceans	1.25 x 10^{17} mol	Palmer and Edmond (1989)
F_{silw}	Silicate weathering flux of Sr to oceans	1.05 x 10^{16} mol/Myr	Li and Elderfield (2013)
F_{carbw} (F_{sedw})	Carbonate weathering flux of Sr to oceans	2.35 x 10^{16} mol/Myr	Li and Elderfield (2013)
F_{hyd}	Hydrothermal flux of Sr to oceans	1.46 x 10^{16} mol/Myr	Li and Elderfield (2013), taken as the sum of the island basalt weathering and hydrothermal fluxes
F_{dia}	Diagenetic flux of Sr to oceans	7.80 x 10^{15} mol/Myr	Calculated to arrive at steady state of R_{sw} = 0.709175
R_{silw}	$^{87}Sr/^{86}Sr$ composition of silicate weathering flux	0.7203	Li and Elderfield (2013), following Li et al. (2009)
R_{carbw}	$^{87}Sr/^{86}Sr$ composition of carbonate weathering flux	0.7077	Li and Elderfield (2013), following Li et al. (2009)
R_{hyd}	$^{87}Sr/^{86}Sr$ composition of hydrothermal flux	0.7037	Li and Elderfield (2013), following Bach and Humphris (1999)
R_{dia}	$^{87}Sr/^{86}Sr$ composition of diagenetic flux	0.7084	Li and Elderfield (2013), following Elderfield and Gieskes (1982)
R_{sw}	$^{87}Sr/^{86}Sr$ composition of seawater	0.709175	McArthur et al. (2012)
Os			
N	Os inventory in oceans	6.83 x 10^{7} mol	Oxburgh (2001)
F_{silw}	Silicate weathering flux of Os to oceans	551 x 10^{6} mol/Myr	Li and Elderfield (2013), following Li et al. (2009)
F_{orgw} (F_{sedw})	Organic-rich sediment weathering flux of Os to oceans	1119 x 10^{6}mol/yr	Li and Elderfield (2013), following Li et al. (2009)
F_{hyd}	Hydrothermal flux of Os to oceans	710 x 10^{6} mol/yr	Li and Elderfield (2013), taken as the sum of the island basalt weathering and hydrothermal fluxes
F_{ext}	Extraterrestrial flux of Os to oceans	260 x 10^{6} mol/yr	Calculated to arrive at steady state of R_{sw} = 1.02
R_{silw}	$^{187}Os/^{188}Os$ composition of silicate weathering flux	1.05	Li and Elderfield (2013), following Peucker-Ehrenbrink and Jahn (2001)
R_{orgw}	$^{187}Os/^{188}Os$ composition of organic-rich sediment weathering flux	1.78	Li and Elderfield (2013), following Li et al. (2009)
R_{hyd}	$^{187}Os/^{188}Os$ composition of hydrothermal flux	0.126	Li and Elderfield (2013), following Allègre and Luck (1980)
R_{ext}	$^{187}Os/^{188}Os$ composition of extraterrestrial flux	0.126	Li and Elderfield (2013), following Allègre and Luck (1980)
R_{sw}	$^{187}Os/^{188}Os$ composition of seawater	1.02	Klemm et al. (2005), Burton (2006), Nielsen et al. (2009), obtained using a smoothing spline

Supplementary Table 2: Overview of the uncertainties incorporated in the weathering reconstructions and the different scenarios for the $^{87}Sr/^{86}Sr$ and $^{187}Os/^{188}Os$ compositions of the various weathering fluxes. Scenario 1 represents the default scenario, while in Scenario 2 – 6 linear a linear increase in one or more parameter values is prescribed from 70 Ma to present-day. For these additional scenarios, only the parameters that are different with respect to Scenario 1 are listed.

Scenario	Parameter	Present-day value	Uncertainty	Prescribed 70 Ma value	Reference and Comments
Scenario 1: all present-day values unchanged					All other parameters as in Supplementary Table 1
Sr	R_{silw}	0.7203	± 0.001	0.7203	Uniform uncertainty
	R_{carbw}	0.7077	± 0.001	0.7077	Uniform uncertainty
Os	R_{silw}	1.05	± 0.1	1.05	Uniform uncertainty
	R_{orgw}	1.78	± 0.1	1.78	Uniform uncertainty
Scenario 2: increasing $^{87}Sr/^{86}Sr$ of silicate weathering	R_{silw}	0.7203	-	0.7183	Linear increase from 70 Ma to 0 Ma
Scenario 3: increasing $^{87}Sr/^{86}Sr$ of carbonate weathering	R_{carbw}	0.7077	-	0.7057	Linear increase from 70 Ma to 0 Ma
Scenario 4: increasing $^{187}Os/^{188}Os$ of silicate weathering	R_{silw}	1.05	-	0.60	Linear increase from 70 Ma to 0 Ma
Scenario 5: increasing $^{187}Os/^{188}Os$ of organic-rich sediment weathering	R_{orgw}	1.78	-	1.00	Linear increase from 70 Ma to 0 Ma
Scenario 6: increasing R_{silw} $^{87}Sr/^{86}Sr$ and R_{orgw} $^{187}Os/^{188}Os$					
Sr	R_{silw}	0.7203	-	0.7183	Linear increase from 70 Ma to 0 Ma
Os	R_{orgw}	1.78	-	1.00	Linear increase from 70 Ma to 0 Ma

Chapter 5

Middle Eocene greenhouse warming facilitated by diminished weathering feedback

Middle Eocene greenhouse warming facilitated by diminished weathering feedback

Robin van der Ploeg, David Selby, Margot J. Cramwinckel, Yang Li, Steven M. Bohaty, Jack J. Middelburg and Appy Sluijs

Abstract

The Middle Eocene Climatic Optimum (MECO) represents a ~500 kyr period of global warming ~40 million years ago and is associated with a rise in atmospheric CO_2 concentrations, but the cause of this CO_2 rise remains enigmatic. Here we show, based on osmium isotope ratios ($^{187}Os/^{188}Os$) of marine sediments and published records of the carbonate compensation depth (CCD), that the continental silicate weathering response to the inferred CO_2 rise and warming was strongly diminished during the MECO – in contrast to expectations from the silicate weathering thermostat hypothesis. We surmise that global early and middle Eocene warmth gradually diminished the weatherability of continental rocks and hence the strength of the silicate weathering feedback, allowing for the prolonged accumulation of volcanic CO_2 in the oceans and atmosphere during the MECO. These results are supported by carbon cycle modeling simulations, which highlights the fundamental importance of a variable weathering feedback strength in climate and carbon cycle interactions in Earth's history.

5.1 Introduction

The chemical weathering of silicate rocks represents a negative feedback mechanism that is generally considered to modulate atmospheric CO_2 levels and Earth's climate on geological timescales (Walker et al., 1981; Berner et al., 1983). This phenomenon has been studied for various carbon cycle perturbations and episodes of global warming in the geological past, including Pleistocene deglaciations, the Paleocene-Eocene Thermal Maximum (PETM; ~56 Ma) and the Cretaceous and Jurassic Oceanic Anoxic Events (OAEs), mainly through the application of isotope ratios of marine sediments that are sensitive to shifts in weathering fluxes or compositions on the appropriate timescales (Ravizza et al., 2001; Cohen et al., 2004; Pogge von Strandmann et al., 2013). For many of these phases, it is now relatively well established that enhanced continental weathering contributed to CO_2 drawdown and climatic recovery (Vance et al., 2009; Pogge von Strandmann et al., 2013; Dickson et al., 2015). However, the available data spanning the Middle Eocene Climatic Optimum (MECO; ~40 Ma) pose questions regarding the functioning of the weathering feedback (Sluijs et al., 2013). Over a period of ~500 kyr, global ocean temperatures rose gradually by up to ~5 °C in association with an increase in atmospheric CO_2 concentrations, sourced from a reservoir with a stable carbon isotopic composition ($\delta^{13}C$) close to that of the ocean (Bohaty and Zachos, 2003; Bohaty et al., 2009; Bijl et al., 2010; Boscolo Galazzo et al., 2014; Cramwinckel et al., 2018). Importantly, the inferred rise in atmospheric CO_2 and temperature over ~500 kyr during the MECO should have led to increased weathering and alkalinity supply to the oceans, but reconstructions show that the oceans acidified (Bohaty et al., 2009; Sluijs et al., 2013). Therefore, reconstructing the global weathering response during the MECO is instrumental to improving our fundamental

understanding of carbon cycle dynamics on such intermediate timescales of ~500 kyr (Sluijs et al., 2013).

A promising proxy to reconstruct changes in continental weathering during the MECO is the osmium isotope ratio of marine sediments at the time of deposition ($^{187}Os/^{188}Os_{initial}$, or Os_i) (Peucker-Ehrenbrink and Ravizza, 2000, 2012). The $^{187}Os/^{188}Os$ ratio of the global ocean is governed by the relative input of radiogenic Os ($^{187}Os/^{188}Os$ = ~1.4) through continental weathering of ancient crustal rocks, and the relative input of unradiogenic Os ($^{187}Os/^{188}Os$ = 0.13) through hydrothermal activity at mid-ocean ridges and weathering of fresh mantle-derived rocks, with additional contributions from extraterrestrial sources (Peucker-Ehrenbrink and Ravizza, 2000). Osmium is a quasi-conservative element that is well-mixed in the ocean and has a short oceanic residence time (generally ~10^4 yr in the open ocean, but residence times of ~10^3 yr have been inferred for very restricted settings; Peucker-Ehrenbrink and Ravizza, 2000; Rooney et al., 2016). Variations in the $^{187}Os/^{188}Os$ ratio of seawater are thus indicative of changes in continental weathering relative to the other sources on timescales shorter than, or similar to, climate and carbon cycle processes such as greenhouse warming, ocean acidification and carbonate compensation (Peucker-Ehrenbrink and Ravizza, 2000, 2012). Seawater Os is incorporated in the metalliferous and organic phases of marine sediments without isotopic fractionation, and remains a closed isotopic system from the time of deposition (Ravizza and Turekian, 1992; Cohen et al., 1999; Ravizza and Zachos, 2003). As such, Os_i values are calculated on the basis that radiogenic ^{187}Os ingrowth is derived solely from post-depositional ^{187}Re (rhenium) decay. Shifts to higher (radiogenic) Os_i values, which are attributed to a global increase in continental silicate weathering rates, have been recorded for carbon cycle perturbations such as the Toarcian OAE and the PETM and Eocene Thermal Maximum 2 (ETM2) transient global warming events (Cohen et al., 2004; Peucker-Ehrenbrink and Ravizza, 2012; Them et al., 2017).

A second parameter that is often used to constrain changes in continental weathering is the carbonate compensation depth (CCD). The CCD is the depth in the oceans at which carbonate delivery is balanced by carbonate dissolution, and is modulated by the interplay of volcanic CO_2 degassing, the weathering of silicate rocks and organic-rich sediments on land and the burial of marine carbonates and organic carbon (Ridgwell and Zeebe, 2005). As such, changes in the position of the CCD as reflected in sediments play a crucial role in reconstructions of carbon cycle change, both on multi-million year timescales and during transient perturbations such as the MECO (Pälike et al., 2012).

In this study, we present Os_i records of marine sediments from three locations in different ocean basins in combination with a compilation of published CCD records (Sluijs et al., 2013) to reconstruct global changes in continental weathering during the MECO. Rather than an Os_i increase expected from globally enhanced weathering, we document a modest global Os_i decrease during the MECO that may represent an episode of enhanced volcanism and/or associated basalt weathering. In fact, prolonged CCD shoaling precludes an increase in total continental weathering rates in response to CO_2 rise and greenhouse warming. We employ a series of simulations with the carbon cycle model LOSCAR (Zeebe, 2012a) together with an independent osmium cycle model to demonstrate that this combination of observations can only be successfully reconciled on MECO timescales by invoking enhanced volcanism together with a diminished continental weathering feedback. Finally, we surmise that such a reduced silicate weathering feedback may have resulted from a progressive decrease in the weatherability of the continents during the Eocene. A variable silicate weathering feedback

strength may have been important for other enigmatic climate and carbon cycle perturbations in Earth's history.

5.2 Methods

5.2.1 Sampling

The samples used in this study were derived from middle Eocene sedimentary units from three different sites: organic-rich sediments from ODP Site 959 in the equatorial Atlantic along the African continental margin, carbonate-rich pelagic sediments from ODP Site 1263 on the Walvis Ridge in the south Atlantic and carbonate-rich pelagic sediments from IODP Site U1333 in the equatorial Pacific (Supplementary Fig. 1). The total organic carbon (TOC) contents of these middle Eocene sediments range between 0.1 and 2 %, with the highest TOC abundances occurring at Site 959 (Wagner, 2002). Rock samples of 20 – 40 g were selected across the middle Eocene interval between approximately 42 and 38 Ma, with the highest sampling resolution across the MECO.

5.2.2 Analyses

Bulk samples were freeze-dried or oven-dried at 50 °C and subsequently powdered using a ceramic pestle and mortar, in order to homogenize the Re and Os within the samples. Contact with metal surfaces was avoided so as not to contaminate the sample set. All Re and Os isotope analyses were performed at the Laboratory for Source Rock and Sulfide Geochronology and Geochemistry, and the Arthur Holmes Laboratory at the Durham Geochemistry Centre, Durham University (UK). Samples were digested in a CrO_3-H_2SO_4 solution (0.25 g/g CrO_3 in 8 mL of 4N H_2SO_4) following the well-established methods of Selby and Creaser (2003), which have been shown to significantly limit the contribution of detrital Re and Os to the hydrogenous fraction bound to organic matter.

Powdered samples of approximately 0.3 – 1 g were loaded into Carius tubes with a known amount of ^{185}Re + ^{190}Os tracer solution (spike) and dissolved in 8 mL of CrO_3-H_2SO_4 solution. The Carius tubes were then sealed and heated in an oven at 220 °C for 48 hours. Osmium was isolated from the CrO_3-H_2SO_4 sample solution by using solvent extraction with chloroform ($CHCl_3$) and then back extracted by hydrobromic acid (HBr). The Os was further purified through micro distillation. Rhenium was isolated by evaporating 1 mL of the CrO_3-H_2SO_4 sample solution to dryness, followed by solvent extraction involving sodium hydroxide (NaOH) and acetone (C_3H_6O) (Li et al., 2009; Cumming et al., 2012). The Re was further purified by anion chromatography.

Following purification, the Re and Os fractions were loaded onto Ni and Pt filaments, respectively, together with 0.5 µL $BaNO_3$ and BaOH activator solutions, respectively (Selby and Creaser, 2003). Rhenium and osmium isotope ratios were determined by negative thermal ionization mass spectrometry (N-TIMS), using Faraday cups for Re and a Secondary Electron Multiplier (SEM) for Os in peak-hopping mode.

Re and Os isotope ratios were corrected for instrumental mass fractionation, as well as spike and blank contributions. Procedural blanks for Re and Os in this study were 12 ± 3 pg/g and 0.07 ± 0.05 fg/g, respectively, with an $^{187}Os/^{188}Os$ value of 0.25 ± 0.15 (n = 3). The $^{187}Re/^{188}Os$ and $^{187}Os/^{188}Os$ uncertainties (2σ) include full propagation of uncertainties in weighing, mass spectrometer measurements, spike calibrations, blank corrections and reproducibility of standards.

The $^{187}Os/^{188}Os_{initial}$ ratios (Os_i) were calculated by correcting for post-depositional ^{187}Re decay over time with the following equation:

$$^{187}Os/^{188}Os_{\text{initial}}\,(Os_{\text{i}}) = {}^{187}Os/^{188}Os_{\text{measured}} - {}^{187}Re/^{188}Os_{\text{measured}} * \left(e^{\lambda t} - 1\right) \quad (1)$$

where λ is the ^{187}Re decay constant ($1.666 \cdot 10^{-11}$ yr^{-1}; Smoliar et al., 1996) and t is the age of the rock. Given the high Re abundances in the organic-rich sediments from Site 959, we have used best estimates for the depositional ages of each of these samples. An age of 40 Ma was used for all samples from Sites 1263 and U1333, because improved age estimates would result in variations in Os_i values of 0.1 % or less on average. All results are listed in Supplementary Data 1. The Re-Os isotopic system is expected to have remained closed for the sample set, given that the cores were all fresh, unweathered, and showed no evidence of post-depositional events (e.g., veining, etc.). Further, where the Re-Os data has sufficient spread in isochron plot space to yield statistically robust isochrons, a geologically reasonable Re-Os isochron age is obtained (e.g., Site 959; see below for details).

5.2.3 Evaluation of Re and Os data

Although the studied samples were collected for evaluating changes in Os_i rather than establishing isochrons, the Re-Os data of the sediments from Site 959 show a positive correlation between $^{187}Re/^{187}Os$ and $^{187}Os/^{188}Os$, which results in an isochron age that is in good agreement with the age of the MECO between 40.5 and 40.0 Ma (Supplementary Fig. 2 and 3). In contrast, the $^{187}Re/^{187}Os$ and $^{187}Os/^{188}Os$ data for Sites 1263 and U1333 do not have sufficient spread in isochron plot space, and hence cannot yield statistically geologically meaningful age estimates.

5.2.4 Age models

We adopt the age model of Cramwinckel et al. (2018) for Site 959 (Supplementary Fig. 11). This is based on initial (Shafik et al., 1998) and recently improved (Cramwinckel et al., 2018) calcareous nannofossil biostratigraphy. The model also uses the long-term $^{187}Os/^{188}Os$ minimum at 34.65 Ma recorded at this site (Ravizza and Paquay, 2008), and TEX_{86} data that mark the MECO warming (Cramwinckel et al., 2018). Moreover, we use the highest TEX_{86} value during the MECO peak warming and the lowest TEX_{86} value at the onset of the MECO as reported by Cramwinckel et al. (2018) to tentatively correlate to minima and maxima in the $\delta^{18}O$ records of Bohaty et al. (2009), which were assigned ages of 40.06 and 40.52 Ma, respectively. Better age models are available for the other two sites. For Site 1263, we use a published age model (Bohaty et al., 2009) based on magnetostratigraphy and bulk carbonate $\delta^{18}O$ and $\delta^{13}C$ chemostratigraphy. For Site U1333, an astronomically calibrated magnetostratigraphic age model (Pälike et al., 2006) was used in combination with calcareous nannofossil events (Toffanin et al., 2013). All ages were adjusted to the framework of the GTS 2012 (Gradstein et al., 2012) and tie points for the age models are listed in Supplementary Tables 1, 2 and 3.

5.2.5 Calculating changes in Os fluxes across the MECO

The $^{187}Os/^{188}Os$ composition of seawater is controlled by the balance between input fluxes from continental, mantle-derived and extraterrestrial sources. However, the flux of extraterrestrial Os is generally assumed to be negligible and constant (Peucker-Ehrenbrink, 1996; Pegram and Turekian, 1999), so our Os_i records can be used to directly infer changes in relative

contributions of the continental and mantle-derived Os sources across the MECO. To evaluate an increase in the mantle-derived Os flux, we developed a progressive, two-component mixing model for the release of Os from mantle-derived basalts that incorporates both the Os abundance and $^{187}Os/^{188}Os$ composition of seawater and basalts. This model is an adaptation of the two-component mixing model for strontium (Sr) isotopes of Faure (1986; Equations (9.2) and (9.10)), with modifications to consider the larger range of Os isotope variations in comparison to Sr isotope variations.

From the relative molar concentrations of natural Os isotopes, we know:

$$\frac{[Os]-[^{187}Os]}{[^{188}Os]} = 7.4 \quad (2)$$

where $[Os]$ represents the molar concentration (in mol / kg) of total Os (i.e., $^{186}Os + ^{187}Os + ^{188}Os + ^{189}Os + ^{190}Os + ^{192}Os$), and $[^{187}Os]$ and $[^{188}Os]$ represent the molar concentrations (in mol / kg) of ^{187}Os and ^{188}Os, respectively (Li and Elderfield, 2013).

Equation (2) can be rewritten as:

$$[^{187}Os] = \frac{R}{7.4+R}[Os] \quad (3)$$

$$[^{188}Os] = \frac{1}{7.4+R}[Os] \quad (4)$$

where $R = [^{187}Os]/[^{188}Os]$.

Two-component mixing between seawater and basalts can then be expressed for both ^{187}Os and ^{188}Os as:

$$[^{187}Os]_{\mathrm{mix}} = \frac{[^{187}Os]_{\mathrm{sw}} * M_{\mathrm{sw}} + [^{187}Os]_{\mathrm{bas}} * M_{\mathrm{bas}}}{M_{\mathrm{sw}} + M_{\mathrm{bas}}} \quad (5)$$

$$[^{188}Os]_{\mathrm{mix}} = \frac{[^{188}Os]_{\mathrm{sw}} * M_{\mathrm{sw}} + [^{188}Os]_{\mathrm{bas}} * M_{\mathrm{bas}}}{M_{\mathrm{sw}} + M_{\mathrm{bas}}} \quad (6)$$

where M represents the mass of a component (in kg) and the subscripts *sw, bas* and *mix* represent seawater, basalts and the eventual mix between the two, respectively.

We now define:

$$\Delta M_{\mathrm{bas}} = \frac{M_{\mathrm{bas}}}{M_{\mathrm{sw,initial}}} \quad (7)$$

$$f = \frac{\Delta M_{\mathrm{bas}}}{M_{\mathrm{sw,progressive}} + \Delta M_{\mathrm{bas}}} = \frac{\Delta M_{\mathrm{bas}}}{M_{\mathrm{mix}}} \quad (8)$$

where ΔM_{bas} is an infinitesimal representing the mass of basalts added during a mixing step relative to the mass of seawater initially present, and f represents the amount of basalts added during a mixing step relative to the total amount of seawater and basalts present during progressive mixing (M_{mix}).

Equations (3) – (8) can then be combined as follows:

$$[^{187}Os]_{mix} = f * [^{187}Os]_{bas} + (1-f) * [^{187}Os]_{sw}$$

$$= f * \frac{R_{bas}}{7.4+R_{bas}}[Os]_{bas} + (1-f) * \frac{R_{sw}}{7.4+R_{sw}}[Os]_{sw} \quad (9)$$

$$[^{188}Os]_{mix} = f * [^{188}Os]_{bas} + (1-f) * [^{188}Os]_{sw}$$

$$= f * \frac{1}{7.4+R_{bas}}[Os]_{bas} + (1-f) * \frac{1}{7.4+R_{sw}}[Os]_{sw} \quad (10)$$

Finally, dividing equation (9) by equation (10) yields:

$$R_{mix} = \frac{[^{187}Os]_{mix}}{[^{188}Os]_{mix}} = \frac{f*\frac{R_{bas}}{7.4+R_{bas}}[Os]_{bas}+(1-f)*\frac{R_{sw}}{7.4+R_{sw}}[Os]_{sw}}{f*\frac{1}{7.4+R_{bas}}[Os]_{bas}+(1-f)*\frac{1}{7.4+R_{sw}}[Os]_{sw}} \quad (11)$$

where R is the $^{187}Os/^{188}Os$ composition of the corresponding components (i.e., seawater, basalts and the eventual mix between the two).

Equations (7) – (11) can then be used to estimate the extent of mixing between seawater and basalts during the MECO by progressively calculating R_{mix} until our observed Os_i shift is reproduced (see Supplementary Data 2). We assumed the pre-MECO $^{187}Os/^{188}Os$ ratio of seawater to be ~0.55 based on an average of pre-MECO Os_i values recorded for the three sites and the Os concentration of seawater to be 10 ppq (~53 fmol / kg, similar to present-day values) (Peucker-Ehrenbrink and Ravizza, 2000). Furthermore, we used an $^{187}Os/^{188}Os$ ratio of 0.13 for the mantle and mantle-derived basalts (Martin, 1991; Meisel et al., 2001), as well as an Os abundance of 1 ppt (~5.3 pmol / kg) for basalts (Martin, 1991). Finally, we assumed that the maximum amount of basalt that can theoretically be added to seawater represents ~1 % of the total mass of the ocean, as estimated for OAE2 (Hauff et al., 2000; Du Vivier et al., 2014), and used increments of 0.01 % for the value of ΔM_{bas}.

Based on an Os_i shift of 0.05 from the pre-MECO value of ~0.55 to a peak MECO value of ~0.50, we calculated a relative increase in the mantle-derived Os flux of ~13 % across the event, which would equal the addition of Os from basalts with a mass of ~0.13 % relative to the total mass of the ocean (Supplementary Data 2). Similar results are obtained if we estimate the relative increase in the ^{188}Os flux, rather than the total Os flux. It is important to note that mantle-derived Os could also have been released to seawater through direct addition from magmatic degassing or hydrothermal inputs instead of basalt dissolution, but regardless of the mechanism, a ~13 % increase in the mantle-derived Os flux during the MECO would be sufficient to reproduce our observed Os_i shift and would correspond to the cumulative release of ~9.4×10^6 mol of mantle-derived Os. We also performed our calculations with the Os_i values of each individual site: for Site 959, an Os_i shift from 0.560 to 0.505 would yield a relative

increase in the mantle-derived Os flux of ~14 %; for Site 1263, an Os_i shift from 0.530 to 0.485 would yield an increase of ~12 %; for Site U1333, an Os_i shift from 0.515 to 0.460 would yield an increase of ~16 %. These differences are most likely to be attributed to the resolution of our records. To accommodate for this range of flux estimates, we adopted a best estimate of 10 – 15 % for the increase in the mantle-derived Os flux during the MECO, but also explored the effects of an increase of up to 20 % because we are unlikely to have sampled the lowest Os_i values in any of our records due to the relatively low resolution of our dataset.

5.2.6 LOSCAR and Os cycle modeling

Carbon cycle simulations were performed using the Long-term Ocean-atmosphere-Sediment CArbon cycle Reservoir (LOSCAR) model (Zeebe, 2012a). In this box model, modified from Walker and Kasting (1992), carbon and several other biogeochemical tracers (e.g. alkalinity, phosphate, oxygen) are cycled through atmospheric and oceanic reservoirs. The model ocean is coupled to a sediment module and consists of surface-, intermediate- and deep-water boxes of the four main Paleogene ocean basins (Atlantic, Indian, Pacific and Tethys). The model is designed to simulate the Paleocene-Eocene Thermal Maximum (PETM) at 56 Ma, but the minor changes in paleogeography compared to the middle Eocene at 40 Ma are not of relevance to the simple LOSCAR model. In these simulations, we use default parameter settings for the Paleogene setup. Equilibrium pCO_2 is set at 750 ppm, consistent with pCO_2 estimates based on planktic foraminifer boron isotope ratios ($\delta^{11}B$) (Anagnostou et al., 2016), and by default, silicate and carbonate weathering are implemented in the model as a feedback response to atmospheric CO_2 concentrations. The CCD definition follows the default LOSCAR setup and is taken as the sediment depth level at which sedimentary $CaCO_3$ contents fall below 10 wt %.

We explored the effects of changes in volcanism and/or continental weathering with the constraints from our Os_i records to assess which scenario is able to reproduce a more realistic MECO target. We first simulated several scenarios with a gradual, linear increase in the volcanic CO_2 flux (+10%, +15% and +20%) over ~500 kyr, either while allowing the silicate and carbonate weathering fluxes to vary in response to CO_2 forcing (Supplementary Fig. 4) or while maintaining these weathering fluxes at constant values (Supplementary Fig. 5). Subsequently, we performed several simulations invoking silicate weathering as a forcing rather than a feedback, by prescribing a gradual, linear decrease in the silicate weathering flux (-10%, -15% and -20%) over ~500 kyr, while keeping the volcanic CO_2 flux and the carbonate weathering flux at constant values (Supplementary Fig. 6). Finally, we tested the effect of an increase in volcanism (+5%) combined with a decrease in silicate weathering (-5%) (Supplementary Fig. 7); the effect of a combined decrease in silicate and carbonate weathering (both -10%) (Supplementary Fig. 8); and the effect of a decrease in silicate weathering (-10%) while maintaining a carbonate weathering feedback (Supplementary Fig. 9). For an overview of all model scenarios, see Supplementary Table 4.

In order to demonstrate that our LOSCAR model simulations are consistent with the Os_i records, the scenarios outlined above were also applied to a separate box model of the Os cycle. This Os cycle model is inspired by the work of Richter and Turekian (1993) and many subsequent studies, including Peucker-Ehrenbrink and Ravizza (2000). We fully derive the equations used to model the Os cycle in the ocean below.

We first define N as the total molar inventory of Os (including all Os isotopes) in seawater, and ^{187}N and ^{188}N as the molar inventories of ^{187}Os and ^{188}Os in seawater, respectively. The ^{187}Os/^{188}Os composition of seawater (R_{sw}) is thus expressed as:

$$R_{\mathrm{sw}} = \frac{^{187}N}{^{188}N} \quad (12)$$

Subsequently, changes in R_{sw} over time can be written as:

$$\frac{dR_{\mathrm{sw}}}{dt} = \frac{d}{dt}\left(\frac{^{187}N}{^{188}N}\right) = \frac{^{188}N\frac{d^{187}N}{dt} - {}^{187}N\frac{d^{188}N}{dt}}{(^{188}N)^2} = \frac{1}{^{188}N}\left[\frac{d^{187}N}{dt} - R_{\mathrm{sw}}\frac{d^{188}N}{dt}\right] \quad (13)$$

Multiplying equation (13) by ^{188}N gives:

$$^{188}N\,\frac{dR_{\mathrm{sw}}}{dt} = \frac{d^{187}N}{dt} - R_{\mathrm{sw}}\frac{d^{188}N}{dt} \quad (14)$$

Changes in N, ^{187}N and ^{188}N over time can then be written as follows:

$$\frac{dN}{dt} = F_{\mathrm{riv}} + F_{\mathrm{hyd}} + F_{\mathrm{ext}} - F_{\mathrm{sed}} \quad (15)$$

$$\frac{d^{187}N}{dt} = F_{\mathrm{riv}}\left(\frac{[^{187}Os]}{[Os]}\right)_{\mathrm{riv}} + F_{\mathrm{hyd}}\left(\frac{[^{187}Os]}{[Os]}\right)_{\mathrm{hyd}} + F_{\mathrm{ext}}\left(\frac{[^{187}Os]}{[Os]}\right)_{\mathrm{ext}} - F_{\mathrm{sed}}\left(\frac{[^{187}Os]}{[Os]}\right)_{\mathrm{sed}} \quad (16)$$

$$\frac{d^{188}N}{dt} = F_{\mathrm{riv}}\left(\frac{[^{188}Os]}{[Os]}\right)_{\mathrm{riv}} + F_{\mathrm{hyd}}\left(\frac{[^{188}Os]}{[Os]}\right)_{\mathrm{hyd}} + F_{\mathrm{ext}}\left(\frac{[^{188}Os]}{[Os]}\right)_{\mathrm{ext}} - F_{\mathrm{sed}}\left(\frac{[^{188}Os]}{[Os]}\right)_{\mathrm{sed}} \quad (17)$$

where F represents the fluxes of Os (in mol / yr) from and to various reservoirs and the subscripts *sw, riv, hyd, ext* and *sed* represent seawater, riverine, hydrothermal, extraterrestrial and sediment reservoirs, respectively (Richter and Turekian, 1993; Peucker-Ehrenbrink and Ravizza, 2000).

Substituting equations (3) and (4) into equations (16) and (17), respectively, yields:

$$\frac{d^{187}N}{dt} = F_{\mathrm{riv}}\frac{R_{\mathrm{riv}}}{7.4+R_{\mathrm{riv}}} + F_{\mathrm{hyd}}\frac{R_{\mathrm{hyd}}}{7.4+R_{\mathrm{hyd}}} + F_{\mathrm{ext}}\frac{R_{\mathrm{ext}}}{7.4+R_{\mathrm{ext}}} - F_{\mathrm{sed}}\frac{R_{\mathrm{sed}}}{7.4+R_{\mathrm{sed}}} \quad (18)$$

$$\frac{d^{188}N}{dt} = F_{\mathrm{riv}}\frac{1}{7.4+R_{\mathrm{riv}}} + F_{\mathrm{hyd}}\frac{1}{7.4+R_{\mathrm{hyd}}} + F_{\mathrm{ext}}\frac{1}{7.4+R_{\mathrm{ext}}} - F_{\mathrm{sed}}\frac{1}{7.4+R_{\mathrm{sed}}} \quad (19)$$

Finally, substituting equations (18) and (19) into equation (14) and combining with equation (4) results in:

$$\frac{N}{7.4+R_{\mathrm{sw}}}\frac{dR_{\mathrm{sw}}}{dt} = F_{\mathrm{riv}}\frac{R_{\mathrm{riv}}-R_{\mathrm{sw}}}{7.4+R_{\mathrm{riv}}} + F_{\mathrm{hyd}}\frac{R_{\mathrm{hyd}}-R_{\mathrm{sw}}}{7.4+R_{\mathrm{hyd}}} + F_{\mathrm{ext}}\frac{R_{\mathrm{ext}}-R_{\mathrm{sw}}}{7.4+R_{\mathrm{ext}}} - F_{\mathrm{sed}}\frac{R_{\mathrm{sed}}-R_{\mathrm{sw}}}{7.4+R_{\mathrm{sed}}} \quad (20)$$

which relates changes in R_{sw} over time to the fluxes of total Os (F), the $^{187}Os/^{188}Os$ compositions of these fluxes (R) and the amount of total Os in the ocean (N). Because there is no isotopic fractionation associated with Os burial (i.e., $R_{sed} = R_{sw}$), the net effect of the sedimentary Os flux (F_{sed}) in equation (20) is zero.

Together, equations (15) and (20) can be used to simulate any transient perturbation of the Os cycle. We first constructed a steady state model based on flux estimates and $^{187}Os/^{188}Os$ values for the present-day Os cycle with a $^{187}Os/^{188}Os$ ratio of seawater of 1.06 (see Supplementary Table 5). For the middle Eocene Os cycle, we assumed that the total Os inventory and the total input and output fluxes of Os are similar to present-day values, and recalculated the steady state riverine and hydrothermal Os fluxes for the pre-MECO $^{187}Os/^{188}Os$ ratio of seawater of 0.55 by assuming that the $^{187}Os/^{188}Os$ composition of these fluxes has remained unchanged. Subsequently, we used scaled silicate weathering and volcanic degassing fluxes from the LOSCAR model simulations to force our model of the Os cycle. The modeled changes in the $^{187}Os/^{188}Os$ ratio of seawater are included in the respective figures of all model scenarios (Fig. 3 of the main text and Supplementary Fig. 4 – 9). The full code used to perform the Os cycle model simulations is included as an R script in the Supplementary Software.

5.3 Results

5.3.1 Middle Eocene osmium isotope records

We present Re-Os data and Os_i values for middle Eocene sediments from Ocean Drilling Program (ODP) Site 959 in the equatorial Atlantic along the African continental margin, ODP Site 1263 on the Walvis Ridge in the South Atlantic, and Integrated Ocean Drilling Program (IODP) Site U1333 in the equatorial Pacific (Fig. 1; Supplementary Data 1; Supplementary Fig. 1 – 3). The Re and Os abundances are significantly enriched in the relatively organic-rich, siliceous sediments of Site 959 (Re = 10 – 60 ppb, Os = 100 – 300 ppt) relative to the carbonate-rich pelagic sediments of Sites 1263 and U1333 (Re = 0.02 – 0.2 ppb, Os = 10 – 40 ppt). The abundances of ^{192}Os, the Os isotope best representing the amount of hydrogenous Os chelated by organic matter at the time of deposition (Cohen and Coe, 2002), increase slightly over the study interval at Site 959, but are essentially stable at the other two sites (Fig. 1). We calculate Os_i values of 0.46 to 0.60 at all study sites (Fig. 1), which is in good agreement with previously published middle Eocene Os_i values from Site 959 sediments (Ravizza, 1998; Ravizza and Paquay, 2008) and with Os_i values from ferromanganese crusts that document a progressive increase in the $^{187}Os/^{188}Os$ composition of seawater during the Cenozoic (Klemm et al., 2005; Burton, 2006; Nielsen et al., 2009) (Fig. 2).

At Site 959, the Os_i values range between approximately 0.56 and 0.60 for most of the middle Eocene study interval, with the exception of a decrease to 0.51 during the MECO at ~580 mbsf (Fig. 1). Importantly, the lack of an increase in the Os_i values during the MECO implies that weathering rates of felsic silicate rocks did not increase in response to CO_2 rise and accompanied warming, while such an increase would be expected from theory and published Os_i records from analogous carbon cycle perturbations (Ravizza et al., 2001; Peucker-Ehrenbrink and Ravizza, 2012; Dickson et al., 2015) (Fig. 2b). Furthermore, the relative invariability of both the Os_i records and the ^{192}Os abundances – which scale to organic matter content – implies that the balance of Os fluxes to the oceans and uptake of Os in sedimentary organic matter did not appreciably change during the MECO.

Although the magnitude of the negative Os_i shift at Site 959 is small (~0.05), it exceeds the maximum analytical uncertainty (2σ = 0.01) by a factor of 5. The shift starts at the onset of MECO warming and is also present at Sites 1263 and U1333, where it is similar in magnitude (Fig. 1 and 2). Interestingly, the Os_i profile of Site U1333 is characterized by two separate excursions to lower, less radiogenic values rather than the gradual and continuous decrease that is observed at Site 959. The Os_i profile at Site 1263 shows trends intermediate to Sites 959 and U1333. Nevertheless, the lowest Os_i values in all three records occur towards the end of the MECO, which is coincident with the peak warming phase (Bohaty et al., 2009). In addition, the return towards pre-MECO values is synchronous with the termination of the MECO at all three sites, implying that the Os_i shift lasted for the entire duration of the event (~500 kyr). The absolute Os_i values differ slightly between sites, likely because of differences in coastal proximity and oceanographic setting (Paquay and Ravizza, 2012; Du Vivier et al.,

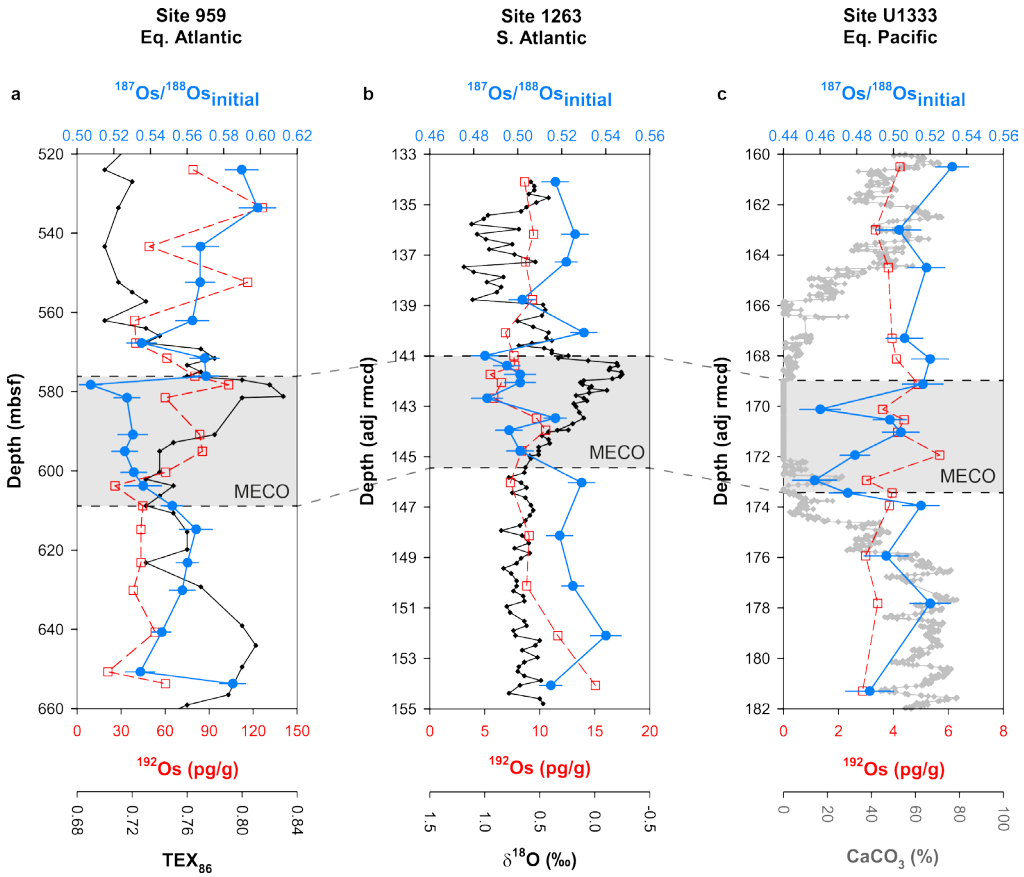

Figure 1: Os_i values (in blue) and ^{192}Os concentrations (in red) for the analyzed middle Eocene sediments from the three different sites. a, ODP Site 959; b, ODP Site 1263; c, IODP Site U1333. The MECO interval is defined based on TEX_{86} values for Site 959 (in black; Cramwinckel et al., 2018) and bulk carbonate stable oxygen isotope ratios ($\delta^{18}O$) for Site 1263 (in black; Bohaty et al., 2009). The MECO is characterized by low carbonate content at Site U1333 (in grey; Westerhold et al., 2014). The error bars indicate fully propagated analytical uncertainties (2σ).

2014). However, the general timing and magnitude of the Os_i shift are reproduced at all sites, indicating that the Os_i shift records a change in the $^{187}Os/^{188}Os$ composition of the global ocean. The global character and synchroneity of the Os_i shift at the end of the MECO also indicate that osmium isotope stratigraphy is a promising tool for correlation of the event between sites in future studies (Fig. 2a).

In principle, the modest negative Os_i shift during the MECO may be caused by an increase in the unradiogenic Os flux from hydrothermal and/or extraterrestrial sources, a decrease in the radiogenic Os flux from continental weathering, or a decrease in the $^{187}Os/^{188}Os$ composition of the continental weathering flux through a transient change in the exposure of different rock types such as basalts (Dickson et al., 2015). There is no evidence for an extraterrestrial impact during the MECO. Furthermore, a reduction in continental silicate weathering rates during an episode of greenhouse warming seems paradoxical and unlikely, even though our Os_i records clearly show no evidence of the expected increase in continental weathering. It is difficult to exclude a warming-induced change in regional climates and precipitation patterns – which could have affected the contributions of rock types with different $^{187}Os/^{188}Os$ compositions to the continental weathering flux (Ravizza et al., 2001; Elsworth et al., 2017) – as a cause for the Os_i shift. However, this would still require a different cause for MECO warming.

Finally, the Os_i shift could reflect a short-lived increase in mid-ocean ridge hydrothermal activity or an episode of increased volcanism and associated weathering of mafic silicate rocks (Cohen and Coe, 2002; Ravizza and Peucker-Ehrenbrink, 2003; Turgeon and Creaser, 2008). Mass balance calculations with a progressive two-component mixing model that involves seawater and basalts (see Methods; Supplementary Data 2) show that the Os_i shift across the MECO may correspond to a 10 – 15 % increase in the contribution of the mantle-derived Os flux relative to the continental Os flux. Although there is no indication for the emplacement of a large igneous province during the middle Eocene (Sluijs et al., 2013), an episode of volcanic activity at mid-ocean ridges or on land could have increased the Os flux from basalts and consequently resulted in a decrease of the $^{187}Os/^{188}Os$ composition of the oceans that is consistent with our Os_i records. Moreover, enhanced volcanism would provide a mechanism for the atmospheric CO_2 rise that has been inferred for the MECO (Bijl et al., 2010; Sluijs et al., 2013), perhaps similar to the Late Cretaceous episode of greenhouse warming associated with volcanic eruptions from the Deccan Traps (Ravizza and Peucker-Ehrenbrink, 2003; Robinson et al., 2009; Henehan et al., 2016). Potential events that have been dated at approximately the right age in the middle Eocene include (1) a pulse of metamorphic decarbonation associated with Himalayan uplift and metamorphism (Kerrick and Caldeira, 1993, 1999), (2) increased arc volcanism around the Pacific rim (Cambray and Cadet, 1996) and especially in the Caribbean, related to an ignimbrite flare-up in the Sierra Madre Occidental of Mexico (McDowell and Mauger, 1994; Sigurdsson et al., 2000; Aguirre-Díaz and Labarthe-Hernández, 2003), (3) an episode of magmatism in the East African Rift zone (Bailey, 1992), in particular in Southern Ethiopia and Northern Kenya (George et al., 1998; Rooney, 2017), and/or (4) mid-ocean ridge volcanism in the North Atlantic, due to rifting in East Greenland and activity of the Iceland hotspot (Torsvik and Cocks, 2005; Mjelde et al., 2008; Torsvik et al., 2015). However, the timing and magnitude of these events are at present not sufficiently well resolved to establish a direct causal link with the MECO. Additionally, it is unclear if increased Himalayan uplift and metamorphism would be compatible with the observed negative Os_i shift, as the Himalayas are generally considered to contribute relatively radiogenic Os to the continental weathering flux

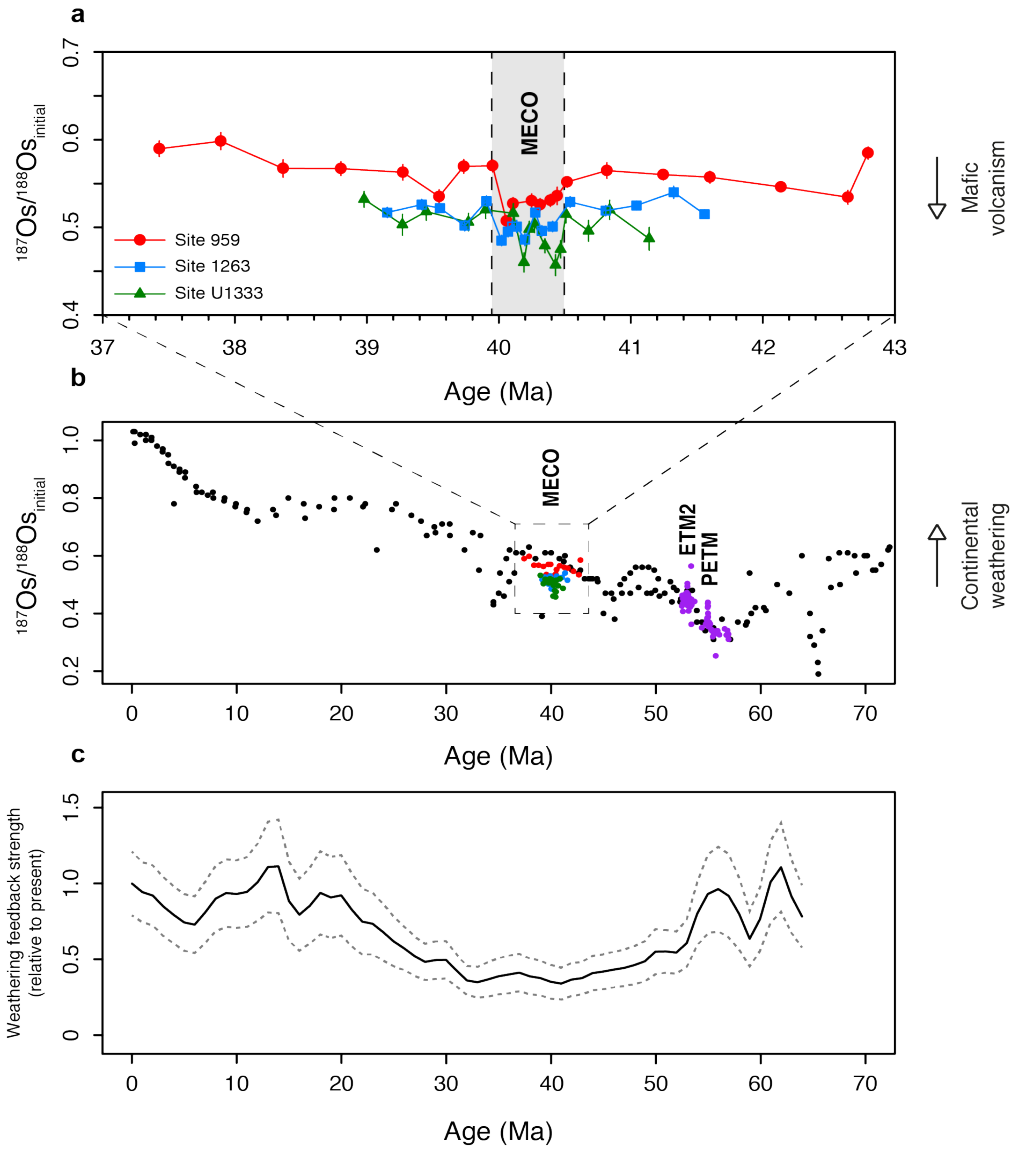

Figure 2: Comparison of Os_i records from the MECO with Os_i records from the PETM and ETM2, shown against the overall Os_i evolution of the Cenozoic and the relative weathering feedback strength of the Cenozoic. a, MECO data from Site 959 (in red), Site 1263 (in blue) and Site U1333 (in green) plotted against age (GTS 2012; Gradstein et al., 2012). See Methods for discussion of the age models for the study sites. b, MECO data from Sites 959, 1263 and U1333 (this study); PETM and ETM2 data from DSDP Site 549 (in purple) as published in Peucker-Ehrenbrink and Ravizza (2012); Cenozoic data from ferromanganese crusts D11 and CD29 (in black) as published in Klemm et al. (2005) and Burton (2006), respectively, based on the updated age model of Nielsen et al. (2009). c, Model estimates of the relative continental weathering feedback strength of the Cenozoic as published in Caves et al. (2016), based on their CO_2 scenario 1 and a logarithmic expression for the weathering feedback.

(Singh et al., 1999; Pierson-Wickmann et al., 2000). Yet, the effects of Himalayan uplift and subsequent weathering on the Cenozoic Os_i record are likely small (Sharma et al., 1999; Paul et al., 2010).

5.3.2 Carbon and osmium cycle modeling

Enhanced volcanism and/or hydrothermal activity may represent the most parsimonious scenario to explain the modest negative Os_i shift and atmospheric CO_2 rise during the MECO. However, a strong silicate weathering response to greenhouse warming through focused weathering of fresh basalts is in disagreement with the extensive carbonate dissolution observed in deep ocean basins (Bohaty et al., 2009; Sluijs et al., 2013). Therefore, total continental weathering fluxes must have remained approximately constant during the event. Collectively, the available data indicate that CO_2 was added to the ocean-atmosphere system through enhanced volcanism, leading to warming, but was not neutralized through the silicate weathering feedback, leading to sustained ocean acidification.

To test the plausibility of scenarios involving enhanced volcanism and/or diminished continental weathering during the MECO, we performed a series of carbon cycle simulations with the box model LOSCAR (Zeebe, 2012a) by prescribing fluxes with the transient shift that is inferred from our Os_i records (see Methods; Fig. 3; Supplementary Fig. 4 – 9). For consistency, we have also modeled the $^{187}Os/^{188}Os$ composition of the global ocean by applying the same LOSCAR carbon cycle fluxes as forcing to a box model of the Os cycle (see Methods; Supplementary Software). In addition to a ~0.05 decrease in the $^{187}Os/^{188}Os$ ratio of seawater, our target scenario for the MECO involves a rise in atmospheric CO_2 concentrations, a slight increase in the $\delta^{13}C$ of dissolved inorganic carbon (DIC) in the deep ocean and a shoaling of the carbonate compensation depth (CCD) over ~500 kyr (Sluijs et al., 2013). Since there are no high-resolution pCO_2 records available for the MECO, the target scenario includes an approximate doubling of atmospheric CO_2 concentrations relative to middle Eocene background values of 500 – 1000 ppmv (Bijl et al., 2010; Anagnostou et al., 2016). Furthermore, the magnitude of CCD change during the event possibly varied between the different ocean basins (Bohaty et al., 2009), so we incorporate a conservative estimate of at least 500 m shoaling in the Atlantic and Pacific in our target scenario.

All model simulations result in a decrease in the $^{187}Os/^{188}Os$ ratio of seawater (Fig. 3; Supplementary Fig. 4 – 9). Although a gradual, linear increase in volcanism of 10 – 20 % over ~500 kyr is sufficient to cause CO_2 accumulation in the ocean-atmosphere system and hence global warming on MECO timescales, this scenario results in a deepening of the CCD instead of the observed shoaling (Fig. 3; Supplementary Fig. 4) (Bohaty et al., 2009; Sluijs et al., 2013). A similar behavior of the CCD is observed in previous LOSCAR simulations of the MECO (Sluijs et al., 2013) and the Late Cretaceous warming episode (Henehan et al., 2016). Crucially, the model is only able to reproduce CO_2 rise in conjunction with shoaling of the CCD on these timescales if we invoke enhanced volcanism together with a diminished weathering feedback by maintaining the silicate and carbonate weathering fluxes constant (Fig. 3; Supplementary Fig. 5). Although the magnitude of this modeled CCD response is smaller than the shoaling inferred from deep-sea carbonate records (Bohaty et al., 2009; Sluijs et al., 2013), we note that the model may underestimate CCD changes because it does not account for the additional effects of biological carbonate compensation (Luo et al., 2016). Such a reduction in net carbonate production resulting from ocean acidification might amplify the CCD response for a given CO_2 rise. In all scenarios, the model reproduces the modest increase in deep-sea

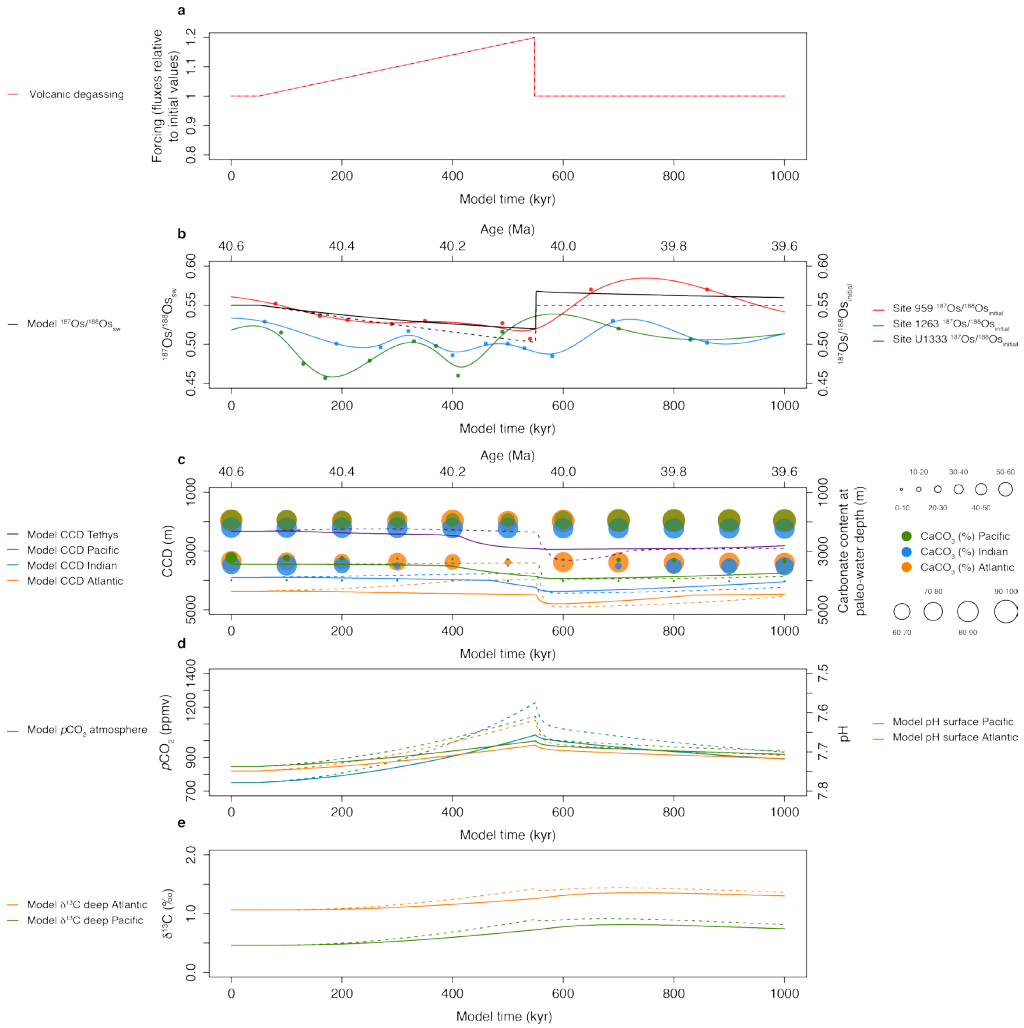

Figure 3: LOSCAR and Os cycle model simulations of the most likely MECO scenario. a, Forcing for two scenarios involving a gradual, transient 20 % increase in the volcanic CO_2 flux over ~500 kyr. The solid lines represent a scenario in which the silicate and carbonate weathering fluxes are allowed to vary in response to CO_2 forcing (normal weathering feedback), while the dashed lines represent a scenario in which these weathering fluxes are kept constant (diminished weathering feedback). Only the latter scenario corresponds to all observations. b, Model response in the $^{187}Os/^{188}Os$ composition of the global ocean, shown against smoothed fits to the MECO Os_i records from the study sites. c, Model CCD response of different ocean basins, shown against carbonate content (wt %) records for different depths in the Atlantic, Indian and Pacific oceans as compiled by Sluijs et al. (2013). d, Model atmospheric pCO_2 response and pH response for the surface Atlantic and Pacific oceans. e, Model $\delta^{13}C$ response for the DIC of the deep Atlantic and Pacific oceans. For a full description of the LOSCAR model, see Zeebe (2012a).

benthic foraminifer $\delta^{13}C$ values during the event (Bohaty and Zachos, 2003; Bohaty et al., 2009) because of a resulting decrease in carbonate versus constant organic carbon burial. Finally, the relatively rapid termination of the MECO is forced by a recovery of silicate weathering. We note that this does not need to represent a pronounced tectonic event, as the absolute magnitude of the flux imbalances is relatively small, but regionally enhanced weathering in the aftermath of the MECO would be consistent with observations from the Tethys region (Spofforth et al., 2010).

5.4 Discussion

To reconcile our Os_i records and model results with global warming and atmospheric CO_2 rise on MECO timescales (Bohaty and Zachos, 2003; Bohaty et al., 2009; Bijl et al., 2010; Sluijs et al., 2013), we hypothesize that a long-term reduction in the strength of the negative silicate weathering feedback occurred in the Eocene (Maher and Chamberlain, 2014; Caves et al., 2016), due to a progressive reduction in the weatherability of the continents – the sum of all factors affecting chemical weathering other than climate (Kump and Arthur, 1997; Kump et al., 2000). For millions of years prior to the MECO, the Earth was generally characterized by high atmospheric CO_2 levels (Anagnostou et al., 2016) and very warm climates (Zachos et al., 2008) (Supplementary Fig. 10), as well as flat continental relief. Thick, cation-depleted soils developed and transport-limited weathering regimes prevailed (West et al., 2005; Froelich and Misra, 2014), and consequently the weatherability of Earth's surface may have gradually decreased over the course of the Eocene. Indeed, such a progressive reduction in weathering feedback strength during the Eocene has been inferred from inverse modeling simulations of weathering fluxes based on Cenozoic pCO_2 and $\delta^{13}C$ records (Caves et al., 2016) (Fig. 2c). With the strength of the weathering feedback strongly diminished, a small increase in volcanism or hydrothermal activity would lead to the accumulation of large amounts of CO_2 in the ocean-atmosphere system, resulting in prolonged warming and ocean acidification during the MECO.

Changes in weatherability have also been suggested to explain other episodes of apparent decoupling between silicate weathering and climate (Kump et al., 2000), for example during major glaciations in the Paleozoic and Neoproterozoic (Kump et al., 1999; Mills et al., 2011; Goddéris et al., 2017). Our interpretations of a limited weathering response during the MECO suggest that a variable silicate weathering feedback strength (Caves et al., 2016) can indeed act as a driver for sustained global warming on geological timescales, with potential importance to other enigmatic phases of carbon cycle change in Earth's history. Moreover, a variable weathering feedback strength governed by the interplay between tectonics, climate and the weatherability of the continents fundamentally challenges the parameterization of the silicate weathering feedback in carbon cycle models, especially those used to model transient perturbations such as the OAEs and the PETM. We therefore argue that future studies of these events should focus on exploring changes in temperature, atmospheric CO_2 and the CCD in conjunction with the strength of the weathering feedback.

Acknowledgements

This research used samples provided by the Ocean Drilling Program (ODP) and Integrated Ocean Drilling Program (IODP). This work was carried out under the program of the Netherlands Earth System Science Centre (NESSC), which is financially supported by the Ministry of Education, Culture and Science (OCW) of the Netherlands. D.S. acknowledges support of the Total endowment fund and the Dida Scholarship of CUG Wuhan. Y.L. thanks

Alan Rooney (Yale University) for intellectual freedom and a grant (SKL-K201706) from the Institute of Geology and Geophysics, Chinese Academy of Sciences. We thank Richard Zeebe (University of Hawai'i) for discussions on LOSCAR modeling, Antonia Hofmann, Geoff Nowell and Chris Ottley (Durham University) and Natasja Welters and Arnold van Dijk (Utrecht Geolab) for laboratory assistance, and Andy Ridgwell and two anonymous reviewers for constructive comments that significantly improved the manuscript.

Author contributions

R.v.d.P., S.M.B., J.J.M. and A.S. designed the study. R.v.d.P. and D.S. generated the osmium isotope records, M.J.C. performed the carbon cycle simulations, R.v.d.P. and Y.L. conducted the osmium cycle modeling and all authors contributed to data interpretation. R.v.d.P. wrote the manuscript with input from all authors.

Data availability

The authors declare that all data supporting the results of this study are available in the Supplementary Information files associated with this manuscript.

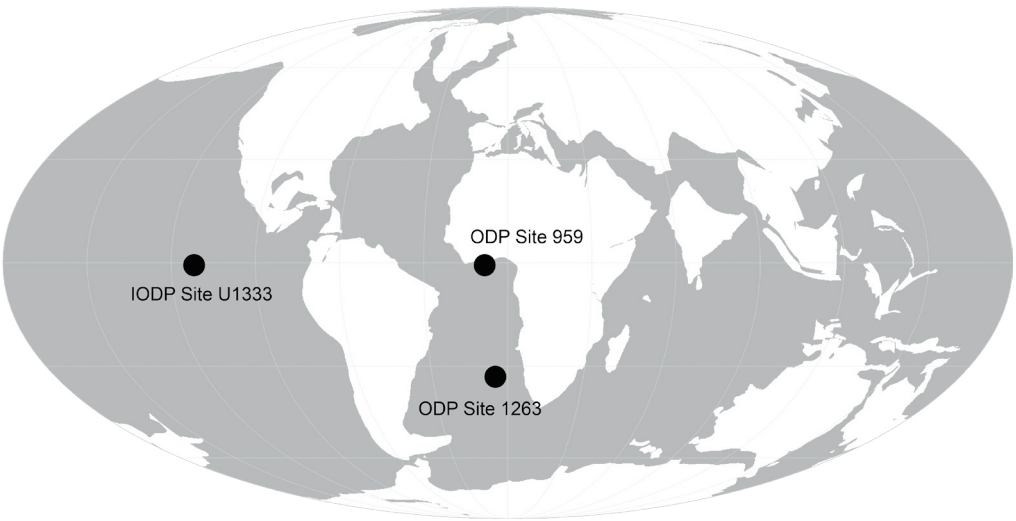

Supplementary Figure 1: Paleogeographic reconstruction of 40 Ma showing the estimated locations of the study sites. Shown are ODP Site 959 in the equatorial Atlantic along the African continent, ODP Site 1263 on the Walvis Ridge in the south Atlantic and IODP Site U1333 in the equatorial Pacific. The map was made with GPlates, based on the tectonic reconstructions of Seton et al. (2012) and the paleomagnetic reference frame of Torsvik et al. (2012).

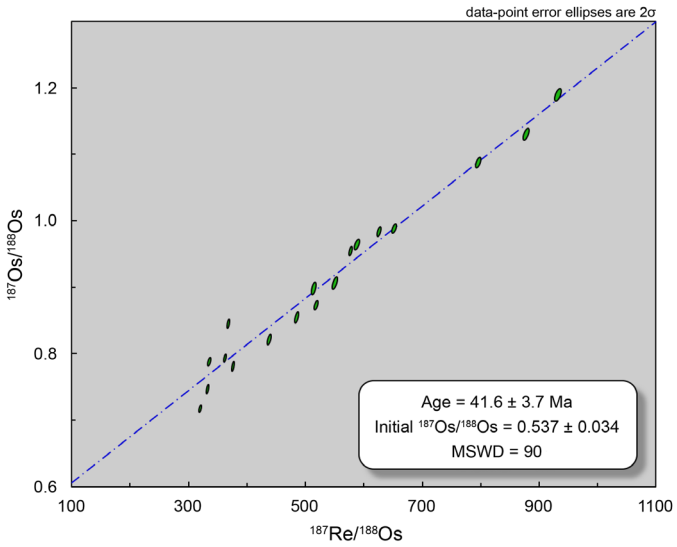

Supplementary Figure 2: Re-Os isochron plot of all Site 959 samples. The significant scatter (MSWD = 90) is best explained by the sample set possessing slightly variable initial $^{187}Os/^{188}Os$ compositions and being deposited over a prolonged interval of time (i.e., several Myr).

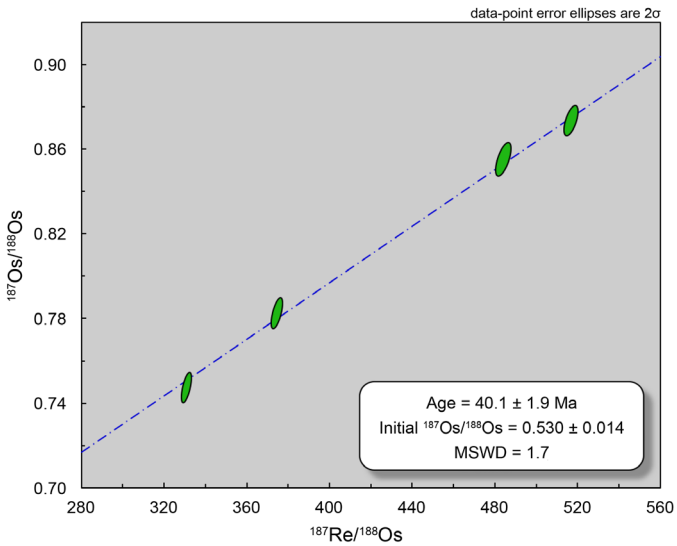

Supplementary Figure 3: Re-Os isochron plot of Site 959 samples in the MECO interval between 600.35 and 581.51 mbsf. These samples were selected because they were deposited in a short time interval (i.e., ~500 kyr), and yield virtually identical initial $^{187}Os/^{188}Os$ compositions. The obtained isochron age of 40.1 Ma is in excellent agreement with the estimated ages of these samples – between 40.4 and 40.1 Ma – based on our age model for Site 959.

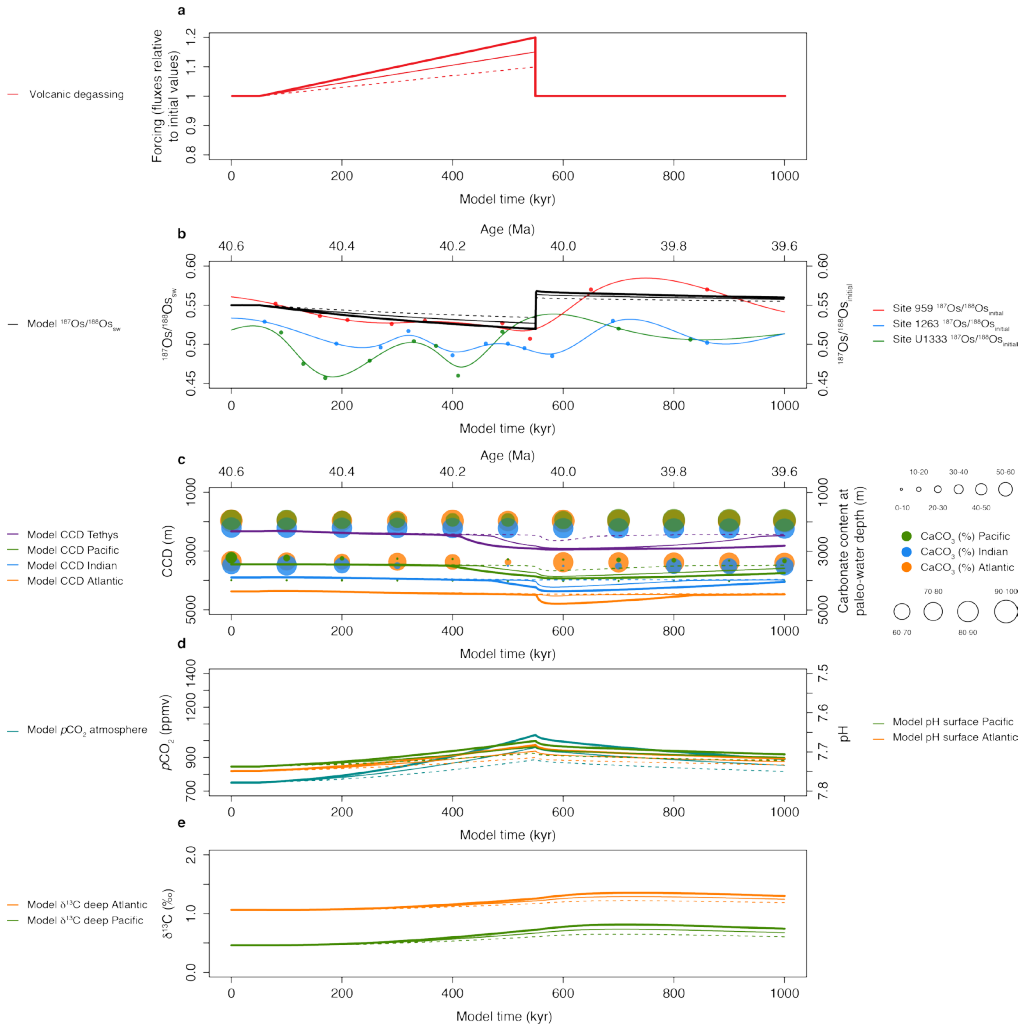

Supplementary Figure 4: LOSCAR and Os cycle model simulations of the MECO. a, Forcing for three scenarios involving a transient increase in the volcanic CO_2 flux of 10% (dashed lines), 15% (thin solid lines) and 20% (thick solid lines) over ~500 kyr, while allowing the silicate and carbonate weathering fluxes to vary as a feedback response. b, Model response in the $^{187}Os/^{188}Os$ composition of the global ocean, shown against smoothed fits to the MECO Os_i records from the study sites. c, Model CCD response of different ocean basins, shown against carbonate content (wt %) records for different depths in the Atlantic, Indian and Pacific oceans as compiled by Sluijs et al. (2013). d, Model atmospheric pCO_2 response and pH response for the surface Atlantic and Pacific oceans. e, Model $\delta^{13}C$ response for the DIC of the deep Atlantic and Pacific oceans.

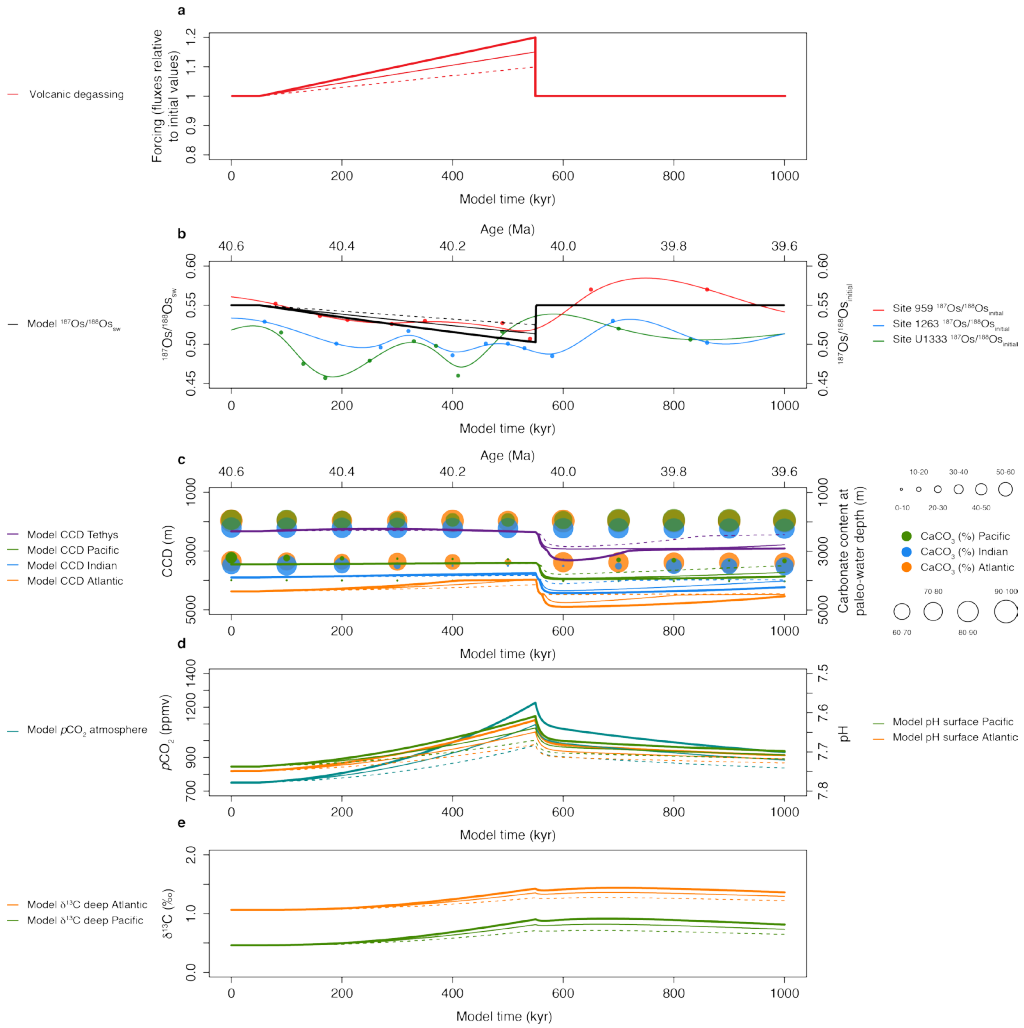

Supplementary Figure 5: LOSCAR and Os cycle model simulations of the MECO. a, Forcing for three scenarios involving a transient increase in the volcanic CO_2 flux of 10% (dashed lines), 15% (thin solid lines) and 20% (thick solid lines) over ~500 kyr, while maintaining the silicate and carbonate weathering fluxes at constant value. b, Model response in the $^{187}Os/^{188}Os$ composition of the global ocean, shown against smoothed fits to the MECO Os_i records from the study sites. c, Model CCD response of different ocean basins, shown against carbonate content (wt %) records for different depths in the Atlantic, Indian and Pacific oceans as compiled by Sluijs et al. (2013). d, Model atmospheric pCO_2 response and pH response for the surface Atlantic and Pacific oceans. e, Model $\delta^{13}C$ response for the DIC of the deep Atlantic and Pacific oceans.

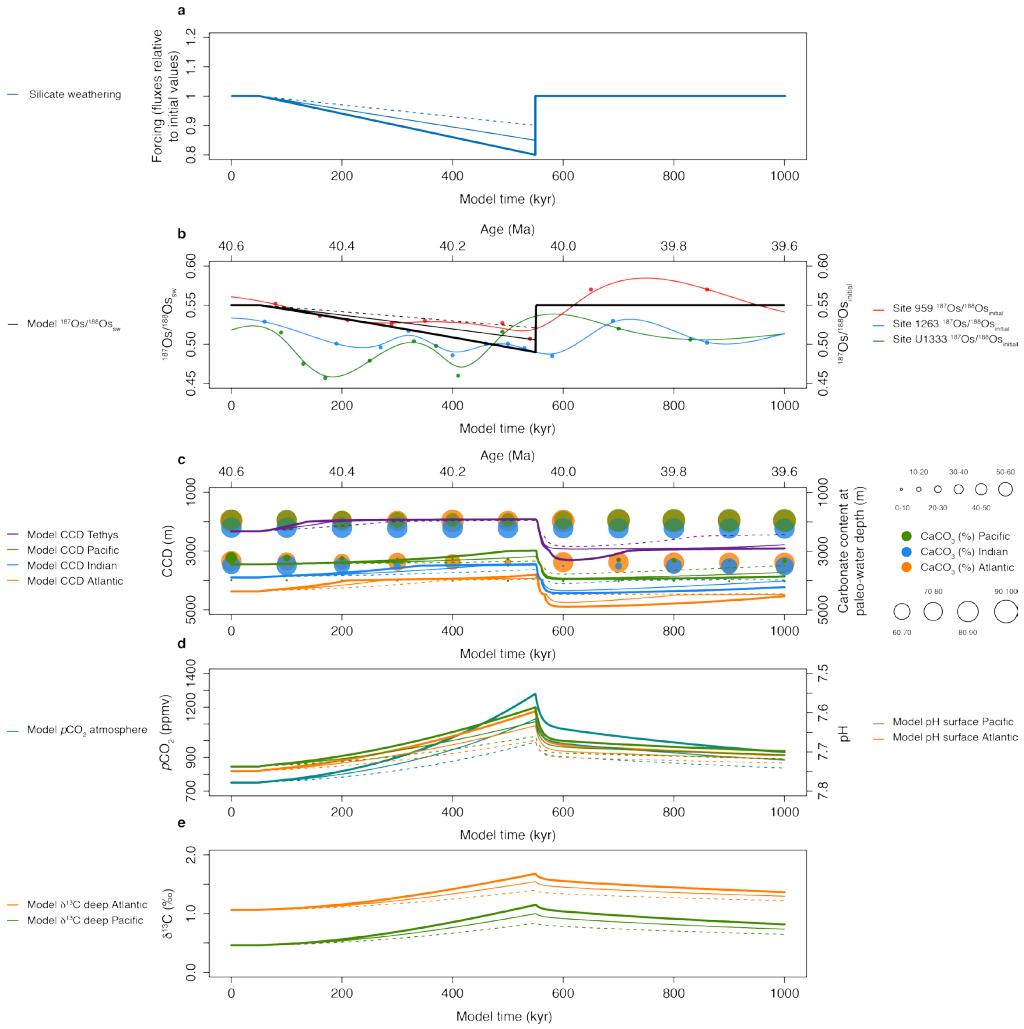

Supplementary Figure 6: LOSCAR and Os cycle model simulations of the MECO. a, Forcing for three scenarios involving a transient decrease in the silicate weathering flux of 10% (dashed lines), 15% (thin solid lines) and 20% (thick solid lines) over ~500 kyr, while keeping the volcanic CO_2 flux and the carbonate weathering flux at constant value. b, Model response in the $^{187}Os/^{188}Os$ composition of the global ocean, shown against smoothed fits to the MECO Os_i records from the study sites. c, Model CCD response of different ocean basins, shown against carbonate content (wt %) records for different depths in the Atlantic, Indian and Pacific oceans as compiled by Sluijs et al. (2013). d, Model atmospheric pCO_2 response and pH response for the surface Atlantic and Pacific oceans. e, Model $\delta^{13}C$ response for the DIC of the deep Atlantic and Pacific oceans.

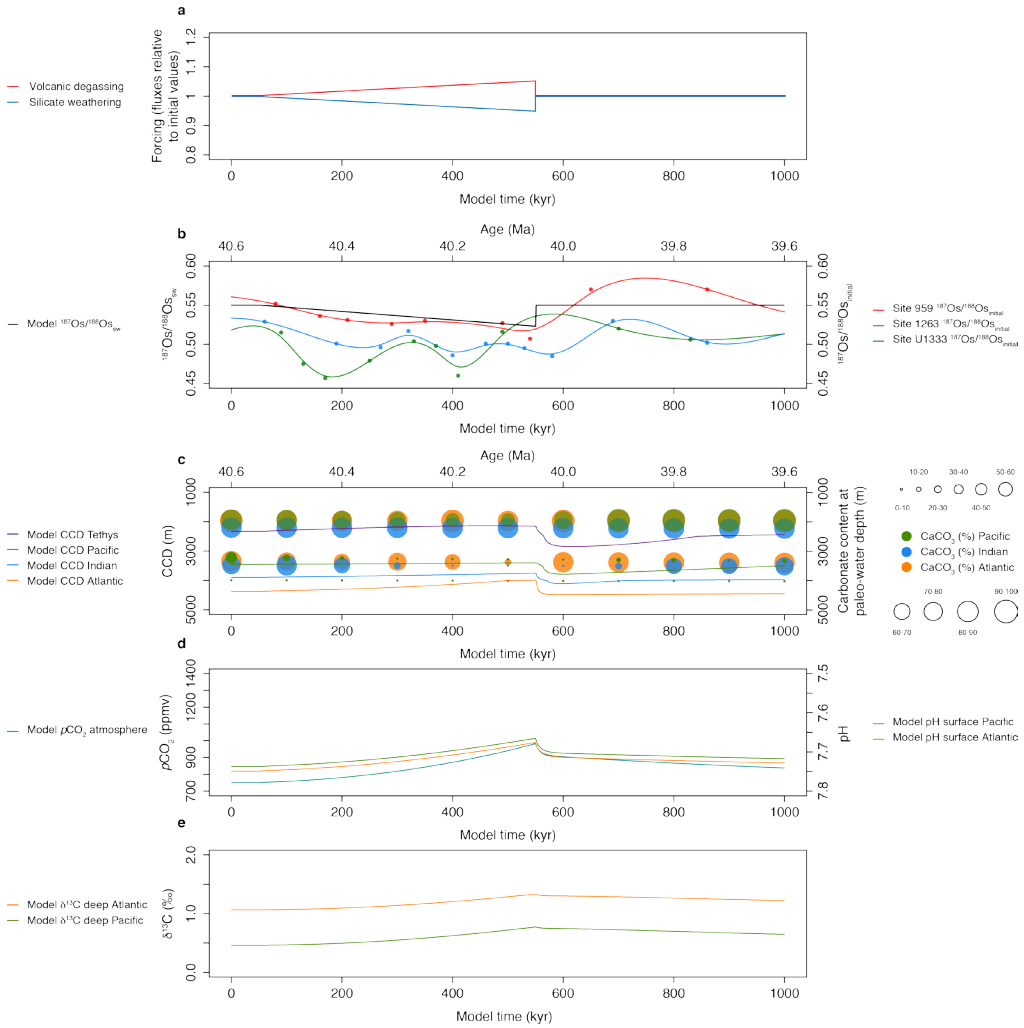

Supplementary Figure 7: LOSCAR and Os cycle model simulations of the MECO. a, Forcing for a scenario involving a transient 5% increase in the volcanic CO_2 flux combined with a 5% decrease in the silicate weathering flux over ~500 kyr, while keeping the carbonate weathering flux at constant value. b, Model response in the $^{187}Os/^{188}Os$ composition of the global ocean, shown against smoothed fits to the MECO Os_i records from the study sites. c, Model CCD response of different ocean basins, shown against carbonate content (wt %) records for different depths in the Atlantic, Indian and Pacific oceans as compiled by Sluijs et al. (2013). d, Model atmospheric pCO_2 response and pH response for the surface Atlantic and Pacific oceans. e, Model $\delta^{13}C$ response for the DIC of the deep Atlantic and Pacific oceans.

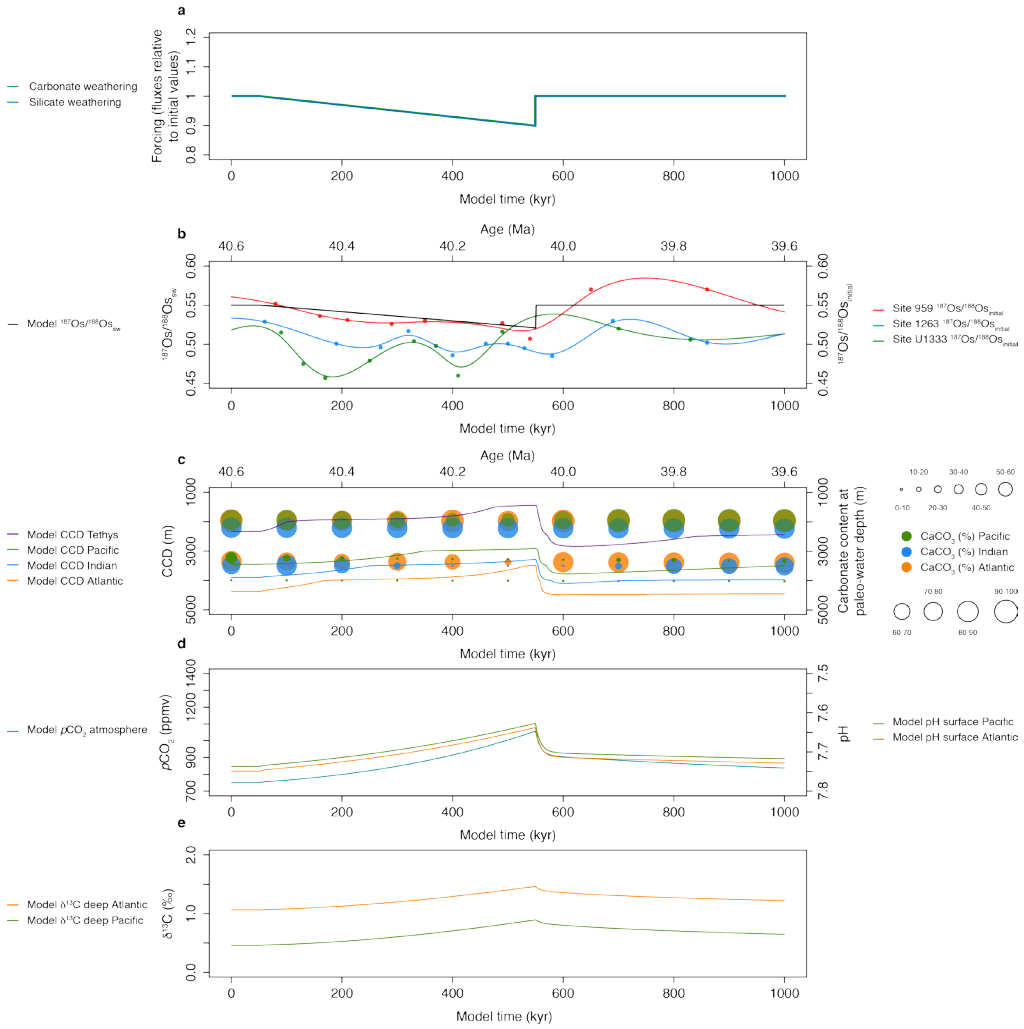

Supplementary Figure 8: LOSCAR and Os cycle model simulations of the MECO. a, Forcing for a scenario involving a transient, combined 10% decrease in the silicate and carbonate weathering fluxes over ~500 kyr, while keeping the volcanic CO_2 flux at constant value. b, Model response in the $^{187}Os/^{188}Os$ composition of the global ocean, shown against smoothed fits to the MECO Os_i records from the study sites. c, Model CCD response of different ocean basins, shown against carbonate content (wt %) records for different depths in the Atlantic, Indian and Pacific oceans as compiled by Sluijs et al. (2013). d, Model atmospheric pCO_2 response and pH response for the surface Atlantic and Pacific oceans. e, Model $\delta^{13}C$ response for the DIC of the deep Atlantic and Pacific oceans.

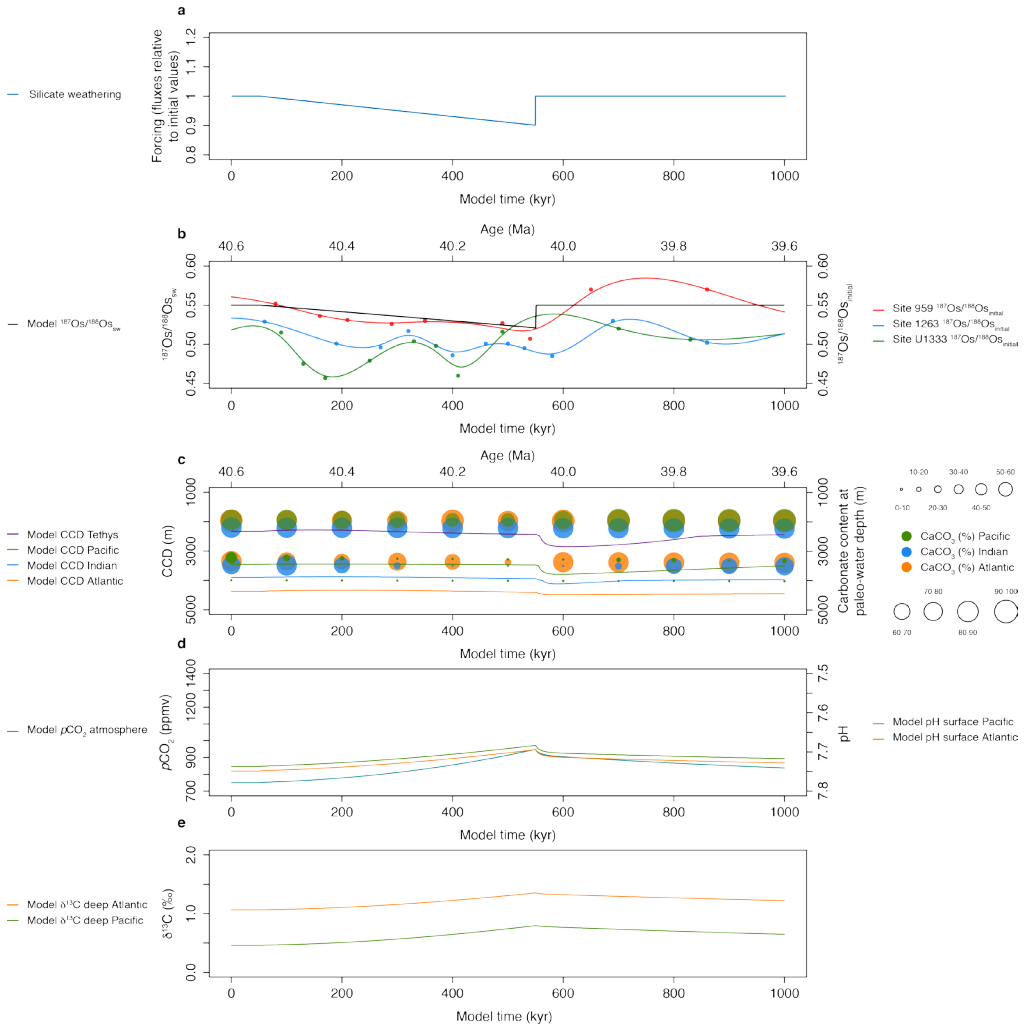

Supplementary Figure 9: LOSCAR and Os cycle model simulations of the MECO. a, Forcing for a scenario involving a transient 10% decrease in the silicate weathering flux over ~500 kyr, while keeping the volcanic CO_2 flux at constant value and allowing the carbonate weathering flux to vary as a feedback response. b, Model response in the $^{187}Os/^{188}Os$ composition of the global ocean, shown against smoothed fits to the MECO Os_i records from the study sites. c, Model CCD response of different ocean basins, shown against carbonate content (wt %) records for different depths in the Atlantic, Indian and Pacific oceans as compiled by Sluijs et al. (2013). d, Model atmospheric pCO_2 response and pH response for the surface Atlantic and Pacific oceans. e, Model $\delta^{13}C$ response for the DIC of the deep Atlantic and Pacific oceans.

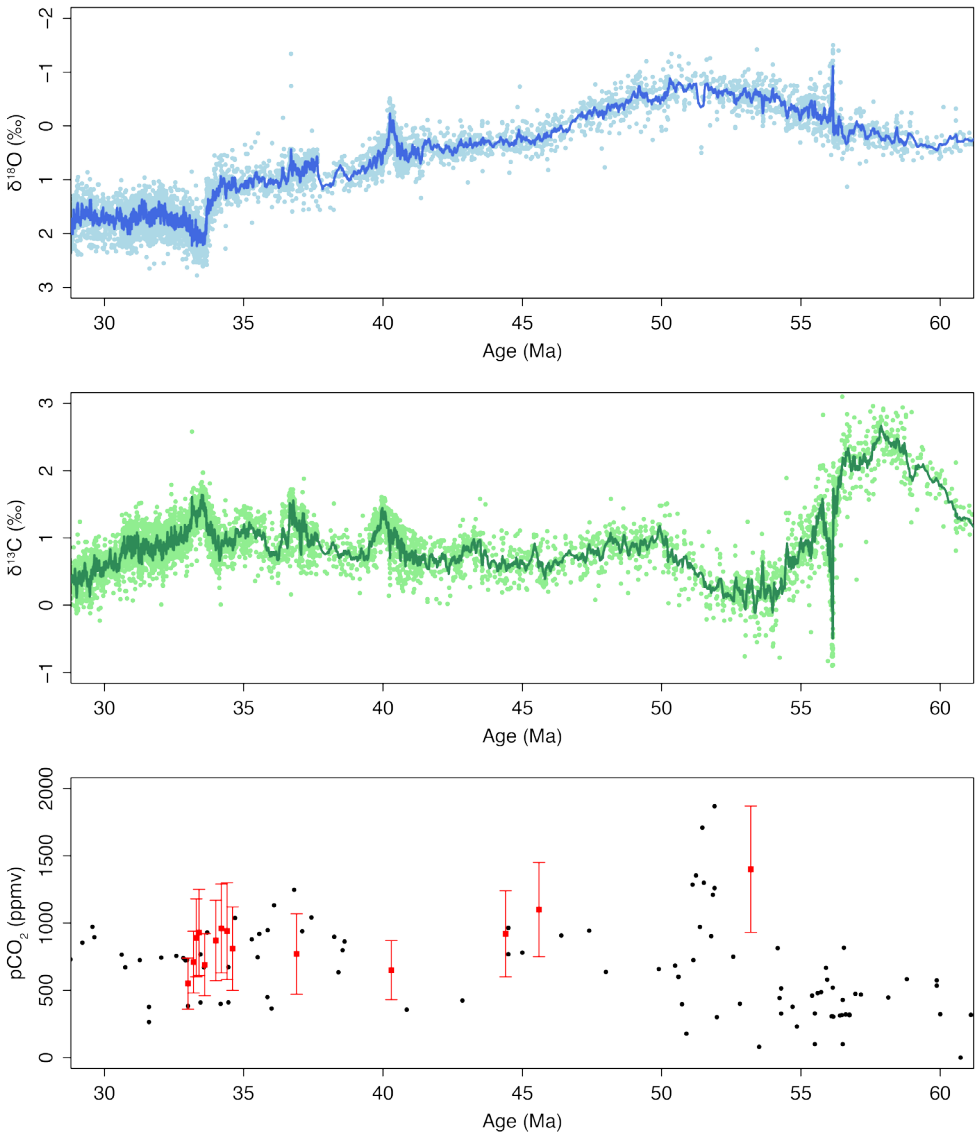

Supplementary Figure 10: Eocene trends in benthic foraminiferal $\delta^{18}O$ and $\delta^{13}C$, and atmospheric pCO_2. a, Benthic $\delta^{18}O$ compilation as published in Cramer et al. (2009), adjusted to the framework of the GTS 2012 (Gradstein et al., 2012) and plotted as individual data points and as a 10-point running average (solid line). b, Benthic $\delta^{13}C$ compilation as published in Cramer et al. (2009), adjusted to the framework of the GTS 2012 (Gradstein et al., 2012) and plotted as individual data points and as a 10-point running average (solid line). c, Atmospheric pCO_2 compilation as published in Foster et al. (2017), with the $\delta^{11}B$-based pCO_2 estimates of Anagnostou et al. (2016) highlighted in red.

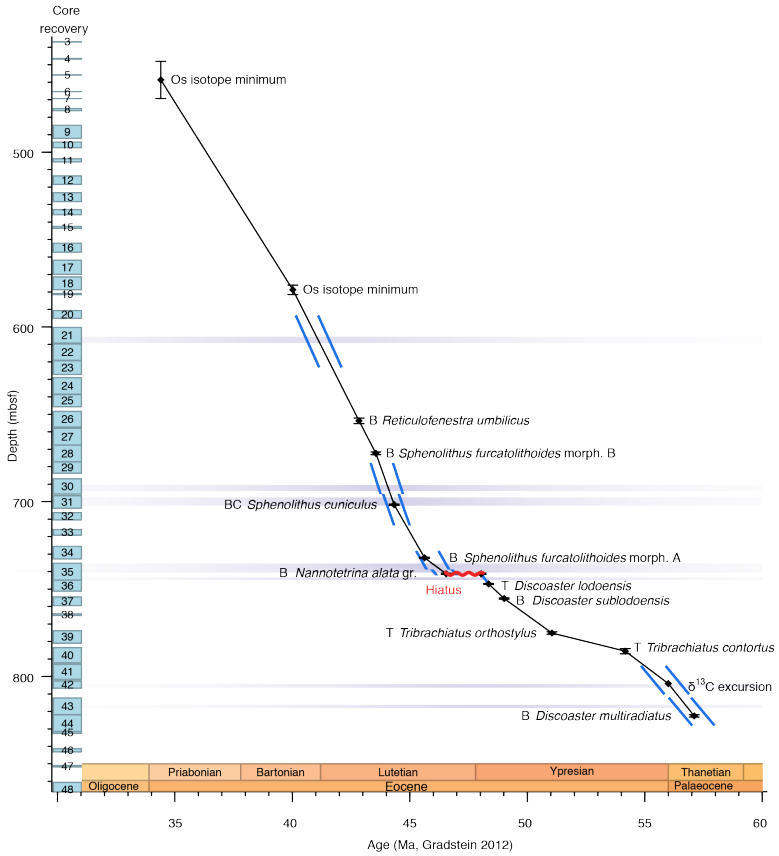

Supplementary Figure 11: Age model for Site 959 Hole D as presented in Cramwinckel et al. (2018). Diamonds with error bars show calcareous nannofossil and chemostratigraphic tie-points, adjusted to the framework of the GTS 2012 (Gradstein et al., 2012). The Os isotope minimum at ~40 Ma is derived from the MECO Os_i records presented in this study.

Supplementary Table 1: Age model for Site 959.

Stratigraphic datum	Depth (mbsf)	Age (Ma) [GTS 2004, Gradstein et al. (2005)]	Age (Ma) [GTS 2012, Gradstein et al. (2012)]	Source
$^{187}Os/^{188}Os$ minimum	466.6	34.5	34.65	Ravizza and Paquay (2008)
TEX_{86} highest value at MECO peak	578.25	-	40.06	This study, based on Cramwinckel et al. (2018), Bohaty et al. (2009)
TEX_{86} lowest value at MECO onset	608.84	-	40.52	This study, based on Cramwinckel et al. (2018), Bohaty et al. (2009)
FCO *Reticulofenestra umbilicus*	654.545	-	42.84	Shafik et al. (1998), Cramwinckel et al. (2018)

Supplementary Table 2: Age model for Site 1263.

Stratigraphic datum	Depth (mbsf)	Depth (adj rmcd) [Westerhold et al. (2015)]	Age (Ma) [Pälike et al. (2006)]	Age (Ma) [GTS 2012, Gradstein et al. (2012)]	Source
$\delta^{13}C$ highest value	113.7	135.27	39.2	39.3	Bohaty et al. (2009)
$\delta^{18}O$ final lowest value at MECO peak	119.6	141.29	39.99	40.06	Bohaty et al. (2009)
$\delta^{18}O$ final highest value at MECO onset	122.6	145.83	40.552	40.52	Bohaty et al. (2009)
$\delta^{13}C$ lowest value	124.9	148.13	40.925	40.81	Bohaty et al. (2009)
C18r - C19n boundary	127.85	151.08	41.358	41.154	Pälike et al. (2006)
C19n - C19r boundary	129.25	152.48	41.51	41.39	Pälike et al. (2006)
$\delta^{13}C$ lowest value	131.6	154.8	41.796	41.64	Bohaty et al. (2009)

Supplementary Table 3: Age model for Site U1333.

Stratigraphic datum	Depth (adj rmcd) [Westerhold et al. (2012)]	Age (Ma) [Pälike et al. (2006)]	Age (Ma) [GTS 2012, Gradstein et al. (2012)]	Source
C17r - C18n.1n boundary	157.3	38.449	38.615	Pälike et al. (2006)
T S. obtusus	158.15	38.562	38.71	Toffanin et al. (2013)
T C. grandis	158.55	38.612	38.76	Toffanin et al. (2013)
T C. solitus	159.95	38.788	38.92	Toffanin et al. (2013)
B S. obtusus	164.15	39.314	39.4	Toffanin et al. (2013)
C18n.1n - C18n.1r boundary	166.075	39.554	39.627	Pälike et al. (2006)
C18n.1r - C18n.2n boundary	166.875	39.602	39.698	Pälike et al. (2006)
C18n.2n - C18r boundary	169.57	40.084	40.145	Pälike et al. (2006)
Bc D. hesslandii	172.69	40.421	40.41	Toffanin et al. (2013)
Bc D. bisectus	172.69	40.421	40.41	Toffanin et al. (2013)
T Furcatolithoides	174.5	40.614	40.56	Toffanin et al. (2013)
C18r - C19n boundary	181.5	41.358	41.154	Pälike et al. (2006)
C19n - C19r boundary	183.225	41.51	41.39	Pälike et al. (2006)

Supplementary Table 4: Overview of all LOSCAR model scenarios. All forcings represent a gradual, linear increase/decrease to maximum values from t = 50 kyr to t = 550 kyr and are followed by a sudden drop to initial values. Initial pCO_2 concentrations were set at 750 ppmv in all simulations.

Scenario and Supplementary Figure	Silicate weathering flux	Volcanic CO_2 flux	Carbonate weathering flux
1 (5)	Feedback	+10%	Feedback
2 (5)	Feedback	+15%	Feedback
3 (5)	Feedback	+20%	Feedback
4 (6)	Constant	+10%	Constant
5 (6)	Constant	+15%	Constant
6 (6)	Constant	+20%	Constant
7 (7)	-10%	Constant	Constant
8 (7)	-15%	Constant	Constant
9 (7)	-20%	Constant	Constant
10 (8)	-5%	+5%	Constant
11 (9)	-10%	Constant	-10%
12 (10)	-10%	Constant	Feedback

Supplementary Table 5: Overview of all default Os cycle parameters. Present-day values are taken from the literature or fitted to match the present-day steady state observations. Pre-MECO values are either assumed to be similar to the present-day values or fitted to match the pre-MECO steady state observations.

Parameter	Parameter description	Value	Reference and Comments
Present-day values			
N	Os inventory in oceans	7.2×10^7 mol	Peucker-Ehrenbrink and Ravizza (2000)
F_{riv}	Riverine Os flux to oceans	1800 mol/yr	Peucker-Ehrenbrink and Ravizza (2000)
F_{hyd}	Hydrothermal Os flux to oceans	483 mol/yr	Calculated for steady state at R_{sw} = 1.06
F_{ext}	Extraterrestrial Os flux to oceans	80 mol/yr	Peucker-Ehrenbrink and Ravizza (2000)
F_{sed}	Sedimentary Os flux from oceans	2363 mol/yr	Calculated for steady state
R_{riv}	$^{187}Os/^{188}Os$ composition of rivers	1.4	Peucker-Ehrenbrink and Ravizza (2000)
R_{hyd}	$^{187}Os/^{188}Os$ composition of hydrothermal fluids	0.13	Meisel et al. (2001)
R_{ext}	$^{187}Os/^{188}Os$ composition of extraterrestrial dust	0.13	Peucker-Ehrenbrink and Ravizza (2000)
R_{sw}	$^{187}Os/^{188}Os$ composition of seawater	1.06	Peucker-Ehrenbrink and Ravizza (2000)
Pre-MECO values			
N	Os inventory in oceans	7.2×10^7 mol	Assumed similar to present-day value
F_{riv}	Riverine Os flux to oceans	865 mol/yr	Calculated for steady state at R_{sw} = 0.55
F_{hyd}	Hydrothermal Os flux to oceans	1418 mol/yr	Calculated for steady state at R_{sw} = 0.55
F_{ext}	Extraterrestrial Os flux to oceans	80 mol/yr	Assumed similar to present-day value
F_{sed}	Sedimentary Os flux from oceans	2363 mol/yr	Assumed similar to present-day value
R_{riv}	$^{187}Os/^{188}Os$ composition of rivers	1.4	Assumed similar to present-day value
R_{hyd}	$^{187}Os/^{188}Os$ composition of hydrothermal fluids	0.13	Assumed similar to present-day value
R_{ext}	$^{187}Os/^{188}Os$ composition of extraterrestrial dust	0.13	Assumed similar to present-day value
R_{sw}	$^{187}Os/^{188}Os$ composition of seawater	0.55	This study

Chapter 6

Surface ocean warming in the North Atlantic during the Middle Eocene Climatic Optimum

Surface ocean warming in the North Atlantic during the Middle Eocene Climatic Optimum

Robin van der Ploeg, Margot J. Cramwinckel, Thomas J. Leutert, Steven M. Bohaty, Chris D. Fokkema, Rogier J. Hidding, Ilja J. Kocken, A. Nele Meckler, Anne E. van der Meer, Jack J. Middelburg, Inigo A. Müller, Francien Peterse, Gert-Jan Reichart, Stefan Schouten, Philip F. Sexton, Paul A. Wilson, Martin Ziegler and Appy Sluijs

Abstract

The Middle Eocene Climatic Optimum (MECO) represents a ~500 kyr episode of widespread ocean warming that occurred ~40 Myr ago, superimposed on the long-term Eocene cooling trend. While surface ocean warming during the MECO has been reconstructed for various ocean basins, the regional expression of warming in the North Atlantic remains unclear. Here, we present a multiproxy surface ocean temperature record of the MECO from the Newfoundland Drifts at IODP Sites U1408 and U1410, based on clumped isotope (Δ_{47}) and Mg/Ca compositions of well-preserved planktonic foraminifera, together with lipid biomarker paleothermometry (TEX_{86} and $U^{K'}_{37}$). All proxies show warming during the MECO, but the reconstructed absolute temperatures and the total degree of warming vary between proxies. Our coupled Δ_{47} and $\delta^{18}O$ data indicate a surface mixed-layer warming of 3–5 °C during the MECO and a concomitant ~1.5‰ shift towards heavier seawater $\delta^{18}O$ compositions corresponding to a sea surface salinity increase of ~2 psu, which we attribute to a northward expansion of warm, saline waters from the North Atlantic gyre. This first Δ_{47}-based temperature record of planktonic foraminifera for a transient Paleogene warming event provides an unprecedented test of the validity of other proxy-temperature relationships. Most notably, we find lower absolute temperatures but more substantial warming for Δ_{47} in comparison to Mg/Ca, suggesting that the established deep-time Mg/Ca-temperature relationships may need to be revisited. In addition, TEX_{86} and $U^{K'}_{37}$ yield higher absolute temperatures but less total warming than Δ_{47} and Mg/Ca. Part of this difference may be related to proxies reflecting temperatures from different water depths and/or seasons, but since these records are derived from sediment drifts it is also likely that TEX_{86} and $U^{K'}_{37}$ are affected by lateral transport of organic matter. These findings highlight the importance of multi-proxy temperature reconstructions for paleoclimate studies and demonstrate the potential of Δ_{47} for reducing uncertainties in absolute temperature estimates.

6.1 Introduction

The Middle Eocene Climatic Optimum (MECO) represents an episode of transient surface and deep ocean warming that occurred around 40 Myr ago (Bohaty and Zachos, 2003; Bohaty et al., 2009; Sluijs et al., 2013) and is associated with atmospheric CO_2 rise (Bijl et al., 2010), carbonate dissolution in the deep ocean (Bohaty et al., 2009; Sluijs et al., 2013) and biotic change (Bijl et al., 2010; Boscolo Galazzo et al., 2013, 2015). This greenhouse warming episode occurred on a timescale of ~500 kyr and is characterized by a gradual onset, followed by a short peak warming phase and a rapid termination. Both the extended duration of warming and the absence of a negative carbon isotope excursion set the MECO apart from the Paleocene-

Eocene Thermal Maximum (PETM; ~56 Myr ago), Eocene Thermal Maximum 2 (ETM-2; ~54 Myr ago) and other short-lived Eocene hyperthermals (Sluijs et al., 2013). Reconstructions suggest that CO_2 release from an episode of enhanced mafic volcanism may have acted as a driver of prolonged MECO warming, but the exact cause of the event remains elusive (Van der Ploeg et al., 2018).

The MECO and/or its associated changes in ocean chemistry and biological communities have now been identified in all major ocean basins (Sluijs et al., 2013) (Figure 1). At high latitudes in the Southern Ocean, where the event was first described, 4–6 °C of warming has been estimated for both the sea surface and the deep sea based on $\delta^{18}O$, $U^{K'}_{37}$ and TEX_{86} records (Bohaty and Zachos, 2003; Bohaty et al., 2009; Bijl et al., 2010). A similar degree of sea surface warming has subsequently been observed at mid-latitude sites in the former Tethys Ocean (Jovane et al., 2007; Spofforth et al., 2010) as well as in the North, South and equatorial Atlantic oceans (Bohaty et al., 2009; Edgar et al., 2010; Boscolo Galazzo et al., 2014; Cramwinckel et al., 2018). However, some of these inferences are based on $\delta^{18}O$ records of bulk carbonate, which are dominantly sourced from surface-dwelling nannofossils but also consist of material formed at greater depths – thus representing a rather crude estimate of sea surface temperature change. By contrast, in the equatorial Pacific Ocean the event is marked by an episode of extensive carbonate dissolution (Bohaty et al., 2009; Sluijs et al., 2013), without very clear signs of warming in $\delta^{18}O$.

Although the MECO has been increasingly studied over the past years, most published records of the event are compromised by the limited temporal resolution and/or the relatively poor preservation state of deep-sea sediments (Bohaty and Zachos, 2003; Bohaty et al., 2009; Bijl et al., 2010; Boscolo Galazzo et al., 2014). In addition, because records from the mid-high

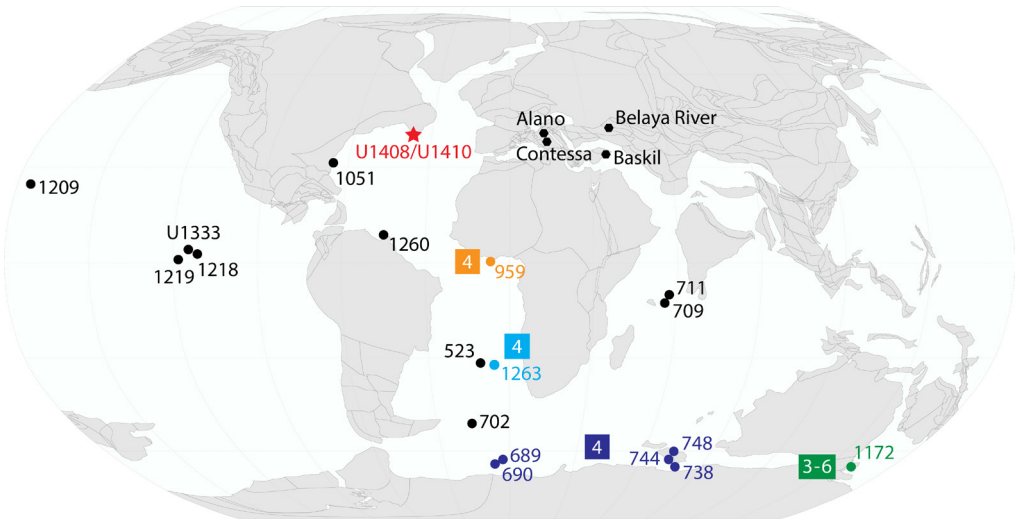

Figure 1: Map of sites with existing MECO records on a paleogeographic reconstruction for the Middle Eocene at 40 Ma. Where available, the degree of MECO warming inferred by previous studies (Bohaty and Zachos, 2003; Bijl et al., 2010; Boscolo Galazzo et al., 2014; Cramwinckel et al., 2018) is shown in boxes with numbers representing °C of warming. The locations of Sites U1408 and U1410 are indicated by the red star. Map made with GPlates using the reference frame of Matthews et al. (2016).

latitudes in the North Atlantic are lacking, it remains questionable whether MECO warming was a truly global phenomenon or whether it mostly affected the southern hemisphere. To address both of these issues, we present novel multi-proxy temperature records derived from deep-sea sedimentary sequences from International Ocean Discovery Program (IODP) Sites U1408 and U1410 from the Newfoundland Drifts in the North Atlantic (see Methods). These sites are presently located along a strong sea surface temperature gradient at the northern edge of the North Atlantic gyre (~41 °N), where warm waters from the Gulf Stream meet the much colder waters from the Labrador Sea Current (Norris et al., 2014a) (Supplementary Figure 1). Sedimentation at the Newfoundland ridges has occurred primarily as drift deposition since ~47 Ma (Boyle et al., 2017) and hence these expanded, clay-rich Middle Eocene sediments yield well-preserved foraminifera (Supplementary Figure 2) and abundant organic matter, allowing for robust multiproxy temperature reconstructions. By integrating high-resolution clumped isotope (Δ_{47}), oxygen isotope ($\delta^{18}O$) and trace element (Mg/Ca) records of planktonic foraminifera with biomarker records based on isoprenoid glycerol dialkyl glycerol tetraether (GDGT) distributions (TEX_{86}) and alkenones ($U^{K'}_{37}$), we aim to determine the full amplitude and character of sea surface warming and cooling during the MECO in the North Atlantic. Crucially, this is the first Δ_{47}-based temperature record of planktonic foraminifera for a transient Paleogene warming event, which allows us to independently assess the fidelity of the other available sea surface temperature proxies applied to the exact same sediments.

$\delta^{18}O$, Mg/Ca, $U^{K'}_{37}$ and TEX_{86} have been widely used as temperature proxies in deep-time paleoclimate studies (Lear et al., 2000; Pearson et al., 2001; Frieling et al., 2017), but the application of carbonate clumped isotope paleothermometry is relatively new. Δ_{47} is based on the degree of binding between the heavy ^{13}C and ^{18}O isotopes in carbonate minerals, which is inversely related to temperature (Eiler, 2011). Unlike $\delta^{18}O$ and Mg/Ca, the Δ_{47} composition of carbonates is independent of the isotopic and elemental composition of seawater, and as such, Δ_{47} has the unique potential of delivering absolute temperature estimates without the need for additional assumptions. In addition, Δ_{47} compositions of planktonic foraminifera appear unaffected by species-specific vital effects (Peral et al., 2018). Importantly, now that consensus is being reached on Δ_{47}-temperature calibrations, the uncertainty in Δ_{47}-based temperature reconstructions is dominated by analytical precision (Kele et al., 2015; Bernasconi et al., 2018) – provided that the quality of carbonate preservation is sufficient and no post-depositional resetting has occurred. Nevertheless, large amounts of material and/or large numbers of replicate analyses are required in order to obtain precise temperature estimates (Schmid and Bernasconi, 2010; Meckler et al., 2014).

No single planktonic foraminiferal species is ubiquitous across the studied MECO interval (Norris et al., 2014b). Therefore, we have constructed a composite record based on three partially overlapping species (groups): *Acarinina (prae-)topilensis*, *Acarinina bullbrooki* and *Globigerinatheka index*. Based on their $\delta^{18}O$–$\delta^{13}C$ relationships, *A. (prae-)topilensis* and *A. bullbrooki* are both considered to have had photosynthetic algal symbionts, and thus reflect surface mixed-layer conditions (Pearson et al., 2001; Sexton et al., 2006) (Supplementary Figure 3). By contrast, *Gk. index* is known to sink to a greater water depth during its reproductive cycle (Premoli-Silva et al., 2006) and may therefore record somewhat lower temperatures from the upper part of the thermocline (Pearson et al., 2001).

6.2 Methods

6.2.1 Site descriptions

IODP Sites U1408 and U1410 are both located on the southeast Newfoundland Ridge in the northwest Atlantic Ocean (Norris et al., 2014a). Site U1408 is situated at 41°26'N, 49°14'W (~3022 m water depth) and Site U1410 is situated at 41°20'N, 49°10'W (~3400 m water depth) (Norris et al., 2014a, 2014b, 2014c). The paleodepth for Sites U1408 and U1410 at 50 Ma is estimated at ~2575 and ~2950 meters below sea level (mbsl), respectively (Norris et al., 2014b, 2014c). Both sites contain sequences of calcareous middle Eocene sediments deposited above the CCD, but the shallower Site U1408 sediments are especially enriched in carbonate and are more expanded than the sediments of Site U1410 (Norris et al., 2014b, 2014c). The MECO interval at Site U1408 consists of alternations between greenish gray nannofossil clays and whitish to light gray nannofossil oozes, which feature a well-developed cyclicity on a decimeter scale and a higher carbonate content than underlying and overlying sediments (Norris et al., 2014b). However, a hiatus may be present in the top of the MECO interval at Site U1408, so incorporating a section of Site U1410 may be needed to construct a composite record that captures the full extent of the MECO.

6.2.2 Sampling and foraminiferal species selection

The MECO interval was sampled at a continuous, high resolution (~3 cm) at Site U1408. In addition, a lower resolution (~30 cm) sample set was taken from the inferred MECO peak warming interval at Site U1410. Samples were washed and sieved, and subsequently specimens of mixed-layer dwelling planktonic foraminifera were picked from the 250–355 μm size fraction for three species (groups): *Acarinina (prae-)topilensis, Acarinina bullbrooki* and *Globigerinatheka index*.

6.2.3 Foraminiferal preservation

Foraminiferal preservation is generally good to excellent at sites U1408 and U1410, owing to the high clay content of the sediments deposited in the Newfoundland Drifts (Norris et al., 2014b, 2014c). In fact, many foraminiferal shells have glassy textures (Supplementary Figure 2), which is regarded as an exceptional preservation state for foraminifera of Eocene age and allows for geochemical reconstructions of original seawater conditions with little to no diagenetic alteration (Sexton et al., 2006; Pearson and Burgess, 2008). A similar high quality of foraminiferal preservation has also been reported for Late Eocene sediments at Site U1411 (Coxall et al., 2018), which is located in close proximity to sites U1408 and U1410.

6.2.4 Cleaning

Shells of the aforementioned planktonic foraminiferal species were cracked and cleaned following the protocol of Barker et al. (2003). For clumped and stable isotope analyses, this involved the cracking of at least 20 foraminiferal shells per sample between two glass plates and the removal of clays and coccoliths in deionized water and methanol (CH_3OH). For trace element analyses, splits of methanol-cleaned and homogenized material were subjected to further cleaning involving the removal of organic matter through oxidative treatment in hot alkali buffered hydrogen peroxide (H_2O_2) and the removal of adsorbed contaminants through weak acid leaching with nitric acid (HNO_3). In order to minimize sample loss, a reductive treatment step was omitted.

6.2.5 Clumped and stable isotope analyses

The clumped isotope paleothermometer (Δ_{47}) is defined based on the excess of the mass-47 CO_2 isotopologue (^{13}C-^{18}O-^{16}O) relative to the expected abundance in a stochastic distribution of the ^{13}C and ^{18}O isotopes among all isotopologues (Eiler, 2011). As such, Δ_{47} is expressed as:

$$\Delta_{47} = \left[\left(\frac{R^{47}}{R^{47*}} - 1\right) - \left(\frac{R^{46}}{R^{46*}} - 1\right) - \left(\frac{R^{45}}{R^{45*}} - 1\right)\right] \cdot 1000 \quad (1)$$

where R^{47}, R^{46} and R^{45} represent the respective abundances of the masses 47, 46, and 45 relative to the mass 44 in a sample, and R^{47*}, R^{46*} and R^{45*} represent the expected ratios of that sample under a stochastic distribution.

Cleaned and homogenized shells of *A. (prae-)topilenis*, *A. bullbrooki* and *Gk. index* were analyzed for clumped (Δ_{47}) and stable ($\delta^{18}O$ and $\delta^{13}C$) isotopic compositions at Utrecht University (UU) and the University of Bergen (UiB). We analyzed 1–2 aliquots per sample in order to generate high-resolution Δ_{47} and $\delta^{18}O/\delta^{13}C$ isotope records simultaneously, with a total of 365 samples and 514 analyses. Samples analyzed at UU consist of *A. (prae-)topilenis*, *A. bullbrooki* and *Gk. index* from the entire studied interval of Sites U1408 and U1410, while samples analyzed at UiB consist of *Gk. index* from the peak-MECO interval of Site U1408 and *A. (prae-)topilenis* from the onset of MECO warming at Site U1408 (Supplementary Figure 4).

At UU, measurements were performed using either a Thermo Scientific MAT 253 mass spectrometer or a Thermo Scientific 253 Plus mass spectrometer coupled to a Thermo Scientific Kiel IV carbonate device. Approximately 120–180 μg material was used per measurement on the MAT 253 and approximately 80–100 μg per measurement on the 253 Plus. Samples were reacted with phosphoric acid (H_3PO_4) at 70 °C and the CO_2 from these samples was passed through a PoraPak Q trap to filter out any organic contaminants (Schmid and Bernasconi, 2010). During each run, 16–20 aliquots of randomly selected samples were analyzed alongside multiple replicates of the ETH-1, ETH-2, ETH-3 and ETH-4 carbonate standards. The analyses on the Thermo Scientific MAT 253 mass spectrometer consisted of 8 cycles of sample and reference gas measurements, while the analyses on the Thermo Scientific 253 Plus mass spectrometer used the Long-Integration Dual-Inlet (LIDI) method (Hu et al., 2014). During LIDI analyses, sample gas was measured continuously for 400 seconds, followed by the reference gas for 400 seconds. At UiB, measurements were performed on a Thermo Scientific 253 Plus mass spectrometer coupled to a Thermo Scientific Kiel IV carbonate device using similar methods (LIDI technique with 400 seconds of integration time for each sample and reference gas; ETH-1, ETH-2, ETH-3 and ETH-4 carbonate standards; 70 °C digestion temperature).

All Δ_{47} measurements were transferred to the Absolute Reference Frame or carbon dioxide equilibrated scale (CDES) (Dennis et al., 2011) using the carbonate standards and corrected for the acid digestion temperature of 70 °C (Müller et al., 2017). The external reproducibility of each Δ_{47} replicate is conservatively estimated at 0.03‰–0.04‰ (1σ). $\delta^{18}O$ and $\delta^{13}C$ values are reported relative to the VPDB standard. Analytical precision was better than 0.1‰ for $\delta^{18}O$ and $\delta^{13}C$. See Supplementary Figure 4 for an overview of all raw Δ_{47} data for Site U1408 and the instruments used to measure each replicate.

6.2.6 Temperature reconstructions using Δ_{47}

We calculated Δ_{47}-based temperatures using the updated Δ_{47}-temperature calibration of Kele et al. (2015) based on the Brand parameters (Brand et al., 2010) as outlined in Bernasconi et al. (2018). This is expressed in the following two equations:

$$\Delta_{47} = 0.0449\ (\pm 0.001) \cdot \frac{10^6}{T^2} + 0.167\ (\pm 0.01) \quad (2)$$

$$T = \sqrt{\frac{0.0449\ (\pm 0.001) \cdot 10^6}{\Delta_{47} - 0.167\ (\pm 0.01)}} \quad (3)$$

where Δ_{47} is given in ‰ (CDES) and T represents the temperature in Kelvin.

We employed a combination of two data analysis approaches to convert our Δ_{47} measurements to temperature estimates (Rodríguez-Sanz et al., 2017). The first approach is based on averaging sets of Δ_{47} replicates from neighboring samples to obtain precise temperature estimates. For this purpose, we selected clusters of at least 20 neighboring measurements per foraminiferal species. Within a cluster, we assigned weights to each of the included measurements by calculating the distance between the depth (age) of a specific measurement and the average depth (age) of all included measurements using a tricube function. These weights were subsequently used to calculate the weighted depth (age) average and the weighted Δ_{47} average for each cluster. The weighted Δ_{47} averages are reported with their respective standard errors of the mean, based on the standard deviation of the included measurements and the number of included measurements. These weighted Δ_{47} averages of these clusters were subsequently converted to temperature using Equation (3). The depth (age) range of the clusters incorporates the full depth (age) range of the included measurements.

The second approach we used to obtain temperature estimates is an adaptation of the so-called non-traditional data analysis approach of Rodríguez-Sanz et al. (2017). This approach uses Monte Carlo simulations in which the analytical uncertainties are fully propagated for each Δ_{47} replicate, followed by filtering to derive a smoothed, continuous temperature record. We first generated 1000 iterations of temperature records by assuming Gaussian error distributions for each Δ_{47} replicate based on a standard deviation (1σ) of 0.03‰. Subsequently, we apply locally weighted smoothing (LOESS) to each of these 1000 iterations of our temperature dataset and calculated the 2.5th, 16th, 50th, 84th and 97.5th percentiles of these LOESS fits to obtain the median temperature estimates and their associated 68% and 95% confidence intervals. For simplicity we ignore the uncertainties associated with the Δ_{47}-temperature calibration, because these calibration uncertainties (± 1 °C at 95% CI) are much smaller than the typical analytical uncertainties for foraminifer-based Δ_{47} estimates (Bernasconi et al., 2018; Peral et al., 2018).

6.2.7 Seawater $\delta^{18}O$ and salinity reconstructions

Our foraminiferal $\delta^{18}O$ records ($\delta^{18}O_{foram}$) and Δ_{47}-based temperature records enable us to estimate changes in the $\delta^{18}O$ composition of seawater ($\delta^{18}O_{sw}$) across the MECO. To this end, we use the linear $\delta^{18}O$-temperature calibration of Erez and Luz (1983), which is based on culturing of the modern planktonic foraminifer *Globigerinoides sacculifer* at a temperature range of 14–30 °C. This is expressed in the following two equations:

$$T = 17.0 - 4.52 \cdot \left(\delta^{18}O_{foram} - \delta^{18}O_{sw}\right) \quad (4)$$

$$\delta^{18}O_{sw} = \frac{T-17.0}{4.52} + \delta^{18}O_{foram} \quad (5)$$

where a factor of +0.22‰ is used to convert the resulting $\delta^{18}O_{sw}$ from VDPB to VSMOW (Pearson, 2012).

First, we generate 1000 iterations of $\delta^{18}O_{sw}$ records using our Monte Carlo simulations of Δ_{47}-based temperatures, which includes analytical uncertainties in $\delta^{18}O_{foram}$ based on a standard deviation (1σ) of 0.1‰. We then apply LOESS fitting and calculate the 2.5th, 16th, 50th, 84th and 97.5th percentiles of these LOESS fits to obtain the median $\delta^{18}O_{sw}$ estimates and their associated 68% and 95% confidence intervals. Additionally, we calculate a $\delta^{18}O_{sw}$ record based on individual $\delta^{18}O_{foram}$ values and the median Δ_{47}-derived temperatures.

Finally, we use our $\delta^{18}O_{sw}$ records to reconstruct changes in sea surface salinity across the MECO. For this purpose, we use the modern $\delta^{18}O_{sw}$-salinity relationship for the Atlantic Ocean (Ostlund et al., 1987; Duplessy et al., 1991) in order to obtain a first-order approximation of absolute salinity. Salinity (S) is calculated as follows:

$$\delta^{18}O_{sw} = -19.264 + 0.558 \cdot S \quad (6)$$

$$S = \frac{\delta^{18}O_{sw}+19.264}{0.558} \quad (7)$$

The slope of this modern $\delta^{18}O_{sw}$-salinity relationship (0.558 ‰/psu) for the Atlantic Ocean is similar to the conservative estimate of 0.50 ‰/psu used in salinity reconstructions for the PETM (Zachos et al., 2003) and ETM-2 (Harper et al., 2018). However, because $\delta^{18}O_{sw}$-salinity relationships are also affected by temperature and the $\delta^{18}O$ value of precipitation (Zachos et al., 1994), the exact expression of this relationship for the Middle Eocene remains uncertain. Therefore, we also present our estimates as salinity anomalies relative to an inferred pre-MECO value of S = 34 psu.

6.2.8 Trace element analyses

Splits of fully cleaned and homogenized shells of *A. (prae-)topilenis* and *Gk. index* were analyzed for trace elemental compositions at the Royal Netherlands Institute for Sea Research (NIOZ) using a Thermo Scientific Element 2 inductively coupled plasma – mass spectrometer (ICP-MS). Samples were dissolved in 0.1 M HNO_3 and were diluted to a Ca concentration of 40 ppm following an initial run to determine optimal Ca concentrations. Quantitative Mg/Ca ratios were calculated against 5 ratio calibration standards with similar matrix using a ratio calibration method (de Villiers et al., 2002). Monitor standards JCp-1 *Porites* spp. and JCt-1 *Tridacna gigas* were measured to monitor the accuracies. Drift corrections were applied to improve the accuracy and were based on replicate analyses of an in-house coral monitor standard. Standard analytical precision at NIOZ is estimated to be better than ± 0.4 %.

The efficiency of our cleaning protocol and potential diagenetic effects on the resulting Mg/Ca ratios were assessed by evaluation of the corresponding Fe/Ca, Mn/Ca, Al/Ca and Sr/Ca ratios (Supplementary Figure 5). We have excluded measurements that displayed high Fe/

Ca ratios (> 0.8 mmol/mol for *A. (prae-)topilensis* and > 0.5 mmol/mol for *Gk. index*) or Al/Ca ratios (> 0.25 mmol/mol for *Gk. index*) compared to the rest of the dataset, but find no substantial evidence for contamination from detrital phases. We observe several *A. (prae-) topilensis* measurements with low Sr/Ca ratios relative to the rest of the dataset, which could hint at signs of diagenetic Sr and Mg loss, but these outliers are automatically excluded based on the aforementioned criteria for Fe/Ca. The resulting accepted Mg/Ca values are shown in Supplementary Figure 6.

6.2.9 Temperature reconstructions using Mg/Ca

Here we adopt the calibration of Gray et al. (2018) to convert our foraminiferal Mg/Ca values (Mg/Ca_{foram}) to absolute temperature estimates. This new calibration for *Globigerinoides ruber* takes changes in both salinity (S) and the carbonate system (either through pH or [CO_3^{2-}]) into account and arrives at a different, more robust Mg/Ca-temperature relationship than the canonical calibration of Anand et al. (2003), due to the use of climatological temperature estimates rather than $\delta^{18}O$-based temperature estimates. Consequently, the Gray et al. (2018) calibration yields significantly lower temperatures for a given Mg/Ca_{foram} value. Here we use their calibration for pH, but with modifications to account for differences in the Mg/Ca composition of seawater (Mg/Ca_{sw}) between past and present-day conditions based on Evans and Müller (2012). The resulting expression is:

$$T = \frac{1}{0.060}\left[\ln\left(Mg/Ca_{foram}\frac{\left[Mg/Ca_{sw,t_0}\right]^H}{\left[Mg/Ca_{sw,t}\right]^H}\right) - 0.033\cdot S + 0.83\cdot(pH - 8.0) + 1.07\right] \quad (8)$$

where T represents temperature in °C, Mg/Ca_{sw} (t_o) and Mg/Ca_{sw} (t) respectively represent the Mg/Ca compositions of present-day and past seawater, and H represents the power component of the relationship between Mg/Ca_{foram} and Mg/Ca_{sw} following Evans and Müller (2012).

We calculate absolute temperatures with full propagation of the associated uncertainties using Monte Carlo simulations (n = 1000). These simulations incorporate analytical uncertainty as well as uncertainty in S, pH and Mg/Ca_{sw}. Considering the lack of independent salinity reconstructions for the Middle Eocene and the strong present-day salinity gradient at the study sites (Supplementary Figure 1), we assume a large range of possible S values between 32 and 36 psu. For pH we assume values between 7.6 – 8.0 to reflect a range of probable Middle Eocene estimates from both modelling studies (Tyrrell and Zeebe, 2004) and reconstructions based on boron isotopic compositions ($\delta^{11}B$) of planktonic foraminifera (Anagnostou et al., 2016). For Mg/Ca_{sw} (t) we assume values between 1.5 – 3.0 mmol/mol for the Middle Eocene, which is relatively well-constrained on the basis of a range of reconstructions from fluid inclusions (Horita et al., 2002), calcium carbonate veins (Coggon et al., 2010) and large benthic foraminifera (Evans et al., 2018); for Mg/Ca_{sw} (t_o) we use the present-day value of 5.2 mmol/mol. Finally, for H we use a value of 0.42 based on best estimates for planktonic foraminifera based on *Globigerinoides sacculifer* (Hasiuk and Lohmann, 2010; Dunkley Jones et al., 2013). Following the Monte Carlo simulations based on these parameters, we applied LOESS fitting to every iteration of our dataset and calculated the 2.5th, 16th, 50th, 84th and 97.5th percentiles of these LOESS fits to obtain the median temperature estimates and their associated 68% and 95% confidence intervals.

In addition to our Monte Carlo simulations of Mg/Ca-based temperatures, we also present an optimal scenario based on S = 34 psu, pH = 7.8 and Mg/Ca_{sw} = 2.25 mmol/mol

(Figure 2d). We do not explicitly account for an increase in S as obtained from our Δ_{47}-based reconstructions (Figure 3b) or a potential decrease in pH during the MECO resulting from CO_2 rise and ocean acidification (Sluijs et al., 2013; Van der Ploeg et al., 2018), but note that both of these factors would result in a reduction in the total amount of inferred warming. For our observed range of Mg/Ca_{foram} values, a progressive S increase from 34 to 36 psu would reduce total warming by ~1 °C, while a progressive pH decrease from 7.8 to 7.6 would reduce total warming by ~3 °C. Given the long oceanic residence times of Mg and Ca, we assume no transient change in Mg/Ca_{sw} across the MECO.

Even though we are able to account reasonably well for the uncertainties regarding both pH and Mg/Ca_{sw}, the exact expression of the Mg/Ca-temperature calibration remains the largest source of uncertainty for deep-time Mg/Ca-based temperature reconstructions. Therefore, we also perform our calculations with two different Mg/Ca-temperature relationships (Supplementary Figure 7). First, we followed the Mg/Ca-temperature relationships outlined in Evans et al. (2018), which are based on the Anand et al. (2003) calibration and account for changes in both pH (Evans et al., 2016b) and Mg/Ca_{sw} (Evans et al., 2016a). These Mg/Ca-temperature relationships have been used by Evans et al. (2018) to recalculate existing Mg/Ca-derived temperatures for Eocene planktonic foraminifera and are expressed as:

$$T = \frac{1}{A}\ln\left(\frac{Mg/Ca_{norm}}{B}\right) \quad (9)$$

$$Mg/Ca_{norm} = \frac{Mg/Ca_{foram}}{\frac{0.66}{1+\exp\left(6.9\cdot(pH-8.0)\right)}+0.76} \quad (10)$$

$$B = 0.019 \cdot Mg/Ca_{sw}{}^{2} - 0.16 \cdot Mg/Ca_{sw} + 0.804 \quad (11)$$

$$A = -0.0029 \cdot Mg/Ca_{sw}{}^{2} + 0.032 \cdot Mg/Ca_{sw} \quad (12)$$

For a direct comparison of temperature estimates we again use pH = 7.8 and Mg/Ca_{sw} = 2.25 mmol/mol, similar to the scenario outlined above for the Gray et al. (2018) calibration.

Second, we test the widely applied calibration of Anand et al. (2003), with modifications for changing Mg/Ca_{sw} following Evans and Müller (2012). This Mg/Ca-temperature relationship has, for instance, been used for foraminiferal Mg/Ca records of the PETM (Dunkley Jones et al., 2013; Frieling et al., 2017) and is expressed as:

$$T = \frac{1}{A}\ln\left(\frac{Mg/Ca_{foram}}{B}\frac{\left[Mg/Ca_{sw,t_0}\right]^{H}}{\left[Mg/Ca_{sw,t}\right]^{H}}\right) \quad (13)$$

We use the default values of A = 0.09 and B = 0.38 following Anand et al. (2003), as well as Mg/Ca_{sw} (t) = 2.25 mmol/mol, Mg/Ca_{sw} (t_o) = 5.2 mmol/mol and H = 0.42 for consistency.

Importantly, these alternative Mg/Ca-temperature relationships both yield very similar temperature estimates for our observed range of Mg/Ca_{foram} values (Supplementary Figure 7), but the resulting temperatures are ~5 °C higher than those obtained from the Mg/Ca-temperature calibration of Gray et al. (2018). This large difference has implications for

previous Mg/Ca-based temperature records that are calculated with the Anand et al. (2003) calibration.

6.2.10 Biomarker paleothermometry

For a total of 53 samples from Sites U1408 and U1410, lipids were extracted from 4–6 g freeze-dried and powdered sediment with dichloromethane (DCM):methanol (MeOH) (9:1, v/v) using a Dionex accelerated solvent extractor (ASE 350) at a temperature of 100 °C and a pressure of 7.6×10^6 Pa. Lipid extracts were separated into an apolar, ketone and polar fraction by Al_2O_3 column chromatography using hexane:DCM (9:1), hexane:DCM (1:1) and DCM:MeOH (1:1) as respective eluents. 99 ng of a synthetic C_{46} (m/z = 744) glycerol dialkyl glycerol tetraether (GDGT) standard was added to the polar fraction, which subsequently was dissolved in hexane:isopropanol (99:1, v/v) to a concentration of ~3 mg/mL and passed through a 0.45 µm polytetrafluoroethylene filter. This fraction was then analyzed by high-performance liquid chromatography (HPLC) and atmospheric pressure chemical ionization–mass spectrometry using an Agilent 1260 Infinity series HPLC system coupled to an Agilent 6130 single-quadrupole mass spectrometer at UU following Hopmans et al. (2016) to measure the abundance of GDGTs. The branched and isoprenoid tetraether (BIT) index and TEX_{86} values were calculated according to Hopmans et al. (2004) and Kim et al. (2010), respectively. Temperatures were calculated with the logarithmic TEX_{86}^H calibration, which has an associated calibration uncertainty of ~2.5 °C (Kim et al., 2010). The long-term analytical precision for TEX_{86} at UU based on replicate analyses of an in-house standard is ± 0.3 °C.

Several ratios between the different isoprenoid GDGTs were calculated to assess sourcing by microbes other than surface ocean-dwelling marine Thaumarchaeota. Methane Index (Zhang et al., 2011) (MI) and GDGT-2/crenarchaeol (Weijers et al., 2011) and GDGT-0/crenarchaeol (Blaga et al., 2009) values indicate no large contributions by methanotrophic or methanogenic archaea. Furthermore, GDGT-2/GDGT-3 ratios are <5, indicating that the TEX_{86} signal is not affected by deep-water production. However, branched and isoprenoid tetraether (BIT) index values are very high (0.69 ± 0.11, 1σ). The composition of the brGDGTs, and in particular very low $\#rings_{tetra}$ index values (0.08 ± 0.01, 1σ), suggests them to be soil-derived (Sinninghe Damsté, 2016).

Furthermore, 15 ketone fraction extracts were analyzed for alkenone abundance at NIOZ. These ketone fractions were analyzed for LCAs on an Agilent 6890N gas chromatograph (GC) with flame ionization detection (FID) after dissolving in ethyl acetate. The GC was equipped with a fused silica column with a length of 50 m, a diameter of 0.32 mm, and a coating of CP Sil-5 (film thickness = 0.12 µm). Helium was used as carrier gas, and the flow mode was a constant pressure of 100 kPa. The ketone fractions were injected on-column at a starting temperature of 70 °C, which increased by 20 °C/min to 200 °C followed by 3 °C/min until the final temperature of 320 °C was reached. This end temperature was held for 25 min. Selected fractions were analyzed by GC–mass spectrometry (MS) using an Agilent 7890B gas chromatograph coupled to an Agilent 5977A mass spectrometer. The starting temperature was 70 °C, and increased to 130 °C by 20 °C/min, followed by a linear gradient of 4 °C/min to an end temperature of 320 °C, which was held for 25 min. 1µL was injected, and separation was achieved on a fused silica column (25 m × 0.32 mm) coated with CP Sil-5 (film thickness 0.12 µm). Helium was used as carrier gas with a constant flow of 2 mL/min. The MS operated with an ionization energy of 70 eV. Identification of alkenones was done in full scan mode, scanning between m/z 50–850.

Alkenones could be detected in most analyzed ketone fractions. However, these alkenones consisted only of the $C_{37:2}$ and $C_{38:2}$ alkenones, yielding $U^{K'}_{37} = 1$ (proxy saturation) and hence sea surface temperatures of at least 28 °C (Tierney and Tingley, 2018).

6.2.11 Stratigraphy and age models

We have tentatively used the astronomically tuned age model of Boulila et al. (2018) to assign ages to Site U1408 and U1410 sediments. However, this age model is presently insufficient for the construction of a robust composite record for the MECO interval that incorporates sections from both sites.

6.3 Results

6.3.1 Foraminifera-based reconstructions

Our combined, multi-species $\delta^{18}O$ record shows a total decrease of ~1‰ across the MECO interval (Figure 2a), which is similar in magnitude to most other Atlantic Ocean and Southern Ocean records (Bohaty and Zachos, 2003; Bohaty et al., 2009). Notably, this $\delta^{18}O$ decrease is characterized by several distinct minima and maxima, rather than the more continuous decrease that has been observed in the other records at lower resolution (Bohaty and Zachos, 2003; Bohaty et al., 2009). These variations in $\delta^{18}O$ may hint at orbital forcing, potentially from the obliquity cycle (Boulila et al., 2018; Vahlenkamp et al., 2018), but resolving detailed relationships between orbital parameters and surface ocean warming would require an even higher resolution dataset. We further observe a gradual increase in $\delta^{13}C$ of ~1‰ across the event that is similar to the other records (Figure 2b). Given the relatively consistent offsets between the $\delta^{18}O$ and $\delta^{13}C$ values of *A. (prae-)topilensis* and *Gk. index* across the MECO,

Figure 2 (right): MECO stable isotope and temperature records from Site U1408. a, $\delta^{18}O$ and b, $\delta^{13}C$ records for A. (prae-)topilensis (in red), A. bullbrooki (in purple) and Gk. index (in blue). c, Δ_{47}-derived temperatures for A. (prae-)topilensis (in dark red), A. bullbrooki (in dark purple) and Gk. index (in dark blue). Diamonds represent weighted means of clustered measurements, with vertical error bars indicating 2 standard errors of the mean (2SE) and horizontal error bars indicating age ranges of the included measurements. Curves represent the median (thick solid lines), 68% confidence intervals (dark shaded areas) and 95% confidence intervals (light shaded areas) of LOESS fits to Monte Carlo simulations of Δ_{47}-derived temperatures (n = 1000) in which the associated analytical uncertainties are fully propagated (see Methods). The dashed part of the smoothed A. (prae-)topilensis record indicates the interval between 40.2 and 40.0 Ma where data density is very low and insufficient for precise temperature estimates. For clarity, Δ_{47} data from A. bullbrooki were not included in the Monte Carlo simulations. d, Mg/Ca-derived temperatures for A. (prae-)topilensis (in orange) and Gk. index (in light blue) based on the Mg/Ca-temperature relationships of Gray et al. (2018), with modifications following Evans and Müller (2012). Squares represent estimates from individual samples based on most probable Middle Eocene values for the salinity, pH and Mg/Ca composition of seawater. Curves represent the median (thick solid lines), 68% confidence intervals (dark shaded areas) and 95% confidence intervals (light shaded areas) of LOESS fits to Monte Carlo simulations of Mg/Ca-derived temperatures (n = 1000) in which the analytical uncertainties and uncertainties regarding salinity, pH and Mg/Ca_{sw} are fully propagated (see Methods). e, TEX_{86}^{H}-derived temperatures (in purple) and $U^{K'}_{37}$-derived temperatures (in green), with the solid purple line representing a LOESS fit. Calibration uncertainties for temperatures based on TEX_{86}^{H} are ~2.5 °C (not shown). $U^{K'}_{37}$ was at proxy saturation in all samples where alkenones could be detected, so the resulting temperatures represent absolute minimum estimates upwards of 28 °C, as indicated by arrows. All records are plotted against age following Boulila et al. (2018).

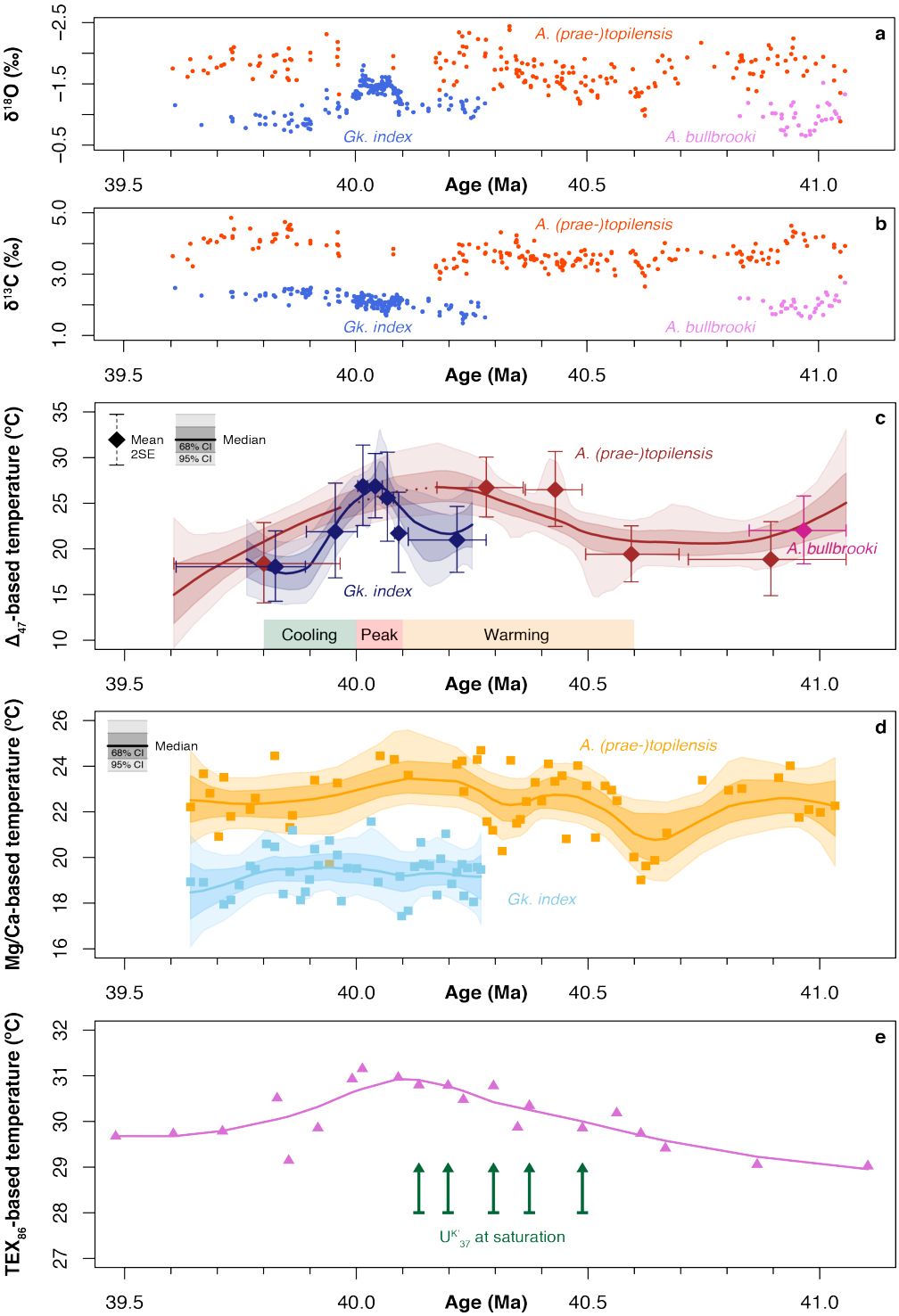
δ18O (‰)
−2.5
−1.5
−0.5
A. (prae-)topilensis
Gk. index
A. bullbrooki
a
39.5
40.0
Age (Ma)
40.5
41.0
δ13C (‰)
5.0
3.0
1.0
A. (prae-)topilensis
Gk. index
A. bullbrooki
b
39.5
40.0
Age (Ma)
40.5
41.0
Δ47-based temperature (°C)
35
30
25
20
15
10
Mean
2SE
68% CI
95% CI
Median
A. (prae-)topilensis
A. bullbrooki
Gk. index
Cooling
Peak
Warming
c
39.5
40.0
Age (Ma)
40.5
41.0
Mg/Ca-based temperature (°C)
26
24
22
20
18
16
68% CI
95% CI
Median
A. (prae-)topilensis
Gk. index
d
39.5
40.0
Age (Ma)
40.5
41.0
TEX86-based temperature (°C)
32
31
30
29
28
27
UK'37 at saturation
e
39.5
40.0
Age (Ma)
40.5
41.0

we find no evidence for migration of *A. (prae-)topilensis* to greater depths in response to progressive warming (Si and Aubry, 2018).

We present our Δ_{47}-based temperature estimates in two ways: (1) as temperature clusters based on weighted Δ_{47} averages of neighboring measurements and (2) as smoothed, continuous records based on Monte Carlo simulations of temperatures and their associated uncertainties from individual Δ_{47} measurements (Figure 2c; see Methods; Supplementary Figure 4). For *A. bullbrooki*, which is only abundantly present in the oldest part of the record, we obtain temperatures of ~22 ± 4 °C (2SE) at ~ 41 Ma. Interestingly, we obtain very similar temperatures for *A. (prae-)topilensis* in this part of the record, despite a clear offset in the $\delta^{18}O$ values between the two species groups. We further reconstruct *A. (prae-)topilensis*-derived temperatures of ~20 ± 3 °C (95% CI) in the pre-MECO interval just before ~40.5 Ma, temperatures of ~26 ± 5 °C (95% CI) roughly midway through MECO warming at 40.2 Ma and temperatures of ~21 ± 3 °C (95% CI) in the post-MECO interval at 39.8 Ma. Unfortunately, the near absence of *A. (prae-)topilensis* between 40.2 and 40.0 Ma impedes reliable temperature reconstructions in the peak warming phase of the MECO based on this species group. This may either be related to carbonate dissolution during peak MECO, as carbonate content is generally low in this interval, or potentially to symbiont bleaching (Edgar et al., 2013). However, *Gk. index* is sufficiently present in this interval to capture the full extent of MECO warming and yields temperatures of ~22 ± 4 °C (95% CI) at 40.2 Ma, ~26 ± 4 °C (95% CI) at 40.0 Ma and ~18 ± 4 °C (95% CI) at 39.8 Ma. These *Gk. index*-derived temperatures are mostly lower than the *A. (prae-) topilensis*-derived temperatures, which is consistent with the offset between the $\delta^{18}O$ records of these two species groups – except for the peak MECO interval. This apparent convergence between *Gk. index*-derived temperatures and *A. (prae-)topilensis*-derived temperatures at ~40.0 Ma suggests that the *A. (prae-)topilensis* record most likely underestimates temperatures during peak MECO warmth. Hence, we infer a conservative estimate of total surface mixed-layer warming of ~5 °C across the event based on Δ_{47}.

In addition, we present absolute Mg/Ca-based temperature estimates based on *A. (prae-) topilensis* and *Gk. index* using Mg/Ca-temperature relationships that account for the effects of changes in salinity, pH and the Mg/Ca composition of seawater (Mg/Ca_{sw}) relative to present-day conditions (Evans and Müller, 2012; Gray et al., 2018) (Figure 2d; see Methods; Supplementary Figure 5; Supplementary Figure 6; Supplementary Figure 7). We employ Monte Carlo simulations to propagate the associated analytical uncertainties and a range of probable Middle Eocene salinity, pH and Mg/Ca_{sw} values, and test for the impact of using different Mg/Ca-temperature calibrations. The resulting Mg/Ca-based records yield similar overall temperatures to the Δ_{47}-based records, but with a more subdued MECO warming. For *A. (prae-)topilensis* we obtain temperatures of ~21 ± 2 °C at 40.6 Ma and ~23 ± 2 °C at 40.1 Ma, which would suggest a total surface mixed-layer warming of ~2 °C. For *Gk. index*, however, we find no significant signs of warming. Instead, we observe temperatures between 19 ± 2 °C and 20 ± 2 °C across the entire studied interval.

6.3.2 Biomarker-based reconstructions

Our TEX_{86}-based record yields the highest sea surface temperatures of all proxies (Figure 2e; see Methods). However, we find very high branched versus isoprenoid tetraether (BIT) index values (0.69 ± 0.11, 1σ) throughout the studied interval (Supplementary Figure 8), indicating that these TEX_{86}-based temperatures could be biased by contributions from soil-derived isoprenoid GDGTs (Weijers et al., 2006). Yet, we find no distinct relationship between BIT

and TEX_{86}, which suggests that the high supply of branched GDGTs did not (indirectly) force trends in TEX_{86}. For the observed range of TEX_{86} values (0.7–0.8), both the logarithmic TEX_{86}^{H} calibration (Kim et al., 2010) and the linear BAYSPAR calibration (Tierney and Tingley, 2014) would result in very similar absolute temperature estimates – here we use the logarithmic TEX_{86}^{H} calibration for simplicity. We reconstruct pre-MECO temperatures of ~30 ± 2.5 °C at 40.5 Ma and peak MECO temperatures of ~31 ± 2.5 °C at 40.0 Ma, which suggests a very modest sea surface warming of only ~1 °C. Moreover, we obtain $U^{K'}_{37}$ values that are consistently at saturation where alkenones could be detected, implying sea surface temperatures of at least 28 °C (Figure 2e; see Methods). Similarly high $U^{K'}_{37}$ values in this part of the North Atlantic around 40 Ma have also been reported from the nearby Site U1404 (Liu et al., 2018). Together, these lines of evidence suggest that the high absolute sea surface temperatures derived from TEX_{86} may be relatively robust.

6.4 Discussion

6.4.1 Reconciling proxy differences

The first implication of our results, irrespective of differences in absolute temperatures between proxy records, is that North Atlantic sea surface temperatures rose during the MECO. Importantly, this reinforces the hypothesis that the MECO was a global warming event and, by extension, favors CO_2 rise and greenhouse warming as the most likely driver for the MECO – as opposed to large-scale circulation changes leading to warming predominantly in the southern hemisphere. The unique potential of our new Δ_{47}-based temperature record, however, is that the estimates from the other proxies and the underlying assumptions can now be further resolved, both in terms of absolute temperatures and the total magnitude of warming.

In general, our biomarker-based reconstructions result in higher absolute temperatures for the studied interval than our foraminifera-based reconstructions. Although temperature proxies may disagree for a variety of reasons, it is likely that part of this difference is related to proxies reflecting temperatures from different water depths and/or seasons. In particular, $U^{K'}_{37}$ may be biased towards summer temperatures relative to the other proxies (Tierney and Tingley, 2018) and GDGT fluxes are likely highest in the (summer) season of highest productivity (Wuchter et al., 2006). Additionally, GDGTs and alkenones accumulating in sediment drifts may be strongly affected by lateral transport in comparison to planktonic foraminifera (Ohkouchi et al., 2002) and could therefore be sourced from warmer regions in the North Atlantic. Moreover, TEX_{86} and $U^{K'}_{37}$ are calibrated to reflect sea surface temperatures (i.e., 0 m water depth), while the planktonic foraminifera-based proxies reflect more integrated surface mixed-layer conditions (Ho and Laepple, 2016; Si and Aubry, 2018). Such offsets between absolute temperatures derived from TEX_{86}, Mg/Ca and $\delta^{18}O$ have also been recognized in other deep-time paleoclimate reconstructions for the Eocene, the PETM and the latest Cretaceous (Hollis et al., 2012; Frieling et al., 2017; Woelders et al., 2018).

The most striking feature in our records, however, is that the majority of our Δ_{47}-based estimates yield significantly lower absolute temperatures but more pronounced temperature change across the MECO compared to the other proxies, including Mg/Ca-based estimates derived from the same sets of foraminiferal specimens. Despite the overall excellent quality of foraminiferal preservation in the studied interval (Supplementary Figure 2), it is possible that some of our Δ_{47}-based temperatures may be biased towards lower values due to some form of diagenetic alteration during burial (Stolper et al., 2018). However, we do not find anomalous

$\delta^{18}O$ values to further support this (Pearson et al., 2001). Solid state clumped isotope bond reordering would theoretically be able to change Δ_{47} without affecting $\delta^{18}O$, but this is highly unlikely given the shallow burial depth of the study sites (Passey and Henkes, 2012). Moreover, an ongoing study testing the effects of diagenetic alteration on planktonic foraminiferal Δ_{47} from the Newfoundland Drifts (sites U1408, U1409 and U1410) found no detectable impact of diagenetic alteration (Leutert et al., in prep.). Alternatively, selective dissolution of Mg from foraminiferal tests could result in Mg/Ca-based temperatures that are biased towards lower temperatures (Regenberg et al., 2014), particularly in the interval of very low carbonate content towards the peak of the MECO between 40.2 and 40.0 Ma. Evaluation of our coupled Δ_{47} and Mg/Ca values relative to the Δ_{47}-Mg/Ca relationships expected from their respective temperature calibrations (Breitenbach et al., 2018) would be a way to potentially resolve this (Supplementary Figure 9), but we cannot make definitive inferences due to the large uncertainties involved in deep-time Mg/Ca-temperature reconstructions (Mg/Ca-temperature relationships, salinity, pH and Mg/Ca_{sw}; see Methods).

6.4.2 Salinity reconstructions

Our temperature records also allow us to reconstruct hydrographic change in the North Atlantic by reliably extracting the $\delta^{18}O$ composition of surface ocean seawater ($\delta^{18}O_{sw}$) from our foraminiferal $\delta^{18}O$ records (see Methods). We use our Δ_{47}-based temperature records for

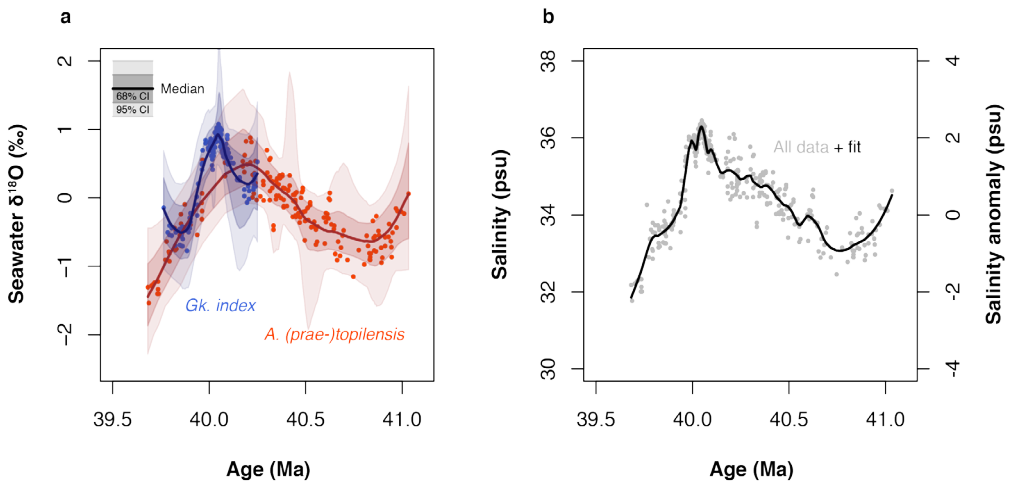

Figure 3: MECO seawater $\delta^{18}O$ and sea surface salinity reconstructions from Site U1408. a, $\delta^{18}O_{sw}$ reconstructions based on $\delta^{18}O$ values and Δ_{47}-derived temperatures for A. (prae-)topilensis (in red) and Gk. index (in blue), using the $\delta^{18}O$-temperature calibration of Erez and Luz (1983). Circles represent $\delta^{18}O_{sw}$ estimates from individual $\delta^{18}O$ values (Figure 2a) and median Δ_{47}-based temperatures (Figure 2c). Curves represent the median (thick solid lines), 68% confidence intervals (dark shaded areas) and 95% confidence intervals (light shaded areas) of LOESS fits to $\delta^{18}O_{sw}$ estimates based on individual $\delta^{18}O$ values and the full range of Monte Carlo simulations of Δ_{47}-derived temperatures (Figure 2c). b, Sea surface salinity reconstructions based on $\delta^{18}O_{sw}$ estimates (Figure 3a) and the modern $\delta^{18}O_{sw}$-salinity relationship of the Atlantic Ocean (Ostlund et al., 1987), presented as absolute values and anomalies relative to S = 34 psu. Grey circles represent estimates from all individual $\delta^{18}O_{sw}$ values and the black line represents a LOESS fit to these combined estimates.

this purpose, because Δ_{47} is least affected by systematic uncertainty of all proxies presented here. We find considerable changes in $\delta^{18}O_{sw}$ across the studied interval, from a pre-MECO value of approximately –0.5‰ to a value of 1‰ during peak MECO warming (Figure 3a). This pre-MECO $\delta^{18}O_{sw}$ value of –0.5‰ is fairly similar to estimates obtained from the present-day latitudinal surface ocean $\delta^{18}O_{sw}$ gradient with corrections for latitude and ice-volume (Zachos et al., 1994), and is also reproduced in general circulation model simulations of the Eocene (Tindall et al., 2010). However, the large ~1.5‰ shift to heavier $\delta^{18}O_{sw}$ values during the MECO implies that assumptions of constant $\delta^{18}O_{sw}$ under ice-free conditions – as often applied in $\delta^{18}O$-based reconstructions of absolute temperatures across Eocene warming events (Pearson, 2012) – are unjustified for this oceanographic setting.

Finally, we use our $\delta^{18}O_{sw}$ records to estimate changes in sea surface salinity (see Methods). We reconstruct salinity values ranging from 32–36 psu based on present-day $\delta^{18}O_{sw}$-salinity relationships for the Atlantic Ocean and estimate a conservative salinity increase of ~2.5 psu during the MECO (Figure 3b). These shifts towards heavier surface ocean $\delta^{18}O_{sw}$ and salinity during MECO warming may best be explained by the northward expansion of warm waters from the North Atlantic gyre (Schmidt, 1999; Tindall et al., 2010). Similar patterns of warming and salinization have been inferred at low-mid latitude sites for the PETM and ETM-2 hyperthermals (Zachos et al., 2003; Harper et al., 2018).

6.5 Conclusions

We present novel, high-resolution records of surface ocean temperatures based on well-preserved planktonic foraminifera and biomarker distributions across the Middle Eocene Climatic Optimum (MECO) from the Newfoundland Drifts in the North Atlantic. The integration of temperature estimates from Δ_{47}, $\delta^{18}O$, Mg/Ca, TEX_{86} and $U^{K'}_{37}$ allows for an unprecedented comparison of the robustness of the available temperature proxies and their associated uncertainties, both in terms of absolute temperatures and the amplitude of warming and cooling. During the MECO, we document 3–5 °C of surface mixed-layer warming based on $\Delta_{47,}$ ~2 °C of warming based on Mg/Ca and ~1 °C of sea surface warming based on TEX_{86}. This provides strong evidence that the North Atlantic warmed during the MECO and that the event was a truly global phenomenon. Moreover, this global extent implies that increasing atmospheric CO_2 concentrations are the most likely driver of the MECO warming. However, the reconstructed absolute temperatures differ substantially between proxies. Part of this difference could reflect that biomarker-based proxies are recording temperatures from different water depths and/or seasons than the foraminifer-based proxies, but given the nature of drift sedimentation at the study sites it is likely that the biomarker-based proxies are also affected by lateral transport from warmer source regions. Importantly, if our Δ_{47}-derived temperatures are taken at face value, the discrepancy between our Δ_{47}-based temperatures and Mg/Ca-based temperatures suggests that deep-time Mg/Ca-temperature relationships and their associated assumptions may need to be revisited. Nevertheless, part of the difference between Δ_{47} and the other proxies may still arise from the analytical uncertainties associated with Δ_{47} paleothermometry – even at the present resolution of our Δ_{47} dataset. Such uncertainties could be greatly reduced by further increasing the resolution of our records.

Acknowledgements

This research used samples provided by the Integrated Ocean Drilling Program (IODP). This work was carried out under the program of the Netherlands Earth System Science Centre

(NESSC), which is financially supported by the Ministry of Education, Culture and Science (OCW) of the Netherlands. We thank Paul Pearson (Cardiff University) for discussions on foraminiferal taxonomy. We further acknowledge Anne Roepert (Utrecht University), Arnold van Dijk (Utrecht Geolab) and Wim Boer and Marcel van der Meer (NIOZ) for laboratory assistance and analytical support.

Data availability

All data presented in this study will be made available upon publication in a scientific journal.

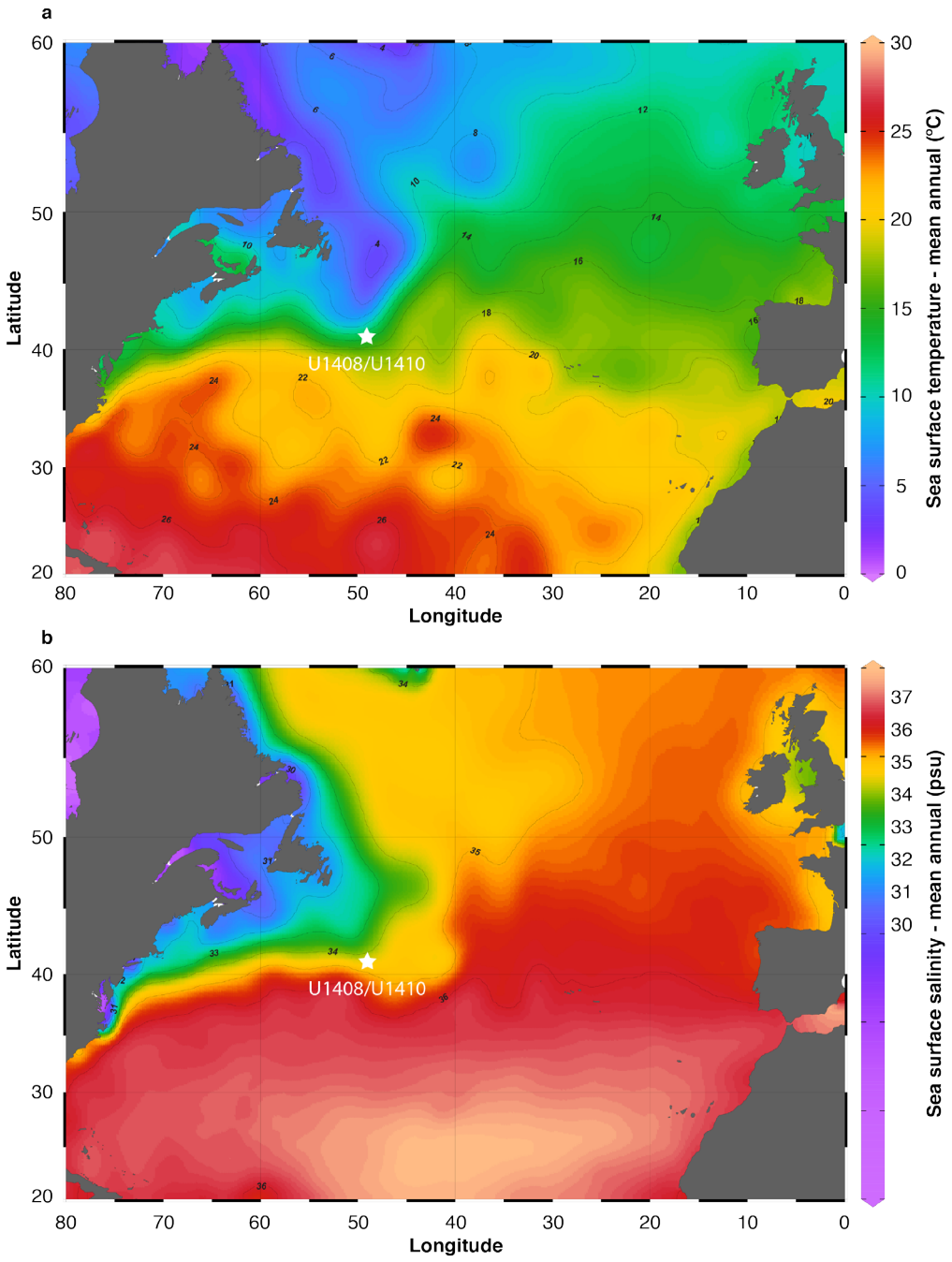

Supplementary Figure 1: Present-day North Atlantic sea surface conditions. a, Mean annual sea surface temperature. b, Mean annual sea surface salinity. Map made with Ocean Data View (Schlitzer, 2015). The locations of Sites U1408 and U1410 are indicated by the white star.

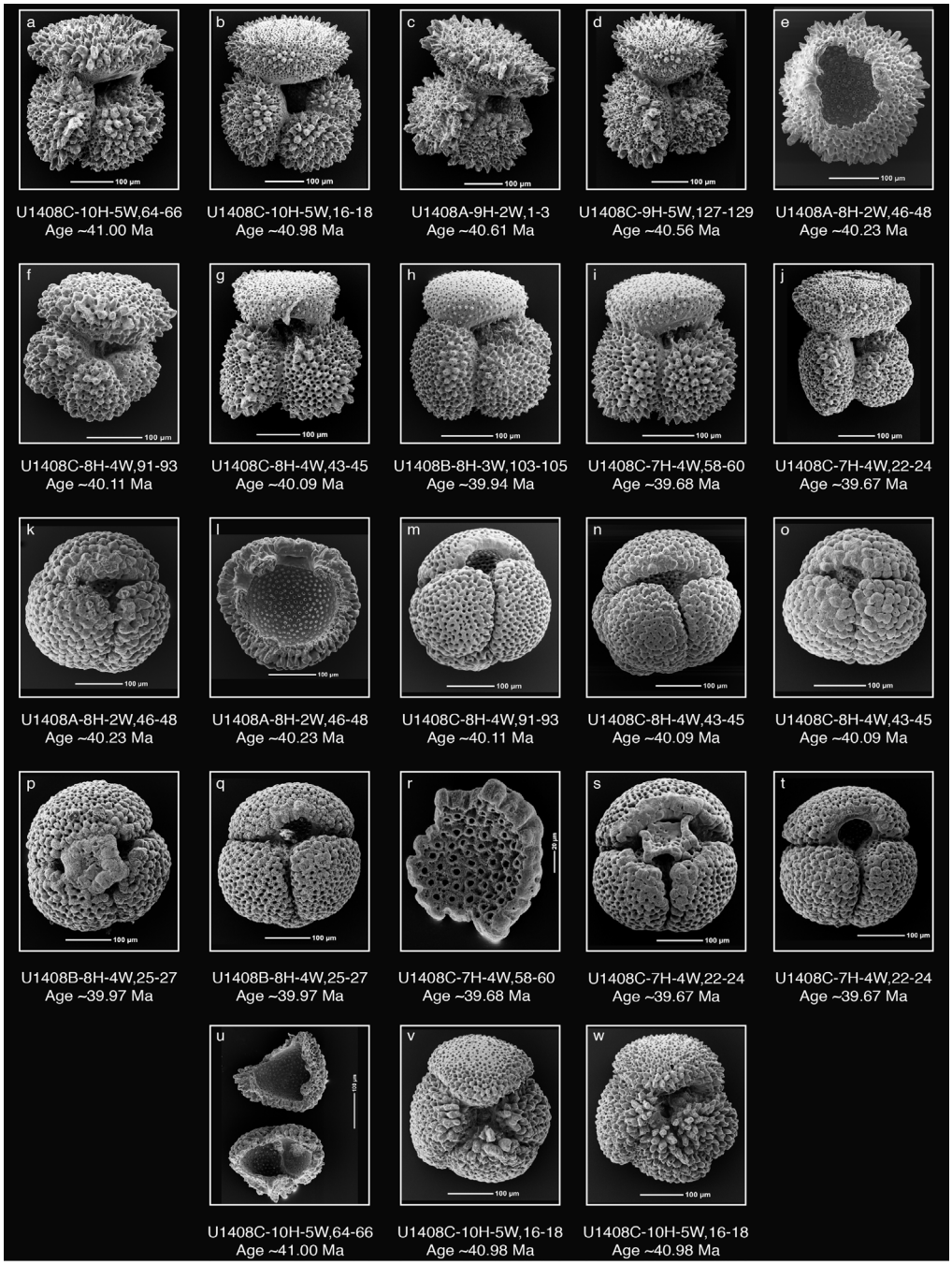

Supplementary Figure 2: Scanning electron microscope (SEM) images of representative specimens of planktonic foraminifera from the studied interval at Site U1408. a-j, *A. (prae-)topilensis*, k-t, *Gk. index*. u-w, *A. bullbrooki*. Sample information and the corresponding ages following Boulila et al. (2018) are included.

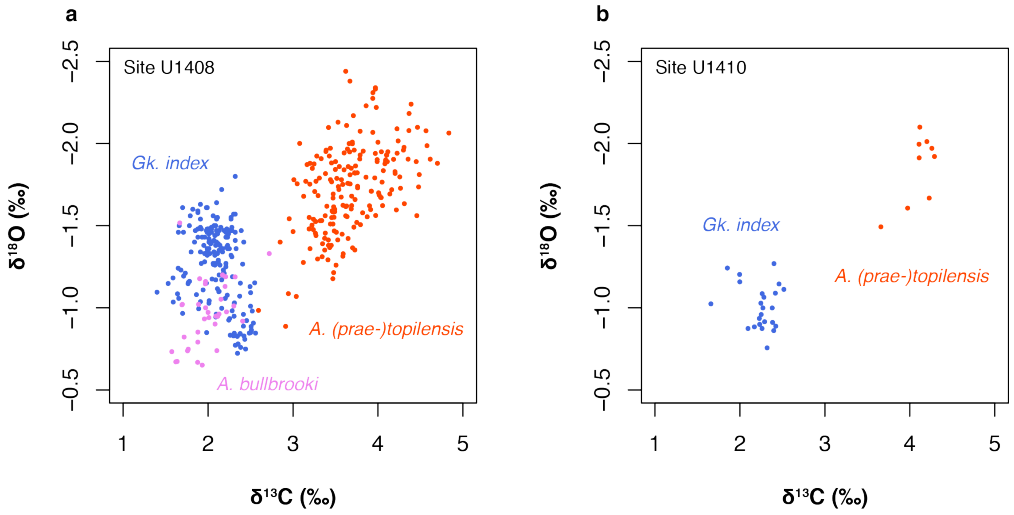

Supplementary Figure 3: $\delta^{18}O$ and $\delta^{13}C$ relationships for the three species groups included in this study. a-b, $\delta^{18}O$ and $\delta^{13}C$ data for *A. (prae-)topilensis* (in red), *A. bullbrooki* (in purple) and *Gk. index* (in blue) from Sites U1408 and U1410.

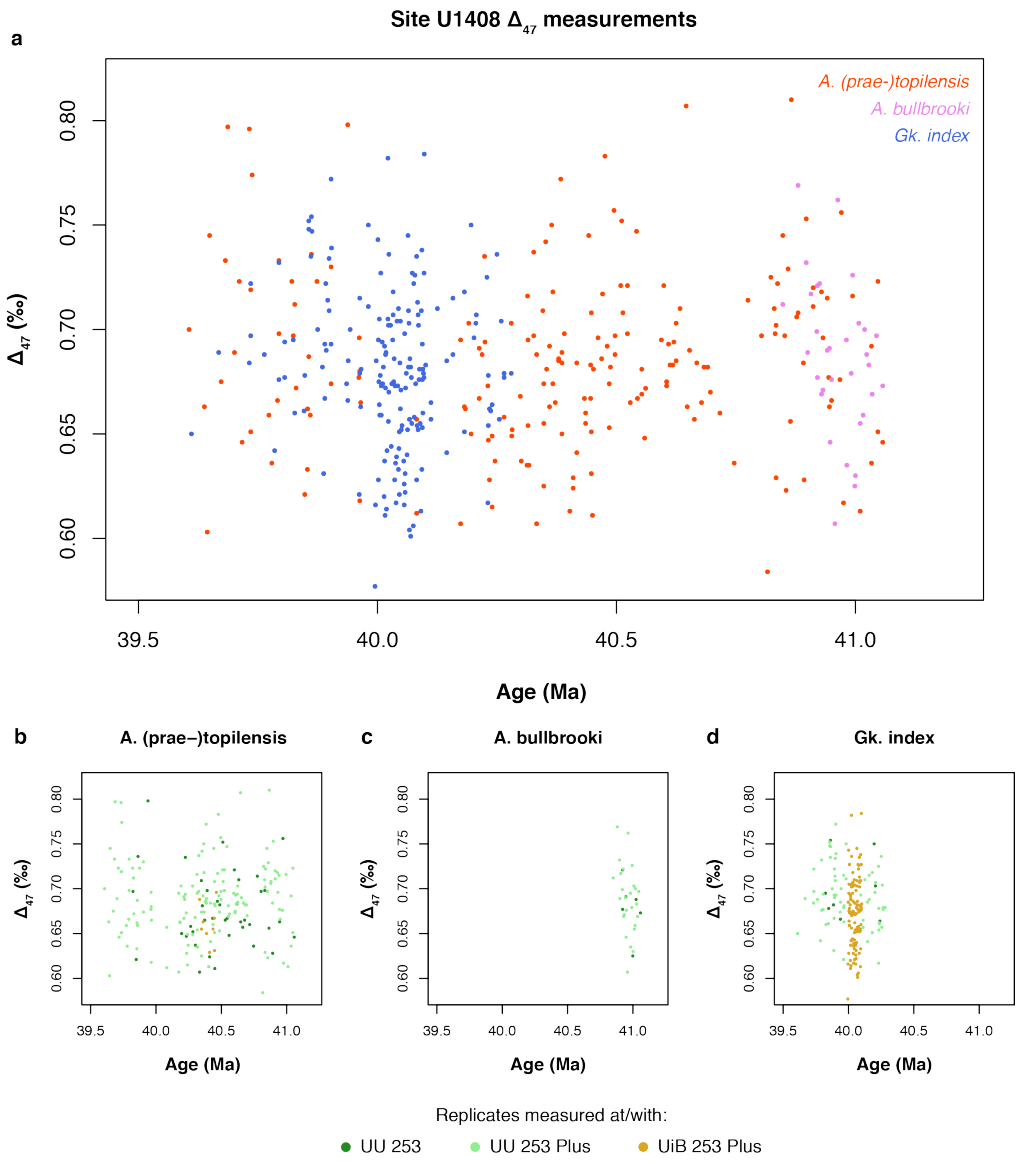

Supplementary Figure 4: Overview of raw Δ_{47} data for Site U1408. a, Δ_{47} replicates for *A. (prae-)topilensis* (in red), *A. bullbrooki* (in purple) and *Gk. index* (in blue), plotted against age following Boulila et al. (2018). b–d, Δ_{47} replicates for each individual species group, with colors indicating the instrument on which they were measured: UU 253 (in dark green), UU 253 Plus (in light green) and UiB 253 Plus (in brown).

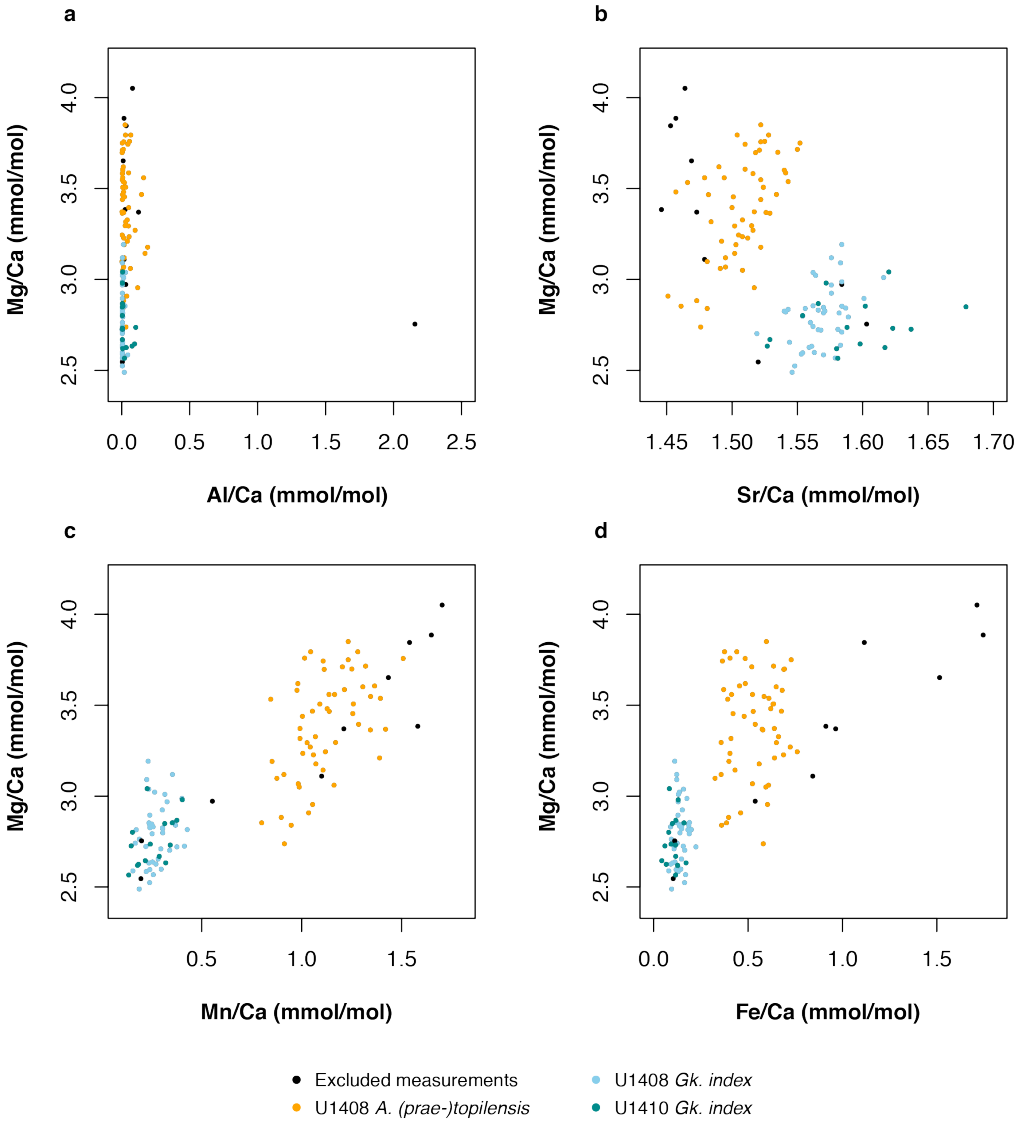

Supplementary Figure 5: Relationships between Mg/Ca and other trace element ratios. a, Mg/Ca versus Al/Ca for *A. (prae-)topilensis* from Site U1408 (in orange), *Gk. index* from Site U1408 (in lightblue) and *Gk. index* from Site U1410 (in greenish blue). b, Mg/Ca versus Sr/Ca. c, Mg/Ca versus Mn/Ca. d, Mg/Ca versus Fe/Ca. All concentrations are in mmol/mol. Measurements excluded on the basis of the criteria described in the Methods are shown in black.

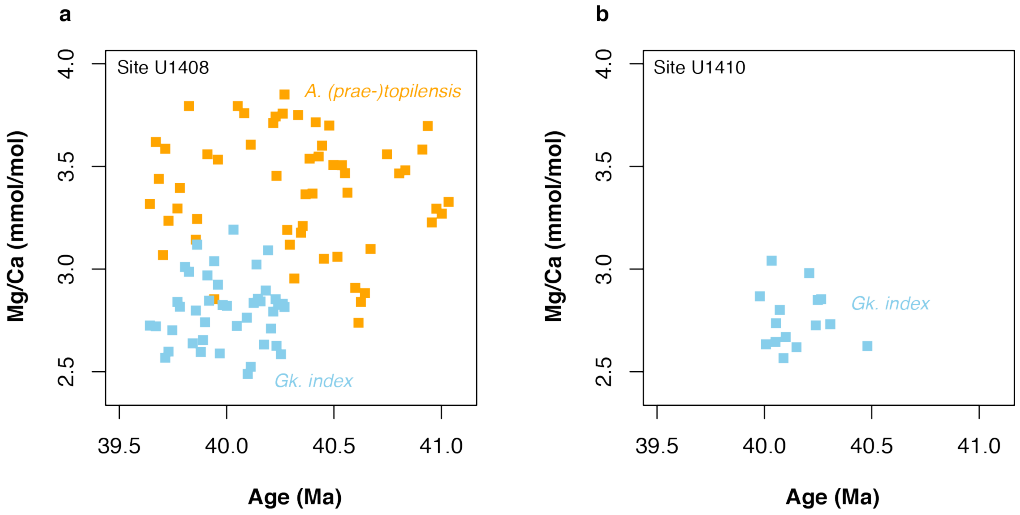

Supplementary Figure 6: Mg/Ca records after trace element screening. a-b, Mg/Ca records for *A. (prae-)topilensis* (in orange) and *Gk. index* (in light blue) from Site U1408 and U1410, plotted against age following Boulila et al. (2018). All concentrations are in mmol/mol.

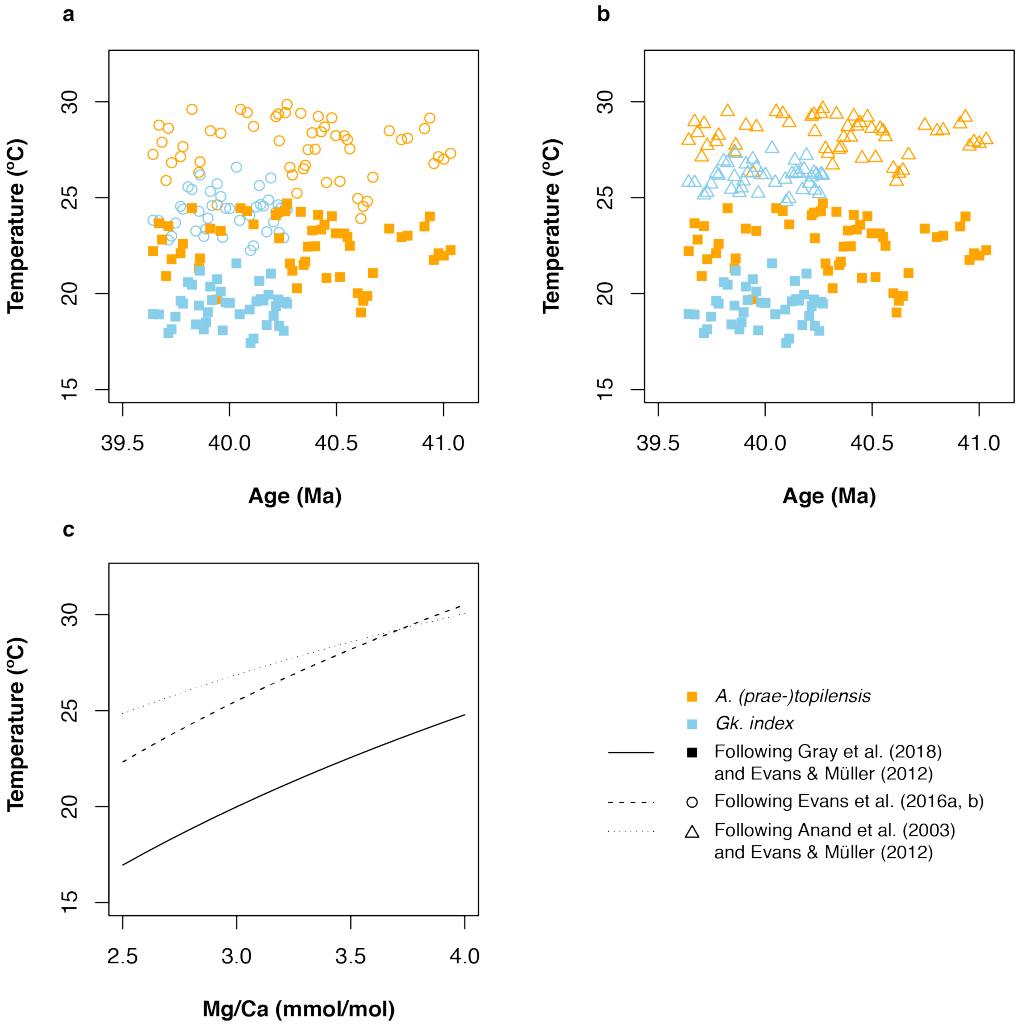

Supplementary Figure 7: Sensitivity of Mg/Ca-based temperature reconstructions to different Mg/Ca-temperature relationships. a-c, Site U1408 temperatures for *A. (prae-)topilensis* (in orange) and *Gk. index* (in light blue), plotted against age following Boulila et al. (2018). Temperatures are calculated with the Mg/Ca-temperature relationships of Gray et al. (2018) with modifications based on Evans and Müller (2012) (filled squares/solid line), Evans et al. (2016b, 2016a) (open circles/dashed line), or Anand et al. (2003) with modifications based on Evans and Müller (2012) (open triangles/dotted line). Mg/Ca-temperature relationships based on pH = 7.8, Mg/Ca_{sw} = 2.25 mmol/mol and S = 34 psu. See Methods for further details.

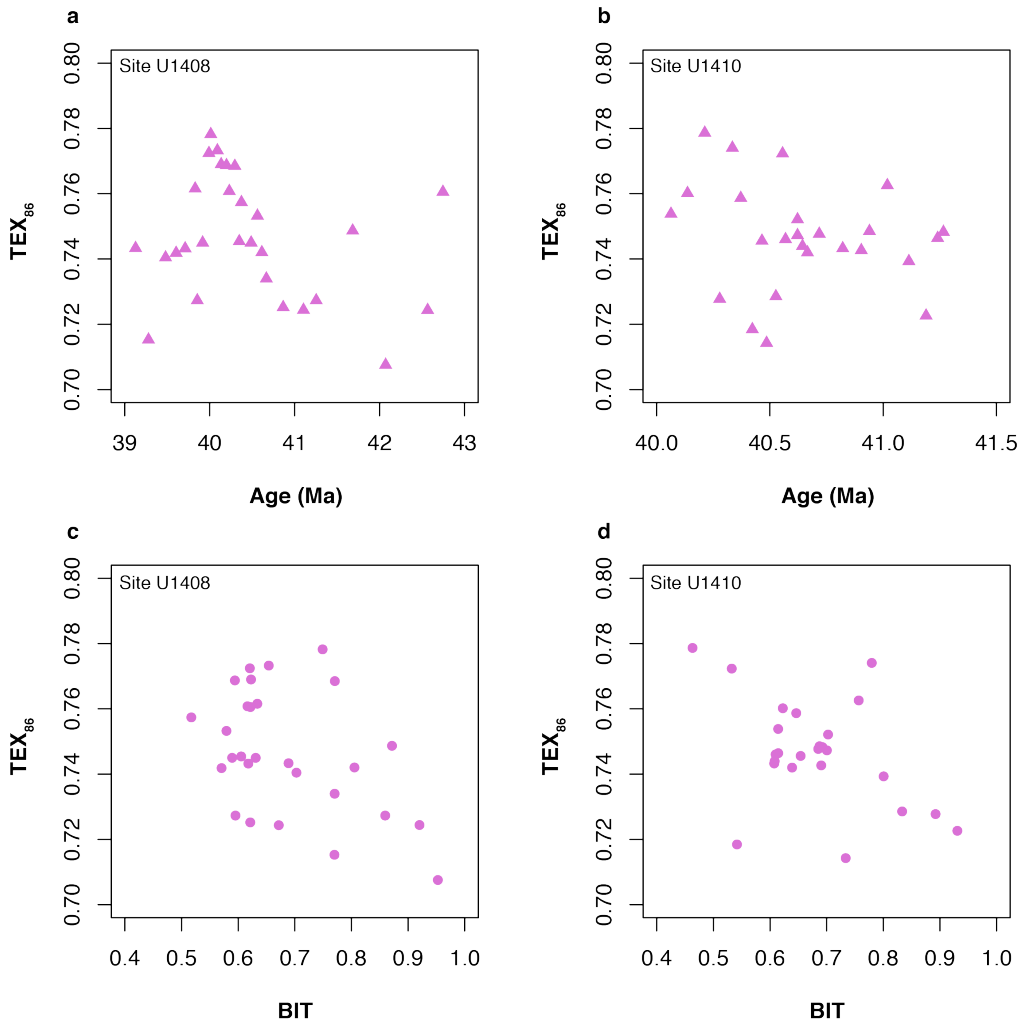

Supplementary Figure 8: TEX_{86} records and relationships between TEX_{86} and BIT. a-b, TEX_{86} records from Site U1408 and U1410, plotted against age following Boulila et al. (2018). c-d, TEX_{86}-BIT relationships from Site U1408 and U1410. Despite the very high absolute BIT values, there is no observable dependency between TEX_{86} and BIT.

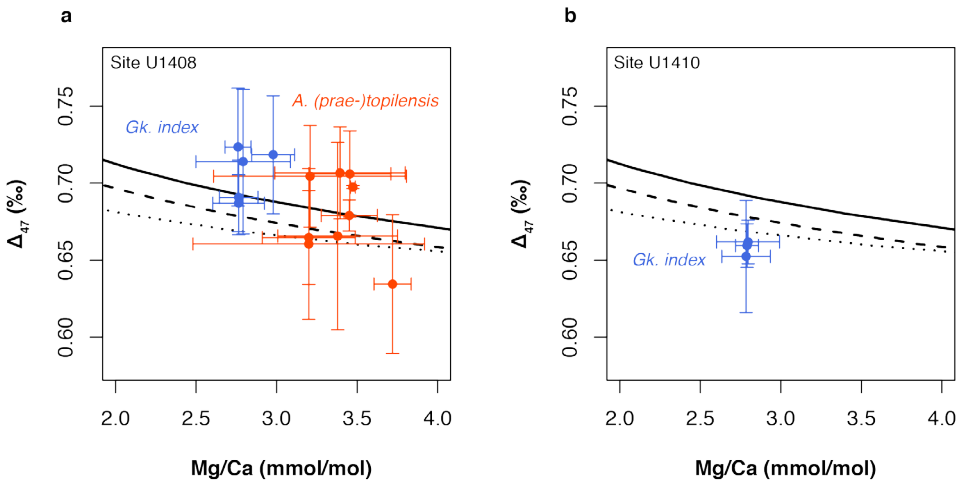

Supplementary Figure 9: Relationships between observed Δ_{47} and Mg/Ca values relative to expected values. a-b, Coupled Δ_{47} and Mg/Ca data for *A. (prae-)topilensis* (in red) and *Gk. index* (in blue) from Site U1408 and U1410. Values represent averages of 2-4 closest neighboring samples from which coupled measurements are available and the vertical and horizontal error bars represent 2 standard errors of the mean for Δ_{47} and Mg/Ca, respectively. Lines represent the expected Δ_{47}-Mg/Ca relationship based on the updated Δ_{47}-temperature calibration of Kele et al. (2015) as outlined in Bernasconi et al. (2018) and the Mg/Ca-temperature relationships of Gray et al. (2018) with modifications based on Evans and Müller (2012) (solid line), Evans et al. (2016b, 2016a) (dashed line), or Anand et al. (2003) with modifications based on Evans and Müller (2012) (dotted line). See Methods for further details.

Chapter 7

Middle Eocene Climatic Optimum warming followed by organic carbon burial in the Tethys realm

Middle Eocene Climatic Optimum warming followed by organic carbon burial in the Tethys realm

Robin van der Ploeg[*], *Margot J. Cramwinckel*[*], *Niels Waarlo, Claudia Agnini, Peter K. Bijl, Annique van der Boon, Henk Brinkhuis, Joost Frieling, Larisa Golovina, Niels A.G.M. van Helmond, Wout Krijgsman, Tamsin Mather, Jack J. Middelburg, Francien Peterse, Sergey V. Popov, Caroline P. Slomp and Appy Sluijs*[1]

*Shared first-authorship

Abstract

The Middle Eocene Climatic Optimum (MECO) was a widespread warming event around 40 million years ago (Ma) that interrupted long-term Eocene cooling. Although there is evidence for elevated atmospheric CO_2 concentrations during the MECO, the exact mechanisms of gradual (~400 kyr) MECO warming and subsequent abrupt (~40-100 kyr) cooling remain unconstrained. Evidence for a reduced silicate weathering feedback, in combination with the relatively short timescale of MECO termination, suggests another process must have played a role in CO_2 sequestration and climatic recovery in the aftermath of the MECO. Here, we assess the signature of the MECO in the Peri-Tethys in relation to climate and carbon cycle change and present a suite of middle Eocene paleoclimate proxy records from the organic-rich Kuma Formation of the Belaya River section, located on the edge of the Scythian Platform in the North Caucasus, Russia. We document MECO warming of about ~2°C to peak sea surface temperatures of ~34°C in the Peri-Tethys based on TEX_{86}^{H} paleothermometry. Strikingly, a large increase in organic matter content occurs during MECO cooling, similar to patterns observed in the central western Tethys Ocean, suggesting a possible role for enhanced organic carbon burial in the recovery of the MECO event.

7.1 Introduction

The Middle Eocene Climatic Optimum (MECO) around 40 Ma stands out as a ~400 kyr phase of widespread warming (Bohaty et al., 2009), that interrupts the general Eocene cooling trend (Zachos et al., 2008; Bijl et al., 2009; Cramwinckel et al., 2018). Over the past decade, MECO warming has been recorded at an increasing number of localities, including the Atlantic and Indian deep ocean (Bohaty and Zachos, 2003; Bohaty et al., 2009) and surface waters of the Atlantic (Edgar et al., 2010; Boscolo Galazzo et al., 2014; Cramwinckel et al., 2018) and southwest Pacific Ocean (Bijl et al., 2010). Increasing atmospheric CO_2 (Bijl et al., 2010) and a weakened silicate weathering feedback (Van der Ploeg et al., 2018) seem to have played a role in the development and prolongation of MECO warmth and associated dissolution of deep-sea carbonates (Bohaty et al., 2009). Although volcanic outgassing likely played a role (Van der Ploeg et al., 2018), the exact cause of MECO warming remains elusive. One of the possible sources is intensified volcanism related to Arabia-Eurasia collision, where peak magmatism is recorded around 40 Ma (Allen and Armstrong, 2008). In addition, a lack of MECO records from continental shelves precludes assessment of a potential shift in the locus of carbonate

burial from deep-ocean to shelf environments as a driver of deep-sea carbonate dissolution, as proposed by Sluijs et al. (2013) based on carbon cycle modeling.

The mechanisms responsible for subsequent MECO cooling and atmospheric CO_2 decline represent a second outstanding question. If the strength of the silicate weathering feedback was indeed reduced in the Middle Eocene (Caves et al., 2016; Van der Ploeg et al., 2018), another negative carbon cycle feedback process may have played a role in rapid CO_2 drawdown and climatic recovery in the aftermath of the MECO. In the central western Tethys, MECO cooling is concurrent with deposition of two organic carbon-rich layers with a thickness of several meters and total organic carbon (TOC) content of ~2% (Spofforth et al., 2010). Simultaneously, planktic and benthic foraminiferal assemblages suggest eutrophic sea surface conditions, high export productivity and oxygen-depleted bottom waters (Luciani et al., 2010; Boscolo Galazzo et al., 2013). Although a stable carbon isotope signature is not apparent from most marine carbonate records, the increased productivity and subsequent enhanced organic carbon burial in the Tethys may have led to substantial carbon drawdown from the exogenic carbon pool, following the MECO. Indeed, Beniamovski et al. (2003) postulated a link between the deposition of the regionally widespread and organic-rich Kuma Formation and global cooling during the middle-late Eocene. Even before severe restriction and associated oxygen depletion of the northern Tethys margin around the Eocene-Oligocene Transition (~34 Ma), the (Peri-) Tethys region has been relatively sensitive to deoxygenation (Popov et al., 1993; Schulz et al., 2005). For example, the Paleocene-Eocene Thermal Maximum (PETM; ~56 Ma), a ~200 kyr episode associated with rapid carbon injection and warming at its onset, was associated with marine anoxia along Tethyan margins (Dickson et al., 2014; Shcherbinina et al., 2016) and epi-continental seas (Frieling et al., 2014).

Here, we present a suite of middle Eocene paleoclimate proxy records from the Kuma Formation of the Belaya River section, located on the edge of the Scythian Platform in the North Caucasus and explore its potential relation to the MECO. To this end, we identify the MECO based on biostratigraphy and chemostratigraphy, perform paleoecological analyses based on palynology and biomarker paleothermometry at the study site, and generate sedimentary Hg abundance data to investigate a relation between the MECO and regional volcanism.

7.2 Methods

7.2.1 Geological setting

The study area is located along the Belaya River in the North Caucasus region of Russia (44.3665 °N, 40.1970 °E, paleolatitude ~42°N at 40 Ma (van Hinsbergen et al., 2015)), ~25 km south of the town of Maikop (Figure 1; Supplementary Figure 1). This section contains an apparently continuous succession of middle-late Eocene sediments divided into the Cherkessk, Keresta, Kuma and Belaya Glina formations (Zakrevskaya et al., 2011; Benyamovskiy, 2012), thought to be deposited in a continental shelf setting (Van der Boon, 2017). Here, we define the base of the section (0 m) by the sharp transition from the green clays of the Cherkessk formation to the white marls of the Keresta formation. The overlying Kuma formation (~6.8–52 m) is represented by brown organic-rich, laminated marls, while the Belaya Glina formation (~52–112.5 m) is again characterized by white marls. Further upwards, the succession continues into the Maikop series (Supplementary Figure 1). An age range that encompasses the Bartonian

Figure 1: Map of paleolocalities of the study site (Belaya section) and Alano di Piave section. Late Eocene paleogeographic map adapted from Popov et al. (2004) and Van der Boon (2017). Grey shaded areas represent presumed subaerial topography during the middle Eocene, light grey lines represent present-day shorelines.

has been inferred for the Kuma formation in this region (~44 – 36.5 Ma; Beniamovski et al. (2003)), which implies the MECO should be expressed within this formation.

7.2.2 Sample collection

Approximately 250 sediment samples were collected from the Kuma formation using a gasoline-powered hand drill during fieldwork in 2017. The average sampling resolution is ~10 cm for the interval between 26–37 m and ~30 cm for the rest of the succession.

7.2.3 Organic geochemistry

Lipids were extracted from ~10 g of powdered freeze-dried sediment (47 samples) with a Dionex accelerated solvent extractor (ASE 350), using (DCM):methanol (MeOH) (9:1, v/v) as solvent. The extracts were separated by small column chromatography into apolar, ketone and polar fractions using hexane:DCM (9:1), hexane:DCM (1:1) and DCM:MeOH (1:1), respectively. A known amount of synthetic C_{46} glycerol dialkyl glycerol tetraether (GDGT) standard was added to the polar fraction, which was subsequently dried, re-dissolved in hexane:isopropanol (99:1) and filtered using a filter syringe and 0.45-µm polytetrafluoroethylene filter to a concentration of ~3 mg ml^{-1}. The GDGT-containing filtrate was analyzed using ultra-high performance liquid chromatography-mass spectrometry (UHPLC-MS) using an Agilent 1260 Infinity series HPLC system coupled to an Agilent 6130 single-quadrupole mass spectrometer in selected ion monitoring mode at Utrecht University. Separation was achieved on two Waters BEH HILIC silica columns (2.1 x 150mm, 1.7 um) preceded by a guard column (2.1 x 5 mm, Waters) packed with the same material. Solvents, elution scheme, and instrument settings were according to Hopmans et al. (2016). TEX_{86} values were calculated following Schouten et

al. (2002) and converted to sea surface temperature (SST) using the Kim et al. (2010) TEX_{86}^{H} calibration. Based on long-term observation of the in-house standard, the analytical precision for TEX_{86} is ±0.3 °C.

7.2.4 Bulk carbonate stable isotopic compositions

For measurements of the bulk carbonate oxygen and stable carbon isotope composition ($\delta^{18}O_{carb}$ and $\delta^{13}C_{carb}$), powdered freeze-dried sediment (~150 samples) was analyzed using a Thermo Finnigan GasBench-II carbonate preparation device coupled to a Thermo Finnigan Delta-V isotope ratio mass spectrometer (IRMS) at Utrecht University, aiming for 50-100 µg of carbonate per measurement. Analytical errors are estimated to be ±0.1‰ for $\delta^{13}C$ and $\delta^{18}O$ based on long-term reproducibility of in-house carbonate standards. Values are reported relative to the Vienna Pee Dee Belemnite (VPDB) standard.

7.2.5 Organic carbon-, carbonate- and nitrogen contents and organic carbon isotopic compositions

Approximately 150 samples were analyzed for elemental composition and carbon isotopes of organic matter ($\delta^{13}C_{org}$). For this purpose, 0.2–0.3 g of powdered freeze-dried sediment was decalcified using 1 M HCl. Residues were oven-dried at 60°C and weighed again to obtain approximate $CaCO_3$ weight percentages. Total organic carbon (TOC) and nitrogen (N) contents, as well as stable carbon isotopic composition of TOC ($\delta^{13}C_{org}$) were determined using a Thermo Scientific Flask 2000 elemental analyzer coupled to a Thermo Scientific Delta V Advantage via a Conflo IV Elemental Analyser-Isotope Ratio Mass Spectrometer (EA-IRMS). Analytical errors are estimated to be <0.1 wt% for TOC, <0.02 wt% for N and ~0.1‰ for $\delta^{13}C_{org}$ based on long-term reproducibility of in-house standards. Values are reported relative to the VPDB standard.

7.2.6 Mercury contents

For analysis of Hg contents, 20 samples were prepared following the protocol described in Percival et al. (2017). Hg contents were measured using a Lumex RA-915 Portable Mercury Analyzer with PYRO-915 pyrolyzer at the University of Oxford, and normalized to TOC to account for increasing Hg enrichment with increasing TOC (Sanei et al., 2012).

7.2.7 Palynology

For palynological analysis, 40 samples from the interval 18.0–46.9 m were processed. Scaled to organic carbon content, between 3 and 10 g of freeze-dried lightly crushed sediment was treated with 30% HCl and ~38–40% HF to dissolve carbonates and silicates, respectively. The residue was sieved using 15 and 250 µm nylon mesh sieves, with ultrasonic bath steps to break up agglutinated organic matter. The resulting 15 - 250 µm palynomorph fraction was mounted on glass microscope slides. A general characterization of palynofacies, as well as a scan for stratigraphic marker species of dinoflagellate cysts (dinocysts), was performed using light microscopy, using the taxonomical classification of Williams et al. (2017).

7.2.8 Calcareous nannofossil biostratigraphy

A set of 7 standard smear slides was examined for presence of stratigraphically relevant calcareous nannofossil species at the University of Padova.

7.3 Results

7.3.1 Biostratigraphy

The inferred Bartonian age of the Kuma formation is confirmed by preliminary biostratigraphy of excellently preserved and abundant calcareous nannofossils. A sequence of nannofossil datums consisting of base *Dictyococcites bisectus* at 29.55 m ± 0.33 m (40.34 Ma, Agnini et al. (2014)) and base *Spenolithus obtusus* and top *Spenolithus spiniger* both at 31.84 m ± 0.47 m (both 39.70 Ma, Fornaciari et al. (2010)) designates these depths to an age encompassing the MECO. Dinocysts present in our palynological slides support the nannofossil-based Bartonian age constraints for this interval, with occasional presence of *Phthanoperidinium distinctum* up to 33.73 m (top 37.94 Ma, Heilmann-Clausen and Van Simaeys (2005)).

7.3.2 GDGTs

Studied GDGT fractions of the Kuma Formation are dominated by isoprenoid GDGTs (iGDGTs). Ratios between the different iGDGTs, including the Methane Index (MI; (Zhang et al., 2011)), GDGT-2/crenarchaeol (Weijers et al., 2011), GDGT-0/crenarchaeol (Blaga et al., 2009), GDGT-2/GDGT-3 (Taylor et al., 2013), and $\%GDGT_{RS}$ (Inglis et al., 2015) are within the ordinary range for production by marine Thaumarchaeota (Supplementary Data), supporting the use of TEX_{86} as SST proxy. Notably, brGDGTs are entirely below detection limit, with resulting BIT values of 0. $TEX_{86}{}^{H}$-based SST estimates are 31–32°C for the middle Eocene background. We attribute the ~2 °C warming to maximum values of 34°C between 26.5 and 31 m to the MECO, which is consistent with the available biostratigraphic constraints (Fig. 2). Peak MECO temperatures at ~31 m are followed by a prolonged cooling phase up to ~41 m. The variability in $TEX_{86}{}^{H}$ values increases towards the top of the record.

7.3.3 Palynofacies and palynological assemblages

The palynofacies of all samples is dominated by poorly-preserved mature, i.e. dark-colored, amorphous organic matter (AOM) and plant-derived debris. Sparse palynomorphs include prasinophytes, e.g. *Tasmanites* and *Cymatiosphaera*, dinocysts and sporomorphs but suboptimal preservation generally hampers determination to the species-level. Dinocyst taxa comprising a large part of the assemblage are *Enneadocysta* spp., *Spiniferites* spp., *Cordosphaeridium* spp., *Cleistosphaeridium* spp., *Batiacasphaera* spp., *Hystrichokolpoma* spp., and some Protoperidinioids and Wetzellioids. Such high-diversity dinocyst assemblages are characteristic for a mid-shelf setting (Sluijs et al., 2005).

7.3.4 Geochemistry

We document relatively stable, high TOC contents (~3%) for most of the studied interval, but observe a major TOC increase to ~6% between 33 and 37 m, corresponding approximately to the darkest sedimentary facies (Figure 2). C/N ratios show a modest decrease from ~20 to ~15 between 20 and 30 m and a subsequent gradual increase to values ranging between ~20 and ~25 towards the top of the succession. Such values suggest a relatively large supply of terrestrial organic matter (Meyers, 1994).

$\delta^{13}C_{org}$ values vary around –27.0‰ in the lower part of the record between 20 and 33 m. Interestingly, we observe a minor $\delta^{13}C_{org}$ decrease to –27.5‰ between 33 and 35 m followed by a rapid increase to values of –26.5‰ between 35 and 37 m. Further upwards, $\delta^{13}C_{org}$ values gradually return to –27.5‰ between 37 m and 50 m. Finally, we find low and variable Hg/TOC

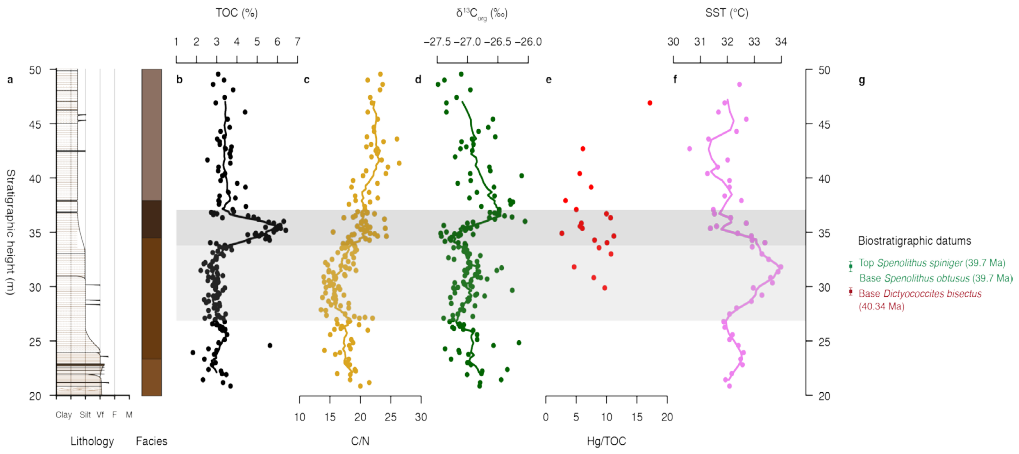

Figure 2: Organic carbon-based proxy records across the MECO interval. a, Schematic sedimentary log and color of the succession. b, Total organic carbon content (TOC, in wt%). c, C/N ratios (in % TOC/% N). d, Organic carbon $\delta^{13}C$ ($\delta^{13}C_{org}$, in ‰ VPDB). e, Hg/TOC ratios (in ng/g Hg/% TOC). f, TEX_{86}^{H}-based sea surface temperature estimates (SST, in °C). g, Height ranges of relevant calcareous nannofossil datum events. Lines represent moving averages and all records are plotted against stratigraphic height (in meters). The base of the succession (0 m; not shown) is defined at the base of the Keresta formation and the Kuma formation starts at ~6.8 m. Gray horizontal shading represents the interval of elevated SST. Within this, dark gray shading corresponds to the interval of transient TOC increase.

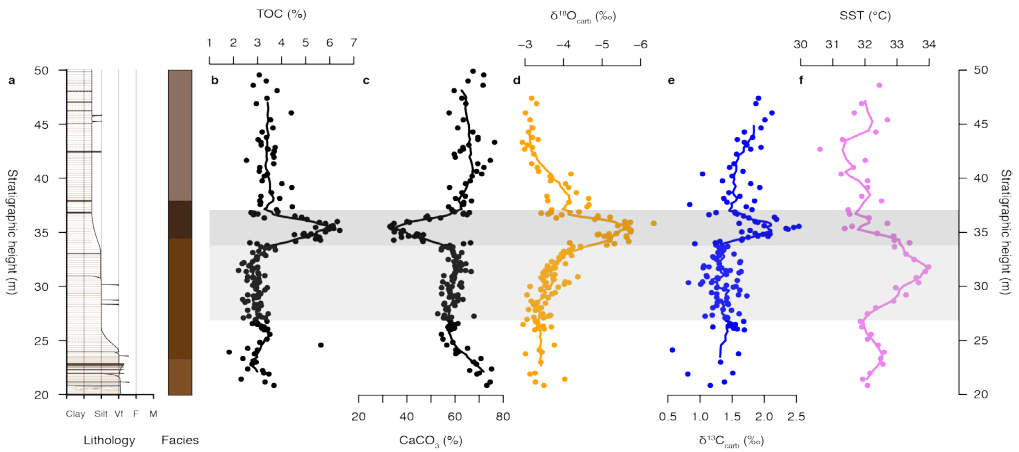

Figure 3: Carbonate-based proxy records across the MECO interval. a, Schematic sedimentary log and color of the succession. b, Total organic carbon content (TOC, in %). c, Carbonate content (in %). d, Bulk carbonate $\delta^{18}O$ ($\delta^{18}O_{carb}$, in ‰ VPDB). e, Bulk carbonate $\delta^{13}C$ ($\delta^{13}C_{carb}$, in ‰ VPDB). f, TEX_{86}^{H}-based sea surface temperature estimates (SST, in °C). Lines represent moving averages and all records are plotted against stratigraphic height (in meters). The base of the succession (0 m; not shown) is defined at the base of the Keresta formation and the Kuma formation starts at ~6.8 m. Gray horizontal shading represents the interval of elevated SST. Within this, dark gray shading corresponds to the interval of transient TOC increase.

ratios between 30 and 50 m, and no relation to any other record is apparent. Notably, the TOC increase and concomitant $\delta^{13}C_{org}$ shift occur in the interval of post-MECO cooling.

We find high carbonate contents (50–80%) across the studied interval, with the exception of a major $CaCO_3$ decrease to ~30% between 33 and 37 m (Figure 3) that coincides with the aforementioned TOC increase. $\delta^{18}O_{carb}$ values are close to those of meteoric water (e.g., Gat, 1996), suggesting a diagenetic overprint, although trends might still reflect a primary signal. $\delta^{18}O_{carb}$ displays a slight decrease from −3.3‰ to −4.0‰ between 20 and 33 m, followed by a transient shift to very depleted values of ~−5.5‰ at ~35m. $\delta^{18}O_{carb}$ subsequently returns to −4.0‰ at 37 m and gradually increases to −3.2‰ towards the top of the studied interval. By comparison, $\delta^{13}C_{carb}$ varies from ~1.0‰ to ~1.5‰ between 20 to 33 m, followed by a transient shift to ~2.5‰ at ~35 m and a final increase from ~1.5‰ to ~2.0‰ from 37 m towards the top of the succession. Importantly, these prominent shifts in both $\delta^{18}O_{carb}$ and $\delta^{13}C_{carb}$ are synchronous with the $CaCO_3$ decrease and occur in the cooling phase after peak MECO warmth.

7.4 Discussion

7.4.1 Depositional setting

Sediments of the Kuma formation at the Belaya River are characterized by relatively high TOC contents (background ~3%), similar to other studied localities on the Russian Platform and Scythian Platform (e.g., Gavrilov et al., 2000; Beniamovski et al., 2003), suggesting high productivity and/or preservation. A conundrum is posed by the composition of the organic matter, which consists of large amounts of plant-derived debris in the palynological residues, with C/N ratios also suggesting pronounced contributions of terrestrial organic matter (Meyers, 1994). However, the lipid fractions are completely devoid of brGDGTs produced by soil-dwelling bacteria. Importantly, the dark coloration of the plant-derived debris suggests a high degree of maturation. The combined evidence therefore suggests that the majority of the terrestrial organic matter was reworked from matured exposed strata. Weathering of TOC-rich sediments could potentially explain the abundances of relatively mature terrestrial palynodebris as well as the absence of brGDGTs, which would be decomposed during maturation. Potentially, a large influx of organic material could have stimulated surface ocean productivity, contributing to more oxygen-depleted conditions in the basin through increased organic matter export fluxes towards the seafloor.

7.4.2 MECO warming

The middle Eocene Peri-Tethys surface ocean was very warm, with SSTs around 32°C. This is higher than coeval TEX_{86}-based temperatures from the equatorial and subtropical Atlantic (Boscolo Galazzo et al., 2014; Cramwinckel et al., 2018). These estimates are in line with high SSTs for the Peri-Tethys region, as simulated with a fully-coupled climate model with high resolution paleogeography (Baatsen et al., 2018). Although sedimentation rates might have changed across the studied interval, MECO warming and cooling appear remarkably symmetrical in the depth domain. Furthermore, there are other available MECO SST records that indicate a more prolonged cooling phase in the surface ocean (Bijl et al., 2010; Boscolo Galazzo et al., 2014; Cramwinckel et al., 2018). This is in sharp contrast to the widespread deep-ocean foraminiferal and bulk carbonate $\delta^{18}O$-based temperature pattern, which is characterized by a gradual ~400 kyrs of warming and much more abrupt (~40-100 kyr) cooling (Bohaty et al., 2009).

7.4.3 Organic carbon deposition during MECO cooling

Strikingly, the major changes in sediment composition ($CaCO_3$ decrease and TOC increase) and the concomitant shifts in $\delta^{18}O_{carb}$ and $\delta^{13}C_{carb}$ do not occur during the MECO warming, but rather during MECO cooling. This essentially implies that $\delta^{18}O_{carb}$ and $\delta^{13}C_{carb}$ are decoupled from SST and instead represent changes in lithology. Furthermore, the balance between carbonate and organic carbon burial at this site did not appreciably change during MECO warming, which neither supports nor disproves a potential redistribution of carbonate burial towards the continental shelves during the MECO (Sluijs et al., 2013).

The sharp increase in TOC and $\delta^{13}C_{carb}$ between 33 and 37 m suggests enhanced organic carbon burial during the MECO cooling phase. In fact, a similar pattern of MECO warming followed by organic carbon burial has been observed in sediments from the Alano di Piave section in Italy (Figure 1). There, two distinct organic-rich intervals are recognized during and after MECO cooling, and are characterized by similar shifts towards heavier $\delta^{13}C_{carb}$ values (Spofforth et al., 2010). Although our age constraints are currently insufficient to provide evidence that these depositional events at Alano di Piave and Belaya River are indeed synchronous, enhanced organic carbon burial may have been a regional phenomenon across the western Tethys and Peri-Tethys. Consequently, large-scale organic carbon deposition in the Tethys realm may have indeed contributed to CO_2 drawdown and climatic recovery following the MECO. Importantly, however, much of the organic matter deposited in this interval at Belaya might represent reworked kerogen (see above). Moreover, it is difficult to assess whether the timing and duration of this organic carbon burial episode are consistent with the timing of MECO climate change and $\delta^{13}C$ signature of the global exogenic carbon pool, as best constrained by the available open ocean records (Bohaty and Zachos, 2003; Bohaty et al., 2009). Collectively, to test if organic carbon burial in the Tethyan realm contributed to the recovery from the MECO, additional datasets with well-constrained accumulation rate estimates from the region as well as simulations with carbon cycle models are necessary.

7.5 Conclusions

The middle Eocene Peri-Tethys is characterized by very high SSTs of 31°C–32°C, on which MECO warming stands out as an additional rise to 34°C. Intriguingly, the most striking changes in sediment properties do not occur during MECO warming or peak warmth, but are concomitant with subsequent cooling. Increased burial of organic carbon during MECO recovery might have been a regional phenomenon in the western Tethys Ocean, suggestive of a causal link.

Data availability

All data presented in this study will be made available upon publication in a scientific journal.

Acknowledgments

This work was carried out under the program of the Netherlands Earth System Science Centre (NESSC), financially supported by the Dutch Ministry of Education, Culture and Science. This study was made possible by the Netherlands Organization for Scientific Research (NWO) grant number 834.11.006, which enabled the purchase of the UHPLC-MS system used for GDGT analyses. We thank Michael Morton and Sarah Davies (University of Leicester) and Stephen Vincent (CASP, University of Cambridge) for field support and discussions. We thank Arnold van Dijk and Natasja Welters (Utrecht Geolab) for analytical support.

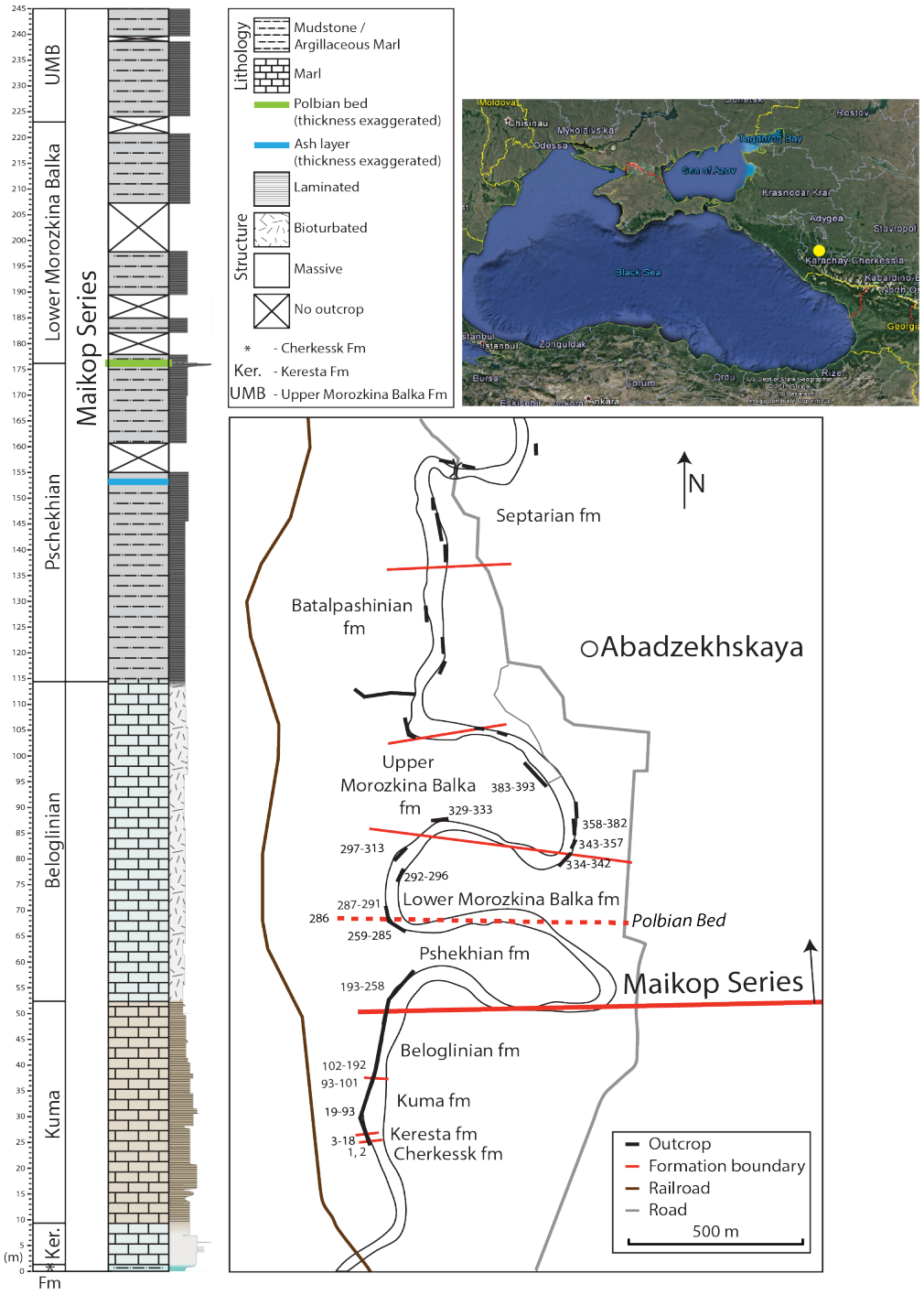

Supplementary Figure 1. Lithological log and sampling location of the Belaya River section, as presented in Van der Boon (2017).

Appendix

Appendix I: ODP Site 1263 Data Report

Robin van der Ploeg, Jack J. Middelburg and Appy Sluijs

Introduction

In this data report we present records of total organic carbon (TOC) contents and stable carbon isotope compositions of organic matter ($\delta^{13}C_{org}$) for the Middle Eocene Climatic Optimum (MECO) from Ocean Drilling Program (ODP) Site 1263 in the South Atlantic Ocean. The aim of this study was to use relative changes in $\delta^{13}C_{org}$ and $\delta^{13}C_{carb}$ across the MECO as a proxy for changes in atmospheric CO_2 concentrations (e.g., Freeman and Hayes, 1992).

Methods

For 36 sediment samples across the MECO interval of Site 1263, two separate 1 g aliquots of powdered and freeze-dried sediment were decalcified using 1 M HCl (72 aliquots in total). Residues were oven-dried at 60°C and subsequently the total organic carbon (TOC) contents and stable carbon isotopic compositions of TOC ($\delta^{13}C_{org}$) were determined using a Thermo Scientific Flask 2000 elemental analyzer coupled to a Thermo Scientific Delta V Advantage via a Conflo IV Elemental Analyser-Isotope Ratio Mass Spectrometer (EA-IRMS) at Utrecht University. Analytical errors are estimated to be <0.1 wt% for TOC and ~0.1‰ for $\delta^{13}C_{org}$ based on long-term reproducibility of in-house standards, and values are reported relative to the VPDB standard. For each sample, the TOC and $\delta^{13}C_{org}$ values obtained for the two aliquots were averaged.

Results

We obtain very low TOC contents across the studied interval (~0.01 wt%) and $\delta^{13}C_{org}$ values ranging between −28.5‰ and −27.0‰ (Figure 1). However, because of these low TOC contents, the $\delta^{13}C_{org}$ values also have relatively large associated uncertainties (± 0.2‰ on average, i.e. significantly larger than analytical uncertainties). Moreover, the TOC and $\delta^{13}C_{org}$ records presented here show no apparent trends across the MECO, which prohibits further reconstructions of changes in carbon cycling and/or atmospheric CO_2 concentrations (e.g., Kump and Arthur, 1999) from these records. This highlights the difficulties of obtaining $\delta^{13}C_{org}$ records from carbonate-rich sediments deposited in pelagic environments.

Acknowledgements

We thank Arnold van Dijk (Utrecht Geolab) for analytical support.

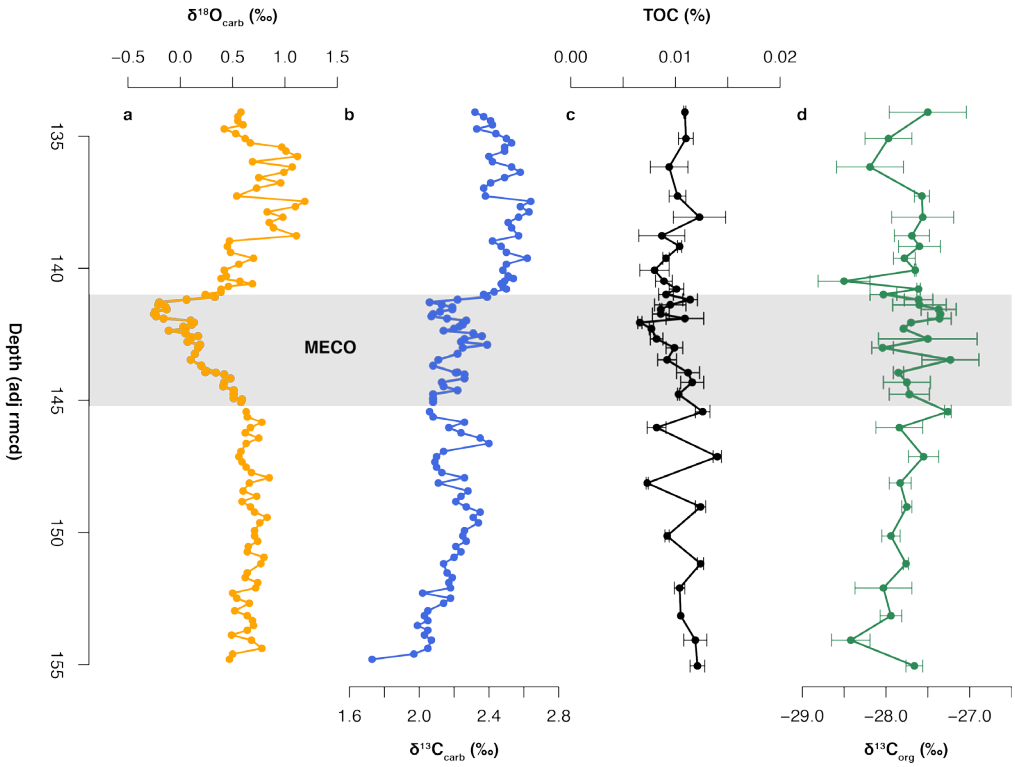

Figure 1: MECO records from Site 1263. a, $\delta^{18}O_{carb}$ (in ‰, VPDB) and b, $\delta^{13}C_{carb}$ (in ‰, VPDB) records of bulk carbonate from Bohaty et al. (2009). The MECO interval is represented by the shaded area. c, TOC content (wt%) and d, $\delta^{13}C_{org}$ records (this study). Data points represent averages based on the two aliquots for each sample and the error bars represent 1 standard deviation (1σ).

Appendix II: IODP Site U1333 Data Report

Robin van der Ploeg, Jack J. Middelburg and Appy Sluijs

Introduction

In this data report we present records of stable oxygen isotope ($\delta^{18}O$) and carbon isotope ($\delta^{13}C$) compositions of bulk carbonate for the Middle Eocene Climatic Optimum (MECO) from International Ocean Discovery Program (IODP) Site U1333 in the equatorial Pacific Ocean. The aim of this study was to reconstruct general temperature trends across the MECO based on changes in bulk carbonate $\delta^{18}O$.

Methods

For 38 sediment samples across the MECO interval of Site U1333, 0.1 – 6 mg aliquots of powdered and freeze-dried sediment (equivalent to 50 – 100 μg of carbonate for each sample) were analyzed for $\delta^{18}O$ and $\delta^{13}C$ compositions using a Thermo Finnigan GasBench-II carbonate preparation device coupled to a Thermo Finnigan Delta-V isotope ratio mass spectrometer (IRMS) at Utrecht University. Analytical errors are estimated to be ~0.1‰ for $\delta^{13}C$ and $\delta^{18}O$ based on long-term reproducibility of in-house carbonate standards. Values are reported relative to the Vienna Pee Dee Belemnite (VPDB) standard.

Results

We document $\delta^{18}O$ values between –2.0‰ and 0.0‰ and $\delta^{13}C$ values between 1.5‰ and 3.5‰ across the studied interval. Remarkably, we find a $\delta^{18}O$ increase of ~1.5‰ during the MECO, which is in sharp contrast to the $\delta^{18}O$ decrease of similar magnitude that has been reported for most other MECO records (Bohaty and Zachos, 2003; Jovane et al., 2007; Bohaty et al., 2009; Spofforth et al., 2010; Boscolo Galazzo et al., 2014). However, this $\delta^{18}O$ increase during the MECO at Site U1333 occurs in an interval where the sediments become virtually devoid of any carbonate due to severe dissolution (Expedition 320/321 Scientists, Site U1333, 2010; Westerhold et al., 2014). As such, the $\delta^{18}O$ record presented here is unlikely to reflect a temperature signal, but rather a change in bulk (carbonate) sediment composition as the sediments become dominated by radiolarian ooze (Expedition 320/321 Scientists, Site U1333, 2010). Consequently, this bulk carbonate $\delta^{18}O$ record cannot be used to reconstruct first-order temperature changes across the MECO.

Acknowledgements

We thank Arnold van Dijk (Utrecht Geolab) for analytical support.

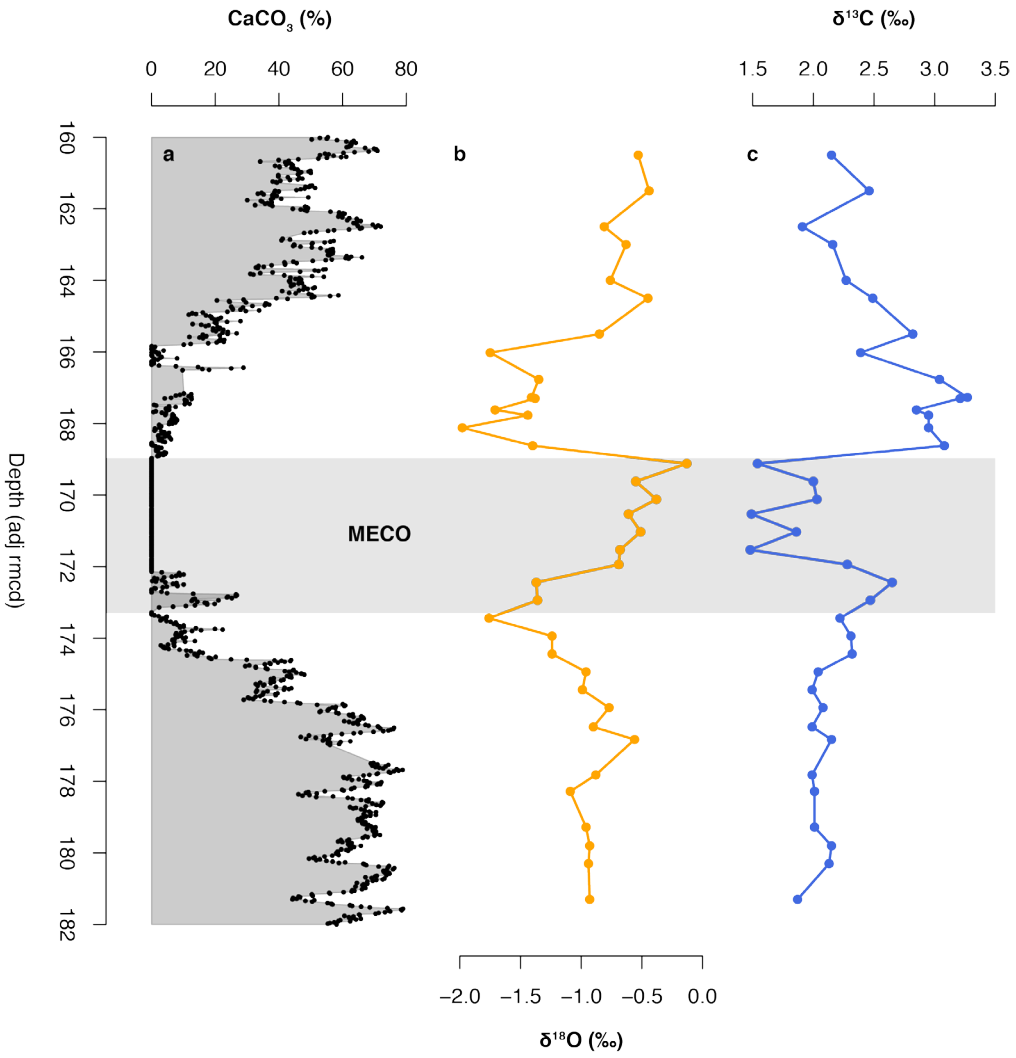

Figure 1: MECO records from Site U1333. a, Carbonate content (wt%) records of Westerhold et al. (2014). The MECO interval is represented by the shaded area. b, $\delta^{18}O$ (in ‰, VPDB) and c, $\delta^{13}C$ (in ‰, VPDB) records of bulk carbonate (this study).

References

References

Agnini, C., Fornaciari, E., Raffi, I., Catanzariti, R., Pälike, H., Backman, J., Rio, D., 2014. Biozonation and biochronology of Paleogene calcareous nannofossils from low and middle latitudes. Newsletters Stratigr. 47, 131–181. https://doi.org/10.1127/0078-0421/2014/0042

Aguirre-Díaz, G.J., Labarthe-Hernández, G., 2003. Fissure ignimbrites: Fissure-source origin for voluminous ignimbrites of the Sierra Madre Occidental and its relationship with Basin and Range faulting. Geology 31, 773–776. https://doi.org/10.1130/G19665.1

Allègre, C.J., Luck, J.M., 1980. Osmium isotopes as petrogenetic and geological tracers. Earth Planet. Sci. Lett. 48, 148–154. https://doi.org/10.1016/0012-821X(80)90177-6

Allen, M.B., Armstrong, H.A., 2008. Arabia-Eurasia collision and the forcing of mid-Cenozoic global cooling. Palaeogeogr. Palaeoclimatol. Palaeoecol. 265, 52–58. https://doi.org/10.1016/j.palaeo.2008.04.021

Amini, M., Eisenhauer, A., Böhm, F., Fietzke, J., Bach, W., Garbe-Schönberg, D., Rosner, M., Bock, B., Lackschewitz, K.S., Hauff, F., 2008. Calcium isotope ($\delta^{44/40}$Ca) fractionation along hydrothermal pathways, Logatchev field (Mid-Atlantic Ridge, 14°45′N). Geochim. Cosmochim. Acta 72, 4107–4122. https://doi.org/10.1016/j.gca.2008.05.055

Anagnostou, E., John, E.H., Edgar, K.M., Foster, G.L., Ridgwell, A., Inglis, G.N., Pancost, R.D., Lunt, D.J., Pearson, P.N., 2016. Changing atmospheric CO_2 concentration was the primary driver of early Cenozoic climate. Nature 533, 380–384. https://doi.org/10.1038/nature17423

Anand, P., Elderfield, H., Conte, M.H., 2003. Calibration of Mg/Ca thermometry in planktonic foraminifera from a sediment trap time series. Paleoceanography 18. https://doi.org/10.1029/2002PA000846

Arvidson, R.S., Mackenzie, F.T., Guidry, M., 2006. MAGic: A Phanerozoic model for the geochemical cycling of major rock-forming components. Am. J. Sci. 306, 135–190. https://doi.org/10.2475/ajs.306.3.135

Baatsen, M., von der Heydt, A.S., Huber, M., Kliphuis, M.A., Bijl, P.K., Sluijs, A., Dijkstra, H.A., 2018. Equilibrium state and sensitivity of the simulated middle-to-late Eocene climate. Clim. Past Discuss. 1–49. https://doi.org/10.5194/cp-2018-43

Bach, W., Humphris, S.E., 1999. Relationship between the Sr and O isotope compositions of hydrothermal fluids and the spreading and magma-supply rates at oceanic spreading centers. Geology 27, 1067–1070. https://doi.org/10.1130/0091-7613(1999)027<1067:RBTSAO>2.3.CO;2

Bailey, D.K., 1992. Episodic alkaline igneous activity across Africa: implications for the causes of continental break-up. Geol. Soc. London, Spec. Publ. 68, 91–98. https://doi.org/10.1144/GSL.SP.1992.068.01.06

Barker, S., Greaves, M., Elderfield, H., 2003. A study of cleaning procedures used for foraminiferal Mg/Ca paleothermometry. Geochemistry, Geophys. Geosystems 4, 1–20. https://doi.org/10.1029/2003GC000559

Bataille, C.P., Willis, A., Yang, X., Liu, X.-M., 2017. Continental igneous rock composition: A major control of past global chemical weathering. Sci. Adv. 3, e1602183. https://doi.org/10.1126/sciadv.1602183

Beerling, D.J., Royer, D.L., 2011. Convergent Cenozoic CO_2 history. Nat. Geosci. 4, 418–420. https://doi.org/10.1038/ngeo1186

Beniamovski, V.N., Alekseev, A.S., Ovechkina, M.N., Oberhansli, H., 2003. Middle to upper Eocene dysoxic-anoxic Kuma Formation (northeast Peri-Tethys): Biostratigraphy and paleoenvironments. Causes Consequences Glob. Warm Clim. Early Paleogene 369, 95.

Benyamovskiy, V.N., 2012. A High Resolution Lutetian-Bartonian Planktonic Foraminiferal Zonation In The Crimean-Caucasus Region Of The Northeastern Peri-Tethys. Austrian J. Earth Sci. 105.

Berger, W.H., Herguera, J.C., 1992. Reading the Sedimentary Record of the Ocean's Productivity, in: Falkowski, P.G., Woodhead, A.D., Vivirito, K. (Eds.), Primary Productivity and Biogeochemical Cycles in the Sea. Springer US, Boston, MA, pp. 455–486. https://doi.org/10.1007/978-1-4899-0762-2_24

Bernasconi, S.M., Müller, I.A., Bergmann, K.D., Breitenbach, S.F.M., Fernandez, A., Hodell, D.A., Jaggi, M., Meckler, A.N., Millan, I., Ziegler, M., 2018. Reducing uncertainties in carbonate clumped isotope analysis through consistent carbonate-based standardization. Geochemistry, Geophys. Geosystems. https://doi.org/10.1029/2017GC007385

Berner, E.K., Berner, R.A., 1996. Global environment: water, air, and geochemical cycles. Princeton University Press.

Berner, R.A., 2006. GEOCARBSULF: A combined model for Phanerozoic atmospheric O_2 and CO_2. Geochim. Cosmochim. Acta 70, 5653–5664. https://doi.org/10.1016/j.gca.2005.11.032

Berner, R.A., 2004. The Phanerozoic Carbon Cycle: CO_2 and O_2. Oxford University Press.

Berner, R.A., 1994. GEOCARB II; a revised model of atmospheric CO_2 over Phanerozoic time. Am. J. Sci. 294, 56–91. https://doi.org/10.2475/ajs.294.1.56

Berner, R.A., 1991. A model for atmospheric CO_2 over Phanerozoic time. Am. J. Sci. 291, 339–376.

Berner, R.A., Kothavala, Z., 2001. GEOCARB III: A revised model of atmospheric CO_2 over Phanerozoic time. Am. J. Sci. 301, 182–204.

Berner, R.A., Lasaga, A.C., Garrels, R.M., 1983. The carbonate-silicate geochemical cycle and its effect on atmospheric carbon dioxide over the past 100 million years. Am. J. Sci. 283, 641–683. https://doi.org/10.2475/ajs.283.7.641

Bice, K.L., Marotzke, J., 2001. Numerical evidence against reversed thermohaline circulation in the warm Paleocene/Eocene ocean. J. Geophys. Res. Ocean. 106, 11529–11542. https://doi.org/10.1029/2000JC000561

Bijl, P.K., Houben, A.J.P., Schouten, S., Bohaty, S.M., Sluijs, A., Reichart, G.-J., Sinninghe Damsté, J.S., Brinkhuis, H., 2010. Transient Middle Eocene atmospheric CO_2 and temperature variations. Science 330, 819–821. https://doi.org/10.1126/science.1193654

Bijl, P.K., Schouten, S., Sluijs, A., Reichart, G.-J., Zachos, J.C., Brinkhuis, H., 2009. Early Palaeogene temperature evolution of the southwest Pacific Ocean. Nature 461, 776–779. https://doi.org/10.1038/nature08399

Blaga, C.I., Reichart, G.J., Heiri, O., Sinninghe Damsté, J.S., 2009. Tetraether membrane lipid distributions in water-column particulate matter and sediments: A study of 47 European lakes along a north-south transect. J. Paleolimnol. 41, 523–540. https://doi.org/10.1007/s10933-008-9242-2

Blättler, C.L., Henderson, G.M., Jenkyns, H.C., 2012. Explaining the Phanerozoic Ca isotope history of seawater. Geology 40, 843–846. https://doi.org/10.1130/G33191.1

Blättler, C.L., Jenkyns, H.C., Reynard, L.M., Henderson, G.M., 2011. Significant increases in global weathering during Oceanic Anoxic Events 1a and 2 indicated by calcium isotopes. Earth Planet. Sci. Lett. 309, 77–88. https://doi.org/10.1016/j.epsl.2011.06.029

Bohaty, S.M., Zachos, J.C., 2003. Significant Southern Ocean warming event in the late middle Eocene. Geology 31, 1017. https://doi.org/10.1130/G19800.1

Bohaty, S.M., Zachos, J.C., Florindo, F., Delaney, M.L., 2009. Coupled greenhouse warming and deep-sea acidification in the middle Eocene. Paleoceanography 24. https://doi.org/10.1029/2008PA001676

Boscolo Galazzo, F., Giusberti, L., Luciani, V., Thomas, E., 2013. Paleoenvironmental changes during the Middle Eocene Climatic Optimum (MECO) and its aftermath: The benthic foraminiferal record from the Alano section (NE Italy). Palaeogeogr. Palaeoclimatol. Palaeoecol. 378, 22–35. https://doi.org/10.1016/j.palaeo.2013.03.018

Boscolo Galazzo, F., Thomas, E., Giusberti, L., 2015. Benthic foraminiferal response to the Middle Eocene Climatic Optimum (MECO) in the South-Eastern Atlantic (ODP Site 1263). Palaeogeogr. Palaeoclimatol. Palaeoecol. 417, 432–444. https://doi.org/10.1016/j.palaeo.2014.10.004

Boscolo Galazzo, F., Thomas, E., Pagani, M., Warren, C., Luciani, V., Giusberti, L., 2014. The Middle Eocene Climatic Optimum: a Multi-Proxy Record of Paleoceanographic Changes in the South Atlantic (ODP Site 1263). Paleoceanography 29, 1143–1161. https://doi.org/10.1002/2014PA002670.Received

Bottini, C., Cohen, A.S., Erba, E., Jenkyns, H.C., Coe, A.L., 2012. Osmium-isotope evidence for volcanism, weathering, and ocean mixing during the early Aptian OAE 1a. Geology 4, 583–586. https://doi.org/10.1130/G33140.1

Boudreau, B.P., Luo, Y., 2017. Retrodiction of secular variations in deep-sea $CaCO_3$ burial during the Cenozoic. Earth Planet. Sci. Lett. 474, 1–12. https://doi.org/10.1016/j.epsl.2017.06.005

Boudreau, B.P., Middelburg, J.J., Hofmann, A.F., Meysman, F.J.R., 2010. Ongoing transients in carbonate compensation. Global Biogeochem. Cycles 24. https://doi.org/10.1029/2009GB003654

Boudreau, B.P., Middelburg, J.J., Luo, Y., 2018. The role of calcification in carbonate compensation. Nat. Geosci. 11, 894–900. https://doi.org/10.1038/s41561-018-0259-5

Boudreau, B.P., Middelburg, J.J., Sluijs, A., Van der Ploeg, R., 2019. Secular variations in the carbonate chemistry of the oceans over the Cenozoic. Earth Planet. Sci. Lett. 512, 194–206. https://doi.org/10.1016/j.epsl.2019.02.004

Boulila, S., Vahlenkamp, M., De Vleeschouwer, D., Laskar, J., Yamamoto, Y., Pälike, H., Kirtland Turner, S., Sexton, P.F., Westerhold, T., Röhl, U., 2018. Towards a robust and consistent middle Eocene astronomical timescale. Earth Planet. Sci. Lett. 486, 94–107. https://doi.org/10.1016/j.epsl.2018.01.003

Boyle, P.R., Romans, B.W., Tucholke, B.E., Norris, R.D., Swift, S.A., Sexton, P.F., 2017. Cenozoic North Atlantic deep circulation history recorded in contourite drifts, offshore Newfoundland, Canada. Mar. Geol. 385, 185–203. https://doi.org/10.1016/j.margeo.2016.12.014

Brand, W.A., Assonov, S.S., Coplen, T.B., 2010. Correction for the ^{17}O interference in $\delta(^{13}C)$ measurements when analyzing CO_2 with stable isotope mass spectrometry (IUPAC Technical Report). Pure Appl. Chem. 82, 1719–1733. https://doi.org/10.1351/PAC-REP-09-01-05

Brazier, J.-M., Suan, G., Tacail, T., Simon, L., Martin, J.E., Mattioli, E., Balter, V., 2015. Calcium isotope evidence for dramatic increase of continental weathering during the Toarcian

oceanic anoxic event (Early Jurassic). Earth Planet. Sci. Lett. 411, 164–176. https://doi.org/10.1016/j.epsl.2014.11.028
Breitenbach, S.F.M., Mleneck-Vautravers, M.J., Grauel, A.L., Lo, L., Bernasconi, S.M., Müller, I.A., Rolfe, J., Gázquez, F., Greaves, M., Hodell, D.A., 2018. Coupled Mg/Ca and clumped isotope analyses of foraminifera provide consistent water temperatures. Geochim. Cosmochim. Acta 236, 283–296. https://doi.org/10.1016/j.gca.2018.03.010
Broecker, W., Lynch-Stieglitz, J., Archer, D., Hofmann, M., Maier-Reimer, E., Marchal, O., Stocker, T., Gruber, N., 1999. How strong is the Harvardton-Bear Constraint? Global Biogeochem. Cycles 13, 817–820. https://doi.org/10.1029/1999GB900050
Broecker, W.S., Peng, T.-H., 1982. Tracers in the sea. https://doi.org/10.1016/0016-7037(83)90075-3
Burke, W.H., Denison, R.E., Hetherington, E.A., Koepnick, R.B., Nelson, H.F., Otto, J.B., 1982. Variation of seawater $^{87}Sr/^{86}Sr$ throughout Phanerozoic time. Geology 10, 516–519. https://doi.org/10.1130/0091-7613(1982)10<516
Burton, K.W., 2006. Global weathering variations inferred from marine radiogenic isotope records. J. Geochemical Explor. 88, 262–265. https://doi.org/10.1016/j.gexplo.2005.08.052
Burton, K.W., Gannoun, A., Parkinson, I.J., 2010. Climate driven glacial–interglacial variations in the osmium isotope composition of seawater recorded by planktic foraminifera. Earth Planet. Sci. Lett. 295, 58–68. https://doi.org/10.1016/j.epsl.2010.03.026
Burton, K.W., Vigier, N., 2011. Lithium Isotopes as Tracers in Marine and Terrestrial Environments, in: Handbook of Environmental Isotope Geochemistry. https://doi.org/10.1007/978-3-642-10637-8
Caldeira, K., 1992. Enhanced Cenozoic chemical weathering and the subduction of pelagic carbonate. Nature 357, 578–581. https://doi.org/10.1038/357578a0
Caldeira, K., Rampino, M.R., 1993. Aftermath of the end-Cretaceous mass extinction: Possible biogeochemical stabilization of the carbon cycle and climate. Paleoceanography 8, 515–525. https://doi.org/10.1029/93PA01163
Cambray, H., Cadet, J.-P., 1996. Synchronisme de l'activité volcanique d'arc: mythe ou réalité? Comptes rendus l'Académie des Sci. Série 2. Sci. la terre des planètes 322, 237–244.
Capo, R.C., Stewart, B.W., Chadwick, O.A., 1998. Strontium isotopes as tracers of ecosystem processes: Theory and methods. Geoderma 82, 197–225. https://doi.org/10.1016/S0016-7061(97)00102-X
Carpenter, J.H., Manella, M.E., 1973. Magnesium to chlorinity ratios in seawater. J. Geophys. Res. 78, 3621. https://doi.org/10.1029/JC078i018p03621
Caves, J.K., Jost, A.B., Lau, K. V., Maher, K., 2016. Cenozoic carbon cycle imbalances and a variable weathering feedback. Earth Planet. Sci. Lett. 450, 152–163. https://doi.org/10.1016/j.epsl.2016.06.035
Charette, M., Smith, W., 2010. The Volume of Earth's Ocean. Oceanography 23, 112–114. https://doi.org/10.5670/oceanog.2010.51
Coggon, R.M., Teagle, D.A.H., Smith-Duque, C.E., Alt, J.C., Cooper, M.J., 2010. Reconstructing Past Seawater Mg/Ca and Sr/Ca from Mid-Ocean Ridge Flank Calcium Carbonate Veins. Science 327, 1114–1117. https://doi.org/10.1126/science.1182252
Cohen, A.S., Coe, A.L., 2002. New geochemical evidence for the onset of volcanism in the Central Atlantic magmatic province and environmental change at the Triassic-Jurassic boundary. Geology 30, 267–270. https://doi.org/10.1130/0091-7613(2002)030<0267:NGEFTO>2.0.CO;2

Cohen, A.S., Coe, A.L., Bartlett, J.M., Hawkesworth, C.J., 1999. Precise Re-Os ages of organic-rich mudrocks and the Os isotope composition of Jurassic seawater. Earth Planet. Sci. Lett. 167, 159–173. https://doi.org/10.1016/S0012-821X(99)00026-6

Cohen, A.S., Coe, A.L., Harding, S.M., Schwark, L., 2004. Osmium isotope evidence for the regulation of atmospheric CO_2 by continental weathering. Geology 32, 157–160. https://doi.org/10.1130/G20158.1

Colleps, C.L., McKenzie, N.R., Stockli, D.F., Hughes, N.C., Singh, B.P., Webb, A.A.G., Myrow, P.M., Planavsky, N.J., Horton, B.K., 2018. Zircon (U-Th)/He Thermochronometric Constraints on Himalayan Thrust Belt Exhumation, Bedrock Weathering, and Cenozoic Seawater Chemistry. Geochemistry, Geophys. Geosystems 19, 257–271. https://doi.org/10.1002/2017GC007191

Coxall, H.K., Huck, C.E., Huber, M., Lear, C.H., Legarda-Lisarri, A., O'Regan, M., Sliwinska, K.K., Van de Flierdt, T., de Boer, A.M., Zachos, J.C., Backman, J., 2018. Export of nutrient rich Northern Component Water preceded early Oligocene Antarctic glaciation. Nat. Geosci. 11, 190–196. https://doi.org/10.1038/s41561-018-0069-9

Coxall, H.K., Wilson, P.A., Pälike, H., Lear, C.H., Backman, J., 2005. Rapid stepwise onset of Antarctic glaciation and deeper calcite compensation in the Pacific Ocean. Nature 433, 53–57. https://doi.org/10.1038/nature03135

Cramer, B.S., Toggweiler, J.R., Wright, J.D., Katz, M.E., Miller, K.G., 2009. Ocean overturning since the late cretaceous: Inferences from a new benthic foraminiferal isotope compilation. Paleoceanography 24, 1–14. https://doi.org/10.1029/2008PA001683

Cramwinckel, M.J., Huber, M., Kocken, I.J., Agnini, C., Bijl, P.K., Bohaty, S.M., Frieling, J., Goldner, A., Hilgen, F.J., Kip, E.L., Peterse, F., Van der Ploeg, R., Röhl, U., Schouten, S., Sluijs, A., 2018. Synchronous tropical and polar temperature evolution in the Eocene. Nature 559, 382–386. https://doi.org/10.1038/s41586-018-0272-2

Cumming, V.M., Selby, D., Lillis, P.G., 2012. Re-Os geochronology of the lacustrine Green River Formation: Insights into direct depositional dating of lacustrine successions, Re-Os systematics and paleocontinental weathering. Earth Planet. Sci. Lett. 359–360, 194–205. https://doi.org/10.1016/j.epsl.2012.10.012

Davies, T.A., Worsley, T.R., 1981. Paleoenvironmental Implications of Oceanic Carbonate Sedimentation Rates, in: Warme, J.E., Douglas, R.G., Winterer, E.L. (Eds.), The Deep Sea Drilling Project: A Decade of Progress. SEPM Society for Sedimentary Geology.

De La Rocha, C.L., DePaolo, D.J., 2000. Isotopic evidence for variations in the marine calcium cycle over the Cenozoic. Science. 289, 1176–1178.

De Nooijer, L.J., Spero, H.J., Erez, J., Bijma, J., Reichart, G.-J., 2014. Biomineralization in perforate foraminifera. Earth-Science Rev. 135, 48–58. https://doi.org/10.1016/j.earscirev.2014.03.013

de Villiers, S., Greaves, M., Elderfield, H., 2002. An intensity ratio calibration method for the accurate determination of Mg/Ca and Sr/Ca of marine carbonates by ICP-AES. Geochemistry, Geophys. Geosystems 3. https://doi.org/10.1029/2001GC000169

Delaney, M.L., Boyle, E.A., 1988. Tertiary paleoceanic chemical variability: Unintended consequences of simple geochemical models. Paleoceanography 3, 137–156. https://doi.org/10.1029/PA003i002p00137

Dennis, K.J., Affek, H.P., Passey, B.H., Schrag, D.P., Eiler, J.M., 2011. Defining an absolute reference frame for "clumped" isotope studies of CO_2. Geochim. Cosmochim. Acta 75, 7117–7131. https://doi.org/10.1016/j.gca.2011.09.025

DePaolo, D.J., 2004. Calcium Isotopic Variations Produced by Biological, Kinetic, Radiogenic and Nucleosynthetic Processes. Rev. Mineral. Geochemistry 55, 255–288. https://doi.org/10.2138/gsrmg.55.1.255

Derry, L.A., France-Lanord, C., 1996. Neogene Himalayan weathering history and river $^{87}Sr/^{86}Sr$: impact on the marine Sr record. Earth Planet. Sci. Lett. 142, 59–74. https://doi.org/10.1016/0012-821X(96)00091-X

Dickens, G.R., Castillo, M.M., Walker, J.C.G., 1997. A blast of gas in the latest Paleocene: Simulating first-order effects of massive dissociation of oceanic methane hydrate. Geology 25, 259–262. https://doi.org/10.1130/0091-7613(1997)025<0259:ABOGIT>2.3.CO;2

Dickens, G.R., O'Neil, J.R., Rea, D.K., Owen, R.M., 1995. Dissociation of oceanic methane hydrate as a cause of the carbon isotope excursion at the end of the Paleocene. Paleoceanography 10, 965–971.

Dickson, A.J., Cohen, A.S., Coe, A.L., 2014. Continental margin molybdenum isotope signatures from the early Eocene. Earth Planet. Sci. Lett. 404, 389–395. https://doi.org/10.1016/j.epsl.2014.08.004

Dickson, A.J., Cohen, A.S., Coe, A.L., Davies, M., Shcherbinina, E.A., Gavrilov, Y.O., 2015. Evidence for weathering and volcanism during the PETM from Arctic Ocean and Peri-Tethys osmium isotope records. Palaeogeogr. Palaeoclimatol. Palaeoecol. 438, 300–307. https://doi.org/10.1016/j.palaeo.2015.08.019

Dosseto, A., Vigier, N., Joannes-Boyau, R., Moffat, I., Singh, T., Srivastava, P., 2015. Rapid response of silicate weathering rates to climate change in the Himalaya. Geochemical Perspect. Lett. 1, 10–19. https://doi.org/10.7185/geochemlet.1502

Du Vivier, A.D.C., Jacobson, A.D., Lehn, G.O., Selby, D., Hurtgen, M.T., Sageman, B.B., 2015. Ca isotope stratigraphy across the Cenomanian–Turonian OAE 2: Links between volcanism, seawater geochemistry, and the carbonate fractionation factor. Earth Planet. Sci. Lett. 416, 121–131. https://doi.org/10.1016/j.epsl.2015.02.001

Du Vivier, A.D.C., Selby, D., Sageman, B.B., Jarvis, I., Gröcke, D.R., Voigt, S., 2014. Marine $^{187}Os/^{188}Os$ isotope stratigraphy reveals the interaction of volcanism and ocean circulation during Oceanic Anoxic Event 2. Earth Planet. Sci. Lett. 389, 23–33. https://doi.org/10.1016/j.epsl.2013.12.024

Dubin, A., Peucker-Ehrenbrink, B., 2015. The importance of organic-rich shales to the geochemical cycles of rhenium and osmium. Chem. Geol. 403, 111–120. https://doi.org/10.1016/j.chemgeo.2015.03.010

Dunkley Jones, T., Lunt, D.J., Schmidt, D.N., Ridgwell, A., Sluijs, A., Valdes, P.J., Maslin, M., 2013. Climate model and proxy data constraints on ocean warming across the Paleocene–Eocene Thermal Maximum. Earth-Science Rev. 125, 123–145. https://doi.org/10.1016/j.earscirev.2013.07.004

Duplessy, J.-C., Labeyrie, L., Juillet-Leclerc, A., Maitre, F., Duprat, J., Sarnthein, M., 1991. Surface salinity reconstruction of the north-atlantic ocean during the last glacial maximum. Oceanol. Acta 14, 311–324.

Ebelmen, J.J., 1845. Sur les produits de la décomposition des espèces minérales de la famille des silicates. Ann. des Mines 7, 66.

Edgar, K.M., Bohaty, S.M., Gibbs, S.J., Sexton, P.F., Norris, R.D., Wilson, P.A., 2013. Symbiont "bleaching" in planktic foraminifera during the Middle Eocene Climatic Optimum. Geology 41, 15–18. https://doi.org/10.1130/G33388.1

Edgar, K.M., Wilson, P.A., Sexton, P.F., Gibbs, S.J., Roberts, A.P., Norris, R.D., 2010. New biostratigraphic, magnetostratigraphic and isotopic insights into the Middle Eocene Climatic Optimum in low latitudes. Palaeogeogr. Palaeoclimatol. Palaeoecol. 297, 670–682. https://doi.org/10.1016/j.palaeo.2010.09.016

Edmond, J.M., 1992. Himalayan Tectonics, Weathering Processes, and the Strontium Isotope Record in Marine Limestones. Science. 258, 1594–1597. https://doi.org/10.1126/science.258.5088.1594

Eiler, J.M., 2011. Paleoclimate reconstruction using carbonate clumped isotope thermometry. Quat. Sci. Rev. 30, 3575–3588. https://doi.org/10.1016/j.quascirev.2011.09.001

Elderfield, H., 1986. Strontium isotope stratigraphy. Palaeogeogr. Palaeoclimatol. Palaeoecol. 57, 71–90. https://doi.org/10.1016/0031-0182(86)90007-6

Elderfield, H., Gieskes, J.M., 1982. Sr isotopes in interstitial waters of marine sediments from Deep Sea Drilling Project cores. Nature 300, 493.

Elderfield, H., Schultz, A., 1996. Mid-Ocean Ridge Hydrothermal Fluxes and the Chemical Composition of the Ocean. Annu. Rev. Earth Planet. Sci. 24, 191–224. https://doi.org/10.1146/annurev.earth.24.1.191

Elsworth, G., Galbraith, E., Halverson, G., Yang, S., 2017. Enhanced weathering and CO_2 drawdown caused by latest Eocene strengthening of the Atlantic meridional overturning circulation. Nat. Geosci. https://doi.org/10.1038/ngeo2888

Emerson, S., Bender, M., 1981. Carbon fluxes at the sediment-water interface of the deep-sea: calcium carbonate preservation. J. Mar. Res. 39, 139–162.

Engel, A.E.J., Engel, C.G., Havens, R.G., 1965. Chemical Characteristics of Oceanic Basalts and the Upper Mantle. Geol. Soc. Am. Bull. 719–734.

Erez, J., Luz, B., 1983. Experimental paleotemperature equation for planktonic foraminifera. Geochim. Cosmochim. Acta 47, 1025–1031. https://doi.org/10.1016/0016-7037(83)90232-6

Esser, B.K., Turekian, K.K., 1993. The osmium isotopic composition of the continental-crust. Geochim. Cosmochim. Acta 57, 3093–3104. https://doi.org/10.1016/0016-7037(93)90296-9

Evans, D., Brierley, C., Raymo, M.E., Erez, J., Müller, W., 2016a. Planktic foraminifera shell chemistry response to seawater chemistry: Pliocene-Pleistocene seawater Mg/Ca, temperature and sea level change. Earth Planet. Sci. Lett. 438, 139–148. https://doi.org/10.1016/j.epsl.2016.01.013

Evans, D., Müller, W., 2012. Deep time foraminifera Mg/Ca paleothermometry: Nonlinear correction for secular change in seawater Mg/Ca. Paleoceanography 27, 1–11. https://doi.org/10.1029/2012PA002315

Evans, D., Sagoo, N., Renema, W., Cotton, L.J., Müller, W., Todd, J.A., Saraswati, P.K., Stassen, P., Ziegler, M., Pearson, P.N., Valdes, P.J., Affek, H.P., 2018. Eocene greenhouse climate revealed by coupled clumped isotope-Mg/Ca thermometry. Proc. Natl. Acad. Sci. 115, 1174–1179. https://doi.org/10.1073/pnas.1714744115

Evans, D., Wade, B.S., Henehan, M., Erez, J., Müller, W., 2016b. Revisiting carbonate chemistry controls on planktic foraminifera Mg / Ca: Implications for sea surface temperature and hydrology shifts over the Paleocene-Eocene Thermal Maximum and Eocene-Oligocene transition. Clim. Past 12, 819–835. https://doi.org/10.5194/cp-12-819-2016

Expedition 320/321 Scientists, 2010. Site U1333, in: Pälike, H., Lyle, M., Nishi, H., Raffi, I., Gamage, K., Klaus, A., Expedition 320/321 Scientists (Eds.), Proceedings of the IODP, 320/321. Integrated Ocean Drilling Program. https://doi.org/10.2204/iodp.proc.320321.105.2010

Falkowski, P.G., Katz, M.E., Milligan, A.J., Fennel, K., Cramer, B.S., Aubry, M.P., Berner, R.A., Novacek, M.J., Zapo, W.M., 2005. The Rise of Oxygen over the Past 205 Million Years and the Evolution of Large Placental Mammals. Science 309, 2202–2204. https://doi.org/10.1126/science.1116047

Fantle, M.S., 2015. Calcium isotopic evidence for rapid recrystallization of bulk marine carbonates and implications for geochemical proxies. Geochim. Cosmochim. Acta 148, 378–401. https://doi.org/10.1016/j.gca.2014.10.005

Fantle, M.S., 2010. Evaluating the Ca isotope proxy. Am. J. Sci. 310, 194–230. https://doi.org/10.2475/03.2010.03

Fantle, M.S., DePaolo, D.J., 2007. Ca isotopes in carbonate sediment and pore fluid from ODP Site 807A: The Ca^{2+}(aq)-calcite equilibrium fractionation factor and calcite recrystallization rates in Pleistocene sediments. Geochim. Cosmochim. Acta 71, 2524–2546. https://doi.org/10.1016/j.gca.2007.03.006

Fantle, M.S., DePaolo, D.J., 2005. Variations in the marine Ca cycle over the past 20 million years. Earth Planet. Sci. Lett. 237, 102–117. https://doi.org/10.1016/j.epsl.2005.06.024

Fantle, M.S., Higgins, J.A., 2014. The effects of diagenesis and dolomitization on Ca and Mg isotopes in marine platform carbonates: Implications for the geochemical cycles of Ca and Mg. Geochim. Cosmochim. Acta 142, 458–481. https://doi.org/10.1016/j.gca.2014.07.025

Fantle, M.S., Tipper, E.T., 2014. Calcium isotopes in the global biogeochemical Ca cycle: Implications for development of a Ca isotope proxy. Earth-Science Rev. 129, 148–177. https://doi.org/10.1016/j.earscirev.2013.10.004

Farkaš, J., Böhm, F., Wallmann, K., 2007. Calcium isotope record of Phanerozoic oceans: Implications for chemical evolution of seawater and its causative mechanisms. Geochim. Cosmochim. Acta 71, 5117–5134. https://doi.org/10.1016/j.gca.2007.09.004

Faure, G., 1986. Principles of Isotope Geology, Wiley International Edition. Wiley.

Feely, R.A., Sabine, C.L., Lee, K., Berelson, W., Kleypas, J., Fabry, V.J., Millero, F.J., 2004. Impact of Anthropogenic CO_2 on the $CaCO_3$ System in the Oceans. Science 305, 362–366.

Fiadeiro, M., 1980. The alkalinity of the deep Pacific. Earth Planet. Sci. Lett. 49, 499–505. https://doi.org/10.1016/0012-821X(80)90090-4

Flower, B.P., Kennett, J.P., 1994. The middle Miocene climatic transition: East Antarctic ice sheet development, deep ocean circulation and global carbon cycling. Palaeogeogr. Palaeoclimatol. Palaeoecol. 108, 537–555. https://doi.org/10.1016/0031-0182(94)90251-8

Fornaciari, E., Agnini, C., Catanzariti, R., Rio, D., Bolla, E.M., Valvasoni, E., 2010. Mid-latitude calcareous nannofossil biostratigraphy and biochronology across the middle to late eocene transition. Stratigraphy 7, 229–264. https://doi.org/10.1128/AAC.8.6.617

Foster, G.L., 2008. Seawater pH, pCO_2 and $[CO_3^{2-}]$ variations in the Caribbean Sea over the last 130 kyr: A boron isotope and B/Ca study of planktic foraminifera. Earth Planet. Sci. Lett. 271, 254–266. https://doi.org/10.1016/j.epsl.2008.04.015

Foster, G.L., Pogge von Strandmann, P. A. E., Rae, J.W.B., 2010. Boron and magnesium isotopic composition of seawater. Geochemistry, Geophys. Geosystems 11. https://doi.org/10.1029/2010GC003201

Foster, G.L., Rae, J.W.B., 2016. Reconstructing Ocean pH with Boron Isotopes in Foraminifera. Annu. Rev. Earth Planet. Sci. 44, 207–237. https://doi.org/10.1146/annurev-earth-060115-012226

Foster, G.L., Royer, D.L., Lunt, D.J., 2017. Future climate forcing potentially without precedent in the last 420 million years. Nat. Commun. 8, 1–8. https://doi.org/10.1038/ncomms14845

Foster, G.L., Vance, D., 2006. Negligible glacial–interglacial variation in continental chemical weathering rates. Nature 444, 918–921. https://doi.org/10.1038/nature05365
Frank, M., 2002. Radiogenic isotopes: Tracers of past ocean circulation and erosional input. Rev. Geophys. 40, 1001. https://doi.org/10.1029/2000RG000094
Freeman, K.H., Hayes, J.M., 1992. Fractionation of carbon isotopes by phytoplankton and estimates of ancient CO_2 levels. Global Biogeochem. Cycles 6, 185–198. https://doi.org/10.1029/92GB00190
Frieling, J., Gebhardt, H., Huber, M., Adekeye, O.A., Akande, S.O., Reichart, G.-J., Middelburg, J.J., Schouten, S., Sluijs, A., 2017. Extreme warmth and heat-stressed plankton in the tropics during the Paleocene-Eocene Thermal Maximum. Sci. Adv. 3, e1600891. https://doi.org/10.1126/sciadv.1600891
Frieling, J., Iakovleva, A.I., Reichart, G.-J., Aleksandrova, G.N., Gnibidenko, Z.N., Schouten, S., Sluijs, A., 2014. Paleocene-Eocene warming and biotic response in the epicontinental West Siberian Sea. Geology 42, 767–770. https://doi.org/10.1130/G35724.1
Frieling, J., Svensen, H.H., Planke, S., Cramwinckel, M.J., Selnes, H., Sluijs, A., 2016. Thermogenic methane release as a cause for the long duration of the PETM. Proc. Natl. Acad. Sci. 201603348. https://doi.org/10.1073/PNAS.1603348113
Froelich, P.N., Misra, S., 2014. Was the Late Paleocene-Early Eocene Hot Because Earth Was Flat? An Ocean Lithium Isotope View of Mountain Building, Continental Weathering, Carbon Dioxide, and Earth's Cenozoic climate. Oceanography 27, 36–49.
Gaillardet, J., Dupré, B., Louvat, P., Allègre, C.J., 1999. Global silicate weathering and CO_2 consumption rates deduced from the chemistry of large rivers. Chem. Geol. 159, 3–30. https://doi.org/10.1016/S0009-2541(99)00031-5
Garrels, R.M., Lerman, A., 1981. Phanerozoic cycles of sedimentary carbon and sulfur. Proc. Natl. Acad. Sci. 78, 4652–4656. https://doi.org/10.1073/pnas.78.8.4652
Gat, J.R., 1996. Oxygen and Hydrogen Isotopes in the Hydrologic Cycle. Annu. Rev. Earth Planet. Sci. 24, 225–262. https://doi.org/10.1159/000088336
Gavrilov, Y.O., Shcherbinina, E.A., Muzylöv, N.G., 2000. A Paleogene sequence in central North Caucasus: A response to paleoenvironmental changes. GFF 122, 51–53. https://doi.org/10.1080/11035890001221051
Georg, R.B., West, A.J., Vance, D., Newman, K., Halliday, A.N., 2013. Is the marine osmium isotope record a probe for CO_2 release from sedimentary rocks? Earth Planet. Sci. Lett. 367, 28–38. https://doi.org/10.1016/j.epsl.2013.02.018
George, R., Rogers, N., Kelley, S., 1998. Earliest magmatism in Ethiopia: Evidence for two mantle plumes in one flood basalt province. Geology 26, 923. https://doi.org/10.1130/0091-7613(1998)026<0923:EMIEEF>2.3.CO;2
Goddéris, Y., Donnadieu, Y., Carretier, S., Aretz, M., Dera, G., Macouin, M., Regard, V., 2017. Onset and ending of the late Palaeozoic ice age triggered by tectonically paced rock weathering. Nat. Geosci. 10, 382–386. https://doi.org/10.1038/ngeo2931
Goddéris, Y., François, L.M., 1995. The Cenozoic evolution of the strontium and carbon cycles: relative importance of continental erosion and mantle exchanges. Chem. Geol. 126, 169–190. https://doi.org/10.1016/0009-2541(95)00117-3
Goldstein, S.J., Jacobsen, S.B., 1988. Nd and Sr isotopic systematics of river water suspended material: implications for crustal evolution. Earth Planet. Sci. Lett. 87, 249–265. https://doi.org/10.1016/0012-821X(88)90013-1

Gradstein, F.M., Ogg, J.G., Schmitz, M., Ogg, G., 2012. The Geologic Time Scale 2012 2-Volume Set. Elsevier.

Gradstein, F.M., Ogg, J.G., Smith, A.G., 2005. A Geologic Time Scale 2004. Cambridge University Press, Cambridge. https://doi.org/10.1017/CBO9780511536045

Gray, W.R., Weldeab, S., Lea, D.W., Rosenthal, Y., Gruber, N., Donner, B., Fischer, G., 2018. The effects of temperature, salinity, and the carbonate system on Mg/Ca in Globigerinoides ruber (white): A global sediment trap calibration. Earth Planet. Sci. Lett. 482, 607–620. https://doi.org/10.1016/j.epsl.2017.11.026

Griffith, E.M., Fantle, M.S., Eisenhauer, A., Paytan, A., Bullen, T.D., 2015. Effects of ocean acidification on the marine calcium isotope record at the Paleocene–Eocene Thermal Maximum. Earth Planet. Sci. Lett. 419, 81–92. https://doi.org/10.1016/j.epsl.2015.03.010

Griffith, E.M., Paytan, A., Caldeira, K., Bullen, T.D., Thomas, E., 2008a. A Dynamic Marine Calcium Cycle During the Past 28 Million Years. Science 322, 1671–1674. https://doi.org/10.1126/science.1163614

Griffith, E.M., Paytan, A., Kozdon, R., Eisenhauer, A., Ravelo, A.C., 2008b. Influences on the fractionation of calcium isotopes in planktonic foraminifera. Earth Planet. Sci. Lett. 268, 124–136. https://doi.org/10.1016/j.epsl.2008.01.006

Gutjahr, M., Ridgwell, A., Sexton, P.F., Anagnostou, E., Pearson, P.N., Pälike, H., Norris, R.D., Thomas, E., Foster, G.L., 2017. Very large release of mostly volcanic carbon during the Palaeocene–Eocene Thermal Maximum. Nature 548, 573–577. https://doi.org/10.1038/nature23646

Hain, M.P., Sigman, D.M., Higgins, J.A., Haug, G.H., 2015. The effects of secular calcium and magnesium concentration changes on the thermodynamics of seawater acid/base chemistry: Implications for Eocene and Cretaceous ocean carbon chemistry and buffering. Global Biogeochem. Cycles 29, 517–533. https://doi.org/10.1002/2014GB004986

Hancock, H.J.L., Dickens, G.R., 2005. Carbonate Dissolution Episodes in Paleocene and Eocene Sediment, Shatsky Rise, West-Central Pacific, in: Proceedings of the Ocean Drilling Program, 198 Scientific Results. Ocean Drilling Program. https://doi.org/10.2973/odp.proc.sr.198.116.2005

Hansen, J., Sato, M., Russell, G., Kharecha, P., 2013. Climate sensitivity, sea level and atmospheric carbon dioxide. Philos. Trans. R. Soc. A Math. Phys. Eng. Sci. 371, 20120294–20120294. https://doi.org/10.1098/rsta.2012.0294

Haq, B.U., Hardenbol, J., Vail, P.R., 1987. Chronology of Fluctuating Sea Levels Since the Triassic. Science 235, 1156–1167. https://doi.org/10.1126/science.235.4793.1156

Harper, D.T., Zeebe, R., Hönisch, B., Schrader, C.D., Lourens, L.J., Zachos, J.C., 2018. Subtropical sea-surface warming and increased salinity during Eocene Thermal Maximum 2. Geology 46, 187–190. https://doi.org/10.1130/G39658.1

Hasiuk, F.J., Lohmann, K.C., 2010. Application of calcite Mg partitioning functions to the reconstruction of paleocean Mg/Ca. Geochim. Cosmochim. Acta 74, 6751–6763. https://doi.org/10.1016/j.gca.2010.07.030

Hathorne, E.C., James, R.H., 2006. Temporal record of lithium in seawater: A tracer for silicate weathering? Earth Planet. Sci. Lett. 246, 393–406. https://doi.org/10.1016/j.epsl.2006.04.020

Hauff, F., Hoernle, K., Tilton, G., Graham, D.W., Kerr, A.C., 2000. Large volume recycling of oceanic lithosphere over short time scales: Geochemical constraints from the Caribbean Large Igneous Province. Earth Planet. Sci. Lett. 174, 247–263. https://doi.org/10.1016/S0012-821X(99)00272-1

Hay, W.W., 1985. Potential Errors in Estimates of Carbonate Rock Accumulating Through Geologic Time. Carbon Cycle Atmos. CO_2 Nat. Var. Archean to Present 32, 573–583. https://doi.org/10.1029/GM032p0573

Haywood, A.M., Dowsett, H.J., Dolan, A.M., 2016. Integrating geological archives and climate models for the mid-Pliocene warm period. Nat. Commun. 7, 1–14. https://doi.org/10.1038/ncomms10646

Heilmann-Clausen, C., Van Simaeys, S., 2005. Dinoflagellate cysts from the Middle Eocene to ?lowermost Oligocene succession in the Kysing research borehole, central Danish basin. Palynology 29, 143–204. https://doi.org/10.1080/01916122.2005.9989606

Heinze, M., Ilyina, T., 2015. Ocean biogeochemistry in the warm climate of the late Paleocene. Clim. Past 11, 63–79. https://doi.org/10.5194/cp-11-63-2015

Henehan, M.J., Hull, P.M., Penman, D.E., Rae, J.W.B., Schmidt, D.N., 2016. Biogeochemical significance of pelagic ecosystem function: an end-Cretaceous case study. Philos. Trans. R. Soc. B Biol. Sci. 371, 20150510. https://doi.org/10.1098/rstb.2015.0510

Herold, N., Huber, M., Müller, R.D., Seton, M., 2012. Modeling the Miocene climatic optimum: Ocean circulation. Paleoceanography 27, 1–22. https://doi.org/10.1029/2010PA002041

Higgins, J.A., Schrag, D.P., 2015. The Mg isotopic composition of Cenozoic seawater – evidence for a link between Mg-clays, seawater Mg/Ca, and climate. Earth Planet. Sci. Lett. 416, 73–81. https://doi.org/10.1016/j.epsl.2015.01.003

Higgins, J.A., Schrag, D.P., 2010. Constraining magnesium cycling in marine sediments using magnesium isotopes. Geochim. Cosmochim. Acta 74, 5039–5053. https://doi.org/10.1016/j.gca.2010.05.019

Hilting, A.K., Kump, L.R., Bralower, T.J., 2008. Variations in the oceanic vertical carbon isotope gradient and their implications for the Paleocene-Eocene biological pump. Paleoceanography 23, 1–15. https://doi.org/10.1029/2007PA001458

Hippler, D., Buhl, D., Witbaard, R., Richter, D.K., Immenhauser, A., 2009. Towards a better understanding of magnesium-isotope ratios from marine skeletal carbonates. Geochim. Cosmochim. Acta 73, 6134–6146. https://doi.org/10.1016/j.gca.2009.07.031

Ho, S.L., Laepple, T., 2016. Flat meridional temperature gradient in the early Eocene in the subsurface rather than surface ocean. Nat. Geosci. 9, 606–610. https://doi.org/10.1038/ngeo2763

Hollis, C.J., Taylor, K.W.R., Handley, L., Pancost, R.D., Huber, M., Creech, J.B., Hines, B.R., Crouch, E.M., Morgans, H.E.G., Crampton, J.S., Gibbs, S., Pearson, P.N., Zachos, J.C., 2012. Early Paleogene temperature history of the Southwest Pacific Ocean: Reconciling proxies and models. Earth Planet. Sci. Lett. 349–350, 53–66. https://doi.org/10.1016/j.epsl.2012.06.024

Hönisch, B., Hemming, N.G., 2005. Surface ocean pH response to variations in pCO_2 through two full glacial cycles. Earth Planet. Sci. Lett. 236, 305–314. https://doi.org/10.1016/j.epsl.2005.04.027

Honisch, B., Hemming, N.G., Archer, D., Siddall, M., McManus, J.F., 2009. Atmospheric Carbon Dioxide Concentration Across the Mid-Pleistocene Transition. Science 324, 1551–1554. https://doi.org/10.1126/science.1171477

Hopmans, E.C., Schouten, S., Sinninghe Damsté, J.S., 2016. The effect of improved chromatography on GDGT-based palaeoproxies. Org. Geochem. 93, 1–6. https://doi.org/10.1016/j.orggeochem.2015.12.006

Hopmans, E.C., Weijers, J.W.H., Schefuß, E., Herfort, L., Sinninghe Damsté, J.S., Schouten, S., 2004. A novel proxy for terrestrial organic matter in sediments based on branched and isoprenoid tetraether lipids. Earth Planet. Sci. Lett. 224, 107–116. https://doi.org/10.1016/j.epsl.2004.05.012

Horita, J., Zimmermann, H., Holland, H.D., 2002. Chemical evolution of seawater during the Phanerozoic: implications from the record of marine evaporites. Geochim. Cosmochim. Acta 66, 3733–3756. https://doi.org/10.1016/S0016-7037(01)00884-5

Hu, B., Radke, J., Schlüter, H.J., Heine, F.T., Zhou, L., Bernasconi, S.M., 2014. A modified procedure for gas-source isotope ratio mass spectrometry: The long-integration dual-inlet (LIDI) methodology and implications for clumped isotope measurements. Rapid Commun. Mass Spectrom. 28, 1413–1425. https://doi.org/10.1002/rcm.6909

Huh, Y., Chan, L.-H., Edmond, J.M., 2001. Lithium isotopes as a probe of weathering processes: Orinoco River. Earth Planet. Sci. Lett. 194, 189–199. https://doi.org/10.1016/S0012-821X(01)00523-4

Huh, Y., Chan, L.-H., Zhang, L., Edmond, J.M., 1998. Lithium and its isotopes in major world rivers: implications for weathering and the oceanic budget. Geochim. Cosmochim. Acta 62, 2039–2051.

Hülse, D., Arndt, S., Wilson, J.D., Munhoven, G., Ridgwell, A., 2017. Understanding the causes and consequences of past marine carbon cycling variability through models. Earth-Science Rev. 171, 349–382. https://doi.org/10.1016/j.earscirev.2017.06.004

Inglis, G.N., Farnsworth, A., Lunt, D., Foster, G.L., Hollis, C.J., Pagani, M., Jardine, P.E., Pearson, P.N., Markwick, P., Galsworthy, A.M.J., Raynham, L., Taylor, K.W.R., Pancost, R.D., 2015. Descent toward the Icehouse: Eocene sea surface cooling inferred from GDGT distributions. Paleoceanography 30, 1000–1020. https://doi.org/10.1002/2014PA002723

IPCC, 2018: Global warming of 1.5°C. An IPCC special report on the impacts of global warming of 1.5°C above pre-industrial levels and related global greenhouse gas emission pathways, in the context of strengthening the global response to the threat of climate change, sustainable development, and efforts to eradicate poverty. IPCC, Geneva, Switzerland.

IPCC, 2014: Climate Change 2014: Synthesis Report. Contribution of Working Groups I, II and III to the Fifth Assessment Report of the Intergovernmental Panel on Climate Change. IPCC, Geneva, Switzerland.

Jacobson, A.D., Blum, J.D., 2003. Relationship between mechanical erosion and atmospheric CO_2 consumption in the New Zealand Southern Alps. Geology 31, 865–868. https://doi.org/10.1130/g19662.1

Jacobson, A.D., Blum, J.D., Chamberlain, C.P., Craw, D., Koons, P.O., 2003. Climatic and tectonic controls on chemical weathering in the New Zealand Southern Alps. Geochim. Cosmochim. Acta 67, 29–46. https://doi.org/10.1016/S0016-7037(02)01053-0

Jagniecki, E.A., Lowenstein, T.K., Jenkins, D.M., Demicco, R. V., 2015. Eocene atmospheric CO_2 from the nahcolite proxy. Geology 43, G36886.1. https://doi.org/10.1130/G36886.1

Jahnke, R.A., Craven, D.B., Gaillard, J.-F., 1994. The influence of organic matter diagenesis on $CaCO_3$ dissolution at the deep-sea floor. Geochim. Cosmochim. Acta 58, 2799–2809. https://doi.org/10.1016/0016-7037(94)90115-5

Jahnke, R.A., Jahnke, D.B., 2004. Calcium carbonate dissolution in deep sea sediments: Reconciling microelectrode, pore water and benthic flux chamber results. Geochim. Cosmochim. Acta 68, 47–59. https://doi.org/10.1016/S0016-7037(03)00260-6

Jenkyns, H.C., 2010. Geochemistry of oceanic anoxic events. Geochemistry, Geophys. Geosystems 11, 1–30. https://doi.org/10.1029/2009GC002788

Jovane, L., Florindo, F., Coccioni, R., Dinares-Turell, J., Marsili, A., Monechi, S., Roberts, A.P., Sprovieri, M., 2007. The middle Eocene climatic optimum event in the Contessa Highway section, Umbrian Apennines, Italy. Geol. Soc. Am. Bull. 119, 413–427. https://doi.org/10.1130/B25917.1

Katz, M.E., Wright, J.D., Miller, K.G., Cramer, B.S., Fennel, K., Falkowski, P.G., 2005. Biological overprint of the geological carbon cycle. Mar. Geol. 217, 323–338. https://doi.org/10.1016/j.margeo.2004.08.005

Keir, R.S., 1988. On the late Pleistocene ocean geochemistry and circulation. Paleoceanography 3, 413–445.

Kele, S., Breitenbach, S.F.M., Capezzuoli, E., Meckler, A.N., Ziegler, M., Millan, I.M., Kluge, T., Deák, J., Hanselmann, K., John, C.M., Yan, H., Liu, Z., Bernasconi, S.M., 2015. Temperature dependence of oxygen- and clumped isotope fractionation in carbonates: A study of travertines and tufas in the 6-95°C temperature range. Geochim. Cosmochim. Acta 168, 172–192. https://doi.org/10.1016/j.gca.2015.06.032

Kelly, D.C., Nielsen, T.M.J., McCarren, H.K., Zachos, J.C., Röhl, U., 2010. Spatiotemporal patterns of carbonate sedimentation in the South Atlantic: Implications for carbon cycling during the Paleocene–Eocene thermal maximum. Palaeogeogr. Palaeoclimatol. Palaeoecol. 293, 30–40. https://doi.org/10.1016/j.palaeo.2010.04.027

Kelly, D.C., Zachos, J.C., 2005. Enhanced terrestrial weathering/runoff and surface ocean carbonate production during the recovery stages of the Paleocene-Eocene thermal maximum. Paleoceanography 20, 1–11. https://doi.org/10.1029/2005PA001163

Kennett, J.P., 1982. Marine Geology. Prentice-Hall, Englewood Cliffs, NJ.

Kerrick, D.M., Caldeira, K., 1999. Was the Himalayan orogen a climatically significant coupled source and sink for atmospheric CO_2 during the Cenozoic? Earth Planet. Sci. Lett. 173, 195–203. https://doi.org/10.1016/S0012-821X(99)00229-0

Kerrick, D.M., Caldeira, K., 1993. Paleoatmospheric consequences of CO_2 released during early Cenozoic regional metamorphism in the Tethyan orogen. Chem. Geol. 108, 201–230. https://doi.org/10.1016/0009-2541(93)90325-D

Kim, J.H., Van der Meer, J., Schouten, S., Helmke, P., Willmott, V., Sangiorgi, F., Koç, N., Hopmans, E.C., Damsté, J.S.S., 2010. New indices and calibrations derived from the distribution of crenarchaeal isoprenoid tetraether lipids: Implications for past sea surface temperature reconstructions. Geochim. Cosmochim. Acta 74, 4639–4654. https://doi.org/10.1016/j.gca.2010.05.027

Klemm, V., Levasseur, S., Frank, M., Hein, J.R., Halliday, A.N., 2005. Osmium isotope stratigraphy of a marine ferromanganese crust. Earth Planet. Sci. Lett. 238, 42–48. https://doi.org/10.1016/j.epsl.2005.07.016

Knox, F., McElroy, M.B., 1984. Changes in atmospheric CO_2: Influence of the marine biota at high latitude. J. Geophys. Res. 89, 4629. https://doi.org/10.1029/JD089iD03p04629

Kump, L.R., 2018. Prolonged Late Permian–Early Triassic hyperthermal: failure of climate regulation? Philos. Trans. R. Soc. A Math. Phys. Eng. Sci. 376.

Kump, L.R., 1989. Alternative modeling approaches to the geochemical cycles of carbon, sulfur, and strontium isotopes. Am. J. Sci. https://doi.org/10.2475/ajs.289.4.390

Kump, L.R., Arthur, M.A., 1999. Interpreting carbon-isotope excursions: carbonates and organic matter. Chem. Geol. 161, 181–198.

Kump, L.R., Arthur, M.A., 1997. Global Chemical Erosion during the Cenozoic: Weatherability Balances the Budgets, in: Ruddiman, W. (Ed.), Tectonic Uplift and Climate Change. Plenum Publishing Co., pp. 399–426.

Kump, L.R., Arthur, M.A., Patzkowsky, M.E., Gibbs, M.T., Pinkus, D.S., Sheehan, P.M., 1999. A weathering hypothesis for glaciation at high atmospheric pCO_2 during the Late Ordovician. Palaeogeogr. Palaeoclimatol. Palaeoecol. 152, 173–187. https://doi.org/10.1016/S0031-0182(99)00046-2

Kump, L.R., Brantley, S.L., Arthur, M.A., 2000. Chemical weathering, atmospheric CO_2, and climate. Annu. Rev. Earth Planet. Sci. 28, 611–667.

Kurtz, A.C., Kump, L.R., Arthur, M.A., Zachos, J.C., Paytan, A., 2003. Early Cenozoic decoupling of the global carbon and sulfur cycles. Paleoceanography 18. https://doi.org/10.1029/2003PA000908

Lauretano, V., Littler, K., Polling, M., Zachos, J.C., Lourens, L.J., 2015. Frequency, magnitude and character of hyperthermal events at the onset of the Early Eocene Climatic Optimum. Clim. Past 11, 1313–1324. https://doi.org/10.5194/cp-11-1313-2015

Lear, C.H., Elderfield, H., Wilson, P.A., 2003. A Cenozoic seawater Sr/Ca record from benthic foraminiferal calcite and its application in determining global weathering fluxes. Earth Planet. Sci. Lett. 208, 69–84. https://doi.org/10.1016/S0012-821X(02)01156-1

Lear, C.H., Elderfield, H., Wilson, P.A., 2000. Cenozoic Deep-Sea Temperatures and Global Ice Volumes from Mg/Ca in Benthic Foraminiferal Calcite. Science 287, 269–272. https://doi.org/10.1126/science.287.5451.269

Leon-Rodriguez, L., Dickens, G.R., 2010. Constraints on ocean acidification associated with rapid and massive carbon injections: The early Paleogene record at Ocean Drilling Program Site 1215, equatorial Pacific Ocean. Palaeogeogr. Palaeoclimatol. Palaeoecol. 298, 409–420. https://doi.org/10.1016/j.palaeo.2010.10.029

Leutert, T.J., Sexton, P.F., Tripati, A., Piasecki, A., Ho, S.L., Meckler, A.N. Diagenetic effects on clumped isotope temperatures in fossil benthic and planktic foraminifera. (in prep.)

Li, C., Qu, W.J., Du, A.D., Sun, W., 2009. Comprehensive study on extraction of rhenium with acetone in Re-Os isotopic dating. Rock Miner. Anal. 28, 233–238.

Li, G., Elderfield, H., 2013. Evolution of carbon cycle over the past 100 million years. Geochim. Cosmochim. Acta 103, 11–25. https://doi.org/10.1016/j.gca.2012.10.014

Li, G., Ji, J., Chen, J., Kemp, D.B., 2009. Evolution of the Cenozoic carbon cycle: The roles of tectonics and CO_2 fertilization. Global Biogeochem. Cycles 23, 1–11. https://doi.org/10.1029/2008GB003220

Li, G., West, A.J., 2014. Evolution of Cenozoic seawater lithium isotopes: Coupling of global denudation regime and shifting seawater sinks. Earth Planet. Sci. Lett. 401, 284–293. https://doi.org/10.1016/j.epsl.2014.06.011

Littler, K., Röhl, U., Westerhold, T., Zachos, J.C., 2014. A high-resolution benthic stable-isotope record for the South Atlantic: Implications for orbital-scale changes in Late Paleocene-Early Eocene climate and carbon cycling. Earth Planet. Sci. Lett. 401, 18–30. https://doi.org/10.1016/j.epsl.2014.05.054

Liu, Z., He, Y., Jiang, Y., Wang, H., Liu, W., Bohaty, S.M., Wilson, P.A., 2018. Transient temperature asymmetry between hemispheres in the Palaeogene Atlantic Ocean. Nat. Geosci. 1. https://doi.org/10.1038/s41561-018-0182-9

Lourens, L.J., Sluijs, A., Kroon, D., Zachos, J.C., Thomas, E., Röhl, U., Bowles, J., Raffi, I., 2005. Astronomical pacing of late Palaeocene to early Eocene global warming events. Nature 435, 1083–1087. https://doi.org/10.1038/nature03814

Luciani, V., Giusberti, L., Agnini, C., Fornaciari, E., Rio, D., Spofforth, D.J.A., Pälike, H., 2010. Ecological and evolutionary response of Tethyan planktonic foraminifera to the middle Eocene climatic optimum (MECO) from the Alano section (NE Italy). Palaeogeogr. Palaeoclimatol. Palaeoecol. 292, 82–95. https://doi.org/10.1016/j.palaeo.2010.03.029

Luck, J.M., Turekian, K.K., 1983. Osmium-^{187}/Osmium-^{186} in manganese nodules and the Cretaceous-Tertiary boundary. Science 222, 613–615.

Luo, Y., Boudreau, B.P., Dickens, G.R., Sluijs, A., Middelburg, J.J., 2016. An alternative model for $CaCO_3$ over-shooting during the PETM: Biological carbonate compensation. Earth Planet. Sci. Lett. 453, 223–233. https://doi.org/10.1016/j.epsl.2016.08.012

Lüthi, D., Le Floch, M., Bereiter, B., Blunier, T., Barnola, J.M., Siegenthaler, U., Raynaud, D., Jouzel, J., Fischer, H., Kawamura, K., Stocker, T.F., 2008. High-resolution carbon dioxide concentration record 650,000-800,000 years before present. Nature 453, 379–382. https://doi.org/10.1038/nature06949

Lyle, M., Barron, J., Bralower, T.J., Huber, M., Lyle, A.O., Ravelo, A.C., Rea, D.K., Wilson, P.A., 2008. Pacific ocean and cenozoic evolution of climate. Rev. Geophys. 46, 1–47. https://doi.org/10.1029/2005RG000190

Lyle, M., Olivarez Lyle, A., Backman, J., Tripati, A., 2005. Biogenic Sedimentation in the Eocene Equatorial Pacific-The Stuttering Greenhouse and Eocene Carbonate Compensation Depth, in: Proceedings of the Ocean Drilling Program, 199 Scientific Results. Ocean Drilling Program. https://doi.org/10.2973/odp.proc.sr.199.219.2005

Mackenzie, F.T., Garrels, R.M., 1966. Chemical mass balance between rivers and oceans. Am. J. Sci. 264, 507–525. https://doi.org/10.2475/ajs.264.7.507

Mackenzie, F.T., Morse, J.W., 1992. Sedimentary carbonates through Phanerozoic time. Geochim. Cosmochim. Acta 56, 3281–3295. https://doi.org/10.1016/0016-7037(92)90305-3

Mackenzie, F.T., Ver, L.M., Sabine, C., Lane, M., Lerman, A., 1993. C, N, P, S Global Biogeochemical Cycles and Modeling of Global Change, in: Wollast, R., Mackenzie, F.T., Chou, L. (Eds.), Interactions of C, N, P and S Biogeochemical Cycles and Global Change. Springer Berlin Heidelberg, Berlin, Heidelberg, pp. 1–61.

Maher, K., Chamberlain, C.P., 2014. Hydrologic Regulation of Chemical Weathering and the Geologic Carbon Cycle. Science 343, 1502–1504. https://doi.org/10.1126/science.1250770

Maier-Reimer, E., 1993. Geochemical cycles in an ocean general circulation model. Preindustrial tracer distributions. Global Biogeochem. Cycles 7, 645–677. https://doi.org/10.1029/93GB01355

Marriott, C.S., Henderson, G.M., Crompton, R., Staubwasser, M., Shaw, S., 2004. Effect of mineralogy, salinity, and temperature on Li/Ca and Li isotope composition of calcium carbonate. Chem. Geol. 212, 5–15. https://doi.org/10.1016/j.chemgeo.2004.08.002

Martin, C.E., 1991. Osmium isotopic characteristics of mantle-derived rocks. Geochim. Cosmochim. Acta 55, 1421–1434. https://doi.org/10.1016/0016-7037(91)90318-Y

Martin, R.E., 1995. Cyclic and secular variation in microfossil biomineralization: clues to the biogeochemical evolution of Phanerozoic oceans. Glob. Planet. Change 11, 1–23. https://doi.org/10.1016/0921-8181(94)00011-2

Martínez-Botí, M.A., Foster, G.L., Chalk, T.B., Rohling, E.J., Sexton, P.F., Lunt, D.J., Pancost, R.D., Badger, M.P.S., Schmidt, D.N., 2015. Plio-Pleistocene climate sensitivity evaluated using high-resolution CO_2 records. Nature 518, 49–54. https://doi.org/10.1038/nature14145

Matthews, K.J., Maloney, K.T., Zahirovic, S., Williams, S.E., Seton, M., Müller, R.D., 2016. Global plate boundary evolution and kinematics since the late Paleozoic. Glob. Planet. Change 146, 226–250. https://doi.org/10.1016/j.gloplacha.2016.10.002

McArthur, J.M., 1994. Recent trends in strontium isotope stratigraphy. Terra Nov. 331–358.

McArthur, J.M., Howarth, R.J., Shields, G.A., 2012. Strontium Isotope Stratigraphy, in: The Geologic Time Scale. Felix M. Gradstein, James G. Ogg, Mark Schmitz and Gabi Ogg, pp. 127–144. https://doi.org/10.1016/B978-0-444-59425-9.00007-X

McDonough, W.F., Sun, S.-S., 1995. The composition of the Earth. Chem. Geol. 120, 223–253. https://doi.org/10.1126/science.243.4889.367

McDowell, F.W., Mauger, R.L., 1994. K-Ar and U-Pb zircon chronology of late Cretaceous and Tertiary magmatism in central Chihuahua State, Mexico. Geol. Soc. Am. Bull. 106, 118–132. https://doi.org/10.1130/0016-7606(1994)106<0118:KAAUPZ>2.3.CO;2

Meckler, A.N., Ziegler, M., Millán, M.I., Breitenbach, S.F.M., Bernasconi, S.M., 2014. Long-term performance of the Kiel carbonate device with a new correction scheme for clumped isotope measurements. Rapid Commun. Mass Spectrom. 28, 1705–1715. https://doi.org/10.1002/rcm.6949

Meisel, T., Walker, R.J., Irving, A.J., Lorand, J.P., 2001. Osmium isotopic compositions of mantle xenoliths: A global perspective. Geochim. Cosmochim. Acta 65, 1311–1323. https://doi.org/10.1016/S0016-7037(00)00566-4

Merico, A., Tyrrell, T., Wilson, P.A., 2008. Eocene/Oligocene ocean de-acidification linked to Antarctic glaciation by sea-level fall. Nature 452, 979–982. https://doi.org/10.1038/nature06853

Meyers, P.A., 1994. Preservation of elemental and isotopic source identification of sedimentary organic matter. Chem. Geol. 114, 289–302. https://doi.org/10.1016/0009-2541(94)90059-0

Miller, K.G., Kominz, M.A., Browning, J. V., Wright, J.D., Mountain, G.S., Katz, M.E., Sugarman, P.J., Cramer, B.S., Christie-Blick, N., Pekar, S.F., 2005. The Phanerozoic Record of Global Sea-Level Change. Science 310, 1293–1298. https://doi.org/10.1126/science.1116412

Miller, K.G., Wright, J.D., Fairbanks, R.G., 1991. Unlocking the Ice House: Oligocene-Miocene oxygen isotopes, eustasy, and margin erosion. J. Geophys. Res. Solid Earth 96, 6829–6848. https://doi.org/10.1029/90JB02015

Milliman, J.D., 1993. Production and accumulation of calcium carbonate in the ocean: Budget of a nonsteady state. Global Biogeochem. Cycles 7, 927–957. https://doi.org/10.1029/93GB02524

Milliman, J.D., Syvitski, J.P.M., 1992. Geomorphic/Tectonic Control of Sediment Discharge to the Ocean: The Importance of Small Mountainous Rivers. J. Geol. 100, 525–544. https://doi.org/10.1086/629606

Milliman, J.D., Troy, P.J., Balch, W.M., Adams, A.K., Li, Y.H., Mackenzie, F.T., 1999. Biologically mediated dissolution of calcium carbonate above the chemical lysocline? Deep. Res. Part I Oceanogr. Res. Pap. 46, 1653–1669. https://doi.org/10.1016/S0967-0637(99)00034-5

Millot, R., Gaillardet, J., Dupré, B., Allègre, C.J., 2002. The global control of silicate weathering rates and the coupling with physical erosion: New insights from rivers of the Canadian Shield. Earth Planet. Sci. Lett. 196, 83–98. https://doi.org/10.1016/S0012-821X(01)00599-4

Mills, B., Watson, A.J., Goldblatt, C., Boyle, R., Lenton, T.M., 2011. Timing of Neoproterozoic glaciations linked to transport-limited global weathering. Nat. Geosci. 4, 861–864. https://doi.org/10.1038/ngeo1305

Misra, S., Froelich, P.N., 2012. Lithium Isotope History of Cenozoic Seawater: Changes in Silicate Weathering and Reverse Weathering. Science 335, 818–823. https://doi.org/10.1126/science.1214697

Mjelde, R., Breivik, A.J., Raum, T., Mittelstaedt, E., Ito, G., Faleide, J.I., 2008. Magmatic and tectonic evolution of the North Atlantic. J. Geol. Soc. London. 165, 31–42. https://doi.org/10.1144/0016-76492007-018

Müller, I.A., Violay, M.E.S., Storck, J.C., Fernandez, A., Van Dijk, J., Madonna, C., Bernasconi, S.M., 2017. Clumped isotope fractionation during phosphoric acid digestion of carbonates at 70 °C. Chem. Geol. 449, 1–14. https://doi.org/10.1016/j.chemgeo.2016.11.030

Müller, R.D., Sdrolias, M., Gaina, C., Steinberger, B., Heine, C., 2008. Long-Term Sea-Level Fluctuations Driven by Ocean Basin Dynamics. Science 319, 1357–1362. https://doi.org/10.1126/science.1151540

Nielsen, S.G., Mar-Gerrison, S., Gannoun, A., LaRowe, D., Klemm, V., Halliday, A.N., Burton, K.W., Hein, J.R., 2009. Thallium isotope evidence for a permanent increase in marine organic carbon export in the early Eocene. Earth Planet. Sci. Lett. 278, 297–307. https://doi.org/10.1016/j.epsl.2008.12.010

Nir, O., Vengosh, A., Harkness, J.S., Dwyer, G.S., Lahav, O., 2015. Direct measurement of the boron isotope fractionation factor: Reducing the uncertainty in reconstructing ocean paleo-pH. Earth Planet. Sci. Lett. 414, 1–5. https://doi.org/10.1016/j.epsl.2015.01.006

Norris, R.D., Wilson, P.A., Blum, P., Fehr, A., Agnini, C., Bornemann, A., Boulila, S., Bown, P.R., Cournede, C., Friedrich, O., Ghosh, A.K., Hollis, C.J., Hull, P.M., Jo, K., Junium, C.K., Kaneko, M., Liebrand, D., Lippert, P.C., Liu, Z., Matsui, H., Moriya, K., Nishi, H., Opdyke, B.N., Penman, D., Romans, B., Scher, H.D., Sexton, P., Takagi, H., Turner, S.K., Whiteside, J.H., Yamaguchi, T., Yamamoto, Y., 2014a. Expedition 342 summary, in: Proceedings of the Integrated Ocean Drilling Program. https://doi.org/10.2204/iodp.proc.342.101.2014

Norris, R.D., Wilson, P.A., Blum, P., Fehr, A., Agnini, C., Bornemann, A., Boulila, S., Bown, P.R., Cournede, C., Friedrich, O., Ghosh, A.K., Hollis, C.J., Hull, P.M., Jo, K., Junium, C.K., Kaneko, M., Liebrand, D., Lippert, P.C., Liu, Z., Matsui, H., Moriya, K., Nishi, H., Opdyke, B.N., Penman, D., Romans, B., Scher, H.D., Sexton, P., Takagi, H., Turner, S.K., Whiteside, J.H., Yamaguchi, T., Yamamoto, Y., 2014b. Site U1408, in: Proceedings of the Integrated Ocean Drilling Program. pp. 1–91. https://doi.org/10.2204/iodp.proc.342.109.2014

Norris, R.D., Wilson, P.A., Blum, P., Fehr, A., Agnini, C., Bornemann, A., Boulila, S., Bown, P.R., Cournede, C., Friedrich, O., Ghosh, A.K., Hollis, C.J., Hull, P.M., Jo, K., Junium, C.K., Kaneko, M., Liebrand, D., Lippert, P.C., Liu, Z., Matsui, H., Moriya, K., Nishi, H., Opdyke, B.N., Penman, D., Romans, B., Scher, H.D., Sexton, P., Takagi, H., Turner, S.K., Whiteside, J.H., Yamaguchi, T., Yamamoto, Y., 2014c. Site U1410, in: Proceedings of the Integrated Ocean Drilling Program. pp. 1–87. https://doi.org/10.2204/iodp.proc.342.111.2014

Ohkouchi, N., Eglinton, T.I., Keigwin, L.D., Hayes, J.M., 2002. Spatial and temporal offsets between proxy records in a sediment drift. Science 298, 1224–1227. https://doi.org/10.1126/science.1075287

Omta, A.W., Van Voorn, G.A.K., Rickaby, R.E.M., Follows, M.J., 2013. On the potential role of marine calcifiers in glacial-interglacial dynamics. Global Biogeochem. Cycles 27, 692–704. https://doi.org/10.1002/gbc.20060

Opdyke, B.N., Wilkinson, B.H., 1988. Surface Area Control of Shallow Cratonic to Deep Marine Carbonate Accumulation. Paleoceanography 3, 685–703.
Opfergelt, S., Georg, R.B., Delvaux, B., Cabidoche, Y.-M., Burton, K.W., Halliday, A.N., 2012. Mechanisms of magnesium isotope fractionation in volcanic soil weathering sequences, Guadeloupe. Earth Planet. Sci. Lett. 341–344, 176–185. https://doi.org/10.1016/j.epsl.2012.06.010
Ostlund, H.G., others, 1987. GEOSECS Atlantic, Pacific, and Indian Ocean Expeditions Vol 7.
Oxburgh, R., 2001. Residence time of osmium in the oceans. Geochemistry, Geophys. Geosystems 2, 2954–2976. https://doi.org/http://dx.doi.org/10.1002/ggge.20188
Pälike, H., Lyle, M.W., Nishi, H., Raffi, I., Ridgwell, A., Gamage, K., Klaus, A., Acton, G., Anderson, L., Backman, J., Baldauf, J., Beltran, C., Bohaty, S.M., Bown, P., Busch, W., Channell, J.E.T., Chun, C.O.J., Delaney, M., Dewangan, P., Dunkley Jones, T., Edgar, K.M., Evans, H., Fitch, P., Foster, G.L., Gussone, N., Hasegawa, H., Hathorne, E.C., Hayashi, H., Herrle, J.O., Holbourn, A., Hovan, S., Hyeong, K., Iijima, K., Ito, T., Kamikuri, S., Kimoto, K., Kuroda, J., Leon-Rodriguez, L., Malinverno, A., Moore Jr, T.C., Murphy, B.H., Murphy, D.P., Nakamura, H., Ogane, K., Ohneiser, C., Richter, C., Robinson, R., Rohling, E.J., Romero, O., Sawada, K., Scher, H., Schneider, L., Sluijs, A., Takata, H., Tian, J., Tsujimoto, A., Wade, B.S., Westerhold, T., Wilkens, R., Williams, T., Wilson, P.A., Yamamoto, Y., Yamamoto, S., Yamazaki, T., Zeebe, R.E., 2012. A Cenozoic record of the equatorial Pacific carbonate compensation depth. Nature 488, 609–614. https://doi.org/10.1038/nature11360
Pälike, H., Norris, R.D., Herrle, J.O., Wilson, P.A., Coxall, H.K., Lear, C.H., Shackleton, N.J., Tripati, A.K., Wade, B.S., 2006. The heartbeat of the Oligocene climate system. Science 314, 1894–1898. https://doi.org/10.1126/science.1133822
Palmer, M.R., Edmond, J.M., 1992. Controls over the strontium isotope composition of river water. Geochim. Cosmochim. Acta 56, 2099–2111. https://doi.org/10.1016/0016-7037(92)90332-D
Palmer, M.R., Edmond, J.M., 1989. The strontium isotope budget of the modern ocean. Earth Planet. Sci. Lett. 92, 11–26.
Palmer, M.R., Pearson, P.N., 2003. A 23,000-Year Record of Surface Water pH and PCO_2 in the Western Equatorial Pacific Ocean. Science 300, 480–482. https://doi.org/10.1126/science.1080796
Palmer, M.R., Pearson, P.N., Cobb, S.J., 1998. Reconstructing Past Ocean pH-Depth Profiles. Science 282, 1468–1471. https://doi.org/10.1126/science.282.5393.1468
Panchuk, K., Ridgwell, A., Kump, L.R., 2008. Sedimentary response to Paleocene-Eocene thermal maximum carbon release: A model-data comparison. Geology 36, 315–318. https://doi.org/10.1130/G24474A.1
Paquay, F.S., Ravizza, G.E., 2012. Heterogeneous seawater $^{187}Os/^{188}Os$ during the Late Pleistocene glaciations. Earth Planet. Sci. Lett. 349–350, 126–138. https://doi.org/10.1016/j.epsl.2012.06.051
Passey, B.H., Henkes, G.A., 2012. Carbonate clumped isotope bond reordering and geospeedometry. Earth Planet. Sci. Lett. 351–352, 223–236. https://doi.org/10.1016/j.epsl.2012.07.021
Paul, M., Reisberg, L., Vigier, N., Zheng, Y., Ahmed, K.M., Charlet, L., Huq, M.R., 2010. Dissolved osmium in Bengal plain groundwater: Implications for the marine Os budget. Geochim. Cosmochim. Acta 74, 3432–3448. https://doi.org/10.1016/j.gca.2010.02.034

Pearson, P.N., 2012. Oxygen Isotopes in Foraminifera : Overview and Historical Review. Paleontol. Soc. Pap. 18, 1–38. https://doi.org/10.1017/S1089332600002539
Pearson, P.N., Burgess, C.E., 2008. Foraminifer test preservation and diagenesis: comparison of high latitude Eocene sites. Geol. Soc. London, Spec. Publ. 303, 59–72. https://doi.org/10.1144/SP303.5
Pearson, P.N., Ditchfield, P.W., Singano, J., Harcourt-Brown, K.G., Nicholas, C.J., Olsson, R.K., Shackleton, N.J., Hall, M.A., 2001. Warm tropical sea surface temperatures in the Late Cretaceous and Eocene epochs. Nature 414, 470–470. https://doi.org/10.1038/35106617
Pearson, P.N., Palmer, M.R., 2000. Atmospheric carbon dioxide concentrations over the past 60 million years. Nature 406, 695–699. https://doi.org/10.1038/35021000
Pegram, W.J., Krishnaswami, S., Ravizza, G.E., Turekian, K.K., 1992. The record of seawater $^{187}Os/^{186}Os$ variation through the Cenozoic. Earth Planet. Sci. Lett. 113, 569–576.
Pegram, W.J., Turekian, K.K., 1999. The osmium isotopic composition change of Cenozoic sea water as inferred from a deep-sea core corrected for meteoritic contributions. Geochim. Cosmochim. Acta 63, 4053–4058. https://doi.org/10.1016/S0016-7037(99)00308-7
Peral, M., Daëron, M., Blamart, D., Bassinot, F., Dewilde, F., Smialkowski, N., Isguder, G., Bonnin, J., Jorissen, F., Kissel, C., Michel, E., Vázquez Riveiros, N., Waelbroeck, C., 2018. Updated calibration of the clumped isotope thermometer in planktonic and benthic foraminifera. Geochim. Cosmochim. Acta 239, 1–16. https://doi.org/10.1016/j.gca.2018.07.016
Percival, L.M.E., Ruhl, M., Hesselbo, S.P., Jenkyns, H.C., Mather, T.A., Whiteside, J.H., 2017. Mercury evidence for pulsed volcanism during the end-Triassic mass extinction. Proc. Natl. Acad. Sci. 114, 7929–7934. https://doi.org/10.1073/pnas.1705378114
Peucker-Ehrenbrink, B., 1996. Accretion of extraterrestrial matter during the last 80 million years and its effect on the marine osmium isotope record. Geochim. Cosmochim. Acta 60, 3187–3196. https://doi.org/10.1016/0016-7037(96)00161-5
Peucker-Ehrenbrink, B., Jahn, B.-M., 2001. Rhenium-osmium isotope systematics and platinum group element concentrations: Loess and the upper continental crust. Geochemistry, Geophys. Geosystems 2, 2001GC000172.
Peucker-Ehrenbrink, B., Miller, M.W., Arsouze, T., Jeandel, C., 2010. Continental bedrock and riverine fluxes of strontium and neodymium isotopes to the oceans. Geochemistry, Geophys. Geosystems 11. https://doi.org/10.1029/2009GC002869
Peucker-Ehrenbrink, B., Ravizza, G.E., 2012. Osmium Isotope Stratigraphy, in: The Geologic Time Scale 2012 2-Volume Set. Elsevier, pp. 145–166. https://doi.org/10.1016/B978-0-444-59425-9.00008-1
Peucker-Ehrenbrink, B., Ravizza, G.E., 2000. The marine osmium isotope record. Terra Nov. 12, 205–219. https://doi.org/10.1046/j.1365-3121.2000.00295.x
Peucker-Ehrenbrink, B., Ravizza, G.E., Hofmann, A.W., 1995. The marine $^{187}Os/^{186}Os$ record of the past 80 million years. Earth Planet. Sci. Lett. 130, 155–167.
Pierson-Wickmann, A.C., Reisberg, L., France-Lanord, C., 2000. The Os isotopic composition of Himalayan river bedloads and bedrocks: Importance of black shales. Earth Planet. Sci. Lett. 176, 203–218. https://doi.org/10.1016/S0012-821X(00)00003-0
Pistiner, J.S., Henderson, G.M., 2003. Lithium-isotope fractionation during continental weathering processes. Earth Planet. Sci. Lett. 214, 327–339. https://doi.org/10.1016/S0012-821X(03)00348-0

Pogge von Strandmann, P.A.E., 2008. Precise magnesium isotope measurements in core top planktic and benthic foraminifera. Geochemistry, Geophys. Geosystems 9. https://doi.org/10.1029/2008GC002209

Pogge von Strandmann, P.A.E., Burton, K.W., James, R.H., Van Calsteren, P., Gislason, S.R., Sigfusson, B., 2008. The influence of weathering processes on riverine magnesium isotopes in a basaltic terrain. Earth Planet. Sci. Lett. 276, 187–197. https://doi.org/10.1016/j.epsl.2008.09.020

Pogge von Strandmann, P.A.E., Forshaw, J., Schmidt, D.N., 2014. Modern and Cenozoic records of seawater magnesium from foraminiferal Mg isotopes. Biogeosciences 11, 5155–5168. https://doi.org/10.5194/bg-11-5155-2014

Pogge von Strandmann, P.A.E., Henderson, G.M., 2015. The Li isotope response to mountain uplift. Geology 43, 67–70. https://doi.org/10.1130/G36162.1

Pogge von Strandmann, P.A.E., Jenkyns, H.C., Woodfine, R.G., 2013. Lithium isotope evidence for enhanced weathering during Oceanic Anoxic Event 2. Nat. Geosci. 6, 668–672. https://doi.org/10.1038/ngeo1875

Pogge von Strandmann, P.A.E., Opfergelt, S., Lai, Y.-J., Sigfusson, B., Gislason, S.R., Burton, K.W., 2012. Lithium, magnesium and silicon isotope behaviour accompanying weathering in a basaltic soil and pore water profile in Iceland. Earth Planet. Sci. Lett. 339–340, 11–23. https://doi.org/10.1016/j.epsl.2012.05.035

Popov, S. V, Akhmetev, M.A., Zaporozhets, N.I., Voronina, A.A., Stolyarov, A.S., 1993. Evolution of Eastern Paratethys in the late Eoceneearly Miocene. Stratigr. Geol. Correl. 1, 10–39.

Popov, S. V, Rögl, F., Rozanov, A.Y., Steininger, F.F., Shcherba, I.G., Kovac, M., 2004. Lithological-Paleogeographic maps of Paratethys-10 maps Late Eocene to Pliocene. Courier Forschungsinstitut Senckenberg, v. 250, p. 1–46.

Premoli-Silva, I., Wade, B.S., Pearson, P.N., 2006. Taxonomy, biostratigraphy, and phylogeny of Globigerinatheka and Orbulinoides. Cushman Found. Foraminifer. Res. Spec. Publ. 41, 169–212.

Ravizza, G.E., 1998. Osmium-isotope geochemistry of Site 959: implications for Re-Os sedimentary geochronology and reconstruction of past variations in the Os-isotopic composition of seawater. Proc. Ocean Drill. Program, Sci. Results 159, 181–186.

Ravizza, G.E., 1993. Variations of the $^{187}Os/^{186}Os$ ratio of seawater over the past 28 million years as inferred from metalliferous carbonates. Earth Planet. Sci. Lett. 118, 335–348. https://doi.org/10.1016/0012-821X(93)90177-B

Ravizza, G.E., Norris, R.N., Blusztajn, J., Aubry, M.-P., 2001. An osmium isotope excursion associated with the late Paleocene thermal maximum: Evidence of intensified chemical weathering. Paleoceanography 16, 155–163.

Ravizza, G.E., Paquay, F.S., 2008. Os isotope chemostratigraphy applied to organic-rich marine sediments from the Eocene-Oligocene transition on the West African margin (ODP Site 959). Paleoceanography 23. https://doi.org/10.1029/2007PA001460

Ravizza, G.E., Peucker-Ehrenbrink, B., 2003. Chemostratigraphic Evidence of Deccan Volcanism from the Marine Osmium Isotope Record. Science 302, 1392–1395. https://doi.org/10.1126/science.1089209

Ravizza, G.E., Turekian, K.K., 1992. The osmium isotopic composition of organic-rich marine sediments. Earth Planet. Sci. Lett. 110, 1–6. https://doi.org/10.1016/0012-821X(92)90034-S

Ravizza, G.E., Turekian, K.K., Hay, B.J., 1991. The geochemistry of rhenium and osmium in recent sediments from the Black Sea. Geochim. Cosmochim. Acta 55, 3741–3752. https://doi.org/10.1016/0016-7037(91)90072-D

Ravizza, G.E., Zachos, J.C., 2003. Records of Cenozoic Ocean Chemistry. Treatise on Geochemistry 6, 551–581. https://doi.org/10.1016/B978-0-08-095975-7.00620-3

Raymo, M.E., Ruddiman, W.F., 1992. Tectonic forcing of late Cenozoic climate. Nature 359, 117–122.

Raymo, M.E., Ruddiman, W.F., Froelich, P.N., 1988. Influence of late Cenozoic mountain building on ocean geochemical cycles. Geology 16, 649–653. https://doi.org/10.1130/0091-7613(1988)016<0649

Regenberg, M., Regenberg, A., Garbe-Schönberg, D., Lea, D.W., 2014. Global dissolution effects on planktonic foraminiferal Mg/Ca ratios controlled by the calcite-saturation state of bottom waters. Paleoceanography 29, 127–142. https://doi.org/10.1002/2013PA002492

Richter, F.M., DePaolo, D.J., 1988. Diagenesis and Sr isotopic evolution of seawater using data from DSDP 590B and 575. Earth Planet. Sci. Lett. 90, 382–394. https://doi.org/10.1016/0012-821X(88)90137-9

Richter, F.M., Turekian, K.K., 1993. Simple models for the geochemical response of the ocean to climatic and tectonic forcing. Earth Planet. Sci. Lett. 119, 121–131. https://doi.org/10.1016/0012-821X(93)90010-7

Ridgwell, A., 2005. A Mid Mesozoic Revolution in the regulation of ocean chemistry. Mar. Geol. 217, 339–357. https://doi.org/10.1016/j.margeo.2004.10.036

Ridgwell, A., Hargreaves, J.C., 2007. Regulation of atmospheric CO_2 by deep-sea sediments in an Earth system model. Global Biogeochem. Cycles 21, 1–14. https://doi.org/10.1029/2006GB002764

Ridgwell, A., Zeebe, R.E., 2005. The role of the global carbonate cycle in the regulation and evolution of the Earth system. Earth Planet. Sci. Lett. 234, 299–315. https://doi.org/10.1016/j.epsl.2005.03.006

Ridgwell, A.J., Kennedy, M.J., Caldeira, K., 2003. Carbonate Deposition, Climate Stability, and Neoproterozoic Ice Ages. Science 302, 859–862. https://doi.org/10.1126/science.1088342

Robinson, N., Ravizza, G.E., Coccioni, R., Peucker-Ehrenbrink, B., Norris, R.D., 2009. A high-resolution marine $^{187}Os/^{188}Os$ record for the late Maastrichtian: Distinguishing the chemical fingerprints of Deccan volcanism and the KP impact event. Earth Planet. Sci. Lett. 281, 159–168. https://doi.org/10.1016/j.epsl.2009.02.019

Rodríguez-Sanz, L., Bernasconi, S.M., Marino, G., Heslop, D., Müller, I.A., Fernandez, A., Grant, K.M., Rohling, E.J., 2017. Penultimate deglacial warming across the Mediterranean Sea revealed by clumped isotopes in foraminifera. Sci. Rep. 7, 16572. https://doi.org/10.1038/s41598-017-16528-6

Rooney, A.D., Selby, D., Lloyd, J.M., Roberts, D.H., Lückge, A., Sageman, B.B., Prouty, N.G., 2016. Tracking millennial-scale Holocene glacial advance and retreat using osmium isotopes: Insights from the Greenland ice sheet. Quat. Sci. Rev. 138, 49–61. https://doi.org/10.1016/j.quascirev.2016.02.021

Rooney, T.O., 2017. The Cenozoic magmatism of East-Africa: Part I — Flood basalts and pulsed magmatism. Lithos 286–287, 264–301. https://doi.org/10.1016/j.lithos.2017.05.014

Rowley, D.B., 2002. Rate of plate creation and destruction: 180 Ma to present. Geol. Soc. Am. Bull. 114, 927–933. https://doi.org/10.1130/0016-7606(2002)114<0927:ROPCAD>2.0.CO;2

Royer, D.L., Berner, R.A., Montañez, I.P., Tabor, N.J., Beerling, D.J., 2004. CO_2 as a primary driver of Phanerozoic climate. GSA Today 14, 4. https://doi.org/10.1130/1052-5173(2004)014<4:CAAPDO>2.0.CO;2

Sabine, C.L., Feely, R.A., Key, R.M., Bullister, J.L., Millero, F.J., Lee, K., Peng, T.-H., Tilbrook, B., Ono, T., Wong, C.S., 2002. Distribution of anthropogenic CO_2 in the Pacific Ocean. Global Biogeochem. Cycles 16, 30-1-30–17. https://doi.org/10.1029/2001GB001639

Sanei, H., Grasby, S.E., Beauchamp, B., 2012. Latest permian mercury anomalies. Geology 40, 63–66. https://doi.org/10.1130/G32596.1

Sarmiento, J.L., Gruber, N., 2006. Ocean Biogeochemical Dynamics. Princeton University Press.

Sarmiento, J.L., Toggweiler, J.R., 1984. A new model for the role of the oceans in determining atmospheric P CO_2. Nature 308, 621–624. https://doi.org/10.1038/308621a0

Savin, S.M., 1977. The History of the Earth's Surface Temperature During the Past 100 Million Years. Annu. Rev. Earth Planet. Sci. 5, 319–355. https://doi.org/10.1146/annurev.ea.05.050177.001535

Schlanger, S.O., Jenkyns, H.C., 1976. Cretaceous ocean anoxic events: causes and consequences. Geol. en Mijnb. 55, 179–184.

Schlitzer, R., 2015. Data analysis and visualization with Ocean Data View. C. Bull. SCMO 43, 9–13.

Schmid, T.W., Bernasconi, S.M., 2010. An automated method for 'clumped-isotope' measurements on small carbonate samples. Rapid Commun. Mass Spectrom. 24, 1955–1963. https://doi.org/10.1002/rcm.4598

Schmidt, G.A., 1999. Forward modeling of carbonate proxy data from planktonic foraminifera using oxygen isotope tracers in a global ocean model. Paleoceanography 14, 482–497. https://doi.org/10.1029/1999PA900025

Schouten, S., Hopmans, E.C., Schefuß, E., Sinninghe Damsté, J.S., 2002. Distributional variations in marine crenarchaeotal membrane lipids: a new tool for reconstructing ancient sea water temperatures? Earth Planet. Sci. Lett. 204, 265–274. https://doi.org/10.1016/S0012-821X(02)00979-2

Schulz, H.-M., Bechtel, A., Sachsenhofer, R.F., 2005. The birth of the Paratethys during the Early Oligocene: From Tethys to an ancient Black Sea analogue? Glob. Planet. Change 49, 163–176.

Selby, D., Creaser, R.A., 2003. Re–Os geochronology of organic rich sediments: an evaluation of organic matter analysis methods. Chem. Geol. 200, 225–240. https://doi.org/10.1016/S0009-2541(03)00199-2

Seton, M., Müller, R.D., Zahirovic, S., Gaina, C., Torsvik, T., Shephard, G., Talsma, A., Gurnis, M., Turner, M., Maus, S., Chandler, M., 2012. Global continental and ocean basin reconstructions since 200Ma. Earth-Science Rev. 113, 212–270. https://doi.org/10.1016/j.earscirev.2012.03.002

Sexton, P.F., Wilson, P.A., Pearson, P.N., 2006. Microstructural and geochemical perspectives on planktic foraminiferal preservation: "glassy" versus "frosty." Geochemistry, Geophys. Geosystems 7. https://doi.org/10.1029/2006GC001291

Shafik, S., Watkins, D.K., Shin, I.C., 1998. Calcareous Nannofossil Paleogene Biostratigraphy, Côte D'Ivoire-Ghana Marginal Ridge, Eastern Equatorial Atlantic. Proc. Ocean Drill. Program, Sci. Results 159, 413–431.

Sharma, M., Wasserburg, G.J., Hofmann, A.W., Chakrapani, G.J., 1999. Himalayan uplift and osmium isotopes in oceans and rivers. Geochim. Cosmochim. Acta 63, 4005–4012.

Shcherbinina, E., Gavrilov, Y., Iakovleva, A., Pokrovsky, B., Golovanova, O., Aleksandrova, G., 2016. Environmental dynamics during the Paleocene--Eocene thermal maximum (PETM) in the northeastern Peri-Tethys revealed by high-resolution micropalaeontological and geochemical studies of a Caucasian key section. Palaeogeogr. Palaeoclimatol. Palaeoecol. 456, 60–81.

Shevenell, A.E., Kennett, J.P., Lea, D.D., 2004. Middle Miocene Southern Ocean Cooling and Antarctic Cryosphere Expansion. Science 305, 1766–1770. https://doi.org/10.1126/science.1100061

Si, W., Aubry, M.-P., 2018. Vital effects and ecologic adaptation of photosymbiont-bearing planktonic foraminifera during the Paleocene-Eocene Thermal Maximum, implications for paleoclimate. Paleoceanogr. Paleoclimatology 1–14. https://doi.org/10.1002/2017PA003219

Siegenthaler, U., Wenk, T., 1984. Rapid atmospheric CO_2 variations and ocean circulation. Nature 308, 624–626. https://doi.org/10.1038/308624a0

Sigman, D.M., Boyle, E.A., 2000. Glacial/Interglacial variations in atmospheric CO_2. Nature 407, 859–869. https://doi.org/10.1007/s12170-007-0034-4

Sigurdsson, H., Kelley, S., Leckie, R.M., Carey, S., Bralower, T., King, J., 2000. History of circum-Caribbean explosive volcanism: $^{40}Ar/^{39}Ar$ dating of tephra layers. Proc. Ocean Drill. Program, Sci. Results 165, 299–314.

Sime, N.G., De La Rocha, C.L., Tipper, E.T., Tripati, A.K., Galy, A., Bickle, M.J., 2007. Interpreting the Ca isotope record of marine biogenic carbonates. Geochim. Cosmochim. Acta 71, 3979–3989. https://doi.org/10.1016/j.gca.2007.06.009

Singh, S.K., Trivedi, J.R., Krishnaswami, S., 1999. Re-Os isotope systematics in black shales from the Lesser Himalaya: Their chronology and role in the $^{187}Os/^{188}Os$ evolution of seawater. Geochim. Cosmochim. Acta 63, 2381–2392. https://doi.org/10.1016/S0016-7037(99)00201-X

Sinninghe Damsté, J.S., 2016. Spatial heterogeneity of sources of branched tetraethers in shelf systems: The geochemistry of tetraethers in the Berau River delta (Kalimantan, Indonesia). Geochim. Cosmochim. Acta 186, 13–31. https://doi.org/10.1016/j.gca.2016.04.033

Skulan, J., DePaolo, D.J., Owens, T.L., 1997. Biological control of calcium isotopic abundances in the global calcium cycle. Geochim. Cosmochim. Acta 61, 2505–2510. https://doi.org/10.1016/S0016-7037(97)00047-1

Slotnick, B.S., Lauretano, V., Backman, J., Dickens, G.R., Sluijs, A., Lourens, L., 2015. Early Paleogene variations in the calcite compensation depth: New constraints using old borehole sediments from across Ninetyeast Ridge, central Indian Ocean. Clim. Past 11, 473–493. https://doi.org/10.5194/cp-11-473-2015

Sluijs, A., Pross, J., Brinkhuis, H., 2005. From greenhouse to icehouse; organic-walled dinoflagellate cysts as paleoenvironmental indicators in the Paleogene. Earth-Science Rev. 68, 281–315. https://doi.org/10.1016/j.earscirev.2004.06.001

Sluijs, A., Schouten, S., Donders, T.H., Schoon, P.L., Röhl, U., Reichart, G.-J., Sangiorgi, F., Kim, J.-H., Sinninghe Damsté, J.S., Brinkhuis, H., 2009. Warm and wet conditions in the Arctic region during Eocene Thermal Maximum 2. Nat. Geosci. 2, 777–780. https://doi.org/10.1038/ngeo668

Sluijs, A., Zeebe, R.E., Bijl, P.K., Bohaty, S.M., 2013. A middle Eocene carbon cycle conundrum. Nat. Geosci. 6, 429–434. https://doi.org/10.1038/ngeo1807

Smoliar, M.I., Walker, R.J., Morgan, J.W., 1996. Re-Os Ages of Group IIA, IIIA, IVA, and IVB Iron Meteorites. Science 271, 1099–1102.
Sosdian, S.M., Greenop, R., Hain, M.P., Foster, G.L., Pearson, P.N., Lear, C.H., 2018. Constraining the evolution of Neogene ocean carbonate chemistry using the boron isotope pH proxy. Earth Planet. Sci. Lett. 498, 362–376. https://doi.org/10.1016/J.EPSL.2018.06.017
Sosdian, S.M., Lear, C.H., Tao, K., Grossman, E.L., O'Dea, A., Rosenthal, Y., 2012. Cenozoic seawater Sr/Ca evolution. Geochemistry, Geophys. Geosystems 13. https://doi.org/10.1029/2012GC004240
Spivack, A.J., You, C.-F., Smith, H.J., 1993. Foraminiferal boron isotope ratios as a proxy for surface ocean pH over the past 21 Myr. Nature 363, 149–151. https://doi.org/10.1038/363149a0
Spofforth, D.J.A., Agnini, C., Pälike, H., Rio, D., Fornaciari, E., Giusberti, L., Luciani, V., Lanci, L., Muttoni, G., 2010. Organic carbon burial following the middle Eocene climatic optimum in the central western Tethys. Paleoceanography 25. https://doi.org/10.1029/2009PA001738
Stanley, S.M., Hardie, L.A., 1998. Secular oscillations in the carbonate mineralogy of reef-building and sediment-producing organisms driven by tectonically forced shifts in seawater chemistry. Palaeogeogr. Palaeoclimatol. Palaeoecol. 144, 3–19. https://doi.org/10.1016/S0031-0182(98)00109-6
Stap, L., Sluijs, A., Thomas, E., Lourens, L.J., 2009. Patterns and magnitude of deep sea carbonate dissolution during Eocene Thermal Maximum 2 and H2, Walvis Ridge, southeastern Atlantic Ocean. Paleoceanography 24. https://doi.org/10.1029/2008PA001655
Stolper, D.A., Eiler, J.M., Higgins, J.A., 2018. Modeling the effects of diagenesis on carbonate clumped-isotope values in deep- and shallow-water settings. Geochim. Cosmochim. Acta. https://doi.org/10.1016/j.gca.2018.01.037
Svensen, H., Planke, S., Malthe-Sørenssen, A., Jamtveit, B., Myklebust, R., Rasmussen Eidem, T., Rey, S.S., 2004. Release of methane from a volcanic basin as a mechanism for initial Eocene global warming. Nature 429, 542–545. https://doi.org/10.1038/nature02566
Taylor, K.W.R., Huber, M., Hollis, C.J., Hernandez-Sanchez, M.T., Pancost, R.D., 2013. Re-evaluating modern and Palaeogene GDGT distributions: Implications for SST reconstructions. Glob. Planet. Change 108, 158–174. https://doi.org/10.1016/j.gloplacha.2013.06.011
Teng, F.-Z., Li, W.-Y., Ke, S., Marty, B., Dauphas, N., Huang, S., Wu, F.-Y., Pourmand, A., 2010a. Magnesium isotopic composition of the Earth and chondrites. Geochim. Cosmochim. Acta 74, 4150–4166. https://doi.org/10.1016/j.gca.2010.04.019
Teng, F.-Z., Li, W.-Y., Rudnick, R.L., Gardner, L.R., 2010b. Contrasting lithium and magnesium isotope fractionation during continental weathering. Earth Planet. Sci. Lett. 300, 63–71. https://doi.org/10.1016/j.epsl.2010.09.036
Them, T.R., Gill, B.C., Selby, D., Gröcke, D.R., Friedman, R.M., Owens, J.D., 2017. Evidence for rapid weathering response to climatic warming during the Toarcian Oceanic Anoxic Event. Sci. Rep. 7, 5003. https://doi.org/10.1038/s41598-017-05307-y
Tierney, J.E., Tingley, M.P., 2018. BAYSPLINE: A New Calibration for the Alkenone Paleothermometer. Paleoceanogr. Paleoclimatology 33, 281–301. https://doi.org/10.1002/2017PA003201
Tierney, J.E., Tingley, M.P., 2014. A Bayesian, spatially-varying calibration model for the TEX86 proxy. Geochim. Cosmochim. Acta 127, 83–106. https://doi.org/10.1016/j.gca.2013.11.026
Tindall, J., Flecker, R., Valdes, P., Schmidt, D.N., Markwick, P., Harris, J., 2010. Modelling the oxygen isotope distribution of ancient seawater using a coupled ocean-atmosphere GCM:

Implications for reconstructing early Eocene climate. Earth Planet. Sci. Lett. 292, 265–273. https://doi.org/10.1016/j.epsl.2009.12.049
Tipper, E.T., Bickle, M.J., Galy, A., West, A.J., Pomiès, C., Chapman, H.J., 2006a. The short term climatic sensitivity of carbonate and silicate weathering fluxes: Insight from seasonal variations in river chemistry. Geochim. Cosmochim. Acta 70, 2737–2754. https://doi.org/10.1016/j.gca.2006.03.005
Tipper, E.T., Gaillardet, J., Galy, a., Louvat, P., Bickle, M.J., Capmas, F., 2010. Calcium isotope ratios in the world's largest rivers: A constraint on the maximum imbalance of oceanic calcium fluxes. Global Biogeochem. Cycles 24. https://doi.org/10.1029/2009GB003574
Tipper, E.T., Galy, A., Bickle, M.J., 2008. Calcium and magnesium isotope systematics in rivers draining the Himalaya-Tibetan-Plateau region: Lithological or fractionation control? Geochim. Cosmochim. Acta 72, 1057–1075. https://doi.org/10.1016/j.gca.2007.11.029
Tipper, E.T., Galy, A., Bickle, M.J., 2006b. Riverine evidence for a fractionated reservoir of Ca and Mg on the continents: Implications for the oceanic Ca cycle. Earth Planet. Sci. Lett. 247, 267–279. https://doi.org/10.1016/j.epsl.2006.04.033
Tipper, E.T., Galy, A., Gaillardet, J., Bickle, M.J., Elderfield, H., Carder, E., 2006c. The magnesium isotope budget of the modern ocean: Constraints from riverine magnesium isotope ratios. Earth Planet. Sci. Lett. 250, 241–253. https://doi.org/10.1016/j.epsl.2006.07.037
Toffanin, F., Agnini, C., Rio, D., Acton, G., Westerhold, T., 2013. Middle Eocene to early Oligocene calcareous nannofossil biostratigraphy at IODP Site U1333 (equatorial Pacific). Micropaleontology 59, 69–82.
Torres, M.A., West, A.J., Clark, K.E., Paris, G., Bouchez, J., Ponton, C., Feakins, S.J., Galy, V., Adkins, J.F., 2016. The acid and alkalinity budgets of weathering in the Andes–Amazon system: Insights into the erosional control of global biogeochemical cycles. Earth Planet. Sci. Lett. 450, 381–391. https://doi.org/10.1016/j.epsl.2016.06.012
Torsvik, T.H., Amundsen, H.E.F., Trønnes, R.G., Doubrovine, P. V., Gaina, C., Kusznir, N.J., Steinberger, B., Corfu, F., Ashwal, L.D., Griffin, W.L., Werner, S.C., Jamtveit, B., 2015. Continental crust beneath southeast Iceland. Proc. Natl. Acad. Sci. 112, E1818–E1827. https://doi.org/10.1073/pnas.1423099112
Torsvik, T.H., Cocks, L.R.M., 2005. Norway in space and time: A Centennial cavalcade. Nor. Geol. Tidsskr. 85, 73–86.
Torsvik, T.H., Van der Voo, R., Preeden, U., Niocaill, C.M., Steinberger, B., Doubrovine, P. V., Van Hinsbergen, D.J.J., Domeier, M., Gaina, C., Tohver, E., Meert, J.G., McCausland, P.J.A., Cocks, L.R.M., 2012. Phanerozoic polar wander, palaeogeography and dynamics. Earth-Science Rev. 114, 325–368. https://doi.org/10.1016/j.earscirev.2012.06.002
Tréguer, P.J., De La Rocha, C.L., 2013. The World Ocean Silica Cycle. Ann. Rev. Mar. Sci. 5, 477–501. https://doi.org/10.1146/annurev-marine-121211-172346
Turekian, K.K., 1964. The marine geochemistry of strontium. Geochim. Cosmochim. Acta 28, 1479–1496.
Turgeon, S.C., Creaser, R.A., 2008. Cretaceous oceanic anoxic event 2 triggered by a massive magmatic episode. Nature 454, 323–326. https://doi.org/10.1038/nature07076
Tyrrell, T., Zeebe, R.E., 2004. History of carbonate ion concentration over the last 100 million years. Geochim. Cosmochim. Acta 68, 3521–3530. https://doi.org/10.1016/j.gca.2004.02.018
Urey, H.C., 1952. The planets: their origin and development. Yale Univ. Press.
Vahlenkamp, M., Niezgodzki, I., Vleeschouwer, D. De, Lohmann, G., Bickert, T., Pälike, H., 2018. Ocean and climate response to North Atlantic seaway changes at the onset of long-

term Eocene cooling. Earth Planet. Sci. Lett. 498, 185–195. https://doi.org/10.1016/j.epsl.2018.06.031
Van Andel, T.H., 1975. Mesozoic/cenozoic calcite compensation depth and the global distribution of calcareous sediments. Earth Planet. Sci. Lett. 26, 187–194. https://doi.org/10.1016/0012-821X(75)90086-2
Van der Boon, A., 2017. From Peri-Tethys to Paratethys: Basin restriction and anoxia in central Eurasia linked to volcanic belts in Iran. PhD Thesis. Utrecht University.
Van der Meer, D.G., Zeebe, R.E., Van Hinsbergen, D.J.J., Sluijs, A., Spakman, W., Torsvik, T.H., 2014. Plate tectonic controls on atmospheric CO_2 levels since the Triassic. Proc. Natl. Acad. Sci. U. S. A. 111, 4380–5. https://doi.org/10.1073/pnas.1315657111
Van der Ploeg, R., Selby, D., Cramwinckel, M.J., Li, Y., Bohaty, S.M., Middelburg, J.J., Sluijs, A., 2018. Middle Eocene greenhouse warming facilitated by diminished weathering feedback. Nat. Commun. 9, 2877. https://doi.org/10.1038/s41467-018-05104-9
Van Hinsbergen, D.J.J., de Groot, L. V., Van Schaik, S.J., Spakman, W., Bijl, P.K., Sluijs, A., Langereis, C.G., Brinkhuis, H., 2015. A Paleolatitude Calculator for Paleoclimate Studies. PLoS One 10, e0126946. https://doi.org/10.1371/journal.pone.0126946
Vance, D., 2011. Isotopic tracers of chemical weathering and consequences for marine geochemical budgets. Appl. Geochemistry 26, S311–S313. https://doi.org/10.1016/j.apgeochem.2011.03.090
Vance, D., Teagle, D.A.H., Foster, G.L., 2009. Variable Quaternary chemical weathering fluxes and imbalances in marine geochemical budgets. Nature 458, 493–6. https://doi.org/10.1038/nature07828
Veizer, J., Ala, D., Azmy, K., Bruckschen, P., Buhl, D., Bruhn, F., Carden, G.A.F., Diener, A., Ebneth, S., Goddéris, Y., Jasper, T., Korte, C., Pawellek, F., Podlaha, O.G., Strauss, H., 1999. $^{87}Sr/^{86}Sr$, $d^{13}C$ and $d^{18}O$ evolution of Phanerozoic seawater. Chem. Geol. 59–88.
Vigier, N., Decarreau, A., Millot, R., Carignan, J., Petit, S., France-Lanord, C., 2008. Quantifying Li isotope fractionation during smectite formation and implications for the Li cycle. Geochim. Cosmochim. Acta 72, 780–792. https://doi.org/10.1016/j.gca.2007.11.011
Vigier, N., Gislason, S.R., Burton, K.W., Millot, R., Mokadem, F., 2009. The relationship between riverine lithium isotope composition and silicate weathering rates in Iceland. Earth Planet. Sci. Lett. 287, 434–441. https://doi.org/10.1016/j.epsl.2009.08.026
Vigier, N., Goddéris, Y., 2015. A new approach for modeling Cenozoic oceanic lithium isotope paleo-variations: the key role of climate. Clim. Past 11, 635–645. https://doi.org/10.5194/cp-11-635-2015
Vigier, N., Rollion-Bard, C., Levenson, Y., Erez, J., 2015. Lithium isotopes in foraminifera shells as a novel proxy for the ocean dissolved inorganic carbon (DIC). Comptes Rendus Geosci. 347, 43–51. https://doi.org/10.1016/j.crte.2014.12.001
Vollstaedt, H., Eisenhauer, A., Wallmann, K., Böhm, F., Fietzke, J., Liebetrau, V., Krabbenhöft, A., Farkaš, J., Tomašových, A., Raddatz, J., Veizer, J., 2014. The Phanerozoic $\delta^{88}/^{86}Sr$ record of seawater: New constraints on past changes in oceanic carbonate fluxes. Geochim. Cosmochim. Acta 128, 249–265. https://doi.org/10.1016/j.gca.2013.10.006
Wagner, T., 2002. Late Cretaceous to early Quaternary organic sedimentation in the eastern Equatorial Atlantic. Palaeogeogr. Palaeoclimatol. Palaeoecol. 179, 113–147. https://doi.org/10.1016/S0031-0182(01)00415-1
Walker, J.C.G., Hays, P.B., Kasting, J.F., 1981. A negative feedback mechanism for the long-term stabilization of Earth's surface temperature. J. Geophys. Res. 86, 9776–9782.

Walker, J.C.G., Kasting, J.F., 1992. Effects of fuel and forest conservation on future levels of atmospheric carbon dioxide. Palaeogeogr. Palaeoclimatol. Palaeoecol. 97, 151–189.
Walker, L.J., Wilkinson, B.H., Ivany, L.C., 2002. Continental Drift and Phanerozoic Carbonate Accumulation in Shallow-Shelf and Deep-Marine Settings. J. Geol. 110, 75–87. https://doi.org/10.1086/324318
Walker, R.J., Morgan, J.W., Beary, E.S., Smoliar, M.I., Czamanske, G.K., Horan, M.F., 1997. Applications of the ^{190}Pt-^{186}Os isotope system to geochemistry and cosmochemistry. Geochim. Cosmochim. Acta 61, 4799–4807. https://doi.org/10.1016/S0016-7037(97)00270-6
Wallmann, K., 2001. Controls on the cretaceous and cenozoic evolution of seawater composition, atmospheric CO_2 and climate. Geochim. Cosmochim. Acta 65, 3005–3025. https://doi.org/10.1016/S0016-7037(01)00638-X
Wedepohl, K.H., 1995. Composition of the Continental Crust. Geochim. Cosmochim. Acta 59, 1217–1232.
Weijers, J.W.H., Lim, K.L.H., Aquilina, A., Damsté, J.S.S., Pancost, R.D., 2011. Biogeochemical controls on glycerol dialkyl glycerol tetraether lipid distributions in sediments characterized by diffusive methane flux. Geochemistry, Geophys. Geosystems 12, 1–15. https://doi.org/10.1029/2011GC003724
Weijers, J.W.H., Schouten, S., Spaargaren, O.C., Sinninghe Damsté, J.S., 2006. Occurrence and distribution of tetraether membrane lipids in soils: Implications for the use of the TEX_{86} proxy and the BIT index. Org. Geochem. 37, 1680–1693. https://doi.org/10.1016/j.orggeochem.2006.07.018
West, A.J., 2012. Thickness of the chemical weathering zone and implications for erosional and climatic drivers of weathering and for carbon-cycle feedbacks. Geology 40, 811–814. https://doi.org/10.1130/G33041.1
West, A.J., Galy, A., Bickle, M.J., 2005. Tectonic and climatic controls on silicate weathering. Earth Planet. Sci. Lett. 235, 211–228. https://doi.org/10.1016/j.epsl.2005.03.020
Westerhold, T., Röhl, U., Frederichs, T., Bohaty, S.M., Zachos, J.C., 2015. Astronomical calibration of the geological timescale: Closing the middle Eocene gap. Clim. Past 11, 1181–1195. https://doi.org/10.5194/cp-11-1181-2015
Westerhold, T., Röhl, U., Pälike, H., Wilkens, R., Wilson, P.A., Acton, G., 2014. Orbitally tuned timescale and astronomical forcing in the middle Eocene to early Oligocene. Clim. Past 10, 955–973. https://doi.org/10.5194/cp-10-955-2014
Westerhold, T., Röhl, U., Wilkens, R., Pälike, H., Lyle, M.W., Dunkley Jones, T., Bown, P., Moore, T., Kamikuri, S., Acton, G., Ohneiser, C., Yamamoto, Y., Richter, C., Fitch, P., Scher, H., Liebrand, D., 2012. Revised composite depth scales and integration of IODP Sites U1331-U1334 and ODP Sites 1218-1220. Proc. Integr. Ocean Drill. Progr. 320. https://doi.org/10.2204/iodp.proc.320321.201.2012
Willenbring, J.K., Von Blanckenburg, F., 2010. Long-term stability of global erosion rates and weathering during late-Cenozoic cooling. Nature 465, 211–4. https://doi.org/10.1038/nature09044
Williams, G.L., Fensome, R.A., MacRae, R.A., 2017. The Lentin and Williams Index of Fossil Dinoflagellates 2017 Edition: AASP Contributions Series 48.
Wimpenny, J., Colla, C.A., Yin, Q.-Z., Rustad, J.R., Casey, W.H., 2014. Investigating the behaviour of Mg isotopes during the formation of clay minerals. Geochim. Cosmochim. Acta 128, 178–194. https://doi.org/10.1016/j.gca.2013.12.012

Wimpenny, J., Gíslason, S.R., James, R.H., Gannoun, A., Pogge von Strandmann, P.A.E., Burton, K.W., 2010. The behaviour of Li and Mg isotopes during primary phase dissolution and secondary mineral formation in basalt. Geochim. Cosmochim. Acta 74, 5259–5279. https://doi.org/10.1016/j.gca.2010.06.028

Winguth, C., Winguth, A.M.E., 2012. Simulating Permian-Triassic oceanic anoxia distribution: Implications for species extinction and recovery. Geology 40, 127–130. https://doi.org/10.1130/G32453.1

Woelders, L., Vellekoop, J., Weltje, G.J., de Nooijer, L., Reichart, G.-J., Peterse, F., Claeys, P., Speijer, R.P., 2018. Robust multi-proxy data integration, using late Cretaceous paleotemperature records as a case study. Earth Planet. Sci. Lett. 500, 215–224. https://doi.org/10.1016/j.epsl.2018.08.010

Wombacher, F., Eisenhauer, A., Böhm, F., Gussone, N., Regenberg, M., Dullo, W.-C., Rüggeberg, A., 2011. Magnesium stable isotope fractionation in marine biogenic calcite and aragonite. Geochim. Cosmochim. Acta 75, 5797–5818. https://doi.org/10.1016/j.gca.2011.07.017

Wuchter, C., Schouten, S., Wakeham, S.G., Damsté, J.S.S., 2006. Archaeal tetraether membrane lipid fluxes in the northeastern Pacific and the Arabian Sea: Implications for TEX_{86} paleothermometry. Paleoceanography 21, 1–9. https://doi.org/10.1029/2006PA001279

Yu, J., Elderfield, H., 2007. Benthic foraminiferal B/Ca ratios reflect deep water carbonate saturation state. Earth Planet. Sci. Lett. 258, 73–86. https://doi.org/10.1016/j.epsl.2007.03.025

Zachos, J.C., Dickens, G.R., Zeebe, R.E., 2008. An early Cenozoic perspective on greenhouse warming and carbon-cycle dynamics. Nature 451, 279–283. https://doi.org/10.1038/nature06588

Zachos, J.C., Opdyke, B.N., Quinn, T.M., Jones, C.E., Halliday, A.N., 1999. Early cenozoic glaciation, antarctic weathering, and seawater $^{87}Sr/^{86}Sr$: is there a link? Chem. Geol. 161, 165–180. https://doi.org/Doi: 10.1016/s0009-2541(99)00085-6

Zachos, J.C., Pagani, M., Sloan, L., Thomas, E., Billups, K., 2001. Trends, rhythms, and aberrations in global climate 65 Ma to present. Science 292, 686–693.

Zachos, J.C., Röhl, U., Schellenberg, S.A., Sluijs, A., Hodell, D.A., Kelly, D.C., Thomas, E., Nicolo, M., Raffi, I., Lourens, L.J., McCarren, H.K., Kroon, D., 2005. Rapid acidification of the ocean during the Paleocene-Eocene thermal maximum. Science 308, 1611–1615. https://doi.org/10.1126/science.1109004

Zachos, J.C., Stott, L.D., Lohmann, K.C., 1994. Evolution of Early Cenozoic marine temperatures. Paleoceanography 9, 353–387. https://doi.org/10.1029/93PA03266

Zachos, J.C., Wara, M.W., Bohaty, S.M., Delaney, M.L., Petrizzo, M.R., Brill, A., Bralower, T.J., Premoli-Silva, I., 2003. A transient rise in tropical sea surface temperature during the Paleocene-Eocene thermal maximum. Science 302, 1551–1554. https://doi.org/10.1126/science.1090110

Zakrevskaya, E., Beniamovsky, V., Less, G., Baldi-Beke, M., 2011. Integrated biostratigraphy of Eocene deposits in the Gubs section (Northern Caucasus) with special attention to the Ypresian/Lutetian boundary and to the Peritethyan-Tethyan correlation. Turkish J. Earth Sci. 20, 753–792.

Zeebe, R.E., 2012a. LOSCAR: Long-term Ocean-atmosphere-Sediment CArbon cycle Reservoir model v2.0.4. Geosci. Model Dev. 5, 149–166. https://doi.org/10.5194/gmd-5-149-2012

Zeebe, R.E., 2012b. History of Seawater Carbonate Chemistry, Atmospheric CO_2, and Ocean Acidification. Annu. Rev. Earth Planet. Sci. 40, 141–165. https://doi.org/10.1146/annurev-earth-042711-105521

Zeebe, R.E., Caldeira, K., 2008. Close mass balance of long-term carbon fluxes from ice-core CO_2 and ocean chemistry records. Nat. Geosci. 1, 312–315. https://doi.org/10.1038/ngeo185

Zeebe, R.E., Tyrrell, T., 2018. Comment on "The Effects of Secular Calcium and Magnesium Concentration Changes on the Thermodynamics of Seawater Acid/Base Chemistry: Implications for Eocene and Cretaceous Ocean Carbon Chemistry and Buffering" by Hain et al. (2015). Global Biogeochem. Cycles 32, 895–897. https://doi.org/10.1002/2017GB005786

Zeebe, R.E., Zachos, J.C., 2007. Reversed deep-sea carbonate ion basin gradient during Paleocene-Eocene thermal maximum. Paleoceanography 22, 1–17. https://doi.org/10.1029/2006PA001395

Zeebe, R.E., Zachos, J.C., Dickens, G.R., 2009. Carbon dioxide forcing alone insufficient to explain Palaeocene–Eocene Thermal Maximum warming. Nat. Geosci. 2, 576–580. https://doi.org/10.1038/ngeo578

Zhang, Y.G., Zhang, C.L., Liu, X.L., Li, L., Hinrichs, K.U., Noakes, J.E., 2011. Methane Index: A tetraether archaeal lipid biomarker indicator for detecting the instability of marine gas hydrates. Earth Planet. Sci. Lett. 307, 525–534. https://doi.org/10.1016/j.epsl.2011.05.031

Zhu, P., Macdougall, J.D., 1998. Calcium isotopes in the marine environment and the oceanic calcium cycle. Geochim. Cosmochim. Acta 62, 1691–1698.

Summary in Dutch

(Samenvatting in het Nederlands)

Samenvatting in het Nederlands

De onderstaande Nederlandse samenvatting van dit proefschrift bestaat uit drie delen: een introductie waarin de koolstofkringloop en de klimaatgeschiedenis van het Cenozoïcum worden uiteengezet en de onderzoeksvragen van dit proefschrift worden ingeleid, een synopsis waarin de bevindingen van dit proefschrift per hoofdstuk worden samengevat, en een vooruitblik waarin nieuwe vragen en mogelijkheden voor vervolgonderzoek worden beschreven.

Introductie

De koolstofkringloop is een essentieel onderdeel van het systeem Aarde dat de biosfeer, atmosfeer, oceanen en geosfeer met elkaar verbindt. De uitwisseling van koolstof tussen deze reservoirs bepaalt de hoeveelheid CO_2 in de atmosfeer, die de temperatuur op het aardoppervlak reguleert (Walker et al., 1981; Berner et al., 1983). Op geologische tijdschalen van honderdduizenden tot miljoenen jaren komt CO_2 enerzijds in de atmosfeer en oceanen terecht door vulkanische ontgassing en de oxidatieve verwering van organisch koolstof in sedimenten (Berner, 2004). Anderzijds wordt CO_2 opgenomen tijdens de verwering van silicaatgesteente en uiteindelijk vastgelegd door begraving van organisch en anorganisch koolstof in sedimenten (Figuur 1). Deze instroom en uitstroom van CO_2 moet in nauw evenwicht zijn op geologische tijdschalen om leefbare klimaatomstandigheden op het aardoppervlak te creëren en te onderhouden (Berner, 2004; Zeebe en Caldeira, 2008). Deze stabiliteit in de koolstofkringloop wordt waarschijnlijk veroorzaakt door een negatief terugkoppelingsmechanisme, waarbij de snelheid van silicaatverwering wordt gemoduleerd door klimaat, tektonische processen

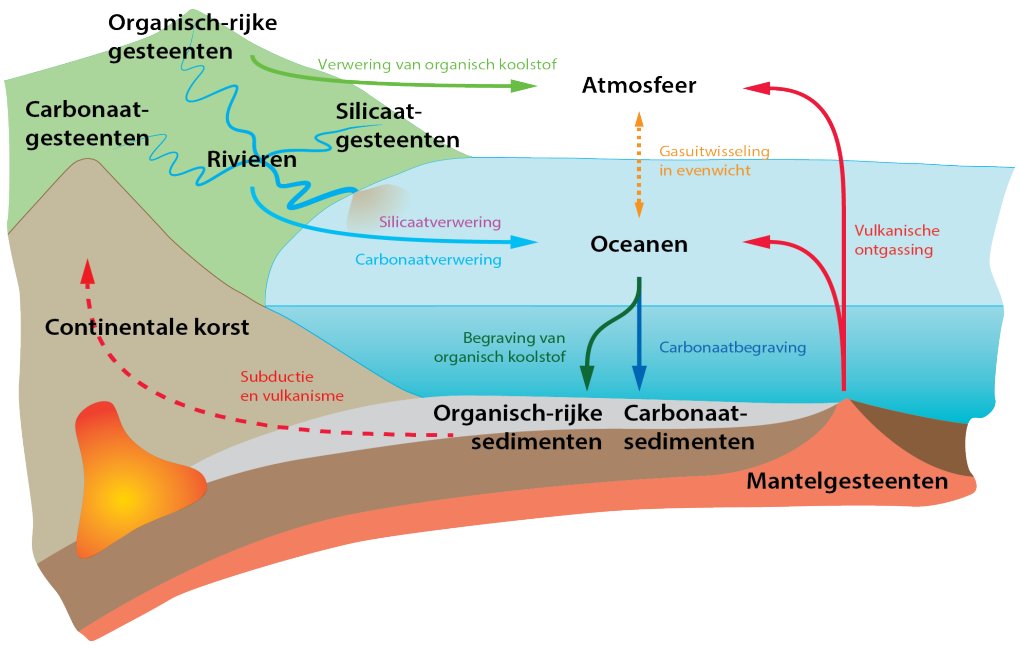

Figuur 1: Schematische weergave van processen die een rol spelen in de geologische koolstofkringloop.

en de verweerbaarheid van de continenten (Walker et al., 1981; Berner et al., 1983; Raymo en Ruddiman, 1992; Kump en Arthur, 1997; Caves et al., 2016). Desalniettemin hebben tijdelijke verstoringen van het klimaat en de koolstofkringloop zich frequent voorgedaan in de geschiedenis van de Aarde (IPCC, 2014). Het geologisch verleden biedt daarom een uniek perspectief op de natuurlijke oorzaken en gevolgen van klimaatverandering en de tijdschalen voor herstel van koolstofkringloopverstoringen.

Het Cenozoïcum, de periode die de laatste ~66 miljoen jaar van de geschiedenis van de Aarde omvat (Gradstein et al., 2012), wordt gekenmerkt door een graduele transitie van een warme broeikaswereld naar een veel koudere ijskaswereld, waarschijnlijk als gevolg van

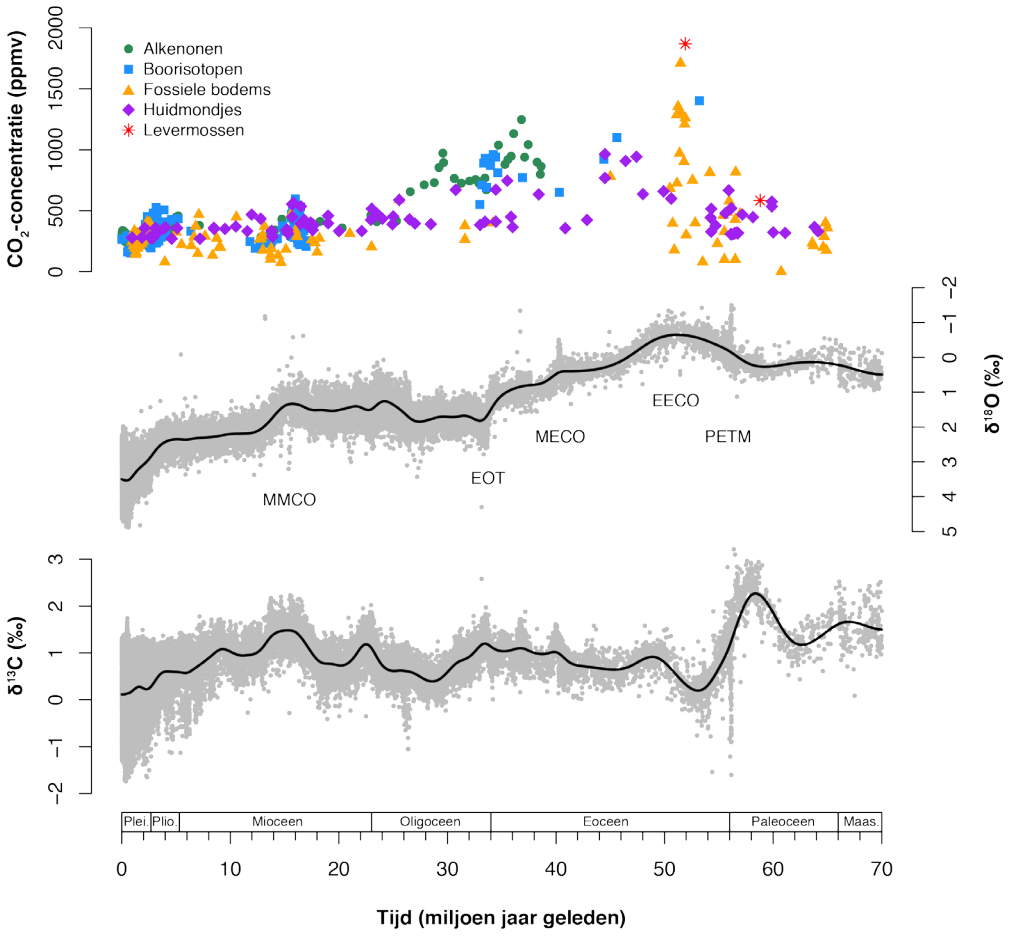

Figuur 2: Evolutie van atmosferische CO_2-concentraties en wereldwijd klimaat tijdens het Cenozoïcum. Atmosferische CO_2-gegevens zijn afkomstig van Foster et al. (2017) en referenties daarin, met schattingen op basis van alkenonen als groene cirkels, boorisotopen als blauwe vierkanten, fossiele bodems als oranje driehoeken, huidmondjes als paarse ruiten en levermossen als rode sterren. Zuurstofisotopen- ($\delta^{18}O$) en koolstofisotopen- ($\delta^{13}C$) datasets van benthische foraminiferen zijn afkomstig van Cramer et al. (2009) en aangepast naar de GTS 2012 (Gradstein et al., 2012). Zwarte lijnen zijn vloeiende curven die het best passen bij de data.

progressief afnemende atmosferische CO_2-concentraties (Savin, 1977; Kennett, 1982; Zachos et al., 2008; Foster et al., 2017; Cramwinckel et al., 2018) (Figuur 2). Over de afgelopen ~150 jaar zijn de atmosferische CO_2-concentraties door antropogene koolstofemissies gestegen van ongeveer 280 volumedeeltjes per miljoen (ppmv) naar waarden groter dan 400 ppmv. Dit heeft tot dusver wereldwijd geleid tot 1 °C opwarming (IPCC, 2018). Ter vergelijking: tijdens de ijstijden van de laatste ~1 miljoen jaar hebben CO_2-concentraties gevarieerd tussen ongeveer 180–280 ppmv (Lüthi et al., 2008). CO_2-concentraties die vergelijkbaar zijn met de huidige omstandigheden (~400 ppmv) zijn voor het laatst voorgekomen in het Plioceen, ongeveer 3–5 miljoen jaar geleden (Martínez-Botí et al., 2015). Nog verder terug in de tijd worden CO_2-concentraties geschat op waarden van ~600 ppmv in het Mioceen rond ~15 miljoen jaar geleden (Sosdian et al., 2018) en waarden van ~1000 ppmv of meer in het Eoceen rond ~50 miljoen jaar geleden (Anagnostou et al., 2016). Gedurende het grootste gedeelte van het Cenozoïcum waren temperaturen, en derhalve ook de zeespiegel, wereldwijd veel hoger dan in het heden (Miller et al., 2005; Herold et al., 2012; Haywood et al., 2016; Cramwinckel et al., 2018). De verschillende fasen van de klimaatevolutie van het Cenozoïcum vormen daarom mogelijke analogieën voor toekomstige klimaatveranderingen door antropogene koolstofemissies (Zachos et al., 2008).

Van bijzonder belang voor studies naar gekoppelde interacties tussen de koolstofkringloop en het klimaat zijn de zogenoemde *hyperthermals* van het laat Paleoceen en het vroeg Eoceen, waaronder het Paleoceen-Eoceen Thermisch Maximum (PETM; ~56 miljoen jaar geleden) en Eoceen Thermisch Maximum 2 (ETM-2; ~54 miljoen jaar geleden). Deze relatief korte perioden van wereldwijde opwarming en oceaanverzuring worden geassocieerd met het snelle vrijkomen van koolstof in de atmosfeer en oceanen (Dickens et al., 1997; Zachos et al., 2003, 2005; Lourens et al., 2005). Deze *hyperthermals* worden gekenmerkt door grote negatieve verschuivingen in de stabiele koolstofisotopensamenstelling ($\delta^{13}C$) van exogeen koolstof. Dit geeft aan dat de extra koolstof mogelijk van methaanhydraten (Dickens et al., 1995), organisch materiaal (Kurtz et al., 2003) of vulkanische bronnen afkomstig kan zijn (Svensen et al., 2004; Gutjahr et al., 2017), of een combinatie van deze mechanismen (Panchuk et al., 2008; Frieling et al., 2016). De tijdschaal van klimaatherstel na afloop van deze *hyperthermals* wordt geschat in de orde van ~100 duizend jaar (Zachos et al., 2003, 2005) en wordt voornamelijk toegeschreven

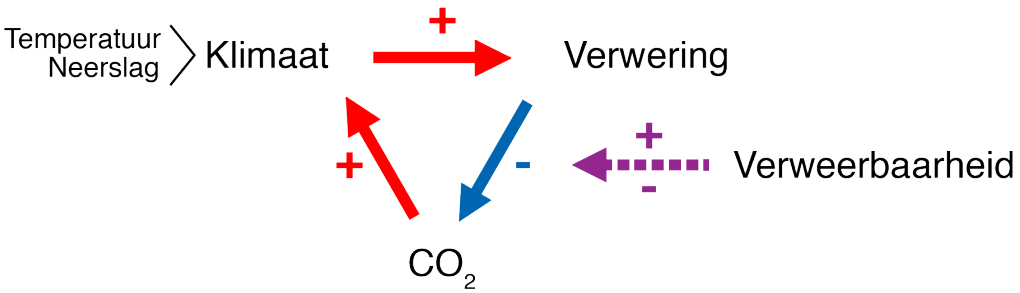

Figuur 3: Schematische weergave van het concept van de verweerbaarheid van de continenten, dat de kracht van de negatieve silicaatverweringsterugkoppeling reguleert. Rode pijlen en plus-symbolen geven processen weer die een positief effect hebben en blauwe pijlen en min-symbolen geven processen weer die een negatief effect hebben. Veranderingen in de verweerbaarheid van de continenten kunnen de effectiviteit van de silicaatverweringsthermostaat beïnvloeden.

aan versnelde verwering van silicaatgesteente als gevolg van opwarming (Ravizza et al., 2001; Kelly en Zachos, 2005; Dickson et al., 2015). Dit komt overeen met voorspellingen voor de silicaatverweringsthermostaat op basis van theorie (Berner, 2004).

De exacte rol van silicaatverwering in de lange-termijn evolutie van CO_2 en klimaat in het Cenozoïcum is veel bediscussieerd sinds de hypothese van de silicaatverweringsthermostaat oorspronkelijk werd voorgesteld door Walker et al. (1981) en Berner et al. (1983). Raymo en Ruddiman (1992) hebben bijvoorbeeld beargumenteerd dat een toename in verwering gerelateerd aan de tektonische opheffing van het Himalaya-gebergte een oorzaak kan zijn geweest van afkoeling in het laat Cenozoïcum. Dit leidt tot de fundamentele vraag of klimatologische of tektonische processen de meest dominante invloed hebben gehad op verwering gedurende het Cenozoïcum en verder terug in de tijd. Kump en Arthur (1997) hebben deze tegengestelde opvattingen met elkaar verzoend door het concept van een variabele verweerbaarheid van de continenten te introduceren, dat wil zeggen de modulatie van verweringssnelheden door lange-termijn veranderingen in de reactiviteit van het aardoppervlak (Figuur 3). Een dergelijke variabele sterkte van de silicaatverweringsterugkoppeling is vervolgens verder onderbouwd door het modelleren van verweringsfluxen op basis van datasets van atmosferische CO_2-concentraties en de oceaanchemie van het Cenozoïcum (Caves et al., 2016). Bovenal impliceert een variabele sterkte van de silicaatverweringsterugkoppeling dat verweringsfluxen relatief onveranderd kunnen zijn gebleven over geologische tijdschalen, terwijl er alsnog een balans in de koolstofkringloop wordt onderhouden bij verschillende achtergrondniveaus van atmosferisch CO_2 (Caves et al., 2016). Dit zou in overeenstemming zijn met verweringsreconstructies die ongeveer constante snelheden van wereldwijde verwering en erosie laten zien over de laatste ~10 miljoen jaar (Willenbring en Von Blanckenburg, 2010).

Alhoewel de interacties tussen CO_2, klimaat en verwering in het geologisch verleden steeds beter worden begrepen, vormt het Midden Eoceen Klimaat Optimum (MECO; ~40 miljoen jaar geleden) een verstoring van de koolstofkringloop waarvan zowel de oorzaak als het uiteindelijke herstel zeer raadselachtig blijven (Sluijs et al., 2013). De MECO is een periode van wijdverbreide opwarming gedurende ~500 duizend jaar die optrad bovenop de lange-termijn trend van afkoeling in het Eoceen en in verband gebracht wordt met CO_2-stijging, biotische veranderingen en oplossing van carbonaatgesteente in de diepe oceanen (Bohaty en Zachos, 2003; Bohaty et al., 2009; Bijl et al., 2010). In tegenstelling tot de *hyperthermals* van het Paleogeen, zoals de PETM, wordt de MECO niet gemarkeerd door een negatieve $\delta^{13}C$-excursie en wordt de MECO gekenmerkt door een gradueel begin van opwarming (~400 duizend jaar), gevolgd door een korte fase van piek-warmte (~50 duizend jaar) en een relatief snelle afkoelingsfase (~50 duizend jaar) (Bohaty et al., 2009; Sluijs et al., 2013) (Figuur 4). Dit sluit het plotseling vrijkomen van grote hoeveelheden van $\delta^{13}C$-arm koolstof uit als oorzaak van of positieve terugkoppeling op MECO-opwarming, en wijst in plaats daarvan op een meer geleidelijk mechanisme dat resulteert in een onbalans in de koolstofkringloop over ~500 duizend jaar (Sluijs et al., 2013). Bovendien trekt deze duur van ~500 duizend jaar het gedrag van de silicaatverweringsthermostaat in twijfel, omdat versterkte verwering en CO_2-opname geacht worden voor klimaatherstel te zorgen binnen 100–200 duizend jaar, zoals tijdens de *hyperthermals* in het Paleogeen (Zachos et al., 2005; Kelly et al., 2010). Derhalve verschilt de MECO van de traditioneel geïdentificeerde trends, ritmes en afwijkingen in het klimaatsysteem (Zachos et al., 2001) en vormt een uitdaging voor de huidige kennis van de dynamiek van de koolstofkringloop en het klimaat op intermediaire tijdschalen (Sluijs et al., 2013).

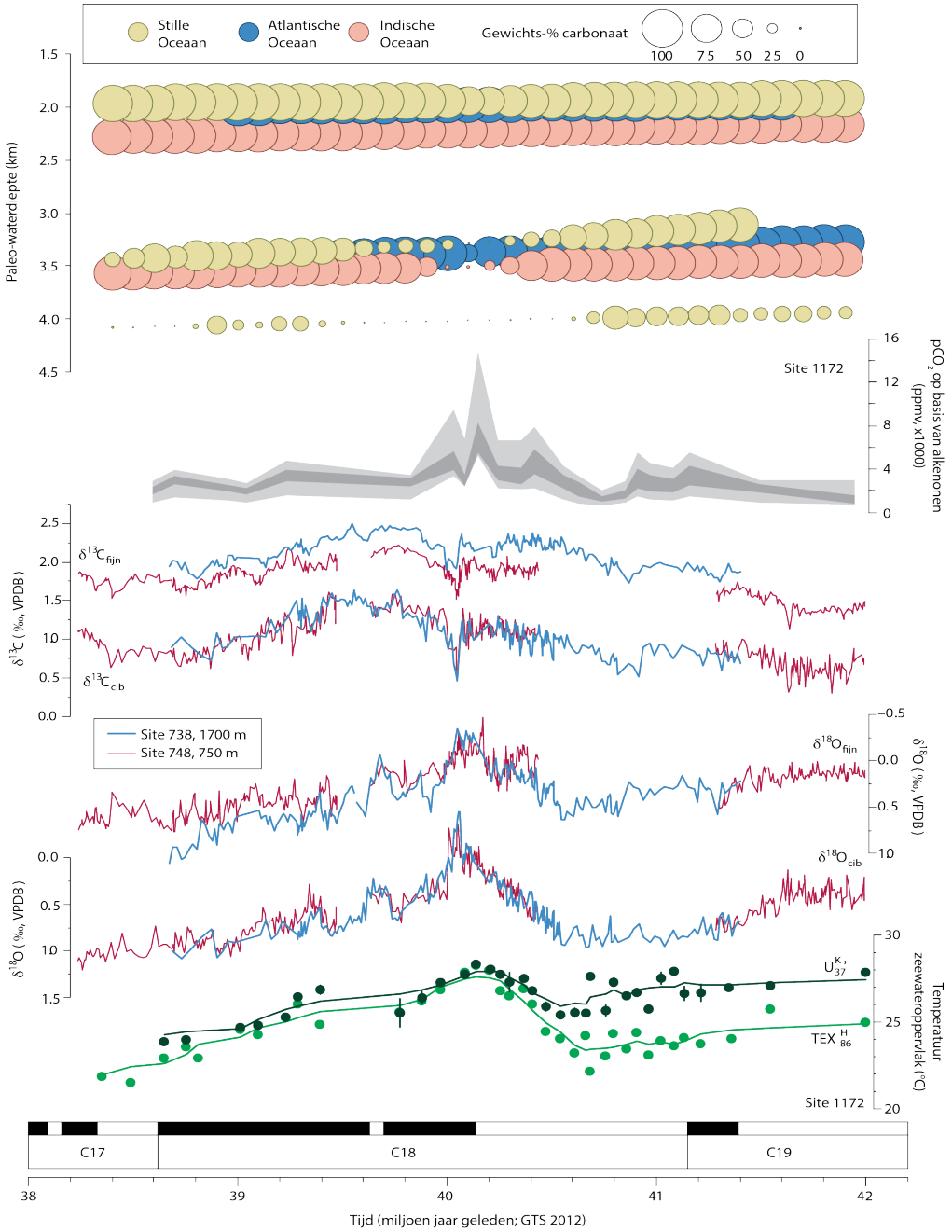

Figuur 4: Compilatie van MECO-gegevens, aangepast van Sluijs et al. (2013). Carbonaatgehalten zijn afkomstig van Hancock en Dickens (2005), Lyle et al. (2005) en Bohaty et al. (2009). $\delta^{18}O$- en $\delta^{13}C$-gegevens zijn afkomstig van Bohaty en Zachos (2003) en Bohaty et al. (2009). Atmosferische CO_2-, TEX_{86}^{H}- en $U^{K'}_{37}$-gegevens zijn afkomstig van Bijl et al. (2010).

Naast het schijnbaar ontbreken van een verweringsrespons worden verschillende andere aspecten van de MECO ook nog niet goed begrepen. Ten eerste is het nog niet duidelijk of opwarming van de oceaan werkelijk een wereldwijd fenomeen was, ondanks dat de MECO of de daarmee geassocieerde veranderingen zoals carbonaatoplossing zijn geïdentificeerd in alle grote oceaanbekkens (Bohaty et al., 2009). Tot dusver is significante opwarming beschreven voor locaties op hoge breedtegraden in de Zuidelijke Oceaan (Bohaty et al., 2009; Bijl et al., 2010), locaties op intermediaire breedtegraden in de noordelijke en zuidelijke Atlantische Oceaan (Bohaty et al., 2009; Edgar et al., 2010; Boscolo Galazzo et al., 2014) en het Tethys-domein (Jovane et al., 2007; Spofforth et al., 2010), alsmede een locatie in de tropische Atlantische Oceaan (Cramwinckel et al., 2018). Echter, net als bij veel andere temperatuurreconstructies in het geologisch verleden, zijn de meeste bestaande datasets van de MECO gebaseerd op de stabiele zuurstofisotopensamenstelling ($\delta^{18}O$) van foraminiferen of bulk carbonaatsedimenten, welke ook zeer gevoelig zijn voor lokale veranderingen in de $\delta^{18}O$-samenstelling van zeewater. Bovendien is opwarming nog niet beschreven voor locaties op hoge breedtegraden in de Noord-Atlantische Oceaan, of voor locaties in de Grote Oceaan. Het bevestigen van het wereldwijde karakter van de MECO-opwarming zou een belangrijke stap voorwaarts betekenen in het identificeren van de oorzaak van deze gebeurtenis, omdat wereldwijde opwarming wijst op forcering door broeikasgassen in plaats van regionale processen, zoals veranderingen in oceanische circulatie.

Terwijl $\delta^{18}O$-datasets goede eerste-orde informatie geven over relatieve temperatuurveranderingen tijdens de MECO, zijn additionele gegevens van proxies zoals Mg/Ca, TEX_{86} of *clumped* isotopen (Δ_{47}) vereist om meer precieze absolute oceaantemperaturen vast te stellen. In een bredere zin is dit ook van belang voor het evalueren van meridionale temperatuurgradiënten en voor het verder verminderen van de voortdurende wanverhouding tussen temperaturen op hoge breedtegraden die afgeleid worden uit proxygegevens en temperatuurvoorspellingen die worden gemaakt op basis van modellen (Sluijs et al., 2009; Hollis et al., 2012; Frieling et al., 2016; Cramwinckel et al., 2018).

Verder is er weinig bekend over milieuveranderingen in gebieden op het continentaal plat tijdens de MECO. Sluijs et al. (2013) stelden dat carbonaatoplossing in de diepe oceanen mogelijk verklaard kan worden door een verschuiving in carbonaatafzetting van de diepe oceanen naar ondiepere wateren als gevolg van zeespiegelstijging, maar tot dusver is deze hypothese nog niet getoetst. De ondiepste pelagische locaties waar de MECO is beschreven bevinden zich in het Tethys-domein (Jovane et al., 2007; Spofforth et al., 2010), dus dit zou een veelbelovend gebied kunnen zijn om MECO gegevens te verkrijgen van een locatie op het continentaal plat.

Tot slot zijn zowel de duur als het mechanisme van de terminatie van de MECO nog steeds onduidelijk (Bohaty et al., 2009). De schijnbare afwezigheid van een effectieve negatieve silicaatverweringsterugkoppeling doet de vraag rijzen of andere processen wellicht hebben bijgedragen aan de relatief snelle afkoeling, zoals gezien wordt in MECO-archieven uit de diepzee (Sluijs et al., 2013). Een mogelijkheid is dat de begraving van organisch koolstof toenam in de nasleep van de MECO, zoals wordt afgeleid uit verhoogde gehalten van totaal organisch koolstof (TOC) op een locatie in de westelijke Tethys Oceaan (Spofforth et al., 2010). De schaal waarop deze mogelijke begraving van organisch koolstof plaatsvond blijft echter onbekend. Daarom is het in kaart brengen van de MECO op additionele locaties in het Tethys-domein van cruciaal belang om te onderzoeken of de begraving van organisch koolstof inderdaad kan hebben bijgedragen aan het afvangen van CO_2 en klimaatherstel na MECO-opwarming.

Synopsis

De strekking van dit proefschrift is tweeledig. Eerst verken ik manieren om ons begrip van de verweringsgeschiedenis en algemene evolutie van de koolstofkringloop tijdens het Cenozoïcum te verbeteren, en vervolgens focus ik op de enigmatische interacties tussen CO_2, verwering en klimaat tijdens de MECO. Binnen het eerste thema vat ik de gevestigde proxies voor reconstructies van wereldwijde chemische verwering samen en modelleer ik verschillende scenario's voor verwering in het Cenozoïcum (Hoofdstuk 2). Daarna modelleer ik veranderingen in de carbonaatchemie van de oceanen tijdens het Cenozoïcum en test ik de robuustheid van gepubliceerde schattingen van atmosferische CO_2 concentraties (Hoofdstuk 3). Ook leid ik snelheden van neritische carbonaatafzetting af voor het Cenozoïcum met een model gebaseerd op een massabalans voor carbonaat-alkaliniteit (Hoofdstuk 4). Vervolgens presenteer ik belangrijke nieuwe datasets om openstaande vragen naar aanleiding van de MECO te beantwoorden. In het bijzonder reconstrueer ik wereldwijde veranderingen in silicaatverwering en gebruik ik modellen van de koolstofkringloop om de meest waarschijnlijke oorzaak voor de MECO te achterhalen (Hoofdstuk 5). Om de kwestie van opwarming tijdens de MECO en mogelijke complicerende factoren in proxies voor oppervlaktetemperaturen van zeewater aan te kaarten, presenteer ik een dataset met oppervlaktetemperaturen van de Noord-Atlantische Oceaan op basis van meerdere proxies in hoge resolutie (Hoofdstuk 6). Tot slot rapporteer ik veranderingen in temperatuur en milieu tijdens de MECO op basis van een sectie met afzettingen van het continentaal plat uit het Tethys-domein (Hoofdstuk 7).

In Hoofdstuk 2 presenteer ik een overzicht van gevestigde proxies voor wereldwijde reconstructies van chemische verwering in het geologisch verleden. Ik vat de hypothese van de silicaatverwering thermostaat samen en illustreer hoe de isotopensystemen van koolstof ($\delta^{13}C$), strontium ($^{87}Sr/^{86}Sr$), osmium ($^{187}Os/^{188}Os$), lithium ($\delta^{7}Li$), calcium ($\delta^{44}Ca$) en magnesium ($\delta^{26}Mg$) gebruikt kunnen worden om veranderingen in verweringssnelheden door de tijd af te leiden. $^{187}Os/^{188}Os$ in het bijzonder is in staat om veranderingen in verwering op klimaat-gerelateerde tijdschalen van 10–100 duizend jaar waar te nemen, terwijl de andere proxies typisch veranderingen in verwering vastleggen op tijdschalen van ~1 miljoen jaar of meer. Ik bediscussieer ook hoe verschillende andere aspecten van de geochemische kringlopen van deze elementen van belang zijn voor verweringsreconstructies. Tot slot presenteer ik verschillende verwerings-scenario's voor het Cenozoïcum op basis van het invers modelleren van datasets van de mariene $^{87}Sr/^{86}Sr$- en $^{187}Os/^{188}Os$-isotopensamenstelling, en licht ik de gevoeligheid van zulke schattingen voor onderliggende aannames uit.

Veranderingen in de mariene carbonaatchemie door de tijd heen vormen een belangrijke basis voor reconstructies voor andere aspecten van de koolstofkringloop, waaronder schattingen van atmosferische CO_2-concentraties in het verleden. In Hoofdstuk 3 wordt een model gebruikt om veranderingen in de carbonaatchemie van de pelagische oceanen tijdens het Cenozoïcum af te leiden. Door gepubliceerde datasets van oceaantemperaturen, atmosferische CO_2-concentraties en de carbonaatcompensatiediepte (CCD) te combineren met schattingen van carbonaat ion- (CO_3^{2-}) concentraties en pelagische carbonaat-afzettingssnelheden, kunnen temporele veranderingen in opgelost anorganisch koolstof (DIC), alkaliniteit en pH worden afgeleid. De relatieve stabiliteit van de berekende DIC- en alkaliniteit-waarden over het Cenozoïcum ondersteunt een evenwicht tussen carbonaat-input en -output op seculaire tijdschalen, maar desondanks kunnen belangrijke trends op lange termijn worden waargenomen. Binnen deze studie gebruik ik de nieuwe alkaliniteit-schattingen om onafhankelijk de aannames voor de parameters van het carbonaatsysteem te

testen die ten grondslag liggen aan gepubliceerde atmosferische CO_2-concentraties van het Cenozoïcum op basis van de boorisotopen-proxy ($\delta^{11}B$). De nieuwverworven alkaliniteit-schattingen komen in het algemeen overeen met de waarden die gebruikt zijn in de literatuur en daardoor vallen de meeste CO_2-concentraties bij herberekening ruim binnen de onzekerheidsmarge van de gepubliceerde waarden. Er zijn echter wel verschillen te zien voor het Mioceen en met name voor het Eoceen. Op basis van de nieuwe alkaliniteit-schattingen bereken ik voor het Mioceen CO_2-concentraties die 50-100 ppmv hoger zijn dan tot nu toe is beschreven. Herberekende CO_2 concentraties voor het Eoceen zijn daarentegen flink lager dan de gepubliceerde schattingen, met een verschil van meer dan 500 ppmv in het vroege Eoceen rond ~53 miljoen jaar geleden. Deze verschillen impliceren dat de evolutie van het carbonaatsysteem in het Eoceen mogelijk onzekerder is dan tot nu toe werd gedacht en onderstrepen de uitdaging van het verklaren van hoge atmosferische CO_2-concentraties ten tijde van een ondiepe positie van de CCD.

Carbonaataccumulatie vindt plaats in zowel pelagische- als in neritische afzettingsmilieus, maar van veranderingen in de begraving van neritische carbonaten door de tijd heen is weinig bekend. Daarom gebruik ik inzichten die gepresenteerd worden in Hoofdstuk 2 en 3 om neritische carbonaatbegraving gedurende het Cenozoïcum te reconstrueren in Hoofdstuk 4. Voor dit doel stel ik een massabalans op voor de instroom en uitstroom van carbonaat-alkaliniteit in de oceanen, die schattingen van alkaliniteit-aanvoer in associatie met continentale verwering incorporeert samen met onafhankelijke schattingen van pelagische carbonaatbegraving. Resulterende veranderingen in neritische carbonaatbegraving lijken gerelateerd te zijn aan belangrijke klimaatverschuivingen en de evolutie van de zeespiegel tijdens het Cenozoïcum. In het bijzonder voorspel ik een grote afname in neritische carbonaatbegraving die samenhangt met afkoeling en zeespiegeldaling tijdens de Eoceen-Oligoceen overgang (~34 miljoen jaar geleden). Vergelijkbare afnames in neritische carbonaatbegraving blijken samen te hangen met de Mi-1-glaciatie (~23 miljoen jaar geleden) en de Midden Mioceen Klimaat Transitie (~14 miljoen jaar geleden). Alhoewel de gevonden trends in neritische carbonaatbegraving van het Cenozoïcum uiteindelijk afhankelijk zijn van het gebruikte verweringsscenario, lijken deze kortstondige, klimaat-gerelateerde verschuivingen in neritische begraving robuust onder een groot scala aan aannames voor verwering. Dit versterkt de theorie dat de accumulatie van neritische carbonaten gemoduleerd wordt door veranderingen in het wereldwijde klimaat en de zeespiegel op geologische tijdschalen.

In Hoofdstuk 5 reconstrueer ik de respons van silicaatverwering tijdens de MECO om meer inzicht te krijgen in veranderingen in de koolstofkringloop op intermediaire tijdschalen van ~500 duizend jaar. Voor dit doel presenteer ik osmiumisotopen-samenstellingen ($^{187}Os/^{188}Os$) voor mariene sedimenten afkomstig van drie locaties in de Atlantische Oceaan en Grote Oceaan. In plaats van de verwachte $^{187}Os/^{188}Os$-toename als gevolg van versterkte continentale verwering na opwarming van het klimaat, zoals is vastgesteld voor de PETM, vind ik een bescheiden $^{187}Os/^{188}Os$-afname van ~0.05 tijdens de MECO. Deze kleine $^{187}Os/^{188}Os$-afname is waarschijnlijk gerelateerd aan versterkt vulkanisme en de daarmee geassocieerde verwering van vers basaltgesteente, maar aanhoudende carbonaatoplossing in de diepzee tijdens de MECO impliceert dat totale verweringssnelheden ongeveer constant moeten zijn gebleven. Ik gebruik vervolgens simulaties met het gevestigde Long-term Ocean-atmosphere-Sediment CArbon cycle Reservoir model (LOSCAR; Zeebe, 2012) om een reeks van scenario's met betrekking tot versterkt vulkanisme en/of verzwakte verwering te testen, en zo te achterhalen

hoe het geheel van MECO-observaties het best kan worden verklaard. In principe zou een 10–20% toename in vulkanisme voldoende zijn om CO_2-accumulatie, en dus opwarming van het klimaat, te veroorzaken. Een dergelijke toename zou echter leiden tot een daling van de CCD in plaats van de waargenomen stijging. Een cruciale bevinding is dat het model alleen in staat is om een CCD-stijging te reproduceren op de tijdschaal van de MECO als versterkt vulkanisme gepaard gaat met een sterk verzwakte silicaatverweringsterugkoppeling. Ik postuleer dat een dergelijke afname in de kracht van de verweringsterugkoppeling gerelateerd kan zijn aan een progressieve afname in de verweerbaarheid van de continenten tijdens het Eoceen (Caves et al., 2016). Als gevolg hiervan kan aanhoudende accumulatie van vulkanisch CO_2 leiden tot langdurige opwarming van het klimaat en oceaanverzuring tijdens de MECO.

In Hoofdstuk 6 presenteer ik een compilatie van nieuwe oppervlaktetemperaturen tijdens de MECO van twee locaties op de Newfoundland Drifts in de Noord-Atlantische Oceaan. Dankzij de hoge kleigehalten bevatten deze diepzeeafzettingen goed bewaarde foraminiferen en veel voorkomend organisch materiaal, wat robuuste temperatuurreconstructies met meerdere proxies mogelijk maakt. Hier integreer ik nieuwe datasets van *clumped* isotopen- (Δ_{47}), zuurstofisotopen- ($\delta^{18}O$) en sporenelementen- (Mg/Ca) verhoudingen van planktonische foraminiferen met datasets op basis van glycerol dialkyl glycerol tetraëder- (GDGT) distributies (TEX_{86}) en alkenonen-distributies ($U^{K'}_{37}$) om de volledige amplitude van opwarming in de Noord-Atlantische Oceaan te bepalen tijdens de MECO. De Δ_{47}- en $\delta^{18}O$-datasets van foraminiferen geven achtergrondtemperaturen van ~20 °C weer en laten een flinke stijging van 3–5 °C zien tijdens de MECO, evenals een ~1.5‰ verschuiving naar zwaardere $\delta^{18}O$-samenstellingen van zeewater die overeenkomen met een toename in zoutgehalte van ~2 ppm. Gezamenlijk suggereert dit dat het Newfoundland-gebied van de Noord-Atlantische Oceaan flink opwarmde tijdens de MECO, waarschijnlijk gerelateerd aan de noordelijke uitbreiding van warme, zoute wateren van de subtropische Noord-Atlantische kolkstroming. Dit levert extra bewijs dat de MECO een wereldwijd fenomeen moet zijn geweest, zoals ook afgeleid wordt in Hoofdstuk 5. Bovendien vormt deze eerste hoge-resolutie dataset van op Δ_{47} gebaseerde temperaturen van planktonische foraminiferen voor het Eoceen een onafhankelijke test voor de validiteit van de gevestigde temperatuurrelaties voor de andere proxies. De op Mg/Ca gebaseerde temperaturen zijn grotendeels vergelijkbaar met de op Δ_{47} gebaseerde temperaturen wat betreft absolute waarden, maar laten een meer ingetogen totale opwarming zien van ~2 °C. Deze discrepantie suggereert dat de bestaande Mg/Ca-temperatuurrelaties voor paleoklimaatreconstructies in het geologisch verleden nog verder verbeterd moeten worden. De op TEX_{86} gebaseerde temperaturen resulteren in de hoogste absolute waarden van alle proxies (30–31 °C) maar laten een opwarming van slechts ~1 °C zien. Op vergelijkbare wijze zijn de $U^{K'}_{37}$ waarden consistent verzadigd, wat impliceert dat temperaturen tenminste ~28 °C moeten zijn geweest. Deze verschillen tussen de op biomarkers gebaseerde proxies en de op foraminiferen gebaseerde proxies kunnen mogelijk voor een gedeelte worden verklaard doordat proxies temperaturen van verschillende waterdiepten of seizoenen vastleggen. Omdat de bestudeerde locaties zich echter in een *sediment drift* bevinden, is het ook mogelijk dat de TEX_{86}-temperaturen en $U^{K'}_{37}$-temperaturen beïnvloed worden door lateraal transport van GDGTs en alkenonen vanuit andere, warmere gebieden in de Noord-Atlantische Oceaan.

Tot slot presenteer ik in Hoofdstuk 7 een suite van paleoklimaatgegevens voor het midden Eoceen en het MECO-interval van de Kuma Formatie van de Belaya Rivier-sectie in de Noord-Kaukasus in Rusland. Deze gelamineerde sedimenten zijn afgezet op het continentaal plat in het Tethys-domein onder variabele zuurstofarme tot zuurstofloze omstandigheden. Deze

sedimenten hebben zowel een hoog carbonaat- ($CaCO_3$) gehalte als een hoog totaal organisch koolstof- (TOC) gehalte. Het MECO-interval van deze sectie wordt geïdentificeerd op basis van de biostratigrafie van kalkrijke nannofossielen en een TEX_{86}-temperatuur dataset, maar een goed diepte-tijd model is nog niet beschikbaar. Gereconstrueerde oppervlaktetemperaturen van zeewater zijn zeer hoog voor het bestudeerde interval (32–34 °C) en laten een MECO-opwarming van ~2 °C zien. Opvallend is dat er geen significante veranderingen in het $CaCO_3$-gehalte worden waargenomen tijdens de opwarmingsfase van de MECO. Bovendien lijkt de daaropvolgende afkoelingsfase langer te duren dan in diepzeedatasets afkomstig uit andere oceaanbekkens. Bulk carbonaat $\delta^{18}O$-waarden laten eveneens weinig verandering zien tijdens de MECO-opwarming, maar bevatten een tijdelijke verschuiving naar zeer negatieve waarden gedurende de MECO-afkoeling die samenvalt met een interval van verminderde $CaCO_3$- en verhoogde TOC-gehalten. Dit patroon van MECO-opwarming gevolgd door een interval van verhoogde TOC-preservatie en/of -begraving tijdens de daaropvolgende afkoelingsfase is ook herkend in de Alano di Piave-sectie in Italië (Spofforth et al., 2010). Deze mogelijk gerelateerde organisch-rijke afzettingen kunnen een regionale periode van begraving van organisch koolstof in de Tethys Oceaan voorstellen die kan hebben bijgedragen aan MECO-afkoeling. Dit is met name belangrijk in verband met de verminderde silicaatverweringsthermostaat tijdens het midden Eoceen zoals wordt voorgesteld in Hoofdstuk 5, omdat de begraving van organisch koolstof een alternatief mechanisme vormt voor CO_2-afvoer en klimaatherstel. Tot slot worden kwik- (Hg) gehalten gebruikt om mogelijk sedimentair bewijs voor vulkanische activiteit tijdens de MECO te onderzoeken. De initiële dataset in lage resolutie laat echter geen significante Hg/TOC-verrijking zien in het bestudeerde interval, en kan daarom dus niet worden gebruikt als bewijs voor een eventuele periode van versterkt vulkanisme als oorzaak van CO_2-stijging en MECO-opwarming.

Vooruitblik

Dit proefschrift presenteert nieuwe inzichten in het functioneren van de koolstofkringloop gedurende het Cenozoïcum, evenals verschillende nieuwe datasets om gekoppelde veranderingen in de koolstofkringloop en het klimaat tijdens de MECO beter te begrijpen. Dit proefschrift doet ook belangrijke nieuwe vragen rijzen die verder onderzoek vereisen. Alhoewel de temporele evolutie van de kringlopen van verschillende elementen over het algemeen steeds beter wordt begrepen, is het nog steeds lastig om een enkele, convergente verweringsgeschiedenis voor het Cenozoïcum af te leiden door middel van inversie van datasets van mariene isotopensamenstellingen. Dit komt gedeeltelijk doordat verweringsproxies verschillend reageren op verschillende forceringen, maar ook doordat potentiële veranderingen in de isotopensamenstelling van belangrijke elementfluxen nog niet goed bekend zijn, zoals ik heb laten zien in Hoofdstukken 2 en 4. Een manier om beter inzicht te krijgen in de isotopensamenstellingen van verweringsfluxen is door temporele veranderingen in de isotopensamenstellingen van verschillende gesteentetypen die bijdragen aan verwering op wereldwijde schaal te reconstrueren op basis van compilaties van datasets van sedimentaire gesteenten en stollingsgesteenten. Dit maakt meer kwantitatieve schattingen van veranderingen in verweringsfluxen uit het verleden mogelijk, die op hun beurt weer nieuwe wegen openen voor vervolgstudies met modellen.

De nieuwe MECO-datasets leiden ook tot nieuwe vragen met betrekking tot de interacties tussen de koolstofkringloop en het klimaat. Als de kracht van de negatieve silicaatverweringsterugkoppeling inderdaad progressief is afgenomen tijdens het Eoceen

als gevolg van verminderde verweerbaarheid van de continenten, zoals voorgesteld wordt in Hoofdstuk 5, zouden zulke veranderingen terug te zien moeten zijn in een graduele verandering in de duur van klimaatherstel van de *hyperthermals* in het Eoceen ten opzichte van de mechanismen die verantwoordelijk zijn voor opwarming. Dit kan mogelijk getest worden door additionele gegevensreeksen in hoge resolutie te verzamelen van verweringsfluxen, atmosferische CO_2-concentraties, oceaantemperaturen en veranderingen in de positie van de CCD voor *hyperthermals* in het tijdsinterval tussen de PETM en de MECO. Daarnaast kan een verminderde silicaatverweringsterugkoppeling ook een rol hebben gespeeld in aanhoudende CO_2-stijging en klimaatopwarming tijdens andere raadselachtige perioden in de geschiedenis van de Aarde, zoals de Perm-Trias transitie of de grootschalige glaciaties van het Paleozoïcum en Neoproterozoïcum.

Verder is de exacte koolstofbron die CO_2-stijging en MECO-opwarming veroorzaakte nog steeds niet gevonden. De $^{187}Os/^{188}Os$-datasets en modelsimulaties van de koolstofkringloop die gepresenteerd worden in Hoofdstuk 5 suggereren een vulkanische CO_2-bron tijdens de MECO, maar in tegenstelling tot de perioden van grootschalige zuurstofloosheid in de oceaan (OAEs) uit het Mesozoïcum is er geen bewijs voor de vorming van een grote vulkanische provincie (LIP) tijdens het midden Eoceen. Deze studie geeft ook aan dat de CO_2-emissies niet noodzakelijkerwijs extreem hoog hoeven te zijn geweest tijdens fasen van verminderde verwering, dus het zou uiteindelijk zelfs onrealistisch kunnen blijken om de exacte bron te bepalen. Toekomstige studies kunnen echter focussen op het verkennen van ontgassingssnelheden van andere mogelijk actieve vulkanische gebieden, zoals continentale vulkanische bogen. Dit kan gekoppeld worden aan het genereren van aanvullende Hg/TOC-datasets van de MECO voor locaties die zich dichtbij een vermoedelijke vulkanische bron bevinden.

De oppervlaktetemperaturen van zeewater in de Noord-Atlantische Oceaan die gepresenteerd worden in Hoofdstuk 6 laten het unieke potentieel zien van het gebruik van meerdere proxies samen met Δ_{47} om op een robuustere wijze absolute temperaturen te reconstrueren. De op Δ_{47} gebaseerde temperatuurschattingen kunnen echter nog steeds verbeterd worden door het genereren van aanvullende data om de bijbehorende analytische onzekerheden verder te verkleinen. Bovendien zou het verder verhogen van de resolutie van de op foraminiferen gebaseerde datasets het mogelijk maken om de relaties tussen de oppervlaktetemperaturen van zeewater en astronomische invloeden op het klimaat op te lossen. Dit is van belang omdat de Newfoundland Drifts momenteel de meest uitgebreide beschikbare sedimentaire archieven van de MECO vormen en gebruikt kunnen worden om een astronomisch afgestemde chronologie van de MECO op te stellen.

Tot slot moet de mogelijke periode van organische koolstofbegraving na de MECO, zoals beschreven in Hoofdstuk 7, beter onderzocht worden. Als de begraving van organische koolstof inderdaad is toegenomen in de nasleep van de MECO, moeten de duur van deze gebeurtenis en de hoeveelheid koolstof die begraven is kwantitatief worden geschat. Dit vereist het gedetailleerd in kaart brengen van een groot gebied met betere stratigrafische begrenzingen. Verder moeten zulke schattingen worden vergeleken met modelsimulaties om te evalueren of deze hoeveelheden organische koolstofbegraving voldoende zijn om MECO-afkoeling op globale schaal te veroorzaken.

Acknowledgements

(Dankwoord)

Dankwoord

In de afgelopen vier jaar hebben vele mensen bijgedragen aan de totstandkoming van dit proefschrift en daar ben ik zeer dankbaar voor. Jullie aanmoediging en vriendschap hebben mij de energie gegeven om deze reis tot een mooi einde te brengen.

Ten eerste wil ik mijn promotoren Appy Sluijs en Jack Middelburg bedanken voor de geweldige kans om aan dit avontuur in de wondere wereld van de wetenschap te beginnen en voor jullie mentorschap, steun en vertrouwen gedurende de jaren. Het enthousiasme van Appy en het realisme van Jack bleken een gouden combinatie voor het aanwakkeren van creativiteit en productiviteit, maar bovenal ben ik erg blij met de inhoudelijke vrijheid die ik heb gekregen om zelf de koers van mijn project te bepalen. Verder kan ik jullie ontspannen houding en gevoel voor humor ook zeer waarderen. Ik vind het een voorrecht dat ik van jullie de mogelijkheid heb gekregen om tijdens mijn promotie meer dan twintig reizen te maken voor onderzoek, congressen, veldwerken en cursussen – dat heeft vele mooie herinneringen opgeleverd, vaak in jullie gezelschap. Ik heb genoten van elke dag dat ik met jullie heb samengewerkt en zie ernaar uit om die samenwerking in de toekomst voort te zetten.

I also wish to express my sincere thanks to my co-advisor Steve Bohaty from the University of Southampton. Your eye for detail and extensive knowledge of the MECO have been instrumental in both the design and completion of this project. As an external advisor you were not always available, but I really appreciate that you facilitated a visit to the National Oceanography Centre in Southampton for me and helped provide access to sample material. I also have fond memories of the various meetings we both attended – in your company I have had nothing but excellent food and drinks.

Vanaf het begin was het duidelijk dat mijn onderzoek verweven zou zijn met het onderzoek van collega-PhD Margot Cramwinckel. De afgelopen vier jaar hebben we onze krachten gebundeld en als Team MECO samengewerkt aan verschillende projecten, met geweldig resultaat. Ik vond het top om samen te kunnen sparren over wetenschap en kijk met plezier terug op de vele koffietjes, borrels en etentjes. Van een zonsopgang in Urbino en sightseeing in San Francisco tot het schrijven van een manuscript in een week tijd – het was mooi om dit avontuur met jou te kunnen delen en ik ben blij dat jij één van mijn paranimfen bent.

In addition, I'd like to thank my other collaborators on various research projects. In particular, I thank Dave Selby for hosting me in his lab at Durham University and introducing me to the ins and outs of osmium isotope analyses for weathering reconstructions. I am grateful to Karline Soetaert for showing me how to code and perform model simulations in R. I thank Bernie Boudreau for discussions on marine carbonate chemistry during his sabbatical stay in Utrecht, which led to two great collaborations. Furthermore, I thank everyone who has contributed to my MECO temperature reconstructions for the North Atlantic, including Phil Sexton, Don Penman and Paul Wilson for sharing sample material, the Clumpy Team in Utrecht – Ilja Kocken, Inigo Müller, Anne van der Meer and Martin Ziegler – for facilitating a very large number of clumped isotope analyses, and Thomas Leutert and Nele Meckler for performing part of the work in their lab at the University of Bergen. In addition, I thank Annique van der Boon, Niels van Helmond and Kevin Vis for a magnificent fieldwork in 2017 along the Belaya River in the Russian Caucasus mountains, where we sampled MECO sediments from the Tethys realm that led to several surprising findings. I also thank Michael Morton, Sarah Davies, Steve Vincent, Sergey Popov and Larisa Golovina for joining us in the field and making this trip possible.

Mijn dank gaat verder uit naar de geologen, geochemici en paleoceanografen van het departement Aardwetenschappen in Utrecht, waaronder Peter Bijl, Bas van de Schootbrugge, Francesca Sangiorgi, Henk Brinkhuis, Martin Ziegler, Frits Hilgen, Lucas Lourens, Gert-Jan Reichart, Francien Peterse, Stefan Schouten, Caroline Slomp, João Trabucho-Alexandre, Wout Krijgsman en Douwe van Hinsbergen. Bedankt voor de discussies, adviezen en samenwerkingen in de afgelopen jaren!

I also appreciate the scientific discussions I've had with Richard Zeebe, Jerry Dickens, Jim Zachos, Andy Ridgwell, Lee Kump, Paul Pearson, Alex Dickson and Gabe Bowen during various meetings and conferences.

Ik wil verder Natasja Welters, Giovanni Dammers, Arnold van Dijk, Michiel Kienhuis en Klaas Nierop van het Utrecht Geolab en Wim Boer van het NIOZ bedanken voor hun assistentie in het laboratorium. Daarnaast bedank ik Marjolein Mullen-Pouw en Tjitske Vos voor alle administratieve ondersteuning en in het bijzonder het versturen van talrijke pakketjes met gesteentemonsters. Ik wil ook NESSC-collega's Mirjam van Kan-Parker en Bjinse Dankert bedanken voor de administratieve ondersteuning en de samenwerkingen op communicatie- en mediagebied.

Dan mijn andere collega's. Laat ik beginnen om mijn (voormalige) kantoorgenoten Arjen Grothe, Carolien van der Weijst, Frida Hoem, Margot Cramwinckel en Joost Frieling te bedanken voor de gezelligheid, discussies en afleiding door de jaren heen. Het was me een genoegen om met jullie in drie verschillende gebouwen een kantoor te delen! De uiteindelijke thematische indeling met Margot, Joost en mijzelf als Team Paleogeen bleek bovendien een succesvol recept voor verschillende gezamenlijke projecten. Ook mijn andere (oud-)collega's van de Mariene Palynologie en Paleoceanografie groep – Tjerk Veenstra, Julian Hartman, Mariska Datema, Johan Vellekoop, Niels van Helmond, Chloé Morales, Martin Schobben en Linda van Roij – wil ik bedanken voor de fijne werksfeer, compleet met espresso's, tafelvoetbalsessies en borrels in de Primus. Ook collega's van andere groepen – Shaun Akse, Wytze Lenstra, Martijn Hermans, Nina Papadomanolaki, Matthias Kuderer, Anne Roepert, Ilja Kocken, Inigo Müller, Cindy Schrader, Anne van der Meer, Loes van Bree, Emily Dearing Crampton-Flood, Bas van der Meulen en Fabian Ercan – bedank ik voor hun bijdragen hieraan. Ik hoop nog veel van jullie te horen!

Over the past years I've also had the pleasure of meeting many NESSC-colleagues at other institutes. Caitlyn Witkowski, Gabriella Weiss, Nadine Smit, Esmee Geerken, Linda Dämmer, Josh Dean, Luke Blauw, Michiel in 't Zandt, Bregje van der Bolt, Els Weinans, Michiel Baatsen, Tijn Berends, André Jüling and many others: thanks for the great discussions, fun times at conferences and nights out after NESSCwork events. I look forward to seeing where your careers will take you in the future!

Ik bedank ook studenten Pam Vervoort, Niels Waarlo, Rogier Hidding en Chris Fokkema voor hun inzet tijdens scriptieprojecten. Het was een leuke en leerzame ervaring om jullie te begeleiden en jullie onderzoeken hebben bovendien mooie resultaten opgeleverd!

Onder de werkreizen die ik heb gemaakt bevinden zich een paar trips die extra memorabel zijn. Als eerste noem ik de roadtrip die ik samen met NESSC-collega's Margot, Loes, Anne, Emily, Carolien, Michiel en Bregje heb gemaakt onderweg naar de legendarische Urbino Summer School in Paleoclimatology in 2015. Deze zomerschool was niet alleen een schitterende inwijding in de wereld van de klimaatmaffia, maar ook een mooie manier om elkaar beter te leren kennen aan het begin van onze PhD projecten. De pizza's, pasta's, ijsjes, biertjes en grappa's waren de kerst op de taart.

Eén van de hoogtepunten van 2016 was de AGU Fall Meeting in San Francisco, waar we met een grote delegatie van MPP & Friends naartoe waren gereisd om nieuwe onderzoeksresultaten te presenteren en de Oscar-esque medaille-uitreiking van Appy te aanschouwen. Hier gaf ik mijn eerste presentatie voor een groot internationaal publiek. Ook de korte trip na afloop van de conferentie langs de Californische kust over Highway 1 was zeer de moeite waard.

In 2017 heb ik meerdere bijzondere reizen gemaakt voor mijn project, maar ik wil de Climatic and Biotic Events of the Paleogene (CBEP) conferentie in de bergen bij Salt Lake City speciaal uitlichten. Deze conferentie op drie kilometer hoogte en de daaropvolgende tweedaagse excursie in Utah waren fenomenaal. Om het plaatje compleet te maken ging ik samen met Joep van Dijk en Stefano Bernasconi voorafgaand nog op reis door Wyoming: van een expeditie naar de PETM-afzettingen van het Bighorn-bekken en een zoektocht naar vermeende sideriet-ontsluitingen tot een paar dagen de toerist uithangen in Yellowstone. Bedankt voor dit toffe avontuur!

Daarnaast zal ik ook de dagen in Boston en New Hampshire met Joost, Niels, Wytze en Martijn na afloop van de Goldschmidt conferentie in 2018 onthouden. Ik aarzelde van tevoren of ik zo vlak voor de finish van mijn project nog wel tijd had voor een laatste vakantie, maar ik had deze reis zeker niet willen missen. De bultrugwalvissen langs de kust en de bergwandelingen in de White Mountains waren erg gaaf, bedankt voor deze mooie momenten!

Verder wil ik Luc en Martin (en Hemmo Abels in het eerste jaar) bedanken voor het driemanschap van het tweedejaarsveldwerk. Vier jaar lang heb ik samen met jullie studenten mogen begeleiden op veldwerk in Spanje, tijdens de nieuwe excursie van het Tremp-bekken in de Pyreneeën naar Zumaia aan de kust van Baskenland. Ik wil jullie bedanken voor de mooie en leerzame ervaringen, de toeristische uitstapjes, de pintxos en de gin-tonics – ik kijk er met veel plezier op terug!

In het bijzonder wil ik mijn studiematen Shaun en Joep bedanken voor hun betrokkenheid en vriendschap in de afgelopen jaren. Vanaf ons tweedejaarsveldwerk in Spanje in 2011 hebben we een band gesmeed en sindsdien hebben we op de universiteit en daarbuiten veel samen opgetrokken. Ik vind het nog steeds mooi dat we na ons gezamenlijke afstuderen alle drie als PhD zijn doorgegaan met aardwetenschappelijk onderzoek en ben blij dat we onze stedentriptraditie na Berlijn en Lissabon uiteindelijk in Parijs hebben kunnen voortzetten. Klimaatverandering, duurzaamheid en wetenschap waren terugkerende thema's bij onze borrels en etentjes, maar bovenal hebben we samen veel kunnen lachen. Joep, ik vond het magisch om direct na het inleveren van mijn proefschrift naar Zwitserland af te reizen om bij jouw eigen verdediging aanwezig te zijn en het dak van de ETH in Zürich eraf te feesten. Shaun, ik vond het top om de afgelopen jaren samen op te trekken in Utrecht en heb genoten van alle keren dat we in bewust of onbewust passende outfits de show hebben gestolen tijdens uitjes en conferenties. Ik kijk er naar uit om jou als paranimf naast me te hebben staan!

Hard werken is alleen mogelijk als je ook tijd neemt voor ontspanning en gelukkig heb ik veel mensen in mijn omgeving die daar hetzelfde over denken. In de eerste plaats wil ik mijn jaarclubgenoten van Titaan bedanken voor hun vriendschap in de afgelopen jaren. Mannen, ik heb genoten van de gezelligheid op dinsdag en onze borrels, feestjes en vakanties, met de lustrumreis naar Cuba als absolute toppunt. Verder bedank ik mijn dispuutsgenoten van het Collegium Illustrissimum Hermandad, met wie ik vrijdagborrels, diners en stedentrips tot kunst heb verheven – ik ben blij dat we binnen zijn. Ook mijn vrienden en collega's van het Geologisch College Miölnir bedank ik voor de bijzondere evenementen en geologische excursies van de afgelopen jaren.

Ik bedank mijn vrienden uit Amersfoort – Kim, Rutger en Koen – voor de gezelligheid tijdens etentjes en film- of spelletjes-avonden. Ik vind het bijzonder dat we elkaar al zo lang kennen en hoop jullie ook in de komende jaren te blijven zien!

Ik bedank ook Paul, Jeroen en Maria voor een bijzonder warme band in de afgelopen jaren. Ik ken weinig mensen die zo wereldwijs zijn als jullie en ik heb veel aan jullie vriendschap en adviezen gehad!

Ik wil mijn familie bedanken voor alle aanmoediging en steun, niet alleen in de afgelopen vier jaar maar ook in de jaren die daaraan vooraf zijn gegaan. Papa, mama en Jorik: jullie hebben mij voor een belangrijk deel gevormd en dat zal ik altijd bij me dragen. Papa en mama, bedankt dat jullie er altijd voor me zijn geweest en me blijven uitdagen om mijn grenzen te verleggen. Jorik, bedankt voor alle streken en dat je al die jaren mijn broederlijke klankbord bent geweest. Verder bedank ik jullie, en in het bijzonder ook oma, voor de inspiratie om aardwetenschappen te gaan studeren. Toen ik negen jaar geleden aan mijn studie begon had ik niet durven dromen dat ik nu een proefschrift op mijn naam zou hebben staan!

En tot slot bedank ik Sabine, mijn meest trouwe partner tijdens dit bijzondere avontuur. Jij hebt als geen ander meegemaakt hoe ik me een weg baande in de wereld van de wetenschap en was er altijd om mijn successen te vieren of om mijn frustraties te verzachten. Dankjewel voor je onvoorwaardelijke steun, raad, geduld en liefde in de afgelopen jaren – ik zal het nooit vergeten.

Robin van der Ploeg
Utrecht, 25 januari 2019

Curriculum Vitae

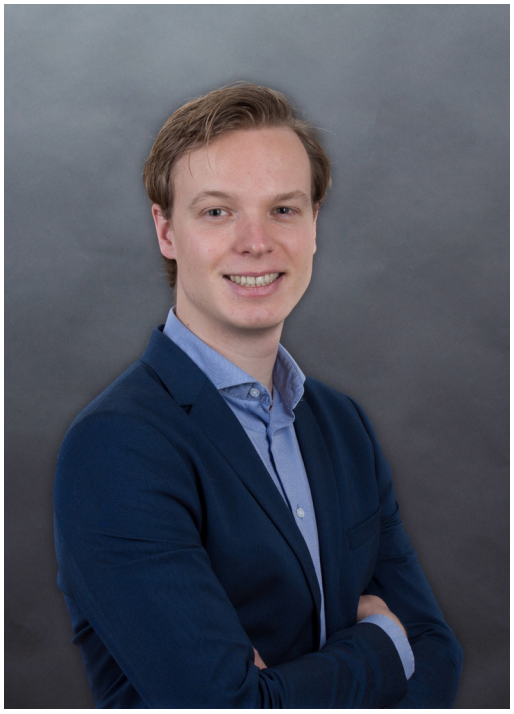

Robin van der Ploeg was born in Amersfoort on June 30th, 1992 and has been fascinated by nature and wildlife since he was little. He completed his secondary education (gymnasium) at Corderius College in Amersfoort in 2009 and subsequently studied Earth Sciences (BSc) and Earth, Life and Climate (MSc) at Utrecht University, where he graduated cum laude in 2012 and 2014, respectively. During his studies in Utrecht, Robin discovered that he was especially interested in climate change, geochemical cycles and the evolution of life in Earth's history. Robin explored these subjects in various research projects, including a BSc thesis on astronomically-paced climate change in the Mediterranean region during the Pleistocene, a research traineeship funded by the Royal Netherlands Academy of Arts and Sciences (KNAW) on temperature reconstructions in the Netherlands during the Eemian, a MSc thesis on plant diversity and biogeography across the Permian-Triassic boundary and an internship in exploration geochemistry at Shell Global Solutions BV in Rijswijk. After his graduation, Robin started working as a PhD candidate at the Department of Earth Sciences at Utrecht University in November 2014. The aim of his PhD project was to reconstruct the carbon cycle evolution of the Cenozoic, with a particular focus on the Eocene greenhouse world and the Middle Eocene Climatic Optimum (MECO). Research subjects included the behavior of the silicate weathering thermostat, reconstructions of atmospheric CO_2 concentrations and ocean temperatures, as well as ocean carbonate and trace element chemistry. Since the start of his PhD, Robin has been actively involved in outreach activities and made several appearances in the media. In addition, Robin founded The Biogeologist (www.biogeologist.com) to share his passion for the natural world with the general public. From January 2019 onwards, Robin continued his career as a postdoctoral researcher in Earth Sciences at Utrecht University.

Peer-reviewed publications

Published

Boudreau, B. P., Middelburg, J. J., Sluijs, A. & **Van der Ploeg, R.** Secular variations in the carbonate chemistry of the oceans over the Cenozoic, *Earth and Planetary Science Letters* 512, 194–206 (2019).

Cramwinckel, M. J., **Van der Ploeg, R.**, Bijl, P. K., Peterse, F., Bohaty, S. M., Röhl, U., Schouten, S., Middelburg, J. J. & Sluijs, A. Harmful algae and export production collapse in the equatorial Atlantic during the zenith of Middle Eocene Climatic Optimum warmth, *Geology* (2019).

Van der Ploeg, R., Selby, D., Cramwinckel, M. J., Yang, L., Bohaty, S. M., Middelburg, J. J. & Sluijs, A. Middle Eocene greenhouse warming conditioned by diminished weathering feedback, *Nature Communications* 9, 2877 (2018).

Cramwinckel, M. J., Huber, M., Kocken, I. J., Agnini, C., Bijl, P. K., Bohaty, S. M., Frieling, J., Goldner, A., Hilgen, F. J., Kip, E. L., Peterse, F., **Van der Ploeg, R.**, Röhl, U., Schouten, S. & Sluijs, A. Synchronous tropical and polar temperature evolution in the Eocene. *Nature* 559, 382–386 (2018).

Submitted

Van der Ploeg, R., Boudreau, B. P., Middelburg, J. J. & Sluijs, A. Cenozoic neritic carbonate burial, *Geology* (in revision).